DEM-CFD ANALYSIS OF CONTACT ELECTRIFICATION AND ELECTROSTATIC INTERACTIONS DURING POWDER HANDLING PROCESSES

CHUNLEI PEI

BEng

A thesis submitted to the University of Birmingham

for the degree of

DOCTOR OF PHILOSOPHY

School of Chemical Engineering

University of Birmingham

September 2013

ABSTRACT

Electrostatic phenomena are pervasive in powder handling processes. In this study, contact electrification and electrostatic interactions during powder handling processes are explored using the discrete element method coupled with computational fluid dynamics (DEM-CFD), in which contact electrification and electrostatic interaction models are developed and implemented. The effects of particle shape on contact electrification are also investigated, for which multi-sphere methods are adapted and implemented into the DEM-CFD.

The electrostatic and dynamic behaviours in various powder handling processes are then analyzed, which include contact electrification of spherical particles during fluidization; electrostatic interactions during deposition of mono-charged and bi-charged particles; contact electrification and electrostatic interactions of spherical particles during fluidization; contact electrification of elongated particles in a vibrating container and particles of arbitrary shapes in a rotating drum.

It is found that charge accumulation and distribution of particles are caused by contact electrification and dispersion of mono-charged particles and agglomeration of bi-charged particles are induced by electrostatic interactions. The combined effects of contact electrification and electrostatic interactions can alter the dynamic behaviours of particles and the performance of powder handling processes. Non-uniform charge distributions can be induced on particles of irregular shapes and the charge accumulation is also affected by particle shapes.

KEYWORDS: contact electrification; electrostatic interactions; discrete element method; computational fluid dynamics; multi-sphere method

ACKNOWLEDGEMENTS

I would like to express my sincere gratitude to Prof. Chuan-Yu (Charley) Wu and Prof. Michael Adams for supervising and mentoring me throughout my PhD study. Their broad knowledge, constructive support and great patience help me to progress in this exciting and amazing research area.

I would like to give my great thanks to Dr. Colin Thornton and many fellow researchers including Drs. Yu Guo and Shen Yu. I benefit from the discussions and communications with them during my PhD study.

I would like to acknowledge Drs. David England, Harald Berchtold and Stephen Byard, from Sanofi (previously sanofi-aventis), for many excellent and helpful comments and advices.

Special thanks to Sanofi (previously sanofi-aventis) for fully funding me this great research project.

Finally, I would like to thank my parents for their heartful support and encouragement.

TABLE OF CONTENTS

CHAPTER 1 INTRODUCTION 1

1.1. Background 1

1.2. Objectives 3

1.3. Outline of this thesis 4

CHAPTER 2 LITERATURE REVIEW 6

2.1. Introduction 6

2.2. Mechanisms of contact electrification 6

2.2.1. Contact electrification between metals 7

2.2.2. Contact electrification between metals and polymers 10

2.2.3. Contact electrification of insulators 15

2.2.4. Frictional electrification 17

2.2.5. The influence factors of contact electrification 18

2.3. Mechanisms of electrostatic interactions 20

2.4. Contact electrification and electrostatic interactions in powder handling processes 23

2.4.1. Contact electrification in powder handling processes 23

2.4.2. Electrostatic interactions in powder handling processes 28

2.4.3. Combined effects of electrification and electrostatic interactions 32

2.5. DEM-CFD for contact electrification and electrostatic interactions 36

2.5.1. The discrete element method 37

2.5.2. DEM-CFD method 47

2.5.3. DEM-CFD applications 50

2.5.4. DEM-CFD analysis of contact electrification and electrostatic interactions 51

2.6. Other numerical methods for contact electrification and electrostatic interactions 59

2.7. Summary 62

CHAPTER 3 CONTACT ELECTRIFICATION FOR SPHERICAL PARTICLES 63

3.1. Introduction 63

3.2. Implementation of electrification into DEM 63

3.2.1. Contact electrification model 63

3.2.2. Model validation 66

3.2.3. Effect of particle size on contact electrification 70
3.3. Contact electrification of spherical particles during fluidization 73
3.3.1. Model setup 73
3.3.2. Results 75
3.4. Discussions 81
3.4.1. The effect of particle size on contact electrification during the impact with a substrate 81
3.4.2. Contact electrification during fluidization 82
3.4.3. Charge relaxation during contact electrification 84
3.5. Summary 84

CHAPTER 4 MODELLING ELECTROSTATIC INTERACTIONS USING DEM-CFD 86

4.1. Introduction 86
4.2. Electrostatic interaction models 86
4.2.1. Basic principles 86
4.2.2. Particle impact with electrostatic interactions 88
4.2.3. Direct truncation (DT) and Hybrid particle – cell (HPC) algorithms 91
4.3. Deposition of mono-charged particles 95
4.3.1. Model setup 95
4.3.2. Deposition behaviour of mono-charged particles 97
4.3.3. Radial distribution function 100
4.3.4. Granular temperature 102
4.4. Deposition of bi-charged particles 104
4.4.1. Model setup 104
4.4.2. The deposition of particles 106
4.4.3. Coordination number 109
4.4.4. Deposition ratio 111
4.5. Discussions 114
4.5.1. Deposition of mono-charged particles 114
4.5.2. Deposition of bi-charged particles 117
4.6. Summary 119

CHAPTER 5 CONTACT ELECTRIFICAITON AND ELECTROSTATIC INTERACTIONS IN FLUIDIZATION 122
5.1. Introduction 122
5.2. Model setup 122
5.3. Results 124
5.3.1. The particle profiles 124
5.3.2. The charge distribution 126
5.3.3. The charge accumulation 130
5.3.4. The performance of fluidization 131
5.4. Discussions 134
5.4.1. The charging process during fluidization 134
5.4.2. Agglomeration during fluidization 135
5.4.3. The performance of fluidization 136
5.4.4. The charge distribution 136
5.4.5. The effect of the column 137
5.5. Summary 138
CHAPTER 6 MULTI-SPHERE METHODS FOR CONTACT ELECTRIFICAITON 139
6.1. Introduction 139
6.2. Contact electrification and charge distribution of elongated particles 139
6.2.1. Introduction 139
6.2.2. The DEM model 139
6.2.3. Model setup 143
6.2.4. Results 146
6.2.5. Discussions 152
6.2.6. Summary 159
6.3. Contact electrification of particle with arbitrary shape 161
6.3.1. Introduction 161
6.3.2. The DEM model 161
6.3.3. The model setup 166
6.3.4. Results 170
6.3.5. Discussions 179

6.3.6. Summary 183

CHAPTER 7 DISCUSSIONS 185

7.1. Introduction 185

7.2. The contact electrification model 185

7.3. The electrostatic interaction model 186

7.4. Contact electrification and electrostatic interactions in powder handling processes 188

CHAPTER 8 CONCLUSIONS AND FUTURE WORK 192

8.1. Introduction 192

8.2. Conclusions 192

8.3. Future work 196

APPENDIX A HPC AND DT METHODS FOR BI-CHARGED PARTICLES 199

APPENDIX B CHARGE ACCUMULATION OF MULTI-SPHERES WITH SAME EQUIVALENT SPHERICAL DIAMETER 201

APPENDIX C AN EXAMPLE OF INPUT FILE 204

C.1. Deposition of particles in a column 204

C.2. Fluidization 207

C.3. CFD setup 209

APPENDIX D SELECTIONS OF DEVELOPED CODES 211

D.1. Codes for contact electrification 211

D.2. Codes for electrostatic interactions 213

REFERENCES 220

LIST OF FIGURES

Figure 2.1 Charges on the metal objects after contact at the critical separation distance. 9

Figure 2.2 The impact process between a particle and a plate for contact electrification (Matsuska *et al.*, 2010). 13

Figure 2.3 The relaxation model (Matsuyama and Yamamoto, 1995a). 14

Figure 2.4 A triboelectric series list excerpted from reference (McCarty and Whitesides, 2008). 16

Figure 2.5 Electrification of particles flowing on a tilted surface (Ireland, 2010a). 26

Figure 2.6 Measurement of charge distribution in the fluidization (Sowinski *et al.*, 2010).... 27

Figure 2.7 Agglomerates of cellulose and acrylic beads (LaMarche *et al.*, 2010). a) Two acrylic beads partially covered by cellulose. b) A bead covered completely in agglomerated cellulose. 30

Figure 2.8 The structure of electrostatic agglomerates (McCarty *et al.*, 2007a). 33

Figure 2.9 A snapshot of DEM simulations of particle deposition on the cylinder (Liu *et al.*, 2010). 56

Figure 2.10 Interface model of aluminium (upper) and PTFE (lower) (Shirakawa *et al.* 2010). 60

Figure 2.11 Instantaneous contours in the bubbling fluidized-bed: (a) electric potential (V) and (b) radial component of electric field (V/m) (Rokkam *et al.* 2013). 61

Figure 3.1 The model set-up for impact of a sphere with a substrate..... 67

Figure 3.2 The variation of transferred charge with maximum contact area. 69

Figure 3.3 The accumulation of electrostatic charge as a function of the number of impacts. 69

Figure 3.4 The accumulation of electrostatic charge on particles of various diameters (d_p). . 71

Figure 3.5 The variation of surface charge density and charge-to-mass ratio with the particle size. 71

Figure 3.6 Transferred charge in each collision as a function of net charge. 72

Figure 3.7 Illustration of the model set-up for contact electrification during fluidization. 73

Figure 3.8 Particle profiles during fluidization at various time instants (v_g = 200 mm·s^{-1}). ... 75

Figure 3.9 Charge density distribution (C·m^{-2}) at defined times (v_g = 200 mm·s^{-1}). ... 76

Figure 3.10 Particle profiles at t = 0.6 s for various superficial gas velocities. ... 77

Figure 3.11 Charge density distributions (C·m^{-2}) at t = 0.6 s for various superficial gas velocities. ... 77

Figure 3.12 Mean net charge distribution along the x-axis at t = 0.6 s. ... 78

Figure 3.13 The charge accumulation in the fluidization. ... 79

Figure 4.1 The electrostatic interaction between two charged particles. ... 87

Figure 4.2 The image force between the particle and inductive surface. ... 87

Figure 4.3 A comparison between the Coulomb and gravitational forces. ... 88

Figure 4.4 The relationship between Coulomb force and distance. ... 89

Figure 4.5 The normal contact force as a function of the time for neutral and charged cases. 90

Figure 4.6 The Coulomb force as a function of time with contact damping for the charged case. ... 91

Figure 4.7 A 2D illustration of the cell list method ... 92

Figure 4.8 DEM model for deposition of mono-charged particles. ... 95

Figure 4.9 Particle profiles at various time instants obtained with the HPC method ... 98

Figure 4.11 Equilibrium packing patterns obtained using the DT method with different R_c . 99

Figure 4.12 Equilibrium packing patterns obtained using the HPC method with different R_c 100

Figure 4.13 RDF profiles obtained using the DT method with different R_c ... 101

Figure 4.14 RDF profiles obtained using the HPC method with different R_c 101

Figure 4.15 The evolutions of granular temperatures obtained using the DT method for different values of R_c 103

Figure 4.16 The evolutions of granular temperatures obtained using the HPC method for different values of R_c 103

Figure 4.17 The computational setup of the deposition of bi-charged particles: w = 5 mm, h_0 = 5 mm, l = 5 mm. 105

Figure 4.18 The deposition of neutral particles in air (ξ = 0.0). 107

Figure 4.19 The deposition of charged particles in air (ξ = 42.0). 108

Figure 4.20 The deposited granular bed of various charged particles: (a) ξ = 42.0, without image force (b) ξ = 7.88, with image force (b) ξ = 7.88, without image force). 109

Figure 4.21 The evolution of coordination number during the deposition process. 111

Figure 4.22 Deposition ratios for bi-charged particles in air and vacuum without image force. 112

Figure 4.23 Deposition ratio for bi-charged particles in air with and without image force. . 112

Figure 4.24 Average deposition rates of various cases. 113

Figure 4.25 Comparison between simulations and experiments. 118

Figure 4.26 Three stages of the deposition process. 118

Figure 5.1 Model setup. 123

Figure 5.2 Fluidization of neutral particles with v_g = 50 mm·s^{-1}. 124

Figure 5.3 Fluidization of chargeable particles with v_g = 50 mm·s^{-1}. 125

Figure 5.4 Positive charge density distribution (C·m^{-2}) of the charged fluidized bed with v_g = 50 mm·s^{-1}. 126

Figure 5.5 Negative charge density distribution (C·m^{-2}) of the charged fluidized bed with v_g = 50 mm·s^{-1}. 126

Figure 5.6 The fluidized beds of chargeable particles with various gas velocities at the same time instant (t = 3.4 s). 128

Figure 5.7 The positive charge density distribution (C·m^{-2}) of chargeable particles with various gas velocities (t = 3.4 s). 128

Figure 5.8 The total net charge distribution (C·m^{-2}) of chargeable particles with various gas velocities (t = 3.4 s). 129

Figure 5.9 The charge accumulation during fluidization. 130

Figure 5.10 Mean coordination number during fluidization. 131

Figure 5.11 A comparison of the pressure drop between fluidizations with neutral and chargeable particles with v_g = 50 mm·s^{-1}. 132

Figure 5.12 The pressure drops of fluidized beds with neutral particles at various gas velocities. 133

Figure 5.13 The pressure drops of fluidized beds with chargeable particles at various gas velocities. 134

Figure 6.1 Contact detection between two particles with constituent primary spheres. 140

Figure 6.2 Illustration of Force calculation and integration of the multi-sphere particle *i*.... 140

Figure 6.3 Model setup. 143

Figure 6.4 Charge distributions for the particles of δ = 0.0 at various time instants..... 147

Figure 6.5 Charge distributions for various shaped particles at t = 0.54 s. 148

Figure 6.6 Mean charge ratio of primary spheres over the particles of different shape factors. 149

Figure 6.7 Evolutions of charge variation on various elongated particles. 150

Figure 6.8 Surface charge difference for various shaped particles. 151

Figure 6.9 Charge accumulating processes of various shaped particles..... 152

Figure 6.10 An illsutration of the orientation of the elongated particle. 152

Figure 6.11 Particle orientations of various particles. 154

Figure 6.12 Mean contact rate during the vibration. 155

Figure 6.13 Contact rate difference of various particles. 156

Figure 6.14 The evolution of mean surface charge density for various particle. 157

Figure 6.15 The geometry of a 3D particle. 161

Figure 6.16 The particle represented by a polyhedron. 162

Figure 6.17 The sample seeds distributed on the surface of the particle. 162

Figure 6.18 The multi-sphere generated with 500 primary spheres by the medial axis method. 163

Figure 6.19 The multi-sphere generated with 10 primary spheres using merge optimization. 164

Figure 6.20 The model setup of the rotating drum. 166

Figure 6.21 Particles represented by polyhedra. 167

Figure 6.22 The multi-spheres used in DEM simulation. 167

Figure 6.23 The deposited granular beds in the drum. 170

Figure 6.24 The profiles of particle I (D_{32} = 3.72×10^{-4} m) during the drum rotation. 171

Figure 6.25 The charge distribution for the particle I (D_{32} = 3.72×10^{-4} m) at t = 0.33 s. 172

Figure 6.26 The charge evolution for the particle I (D_{32} = 3.72×10^{-4} m). 173

Figure 6.27 The charge distributions in the drum with various particles at t = 1.6 s. 174

Figure 6.28 A demonstration of the polar coordinate. 175

Figure 6.29 The evolution of charge density distribution (C·m^{-2}) for the particle I (D_{32} = 3.72×10^{-4} m). 176

Figure 6.30 The charge density distribution (C·m^{-2}) of various particles t = 1.6 s. 177

Figure 6.31 The charge accumulation of various particles. 178

Figure 6.32 The evolution of charge-to-mass ratio for various particles. 178

Figure 6.33 The evolution of mean surface charge density for various particles. 180

Figure 6.34 Typical charge distribution of primary spheres on various particles. 182

Figure 6.35 A schematic illustration of localization of initial charge on a particle (Matsuyama *et al.*, 2003). 183

Figure 7.1 A illustration of segregation of small particles adhered on a large carrier due to electrostatic interaction. 187

Figure A.1 The evolution of coordination number (ξ = 42.0, in air, with image force) by DT method with different cut-off distances. 199

Figure A.2 The evolution of coordination number (ξ = 42.0, in a vacuum, without image force) by DT and HPC methods with different cut-off distances. 199

Figure B.1 The evolution of mean surface charge density of various particles with the same ESD.....202

LIST OF TABLES

Table 3.1 Material parameters 68
Table 3.2 Excessive gas velocities and charging coefficients of various cases 81
Table 4.1 Properties of particles 89
Table 4.2 Material properties of particles and container walls 97
Table 4.3 Properties of particles and walls 106
Table 4.4 Computation time (Unit: hour) required with the DT and HPC methods for a simulation of physical time of 0.68 s 117
Table 5.1 properties of the particle and container 123
Table 6.1 A list of shaped particles 145
Table 6.2 Material parameters of the particle and the container. 145
Table 6.3 The charging coefficients for various particles 158
Table 6.4 The list of various particles 169
Table 6.5 The shape factors and the charging coefficients for various particles 181
Table B.1 Geometrical properties of various particles 201
Table B.2 The charging coefficients of various particles with the same ESD. 202

NOMENCLATURE

Letters:

A_p	surface area of the spherical particle
A_s	surface area of the primary sphere
A_{sp}	equivalent area of the primary sphere (sphere-tree multi-sphere method)
A_g	area of the grid
$\bar{c}_i$	mean contact number on the primary spheres with the same index *i*
C	total number of contacts on all particles
C_0	effective capacitance between the two separated metal surface
d_p	diameter of the spherical particle
D_{32}	Sauter mean diameter
e	elementary charge (1.60217657×10^{-19} C)
E	induced electric field
$g(r)$	radial distribution function
G	shear modulus
G_i, G_j	shear moduli of sphere *i* and *j*
F^n	normal contact force
F^t	tangential contact forces
F^*	reversal points for the transitions from loading-to-unloading
F^{**}	reversal points for the transitions from unloading-to-reloading
k_s	charging constant related with the charge density during each contact
k_0	proportional constant related with induced potential

k_c	charging coefficient of single particle
k_g	charging coefficient of powder handling processes
k_n	normal elastic coefficients (stiffnesses)
k_t	tangential elastic coefficients (stiffnesses)
m_i	mass of particle i
m_h	the mass of particles below the height h
$\overline{m}$	mean deposition rate
I_i	moment of inertia of particle i
n	number of collisions
n_c	number of particles in contact with particle i
n_e	number of particles with electrostatic interactions with particle i
n_f	number of particles inside the fluid cell
n_M	number of particles in the cell M
n_p	number of primary spheres on the particle (multi-sphere)
n_s	number of neighbouring particles in the SI region
N_M	number of cells in the WI region
N	number of particles
p	fluid pressure
q	charge of the particle
q_1, q_2	values of charges on particles i and j
q_a	saturation charge calculated from the air discharge field
q_{ci}	charge of the central primary sphere of the particle i
$\overline{q}_{di}$	mean charge of the two distal primary spheres of particle i
q_s	charge of the primary sphere

q_∞	equilibrium charge
$\overline{q}_{si}$	mean charge of the primary spheres with the same index *i*
$\bar{q}$	mean charge of the particles (multi-spheres)
Q	total net charge of the fluidized bed
Q_0	initial total net charge of the fluidized bed
Q_∞	equilibrium charge of the fluidized
Q_M	total charge of particles in the cell M
r	distance from the centre of the reference particle
r_a	radius of the contact area
r_c	radius of the central primary sphere
r_d	radius of the distal primary sphere
r_p	radius of the particle
r_s	radius of the primary sphere
$r_{p\min}$	radius of the smallest particle
r_{21}	distance between the centres of two particles 1 and 2
$\bar{r}$	mean radius of the particle (multi-sphere)
R_i, R_j	radii of spheres *i* and *j*, for spherical particle, $R = r_p$
R^*	equivalent radius
R_c	cut-off distance
S	maximum contact area during the contact
t	physical time
T_g	granular temperature
u_{mf}	minimum fluidization velocity

u_e	excessive fluidization velocity
v_b	vibrating velocity of the container
v_g	superficial gas velocity for fluidization
V_c	contact potential difference (CPD)
V_i, V_j	work function potentials of materials *i* and *j*
V_s	work function potential of the surface
V_p	work function potential of the polymer particle
V'	induced potential at the separation distance
W_i, W_j	work functions of materials *i* and *j*
Y_i, Y_j	Young's moduli of spheres *i* and *j*
Y^*	equivalent Young's modulus
z	contact gap or the separation distance
Z	coordination (contact) number

Greeks:

Δq	transferred charge
Δq_e	equilibrium transferred charge on metals
$\Delta\sigma$	transferred charge per unit contact area
ΔF^n	incremental normal force
ΔF^t	incremental tangential force
ΔV	total potential difference
α_n	normal displacement

α_t	tangential displacements
δ	shape factor
ε_0	permittivity of a vacuum (8.854×10^{-12} F/m)
ε_r	relative permittivity of the medium in the vicinity of the particles
η	loading parameter for Mindlin and Deresiewicz theory
κ	local void fraction of the fluid cell
κ_{mf}	voidage of the fluidized bed at the minimum fluidization
μ	friction coefficient
μ_s	viscosity of the gas
ς	dimensionless sphericity
$\zeta(\varepsilon_r, z)$	image correction factor
ξ	dimensionless ratio of electrostatic force to the gravitational force
ρ_p	material density of the particle
ρ_f	fluid density
τ_c	contact rate of the primary sphere
υ	Poisson's ratio
υ_i , υ_j	Poisson's ratios of particles *i* and *j*
ψ	volume of the particle
ψ_c	volume of the fluid cell
φ_i	mean charge ratio of the primary spheres with the index of *i*
ϕ	electric potential
σ	surface charge density of the particle

σ_p mean surface charge density of the particle (multi-sphere)

σ_s surface charge of the primary sphere

σ_n mean number density of particles in the granular bed

$\overline{\sigma}_{di}$ mean surface charge density of two distal primary spheres of particle *i*

σ_{ci} surface charge density of the central primary sphere of particle *i*

σ_g charge density in each grid

Vectors and tensors:

$\mathbf{d}_s$ vector from the particle centroid to the centre of the primary sphere *s*

$\mathbf{E}$ electric field strength

$\mathbf{F}^e$ electrostatic force

$\mathbf{F}^{\mathrm{e}}_{21}$ electrostatic force of q_2 to q_1

$\mathbf{F}_i$ resultant force acting on particle *i*

$\mathbf{F}^c_{ij}$ resultant contact force on particle *i* from particle or wall *j*

$\mathbf{F}^e_{ik}$ electrostatic force on particle *i* from particle *k*

$\mathbf{F}^e_{iM}$ electrostatic force between particle *i* and cell *M*

$\mathbf{F}^f_i$ particle-fluid interaction force on particle *i*

$\mathbf{F}'_{di}$ skin friction and drag component to the particle-fluid interaction

$\mathbf{T}_i$ resultant torque acting on particle *i*

$\mathbf{f}^s_{\mathrm{n}c}$ normal contact force at contact point *c* on the primary sphere *s*

$\mathbf{f}^s_{\mathrm{t}c}$ tangential contact force at contact point *c* on the primary sphere *s*

$\mathbf{r}_{sc}$	vector from the centre of the primary sphere to the contact point *c*
$\mathbf{f}_s$	resultant force of the primary sphere *s*
$\mathbf{T}_s$	resultant moment of the primary sphere *s*
$\mathbf{f}_p$	resultant force of the particle (multi-sphere)
$\mathbf{T}_p$	resultant moment of the particle (multi-sphere)
$\boldsymbol{g}$	gravitational acceleration
$\mathbf{x}_i$	translational coordinates of particle *i*
$\boldsymbol{\theta}_i$	rotational coordinates of particle *i*
$\mathbf{v}_i$	translational velocity of particle *i*
$\boldsymbol{\omega}_i$	angular velocity of particle *i*
$\mathbf{u}$	fluid velocity
ξ_f	total local average stress tensor
$\boldsymbol{\tau}_f$	viscous stress tensor
$\mathbf{n}_{21}$	unit vector of q_2 to q_1
Γ	identity tensor

CHAPTER 1 INTRODUCTION

1.1. Background

Powder technology is a branch of science and engineering dealing with the handling and processing of particulate materials (Seville *et al.*, 1997). They are often referred to as particles, granules or powders, and they are widely used in various industries, such as pharmaceuticals, food, metallurgy and fine chemicals. The handling and processing of powders can be divided into a vast range of operations, including characterization, fluidization, mixing/blending, storage, etc. During powder processing operations, particles make contacts with other particles and objects. Such contact interactions govern the dynamic behaviour of the particles and subsequently affect the performance of powder handling and processing operations, which play a vital role in controlling the quality of final products in the industries.

During powder handling processes, enormous electrostatic phenomena including contact electrification and electrostatic interactions can inevitably occur (Bailey, 1984). Contact electrification is described as the charge transfer and accumulation process between contacting objects. Electrons or ions can migrate from one material surface to another during a contact due to the different surface or material properties, after which the objects can attain excessive charges. Electrostatic interactions (Moore, 1973) generally refer to the electrical field and interactions between objects caused by the presence of electrical charges, specifically these charges and their positions rather than the motion of the charges. Generally, the magnetic and thermal effects generated by the motion of charges are not considered in

electrostatic analysis. The most fundamental research focuses on point charges and the electromechanics of particles subjected to electrostatics.

The presence of net charge and the induced electrostatic interactions can affect various powder handling processes. The presence of static charge can be detrimental since it can cause fatal hazards in powder handling industries, such as ignition, combustion and even explosions (Nifuku and Katoh, 2003). When particles are smaller than hundreds of microns, the induced electrostatic forces can be dominant compared with gravity and van der Waals force (Feng and Hays, 2003). Then the electrostatic interaction will cause dispersion of particles or cohesion and adhesion between particles and walls, especially for fine particle systems. For instance, in the pharmaceutical industry, this phenomenon results in segregation and agglomeration during powder handling processes and affects powder flow and reduces fill and dose uniformity (Engers *et al*, 2006; Watanabe *et al*, 2007). On the other hand, it can also be beneficial since electrostatic interactions can be utilized to control the motion of particulate systems in some powder manipulating processes, such as powder coating, separation and mixing processes (Ye *et al*, 2002; Lu and Hsiau, 2005; Saeki *et al*, 2006). Therefore, understanding the mechanisms of contact electrification and electrostatic interactions during powder processing is of fundamental importance.

The discrete element method coupled with computational fluid dynamics (DEM-CFD) can be used to investigate the influence of contact electrification and electrostatic interactions on powder processing. In DEM-CFD, the particles are governed by the pre-defined particle properties and inter-particle interactions, such as contact and electrostatic interactions. In addition, detailed information on each particle can be obtained to understand the fundamental

mechanisms, which are especially useful for studying electrostatic behaviour. For instance, the charge of each particle, the charge transfer mechanism and electrostatic interactions can be defined and implemented in DEM-CFD codes. Then the dynamics of the particles and the charge distribution and accumulation in a specific process can be modelled and obtained. This approach has considerable advantages compared with the traditional experimental methods since it is difficult, and invariably impossible, to determine and produce such specific information especially in a dynamic process. Therefore, with dedicated development and implementation, DEM-CFD can be used to explore the electrostatic behaviour of particles in powder handling processes.

1.2. Objectives

This current project aims to explore the influence of contact electrification and electrostatic interactions on powder handling processes, especially for pharmaceutical powder handling. The specific objectives are:

(1) To develop and implement a contact electrification model for a DEM/CFD code so that the successive contact charging process can be modelled. The dynamic charging process of particles will be explored by considering charge distribution and charge accumulation during a particular process.

(2) To develop and implement an electrostatic interaction model for a DEM/CFD code that is capable of simulating and analysing the dispersion and agglomeration of mono-charged and bi-charged particles during powder handling processes.

(3) To investigate the combined effects of contact electrification and electrostatic interactions on the dynamics of particles during powder handling processes.

(4) To investigate the effects of particle shape on the contact electrification process. Two multi-sphere approaches will be employed to study the charge distribution over the surface of irregular "multi-sphere" particle and the charge accumulation of the particle system.

(5) To explore the link between the properties of individual particles and the dynamic behaviour of the entire particle system using the developed DEM-CFD model. The influence of contact electrification and electrostatic interactions during powder processing will be investigated.

1.3. Outline of this thesis

In Chapter 2, the published literature on experimental, theoretical and numerical work of contact electrification and electrostatic interactions between particles and during powder processing operations are reviewed. The DEM-CFD approach used in this study is also briefly introduced.

In Chapter 3, a successive contact electrification model for the DEM-CFD code is developed and validated. The effects of particle size on contact electrification are examined. The charge distribution and accumulation during fluidization is also investigated.

In Chapter 4, the electrostatic interactions between particles are considered during the deposition of mono-charged particles and bi-charged particles, respectively. A hybrid particle-cell algorithm to calculate the electrostatic interaction between mono-charged particles is developed and compared with the direct truncation method. The micro-structure and macro-structure of the particle system affected by the electrostatic interactions during the deposition are investigated.

In Chapter 5, the combined effects of contact electrification and electrostatic interactions in fluidization are considered. The micro-structure of the fluidized bed and the pressure drop of the fluidization are examined. The charge distribution and accumulation during fluidization are also investigated.

In Chapter 6, the effect of particle shape on contact electrification is considered. The charging process of elongated particles in a vibrating container is presented in Section 6.2 and the charging process of particles with arbitrary shapes in a rotating drum is presented in Section 6.3 The charge distribution and accumulation process of the particle system are investigated.

In Chapter 7, the effects of contact electrification and electrostatic interactions are discussed. The limitations and restrictions of the current study are also highlighted. The conclusions and future work are presented in Chapter 8.

CHAPTER 2 LITERATURE REVIEW

2.1. Introduction

The research on contact electrification and electrostatic interactions for dry solid materials/ particles during powder handling processes is reviewed in this chapter. Firstly, the mechanisms of contact electrification and electrostatic interactions are presented. Secondly, electrostatic phenomena during powder handling processes are discussed. Then the DEM-CFD method is briefly reviewed and the DEM-CFD study on electrification and electrostatic interactions of particles during powder handling processes is also presented. Finally, other related numerical models of contact electrification and electrostatic interactions of particles are also briefly summarised.

2.2. Mechanisms of contact electrification

Materials can become electrically charged during mechanical interactions, such as impacts and frictional sliding (Loeb, 1945). During the charging process, the electrical charge can migrate from one surface to the other. After separation of the two surfaces, they will show electrostatic polarities. When objects are charged during contact without any sliding, it is often called contact electrification or contact charging. If sliding occurs, it is referred to as frictional electrification or triboelectrification (Matsusaka *et al.*, 2010). The charging processes during mechanical contact have been extensively investigated for conductive (metal) and insulating/dielectric materials (Lowell and Roseinnes, 1980; Matsusaka *et al.*, 2010).

The charged materials carry excessive static charges on their surfaces, which are transferred between them during the electrification process (Harper, 1967). It is extremely difficult to directly observe the charge transfer process experimentally. However, the existence of the excess charge after contact electrification can be used to determine the physical mechanism of the charge transfer process. In principle, it is the excess of protons or electrons that manifest the electrostatic polarities of the material. In the experiments of Lowell (1975) and Diaz and Guay (1993), electrons, ions and even polarized materials were observed and considered as the transferred charge between materials, depending on the properties of the materials and the operating conditions. In other words, electrons, ions and polarized materials are transferred from one surface to another and cause the materials to be electrified during mechanical contacts. Therefore, electron transfer, ion transfer and even material transfer are regarded as the primary physical mechanisms for the charge transfer process (McCarty and Whitesides, 2008, Matsusaka *et al.*, 2010).

2.2.1. Contact electrification between metals

Contact electrification between metals is caused by electron transfer between the surfaces. Based on solid-state theory, the minimum energy required to remove an electron from the bulk is defined as the work function. For most materials (metals and insulators), the work function is in the range of 3-6 eV (Kittaka, 1959; Arridge, 1967; Diaz and Guay, 1993). The work function represents the potential (work function potential) that confines the free electrons inside the material surface. When two materials are in contact, the contact potential difference (CPD) is defined as the difference of work function potentials. When a material, i, makes contact against a material, j, the CPD can be calculated as (Harper, 1951, 1967):

$$V_c = -\left(\frac{W_i}{e} - \frac{W_j}{e}\right) = -\left(V_i - V_j\right) \tag{2.1}$$

where, V_c is the CPD; e is the elementary charge of 1.60217657×10^{-19} C; W_i and W_j are the work functions of materials i and j; V_i and V_j are the work function potentials which are the work functions divided by the elementary charge, respectively. Because of the CPD, the electrons will flow from the material with a lower work function potential (high electron energy) to the material with higher work function (low electron energy) during a contact. For instance, in Eq. (2.1), when $V_i < V_j$, the electron will flow from material i to material j so that the charge of material i is positive and the charge of material j is negative.

The transferred charge on metals depends on the charge transfer process during the separation of the materials. In Lowell's experiment (1975), a metal sphere was brought into contact with the flat surfaces of different metals and then separated. The charge on the sphere was measured by an electrometer and the contact potential difference between two metal surfaces was measured by a standard Kelvin (vibrating capacitor) method (Melitz *et al*, 2011). Lowell suggested that electrons were transferred during the separation of the sphere from the plane after the contact. When a critical separation distance between the two objects is reached, the electrical resistance rapidly cuts off the electron transfer and the charges on both objects are fixed. This phenomenon is also called the tunnelling effect and the critical separation distance is also called the tunnelling distance/gap as shown in Figure 2.1. The critical separation distance is influenced by the surface topography and is in a range of a few hundreds of nano-meters (Lowell, 1975; Lowell and Roseinnes, 1980). In addition, it is also observed that the transferred charge does not depend on the velocities of the contact and separation, which indicates that the charge transfer reaches the equilibrium state immediately after the

separation. Moreover, the transferred charge is also not sensitive to sliding between the metal surfaces.

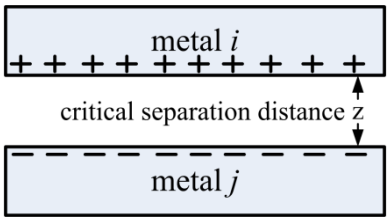

Figure 2.1 Charges on the metal objects after contact at the critical separation distance.

The charge transfer eventually reaches an equilibrium state, which is analogous to a thermodynamic equilibrium process. If the two separated metal surfaces at the critical separation distance are considered as a capacitor (condenser), then the relationship between the equilibrium transferred charge and the potential difference can be determined as:

$$\Delta q_e = C_0 V_c \tag{2.2}$$

where Δq_e is the equilibrium transferred charge; C_0 is the effective capacitance between the two separated metal surface. According to Eq. (2.1), if $V_c > 0$, then $\Delta q_e > 0$. So the charge on material *i* is Δq_e and the charge on material *j* is $-\Delta q_e$. Lowell's experiment (1975) on various metals showed the validity of this relationship, in which the equilibrium transferred charge has a linear relationship with the contact potential difference. Many researchers (Harper, 1951; Lowell, 1975; Matsusaka *et al.*, 2010) used this linear relationship between the equilibrium transferred charge and CPD as a criterion to determine whether the electron transfer is the main charge transfer mechanism of contact electrification between materials.

2.2.2. Contact electrification between metals and polymers

The contact electrification of polymers impacting with metals has been extensively explored experimentally. Various polymers and conductive metals were used. During these experiments, the polymer and the conductive metal (usually earthed) were allowed to make a single contact or a number of successive contacts. The charge on the polymer was usually measured by a Faraday cage and the work function of the conductive metal was usually measured by the Kelvin method (Melitz *et al.*, 2011). It was found that the charge transfer process between the polymer and the metal depends on the contact area, the initial charge of the polymer, the number of successive contacts and the work functions of the polymer and the metal.

For a single impact, the transferred charge is related to the initial charge of the polymer, the contact area and the work functions. Matsusaka *et al.* (2000) brought a rubber sphere into contact with a steel plate with different initial charge and different impact velocity and then measured the charge of the sphere. At the same impact velocities, the transferred charge on the rubber sphere had a linear relationship with the initial charge. The transferred charge on the rubber sphere decreased as the initial charge of the sphere increased. When different impact velocities were applied, it was observed that the transferred charge was proportional to the maximum contact area and the proportional constant which is the charge density on the contact area of the rubber sphere. The proportional constant was in the range of 10^{-5} – 10^{-3} $C \cdot m^{-2}$, which is in the same order of magnitude found in various experiments (Lowell, 1980; Masui and Murata, 1983; Watanabe *et al.*, 2007). The study of the contact electrification of various pharmaceutical particles during impact with a steel target performed by Watanabe *et*

al. (2007) revealed similar phenomena. It was also found that when different pharmaceutical materials were used, the transferred charge in a single impact for different materials were different, indicating that the charge transferred in the single impact also depended on the work function of the materials. The charge transfer can be accomplished in a very short time period (i.e. in the order of 10^{-2} s) (Lowell and Roseinnes, 1980).

The charging process of a polymer impacting with a metal during successive contacts is an accumulating process. Kittaka (1959) examined the generation of the static charge on high molecular weight polymers (polystyrene, Acrylite and Teflon) in contact with a metal. It was found that the charge on the polymer eventually reached saturation (equilibrium) after a number of successive contacts, which shows similar results as the experiments of Matsusaka *et al.* (2000). Davies (1969) investigated the charge generation on dielectric surfaces in contact with different metals. The metals were mounted on a rotating wheel and the polymer films were brought into contact with the metals on a rotating drum. The rotation continued until the charge on the polymer film was saturated. It was found that the equilibrium charge was linearly related to the work function of the metal, which indicates that the charge transfer between the polymer and the metal can be attributed to electron transfer (Davies, 1969; Castle and Schein, 1995; MaCarty and Whitesides, 2008; Matsusaka, *et al.*, 2010;).

Analytical models have been introduced to analyze the contact electrification process between insulating/polymer particles and metals (Masuda and Iinoya, 1978; Matsuyama and Yamamoto, 1995a; Matsuska *et al.*, 2000; Matsuska *et al.*, 2000). As the electron transfer is the mechanism of charge transfer, the charge transfer is due to the difference of the energy levels of the two materials, which will be eventually equalized. Although the electronic

structure of a polymer is different from the metal, the work function (or effective work function) (Matsuska *et al.*, 2010) can still be used to indicate the surface energy level as in Eq. (2.1). According to the experiments on the contact electrification between polymers and metals, the transferred charge in each contact on a polymer particle impacting with a conductive metal surface (Figure 2.2) can be defined as (Matsuyama and Yamamoto, 1995a; Matsuska *et al.*, 2000; Matsuska *et al.*, 2010):

$$\Delta q = k_s S\left(V_s - V_p - V^{'}\right) = k_s S\left(V_s - V_p - k_0 q\right) \tag{2.3}$$

where k_s is a charging constant related with the charge density during each contact; S is the maximum contact area during the contact; V_s and V_p are the work function potentials of the conductive surface and the polymer particle; $V^{'}$ is the induced potential at the separation distance by the charge on the polymer particle, which is assumed to be proportional to the net charge q on the particle surface with a constant of k_0. If the charge distribution and the electrostatic field on the surface of the particle are assumed to be distributed uniformly, k_0 can be determined by the charge of the particles as (Matsuyama and Yamamoto, 1995a):

$$k_0 = \frac{qz}{4\pi\varepsilon_0 r_p^2} \tag{2.4}$$

where z is the contact gap or the separation distance for the tunnelling relaxation; r_p is the radius of the particle. From Eq. (2.3), it can be seen that the transferred charge in each contact is a function of the contact area, the charge of the particle and the CPD between the polymer and the metal, which coincides with the experimental observations.

For successive contacts, the charge on a particle will continue accumulating (Figure 2.2) until the induced potential equalizes the CPD, which can be written as:

$$V_s - V_p = k_0 q_\infty \tag{2.5}$$

where the equilibrium charge of the particle, q_∞, is:

$$q_\infty = \frac{V_s - V_p}{k_0} \tag{2.6}$$

It can be seen that the equilibrium charge is linearly related to the CPD, which gives a similar form as the condenser shown in Eq. (2.2). Therefore, this model is also called a condenser model. In addition, as the transferred charge on a particle in each contact is linearly proportional to the charge on the particle, the model is analogue to a first-order kinetic theory. The accumulating process shows an exponential relationship with the number of contacts (see Section 3.2). The electrification process of a rubber sphere with repeated impact on a metal plate (Matsusaka *et al.*, 2000) shows an excellent agreement with the exponential relationship, in which the charge dissipation is also considered as an exponential relationship.

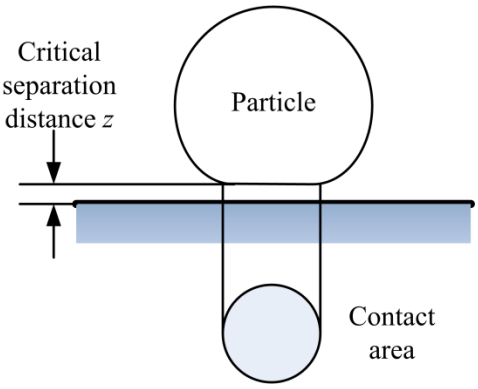

Figure 2.2 The impact process between a particle and a plate for contact electrification (Matsuska *et al.*, 2010).

Although the condenser model can give a prediction of the charging process, there are still some limitations. Matsuyama and Yamamoto suggested (1995a) that as the charge on the polymer particle can induce and polarize the metal plate, this so called image effect should be considered as:

$$k_0 = \frac{qz}{4\pi\varepsilon_0 r_p^2}\zeta(\varepsilon_r, z) \tag{2.7}$$

where $\zeta(\varepsilon_r, z)$ is the image correction factor which is a function of separation distance and the relative dielectric constants of ε_r within the range of 1 - 10. Furthermore, many authors have pointed out that the equilibrium charge calculated by the condenser model with a theoretical value of the separation distance of 1 nm was much higher than the experimental results. Lowell's research showed that the actual separation distance was much larger than the theoretical value due to the surface topology, which induced a small equilibrium charge. On the other hand, Matsuyama and Yamamoto (1995a) proposed a charge relaxation model as shown in Figure 2.3. In this model, the air discharge during the separation between two particles dominates the charging process. When two materials are brought into contact and then separated, the charge will be transferred due to the tunnelling process. As the separation distance becomes larger, the potential difference between the two charged surfaces becomes larger. When the potential difference is larger than a critical value, it will cause gaseous discharge in which the charge on both surfaces will be transferred back and become smaller. Although this model can improve the accuracy of the condenser model, some details of this theory are still difficult to determine, such as the potential difference and the electric strength between the separating surfaces.

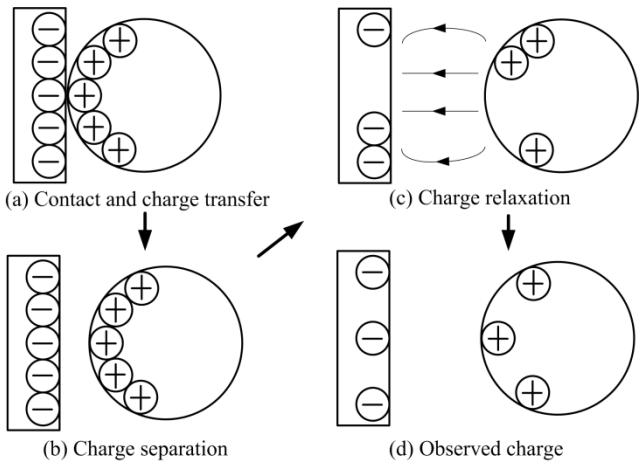

Figure 2.3 The relaxation model (Matsuyama and Yamamoto, 1995a).

2.2.3. Contact electrification of insulators

The contact electrification between insulators, especially for polymers, is rather complicated due to the different molecular structure and surface conditions of polymers, which is not well understood. Both electron transfer and ion transfer mechanism have been used to analyze the charging process with different materials and contact conditions.

The contact electrification of polymers can be explained by an electron transfer mechanism. Schein and LaHa (1991) examined the electrostatic charging between toners (styrene/acrylic resin) and carriers (polymer/insulators). The toners and the carriers were mixed in a V-blender. The charge accumulation and saturation of the toners were observed. Castle and Schein (1995) compared 70 experimental results of toner-carrier mixtures. It was shown that the charge transfer between insulating surfaces primarily relied on the electric field generated by the net charge of the insulating surfaces. A surface state model is proposed by Castle and Schein (1995) as follows:

$$\Delta\sigma = \frac{\varepsilon_0}{ze}\left(W_i - W_j - Eze\right) = \frac{\varepsilon_0}{z}\left(\frac{W_i}{e} - \frac{W_j}{e} - Ez\right) \tag{2.8}$$

where $\Delta\sigma$ is transferred charge per unit contact area; W_i and W_j are the effective work functions of material i and j, respectively; E is the induced electric field by the charge on materials i and j. In Eq. (2.8), $\left(W_i/e - W_j/e\right)$ is the contact potential difference as illustrated in Eq. (2.2). It can be seen this so called surface state model shows a similar form as the condenser model, which indicates that the contact electrification process can be caused by electron transfer. Hence, for different materials with different work functions, a "triboelectric series" can be listed based on the work functions of materials as shown in Figure 2.4

(McCarty and Whitesides, 2008), in which the materials with a lower work function will be charged positively and the materials with a higher work function will be charged negatively. However, this surface state model does not consider the dielectric properties of the material, the surface atomic or molecular structure, and the surface properties etc. Therefore, McCarty and Whiteside (2008) suggested that the electron transfer can only occur for polymer surfaces with well-matched donor and acceptor orbitals for electrons.

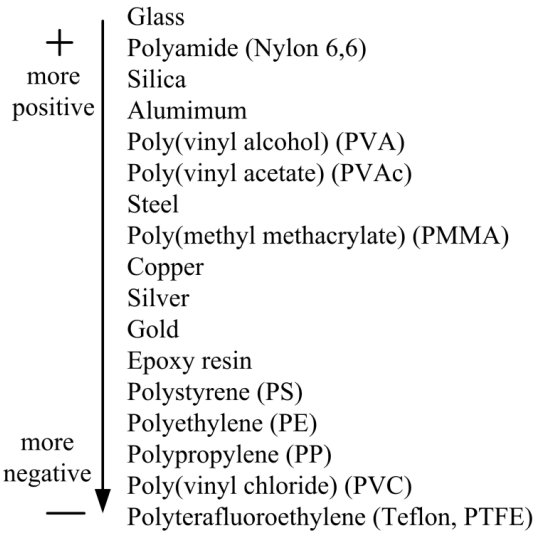

Figure 2.4 A triboelectric series list excerpted from reference (McCarty and Whitesides, 2008).

Ion transfer is also observed during the contact electrification between polymers especially with covalently bound ions and mobile couterions. In the experiments of Diaz *et al.* (Diaz *et al.*, 1990; Diaz and Guay, 1993; Diaz, 1998), the blended ionomer powders were mixed with ferrite beads. Consequently, the powder was charged positively and the ferrite beads were charged negatively. The mobile ion (OTs^-) is observed on the surface of the beads using X-ray photoelectron spectroscopy (XPS). McCarty *et al.* (2007b) fabricated cross-linked polystyrene spheres with ionic functional groups (containing mobile ions) and let the spheres roll down

sheets made of Nylon and PTFE. It was found that the charge on the spheres with Nylon and PTFE showed the same sign and similar magnitudes despite the difference between work functions of Nylon and PTFE in the "triboelectric series". The charge of a sphere was proportional to the surface area and was limited by the air discharge limit, which is considered as the basis of the ion transfer model (McCarty *et al.*, 2007b; McCarty and Whitesides, 2008). In addition, it was suggested that the ion transfer process should produce two consequent results that the sign of the ionic material should be the same as the covalently bound ion and the mobile ion should be observed on the other surface after the contact (McCarty *et al.*, 2007). Furthermore, polarized materials instead of ions can also be transferred from one surface to another and lead to charging, which is the so-called material transfer mechanism (Tanoue *et al.*, 1999; Matsusaka *et al.*, 2010). The ion transfer and material transfer process show that the charge transfer during the contact between insulators can be related to the surface structure and material properties, but it is difficult to establish a general model to evaluate the charge transfer process for different materials and contact conditions.

2.2.4. Frictional electrification

Materials can also become charged by sliding or rubbing against each other, which is the so-called frictional electrification or tribo-electrification. Kornfeld (1976) rubbed the end surfaces of two cylindrical samples (PMMA and Teflon) using a rotating device, and found that the PMMA was positively charged and the Teflon was negatively charged. An equilibrium charge value for each material was then obtained and the summation of the equilibrium values of the rubbed pair was equal to zero. This phenomenon can be explained using the triboelectric series as shown in Figure 2.4. Ireland (2008) analyzed the change of

contact area (changing contact pattern) during sliding. It was shown that the changing contact pattern invariably resulted in a transferred charge greater than that for static contact due to a larger total available contact area. Liu *et al.* (2013) examined the effects of the contact force and the rubbing speed on the charge accumulation of three polymer surfaces (nylon, PTFE and PP) rubbed against a stainless steel surface. The charge on a nylon surface increased with repeated rubbing and reached saturation after about 40-50 cycles. However, the charge on PTFE and PP reached saturation with only 2 or 3 cycles. It was observed that the charge on PTFE and PP increased as the contact force increased, while the charge generated on nylon was less sensitive to the contact force. Furthermore, the charge generation on these three polymers is not influenced by the rubbing speed. This is different from the observations of Hersh and Montgometry (1955) that the charge of Teflon rubbing with metals increases with the rubbing speed. Liu *et al.* (2013) suggested that this is due to the different molecular structures of the polymer surfaces, such as number of free electrons or ions and the polarizablity. Electron, ion and even material (polarized and trapped on the surface) transfer mechanisms (Medley, 1953; Kornfeld, 1976; Lowell and Rose-Innes, 1980; Ireland, 2003; Liu *et al.*, 2013) were used to interpret the charge transfer process during frictional electrification. However, due to the complexity, it is still difficult to analyze frictional electrification with a simple and general analytic model.

2.2.5. The influence factors of contact electrification

Contact electrification is also related to various factors, such as the particle size and shape, the dielectric constants and material properties of the particles, environmental conditions etc.

The influence of particle size on the charge accumulation of a particle is complicated. According to the condenser model (e.g. Eqs. (2.6) and (2.7)), a smaller particle can possess a large charge-to-mass ratio (Masuda *et al.*, 1976; Chen *et al.*, 2003). However, some researches (Armour-Chélu and Woodhead, 2002; Zhu *et al.*, 2007b; Saleh et al 2011) showed that no apparent or even contradictory dependence of the charge-to-mass ratio on the particle size. In addition, bipolar charges occurred on particles with the same material but different sizes (Lacks and Sankaran, 2011). The smaller particles tended to be charged negatively while the larger particles became positively charged (Sharmene Ali *et al.*, 1998; Zhao *et al.*, 2002). However, in one of the polymer powders tested by Sharmene Ali *et al.* (1998), the small particles charged positively while the coarse ones charged negatively. It was suggested that this phenomena might be caused by the different energy states and the ion transfer at the surface of the particles (Zhao *et al.*, 2002; Lacks and Sankaran, 2011).

Particle shape plays an important role in the charge transfer between particles during contact electrification. Watanabe *et al.* (2007) investigated the contact electrification of various pharmaceutical particles impacting with a steel surface. It was found that the irregular ethlycellulose particle obtained a different transferred charge from the calculated value by assuming a spherical particle shape. Ireland (2012) also argued, for the contact electrification of an elliptic particle during impact (bouncing) with a surface, a smaller radius of contact curvature could lead to a small contact area, which results in a smaller transferred charge.

The relaxation and dissipation of charge on a surface are referred to as the charge redistribution on the surface and the charge leakage/discharge from the particle surface to the environment. For highly insulating materials, (Kittaka, 1959; Arridge, 1967; Kornfeld, 1976),

the relaxation process is slow and takes up to hours. Due to this reason, Matsuyama and Yamamoto (1995b, Matsuyama *et al.*, 2003) suggested that non-uniform surface charge distribution occurs on the surface of the polymer particles. It is also found that the charge on the remote surface of a particle with respect to the underlying contact area has less effect on the charge transfer at the contact area. This leads to a different charge accumulation process from the assumption of the uniform surface charge distribution on the particle surface (Matsuyama and Yamamoto, 1995b; Matsuyama *et al.*, 2003; Matsusaka *et al.*, 2010).

The contact electrification process can also be influenced by environmental conditions, such as, humidity, air pressure, oxygen conditions etc. Kittaka (1959) found that the charge on polystyrene after contact with a metal was positive in dry air but negative in 60% R.H. air. In addition, a higher oxygen concentration level at a higher air pressure could induce a higher work function on the material surface (Brattain and Bardeen, 1953). So the negative charge on a Teflon surface after impact with the metal was greater at a high air pressure than that in a lower value.

2.3. Mechanisms of electrostatic interactions

The net electrostatic charge on particles, specifically on the surface of particles, varies depending on the material properties, environmental conditions and handing process. For example, the charge for aerosol dust varies from 10^{-6} to 10^{-3} nC (Ji and Shen, 2009), whilst for a pharmaceutical powder, which usually is presented as the charge-to-mass ratio which is defined as the charge divided by the mass of the particles, is in the range of 1 - 100 $nC \cdot g^{-1}$ (Rowley, 2001; Elajnaf, *et al.*, 2006).

Electrostatic interactions, as one kind of long-range interactions, are induced by the presence of net charge. Coulomb's law states that the magnitude of the electrostatics force of interaction between two point charges can be written as:

$$\mathbf{F}_{21}^{\mathrm{e}} = \frac{1}{4\pi\varepsilon_0\varepsilon_r}\frac{q_1 q_2}{r_{21}^2}\mathbf{n}_{21} \tag{2.9}$$

where $\mathbf{F}_{21}^{\mathrm{e}}$ is the electrostatic force from q_2 to q_1, ε_0 is the permittivity of free space (8.854×10^{-12} F/m), ε_r is the relative permittivity of the medium in the vicinity of the particles, q_1 and q_2 are the values of charges on each particle, r_{21} is the distance between the centres of the two particles and $\mathbf{n}_{21}$ is the unit vector from q_2 to q_1. It can be seen that the Coulomb force is directly proportional to the scalar multiplication of the magnitudes of charges and inversely proportional to the square of the distances between them. If two charges have the same sign, the electrostatic force between them is repulsive; if they have a different sign, the force between them is attractive.

The electrostatic interactions between charged particles vary with their properties and the distance between them. For both conductive and dielectric spheres, it is found that when the distance between a conductive sphere is sufficiently large (say, 5-6 times of the radius), the two charged spheres can be treated as two point charges and the force between the two charged spheres can be determined using Coulomb's law (Nakajima and Sato, 1999; Bichoutskaia, *et al.*, 2010; Kolikov *et al.*, 2012). However, if two charged spheres are close to each other, a deviation can be induced from the value calculated using Coulomb's law. For conductive materials, the deviation is caused by the redistribution of the charge on the surface (Kolikov *et al.*, 2012) while for dielectric materials, the deviation is induced by the

polarization of the molecule on the surface which is related to the relative permittivity of the dielectric materials (Nakajima and Sato, 1999; Bichoutskaia, *et al.*, 2010). More complicatedly, mono-charged spheres can experience an attractive force between each other due to the charge redistribution or polarization on the surfaces of the spheres (Nakajima and Sato, 1999; Bichoutskaia, *et al.*, 2010; Kolikov *et al.*, 2012).

The electrostatic force can dominate the dynamic behaviour of powders, especially when the particles are relatively small. Theoretically, the electrostatic force and other interparticle forces, such as van der Waals force, can potentially exceed the particle inertia when the size of the particle is less than 1 mm. In practice, however, interparticle forces and particle inertia can be comparable for particles with a size of about 100 μm (Seville *et al.*, 1996, Matsuyama *et al.*, 2003). Mathematical analysis (Feng and Hays, 2003) indicates that the electrostatic force on a charged particle is likely to be greater than the van der Waals force, when the particle size is greater than 10 μm. Gady *et al.* (1996) measured the interaction force between a micrometer-size (3 μm) sphere and a flat substrate using an atomic force microscope (AFM). The electrostatic force and the van der Waals force were then used to fit the measured data. It was found that the van der Waals interaction could fit well when the separation distance between the sphere and the flat substrate was smaller than 30 nm. As the separation distance increased, the electrostatic interaction became dominant. A study on nanoparticulate aggregates (Moreno-Atanasio *et al.*, 2009) showed that the electrostatic interactions could induce a rapid increase of the coordination number to form the aggregates and also a large failure strain in aggregates because of its long-range nature, even when the electrostatic and van der Waals forces had the same magnitude. This indicates that the electrostatic interactions

can exert a significant influence on the dynamic behaviour of powders in powder handling processes.

2.4. Contact electrification and electrostatic interactions in powder handling processes

Contact electrification and electrostatic interactions occur simultaneously and play important roles in powder handling processes. Contact electrification results in the charge distribution and accumulation of particle system during processing and handling while electrostatic interactions can change the particle dynamic behaviour, such as dispersion and agglomeration. Apparently, both contact electrification and electrostatic interactions are interrelated and lead to more complicated particle dynamic behaviour.

2.4.1. Contact electrification in powder handling processes

To explore the charging behaviour, the correlation between charging phenomena, e.g. charge accumulation and distribution, in conjunction with material properties and process conditions, has been investigated during powder handling processes

The charge on the particles can be accumulated to an equilibrium state during powder handling processes. Liao *et al.* (2011) investigated the electrification of glass beads in a vibrating container, and showed that the charge of the particle system reached a saturated level. The maximum charge of the particles increased with the dimensionless vibrational acceleration and velocity, but decreased with an increase in the vibration frequency.

Guardiola *et al.* (1996) investigated electrification during fluidization using glass beads of various sizes at different fluidization velocities and relative humidities. The potential difference obtained with the electric probes in contact with the granular bed and the earthed distributor bed was used to indicate the degree of electrification. The results showed that the degree of electrification could reach a constant value under various conditions as the fluidizing process continues. Specifically, the degree of electrification increased with increasing fluidization velocity with a relatively lower humidity. This is because a larger gas velocity can increase the motion of the fluidized bed and the collisions between particles, and the lower humidity causes less charge dissipation. Similar phenomena were observed by Saleh *et al.* (2011) for the electrification of glass beads in pneumatic conveying, who found that the charge on the particles increased exponentially with time and eventually reached a saturated level. The air velocity and the transport regime played an import role in the tribo-electrification process. At lower air velocities, the particle-wall friction was primarily responsible for the electrification, whilst at higher air velocities, the charge increase was dominated by energetic collisions.

The charge accumulating process varies with the properties of the particles and the operating conditions. Engers *et al.* (2007) examined the relationship between the charge accumulation and the dielectric properties of pharmaceutically relevant mixtures in a low-shear tumble blending process. It was shown that pure microcrystalline cellulose with a dielectric constant of 4.0 obtained a negative charge-to-mass ratio. When the microcrystalline cellulose was mixed with a low concentration of acetaminophen with a dielectric constant of 2.8, the charge-to-mass ratio of the mixture increased, indicating that the particle system acquired excess positive charge. When the concentration of acetaminophen was increased, the charge-

to-mass ratio of the particle system gradually decreased to become more negative. These observations indicated that the mixture and the interfaces between the particles with different dielectric properties can influence the charge generation and accumulation.

Šupuk *et al.* (2012) assessed the magnitude of tribo-electric charging of active pharmaceutical ingredients (APIs) and excipients. Each material sample was charged in a cylindrical container, which was made of stainless steel and shaken in a horizontal direction, and then measured by a Faraday cup. The APIs showed a higher charge level and a greater variability than the excipients, implying that the charge of APIs plays a dominant role in the electrostatic charge of pharmaceutical blends of powders.

Ireland (2010a; 2010b) investigated the electrification of particles (silica) flowing on a tilted surface (stainless steel). Different modes of contact, such as sliding, rolling and bouncing, were observed during the particle flow (Figure 2.5). The percentages of particles in different modes of contact (sliding, rolling and bouncing fraction) were counted. When the tilt angle of the surface increased, the sliding fraction decreased and the rolling and bounding fractions increased. It was found that the charge level (charge-to-mass ratio) varied with the modes of contact. Generally, a larger sliding (contact friction) and a longer contact time during the flow produced a higher charge level of particles. However, Ireland (2010a; 2010b) suggested that for the complex modes of contact, such as rolling and bouncing, the charging process cannot be simply described by the condenser (capacitor) model.

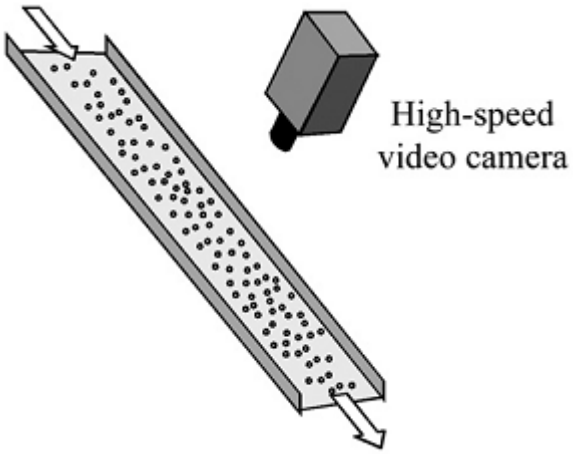

(a) Experimental setup

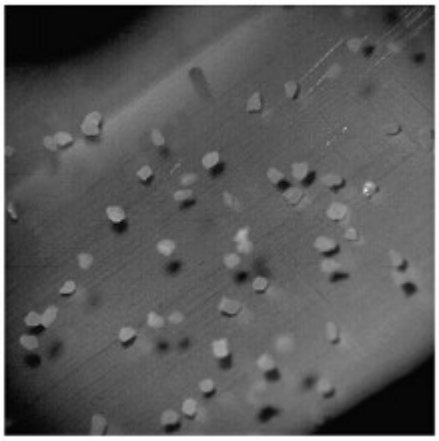

(b) Camera view of particle sliding, rolling and bouncing

Figure 2.5 Electrification of particles flowing on a tilted surface (Ireland, 2010a).

The charge distribution in a particle system varies with the type of powder handling process. LaMarche *et al.* (2009) examined the charging process of dielectric particles flowing through a metal cylinder and showed that the net charge on the particles increased linearly with an increase in the contact surface area between the particles and the cylinder, while the net charge density of the powder was greater in the region close to the wall compared with that at the centre. They attributed this to the charge acquisition of the powder occurring only during the contact between the particles and the cylinder. Chen *et al.* (2003; Bi, 2005, Chen *et al.*,

2007) measured the charge distribution of a gas bubble in fluidization of glass beads when the bubble passed the probe placed at the centre of the fluidized bed. It is found that the charge inside the gas bubble is almost zero while the charge increases gradually toward the dense region of particles outside the bubble. This indicates that the particle-particle contact is one of the dominant charge generation mechanisms in gas fluidized beds.

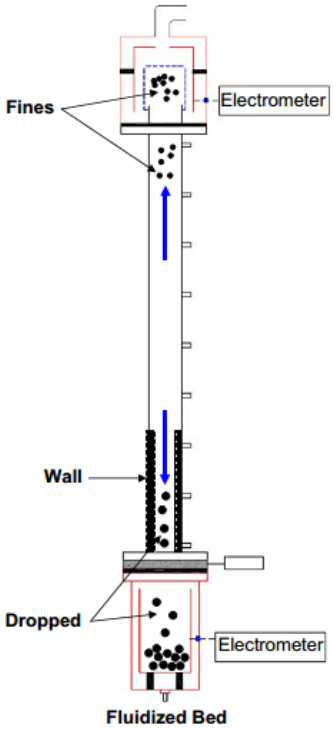

Figure 2.6 Measurement of charge distribution in the fluidization (Sowinski *et al.*, 2010).

Sowinski *et al.* (2009; 2010) examined the charge accumulation during fluidization of polyethylene particles with a wide particle size distribution (PSD) for i) particles in the fluidized bed, ii) particles adhered on the column walls and iii) fine particles entrained at the top of the column (Figure 2.6). The charges of these particles were measured using a Faraday cup after the fluidization. It was found that the charge and mass of these particles varied with the superficial gas velocity. By increasing the fluidizing gas velocity, the mass and net charge

of the entrained fine particles at the top increased, whereas those for the particles adhered on the walls decreased. The charge and mass of dropped particles from the fluidized bed remained constant. This is due to the migration of particles by the gas velocity. More particles and larger particles are transported to the top by a higher gas velocity, instead of being adhered to the wall. However, the charge-to-mass ratio of the particles entrained at the top was lower as more larger particles were transported to the top at a higher gas velocity.

Although charge accumulation and distribution can be experimentally observed, the measurement of the charge accumulation and distribution of particles still involves some challenging techniques, especially for a bi-charged particle system (Beleca *et al.*, 2010; Karner and Urbanetz, 2011) or without interfering the powder process (Guardiola *et al.*, 1996; Chen *et al.*, 2003; Beleca *et al.*, 2010; Sowinski et al, 2010; Karner *et al.*, 2011).

2.4.2. Electrostatic interactions in powder handling processes

The presence of the net charge on particles can induce electrostatic interactions. When the electrostatic interactions are dominant, the dynamics of particles during powder handling processes will be influenced by the repulsive and/or attractive forces, which will lead to various phenomena during the powder handling processes.

2.4.2.1. Dispersion induced by the repulsive force

The repulsive force between mono-charged (similarly charged) particles can lead to the dispersion of particles. Adachi *et al.* (1985) examined the dynamics of aerosol particles with a

unipolar charge on a container. It was observed that the aerosol particles moved away from each other to the surface of the container with increasing velocities. The particle number concentration decreased with time. This indicates that the aerosol particles were dispersed by an electrostatic repulsive force. Wu *et al.* (2008) investigated the self-assembly phenomenon of similarly charged granular particles. In their experiments, stainless-steel particles in one layer were pre-charged by contact electrification with the base of the polystyrene box and the box was then tilted by an angle of 9°. It was found that the gravitational forces acting on the particles were balanced by the repulsive Coulomb force and the particles formed a dispersed structure (see Figure 4.10). Ren *et al.* (2001) explored the electrostatic dispersion of fine particles. The fine particles were treated by Corona discharge to have the same polarity. It was shown that the treated particles had a better flowability than the untreated particles. They proposed a simple criterion that when the electrostatic repulsive force is larger than the adhesive forces (van der Waals force and liquid bridge force), particles can be dispersed during the process. Masuda (2009) also suggested that if all of the particles are charged with the same polarity, it will facilitate the dry dispersion of the fine particles. However, it is difficult to control the charge in particle systems and implement it in powder handling processes (Adachi *et al.*, 1985; Masuda, 2009).

2.4.2.2. Agglomeration and segregation effects

Bi-charged particles can form agglomerates due to the mutual repulsive and attractive forces. Grzybowski *et al.* (2003) investigated the electrostatic self-assembly of bi-charged spheres using contact electrification. The spheres with diameters of millimetres were made of two different polymers (PMMA and Teflon) and then shaken in a box coated by a film of gold.

The PMMA spheres became charged positively, and the Teflon spheres were charged negatively. It was observed that the oppositely charged spheres formed agglomerates with crystalline structures. In addition, the crystalline structures showed square, pentagonal and hexagonal arrays depending on the different numbers of positively charged spheres and negatively charged spheres (see Figure 4.25). This illustrated how the mutual repulsive and attractive forces can cause agglomeration of bi-charged particles. LaMarche *et al.* (2010) observed the agglomeration of pharmaceutical particles. In their experiments, charged acrylic beads were poured onto a bed of cellulose particles. It is found that the charged acrylic beads could attract the cellulose particles at areas where the acrylic beads were in contact with the cellulose (Figure 2.7). If the charge distribution on the acrylic beads is not uniform, the cellulose particles will be only adhered and segregated on the charged area of the acrylic beads. This phenomenon is attributed to the dielectrophoresis (DEP) that the tendency of particles to be attracted to the high electric field (LaMarche *et al.*, 2010).

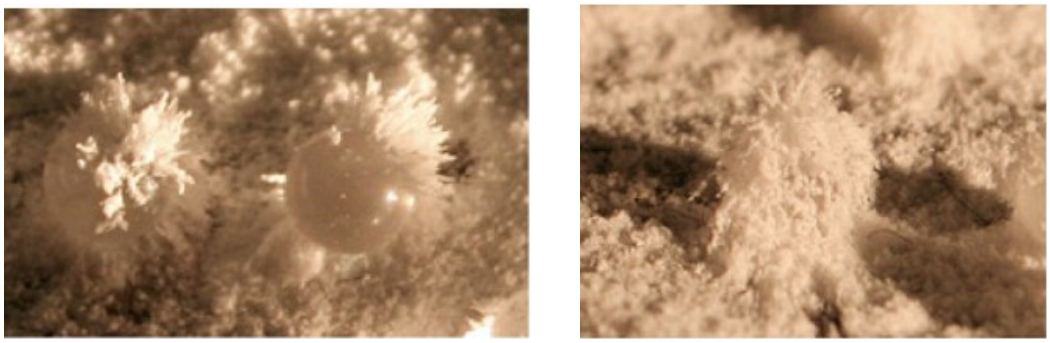

(a) (b)

Figure 2.7 Agglomerates of cellulose and acrylic beads (LaMarche *et al.*, 2010). a) Two acrylic beads partially covered by cellulose. b) A bead covered completely in agglomerated cellulose.

Electrostatic interactions play an important role in the handling processes of pharmaceutical powders. The charged particles tend to adhere to walls and contaminate the equipment

(Eilebeck *et al.*, 2000). Šupuk *et al.* (2012) found that, due to the higher charge level (larger charge-to-mass ratio) of APIs, the extent of API particles adhering on the container walls was much greater than that of excipients. This may cause segregation of an API during a powder handling process. Lachiver *et al.* (2006) examined the formation of agglomerates during the mixing of a dry particle system in a neutralised plastic bag. The greatest number of agglomerates occurred when one component (Xylitab) was charged negatively and the other component (MaSt) was charged positively. This phenomenon was caused by the mutual electrostatic interactions as demonstrated by Grzybowski *et al.* (2003).

Pu *et al.* (2009) investigated the effects of electrostatic interactions on the homogeneity of pharmaceutical powder blending. Two binary systems, lactose (excipient) with caffeine (API) and MCC (excipient) with caffeine (API), were selected. Three blending procedures were examined: (1) conventional blending without any charge control; (2) blending with simultaneous charge neutralisation using bipolar ionized air; (3) controlled blending with a corona charging process in which the excipient and API particles were charged oppositely. In each procedure, several samples were taken from the blended particle system. The API concentration variation was defined as the deviation of the actual caffeine concentration of each sample relative to the target caffeine concentration. It was found that the API concentration variation increased as the charge-to-mass ratio of the final blend sample of the excipient and API increased in the uncontrolled procedure. The charge neutralisation did not reduce the API concentration variation. On the contrary, for the controlled procedure, especially when the lactose was charged positively and the caffeine was charged negatively, the API concentration variation decreased, indicated a better blending homogeneity. Pu *et al.* (2009) suggested that the optimised charge distribution and the induced electrostatic

interaction can promote the equal chance of interactions between excipients and APIs, which leads to a stable ordered mixture.

2.4.3. Combined effects of electrification and electrostatic interactions

Contact electrification and electrostatic interactions usually occur simultaneously. In the experiments of LaMarche *et al.* (2009), a mixture of 3 mm acrylic beads and 300 μm sand was deposited in a steel cylinder and then flow was initiated through the cylinder. It was observed that the sand was coated on the surface of the acrylic beads, which affects the net charge accumulation of the particle system during the flow. LaMarche *et al.* (2009) suggested that as the acrylic beads and sand flowed through the cylinder, they obtained opposite charges on their surfaces due to the contact electrification between each other and between the cylinder. The acrylic beads were charged negatively and the sand was charged positively. The mutual electrostatic interactions lead to agglomeration between the acrylic beads and the sand. In addition, when the sand was coated on the surface of the acrylic beads, it prevented them from charging further. McCarty *et al.* (2007a) prepared poly (styrene-co-divinylbenzene) microspheres with two covalently bound functional groups: tetraalkylammonium groups and sulfonate groups. It was observed that when the microspheres were agitated on an aluminium dish, the tetraalkylammonium microspheres were positively charged and the sulfonate microspheres were negatively charged. When 200 μm diameter sulfonate microspheres and 20 μm diameter tetraalkylammonium microsphere were agitated on the aluminium dish, each 200 μm sphere became coated with a monolayer of the 20 μm spheres (Figure 2.8). When the two oppositely charged spheres were the same size, extended agglomerates were formed with a local crystalline structure due to Coulombic ordering (e.g., (+)(-)(+)(-)) but there was no long-

range order as found in the experiments of Grzybowski *et al.* (2003). In addition, it was also shown that the like-charged spheres remained uncoated due to the repulsive force. In this research the functional groups contain mobile ions. Therefore, the spheres were charged due to the ion-transfer, as suggested by McCarty *et al.* (2007a).

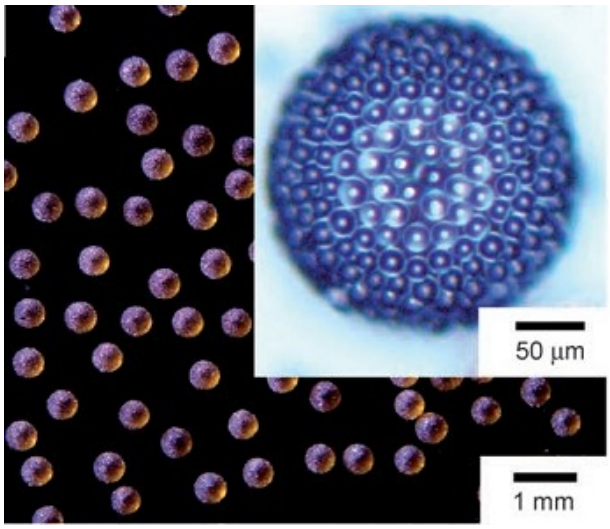

Figure 2.8 The structure of electrostatic agglomerates (McCarty *et al.*, 2007a).

In fact, the combined effects of contact electrification and electrostatic interactions are also observed in the experiments discussed in the previous sections. For instance, in the experiments of Sowinski *et al.* (2009; 2010), charged particles due to contact electrification in fluidization were found adhering on the walls of the column. The adhered particles on the walls could further compromise the charge transfer between the particles and the walls. Šupuk *et al.* (2012) showed that the API particles were more prone to be charged and adhere to the walls of the container during contact electrification in the blending process, which can cause significant segregation of API in pharmaceutical powders (Šupuk *et al.* 2011). It is clear that contact electrification and electrostatic interactions can affect each other during powder handling process. The combined effects of contact electrification and electrostatic interactions

can lead to different electrostatic phenomena when the particles are sensitive to electrostatic interactions, especially for fine particles, which will increase the difficulties in dealing with the electrostatic behaviour of particles during powder handling processes.

In the work on the electrostatic behaviours of pharmaceutical particles in mixers by Zhu *et al.* (2007b), particles were found to be charged to a saturated value during mixing and they adhered to the inner wall of the mixers. The charge of the coarse particles increased monotonically with the mixing time until it reached saturation, while the charge on the fine particles increased initially and then decreased to a smaller saturated value. It was suggested that the adhesion of particles to walls was more significant for fine particles, which lead to a different charge accumulation process. Karner and Urbanetz (2011, 2012) reviewed the effects of contact electrification and electrostatic interactions of inhalation powders. They suggested that the electrostatic behaviour depended on the properties of the particles (e.g. work functions, mechanical factor and particle size and shape), the properties of the particle system (e.g. mixing ratio and charge dissipation) and the operating conditions (e.g. relative humidity, contact energy and mixing speed). The induced electrostatic forces have a considerable impact on the performance of the inhalation process. For instance, the adhesive force can potentially reduce the emitted dose of dry powder inhalation (DPI) (Zhu *et al.* 2008b; Karner and Urbanetz, 2011). On the other hand, the electrostatic charge can also be beneficial. The electrostatic interactions can disperse like-charged particles and selectively attract unlike-charged particles in a mixture (Telko *et al.*, 2007; Karner and Urbanetz, 2011).

Contact electrification and electrostatic interactions have been observed and utilized in many powder handling processes. In electrophotography (Schein *et al.*, 1992; Castle and Schein,

1995), small toner particles (average 10 μm) and larger carrier particles (200 μm) are mixed in a drum and became oppositely charged due to contact electrification. Then the smaller toner became coated on the surface of the larger particles for further handing processes. In the powder coating process (Moyle and Hughes, 1985; Mazumder *et al.*, 1997), the charged particles could even be used to paint cars (Thomas *et al.*, 2009). The charged particles are sprayed and adhered on the work piece due to the image force. The adhered particles are then heated and melted to form a uniform layer. For the particle (powder) separation process (Saeki, 2006), the triboelectric separation is a technique in which the particles are triboelectrically charged in a charging device and then separated in an electric field for particles with different sizes and masses. Saeki (2006) proposed a type of vibratory device to separate the mixture of plastic particles. The plastic particles were charged in a rotating cylindrical drum by contact and frictional electrification and then delivered to a vibrating device. The device consists of a vibrating plate and two inclined electrodes on which an electric field is applied. The vibrating plate can prevent bi-charged particles from adhering and the positively charged particles can be separated from the negatively charged particles due to their different displacement directions in the electric field. In summary, contact electrification and electrostatic interactions provide a convenient way to manipulate particles during powder handling processes.

Contact electrification and electrostatic interactions in experimental work and powder handing processes are very sensitive to extrinsic conditions, such as humidity (Guardiola *et al.*, 1996; Greason, 2000; Kwok and Chan, 2008), contamination (Eilbeck *et al.*, 2000), temperature (Greason, 2000) and even atmospheric pressure (Hogue *et al.*, 2004). Consequently, it is extremely difficult to achieve acceptable reproducibility of experimental

data, which inhibits a full understanding of electrostatic phenomena. The instruments that are used to measure the charge of particles during powder handling processes may not be able to function precisely. For instance, the electrostatic probe that is used to measure the voltage of a granular bed during fluidization can lose its accuracy when fine particles are adhered on the probe (Guardiola *et al.*, 1996; Sowinski *et al.*, 2010). In addition, many experimental methods cannot provide more detailed information of the particles, such as the trajectory of the particle, the interactions between particles, the charge of specific particles, the charge distribution and accumulation during powder handling processes. Therefore, it is still difficult to investigate the relationship between the dynamics of particles and the electrostatic behaviour of particles using experimental methods.

2.5. DEM-CFD for contact electrification and electrostatic interactions

The discrete element method (DEM) was initially introduced and applied to soil and rock mechanics by Cundall and Strack (1979). DEM is a numerical method to model the dynamics of particles based on classical (Newtonian) mechanics. It can provide specific dynamic information about particles, such as their trajectory, the interactions between them, etc. The discrete element method coupled with computational fluid dynamics (DEM-CFD) can be used to analyze the dynamic behaviour of particles and a fluid (gas/liquid) when the particles and the fluid are interacting with each other. Hence, in recent decades, DEM-CFD has been extensively used to analyze detailed information about powder handling processes, which is often considered difficult for experimental work, including contact electrification and electrostatic interactions.

2.5.1. The discrete element method

2.5.1.1. The discrete element

In DEM, a particle is treated as a discrete element. Two types of discrete elements are commonly used: hard-sphere and soft-sphere. In the hard-sphere model, the collision between the particles is assumed to be binary and instantaneous and the interaction force is impulsive and implicit (Hoomans *et al.*, 1996; Li and Kuipers, 2002; Richardson *et al.*, 2011). The velocities of the particles after the instantaneous collision are the result of the exchange of momentum and energy. The hard-sphere model is suitable for rapid granular flow (Hoomans, *et al.*, 1996; Zhu *et al.*, 2007a). However, this model cannot provide detailed information of interparticle interactions during a collision. In the soft-sphere model, the collision between particles is considered progressive and the deformation (overlap) and the interparticle interactions are determined explicitly at each time step. The velocities and the dynamics of the particles can then be calculated using Newton's second law of motion. Hence, the soft-sphere model has been extensively used to explore the detailed information about the dynamic behaviour of particles. In this study, the soft-sphere method is employed and discussed.

The most common shapes of discrete elements are the circular disc in 2-D (Cundall and Strack, 1979) and the sphere in 3-D (Guo *et al.*, 2011). The advantage of the circular and spherical elements is their computational simplicity in terms of contact detection and interparticle interaction models. However, the particle shape can change the mechanical behaviour of particles during a powder handling process (Shinohara *et al.*, 2000; Latham and Munjiza, 2004). For instance, Shinohara *et al.* (2000) implemented triaxial compression tests

to investigate the effect of particle shape on the angle of internal friction of fine powders. It was found that the angle of internal friction increased with increasing angularity of the particles owing to the increase of the interlocking effect.

The particle shape should be considered in DEM, especially for powder handling processes, where the particle shape may play an important role. Generally, two methods have been employed to represent particle shape in DEM (Höhner *et al.*, 2011): the single-particle method and the multi-sphere method.

In the single-particle method, the particle is a single object defined with a complicated geometry, such as polyhedron (Cundall, 1988; Latham and Munjiza, 2004), ellipsoid (Lin and Ng, 1997) and superquadric (Hogue, 1998). A wide variety of complex particle shapes can be represented by this single-particle method especially with the polyhedron and superquadric methods. However, due to the complexity of geometrical shape, the contact detection process becomes computationally expensive for the single-particle method (Hogue, 1998). Furthermore, the contact force model between two polyhedral particles is still not well understood (Höhner *et al.*, 2011).

In the multi-sphere method, the particle (multi-sphere) is constructed by a cluster of primary spheres (Favier *et al.*, 1999; Kodam *et al.*, 2009; Höhner *et al.*, 2011). The sizes of the primary spheres and the connection (overlap) between spheres vary in different applications to mimic the specific geometrical surfaces or shapes. The relative position of the primary sphere with respect to the centroid of the particle can remain fixed and the multi-sphere is treated as a rigid body. Favier *et al.* (1999) proposed a symmetric multi-sphere method in

which the particle is represented by a row of primary spheres with different sizes to model particles with axi-symmetric shapes. For particles with more complex shapes, a cluster of primary spheres can be used to construct and fit the polyhedral particle, which is the so-called sphere-tree construction method (Bradshaw and O'Sullivan, 2004; Wang *et al.*, 2006). However, the fit error, e.g. the volume difference between the multi-sphere and the polyhedron can be very high (Wange *et al.*, 2006). In the multi-sphere method, the contact detection and contact force model are based on the primary spheres, which is essentially the same as the spherical particle model in DEM (Höhner *et al.*, 2011). Due to this simplicity, the multi-sphere method has been widely used to simulate particles with irregular shapes in DEM (Kodam *et al.*, 2009)

2.5.1.2. Governing equation

The dynamics of the particle in DEM are governed by Newton's second law of motion:

$$m_i \frac{d\mathbf{v}_i}{dt} = \mathbf{F}_i \tag{2.10}$$

$$I_i \frac{d\boldsymbol{\omega}_i}{dt} = \mathbf{T}_i \tag{2.11}$$

where m_i and I_i are the mass and the moment of inertia of particle i; $\mathbf{v}_i$ and $\boldsymbol{\omega}_i$ are the translational and angular velocities of particle i; $\mathbf{F}_i$ and $\mathbf{T}_i$ are the resultant force and torque acting on particle i; t is the time. The resultant force on the particle i can be expressed as:

$$\mathbf{F}_i = \sum_j^{n_c} \mathbf{F}_{ij}^c + \sum_k^{n_e} \mathbf{F}_{ik}^e + \mathbf{F}_i^f + m_i \mathbf{g} + \ldots \tag{2.12}$$

where $\mathbf{F}_{ij}^c$ is the contact force, including the normal and tangential forces, on particle i by particle or wall j; n_c is the number of particles in contact with particle i; $\mathbf{F}_{ik}^e$ is the electrostatic

force on particle *i* with particle *k*; n_e is the number of particles with electrostatic interactions with particle *i*; $\mathbf{F}_i^f$ is the particle-fluid interaction force on particle *i*; $m_i g$ is the gravitational force of particle *i*; $\boldsymbol{g}$ is the gravitational acceleration. When the direction of the force does not coincide with the centroid (centre) of the particle, the torque on the particle is the cross product of the lever-arm distance and force, which changes the rotational motion of the particle, such as tangential contact force.

An explicit numerical scheme is usually adopted to solve the dynamics of the particles in DEM. The computation procedure of DEM is divided into explicit time steps. The time step Δt should be small enough to ensure that the contact process between particles is progressive, i.e. the overlap between particles should propagate incrementally across time steps. The value of the time step is determined by the properties of the particles (Kafui *et al.*, 2002). For spherical particles, the time step is determined by the properties of smallest particles (Kafui *et al.*, 2002):

$$\Delta t = \frac{\pi r_{p\min}}{\lambda}\sqrt{\frac{\rho_p}{G}} \tag{2.13}$$

where

$$\lambda = 0.1631\upsilon + 0.8766 \tag{2.14}$$

$r_{p\min}$ is the radius of the smallest particle; ρ_p is the material density of the smallest particle; *G* is the shear modulus of the smallest particle and υ is the Poisson's ratio. If the velocity of the particle is very large, the time step has to be further reduced to ensure that contact detection can be determined correctly. The interparticle interactions between particles are determined in each time step. Then an explicit integration (Euler) method can be used to calculate the translational and rotational velocities and displacements of particles as:

$$\mathbf{v}_i^{t+\Delta t} = \mathbf{v}_i^t + \frac{d\mathbf{v}_i}{dt}\Delta t \text{ and } \boldsymbol{\omega}_i^{t+\Delta t} = \boldsymbol{\omega}_i^t + \frac{d\boldsymbol{\omega}_i}{dt}\Delta t \tag{2.15}$$

$$\mathbf{x}_i^{t+\Delta t} = \mathbf{x}_i^t + \mathbf{v}_i^{t+\Delta t}\Delta t \text{ and } \boldsymbol{\theta}_i^{t+\Delta t} = \boldsymbol{\theta}_i^t + \boldsymbol{\omega}_i^{t+\Delta t}\Delta t \tag{2.16}$$

where $\mathbf{x}_i$ and $\boldsymbol{\theta}_i$ are the translational and rotational coordinates of particle *i*. From *t* to $t+\Delta t$, the translational and rotational velocities and the displacements of particles are updated incrementally.

2.5.1.3. Contact interactions

The contact interaction between particles in DEM is based on force-displacement relationships. In reality, the contact between particles causes deformation of the particles at the contact area. The deformation is generally represented by the overlap between particles in DEM and the contact area is approximated by the intersection area, which is a circular area lying at the intersection circle when the spherical particles are considered. Hence, in DEM, the force-displacement relationship is essentially the relationship between the contact force and the overlap of particles. The contact force can be decomposed into two components: normal contact force which is normal to the contact (area) plane and the tangential force which is parallel to the contact (area) plane.

Various models were developed to determine the normal and tangential forces with respect to the normal and tangential displacements. A simple linear model was first introduced by Cundall and Strack (1979), which can be written as:

$$F^n = k_n \alpha_n \tag{2.17}$$

$$F^t = k_t \alpha_t \tag{2.18}$$

where F^n and F^t are the normal and tangential contact forces; k_n and k_t are the normal and tangential elastic coefficients (stiffnesses); α_n and α_t are the normal and tangential displacements. The damping effects, which are proportional to the relative velocities, can also be considered as the viscous dissipation in the normal and tangential directions during the contact. This model is the so-called spring-dashpot model where the spring is used for the linear relation between the force and the displacement and the dashpot is used for the viscous dissipation. In addition, when the tangential force is equal to the maximum tangential force defined by Coulomb's law of friction, the contacting particles will slide against each other at the contact area and the tangential force becomes:

$$\left|F^t\right| = \mu\left|F^n\right| \tag{2.19}$$

where μ is the friction coefficient. Due to the simplicity, the spring-dashpot model has been widely used for DEM (Cundall and Strack, 1979; Tsuji *et al.*, 1993; Xu and Yu, 1997).

The rigorous theories of frictional elastic contact mechanics were developed by Hertz (Johnson, 1985) and Mindlin and Deresiewicz (1953) for the normal and tangential contact of spheres. These theories show that the force-displacement relationships are nonlinear.

According to Hertz theory (Johnson, 1985), the normal contact force between two spheres can be written as:

$$F^n = \frac{4}{3} Y^* \sqrt{R^*} \alpha_n^{3/2} \tag{2.20}$$

where Y^* and R^* are the equivalent Young's modulus and the equivalent radius, which are defined as:

$$Y^* = \left(\frac{1-\upsilon_i^2}{Y_i} + \frac{1-\upsilon_j^2}{Y_j} \right)^{-1} \tag{2.21}$$

$$R^* = \left(\frac{1}{R_i} + \frac{1}{R_j} \right)^{-1} \tag{2.22}$$

where Y_i and Y_j are the Young's moduli of spheres *i* and *j*; υ_i and υ_j are the Poisson's ratios of spheres *i* and *j*; R_i and R_j are the radii of spheres *i* and *j*. The radius of the contact area can be given as:

$$r_a = \sqrt{R^* \alpha_n} \tag{2.23}$$

Then the contact area is:

$$S = \pi r_a \tag{2.24}$$

It can be seen that the contact area of the spheres is assumed to be circular and the relationship between the normal contact force and the normal displacement is nonlinear.

Mindlin and Deresiewicz (1953) demonstrated that the force-displacement relationship in the tangential direction depends on the whole loading history and instantaneous rate of change of the normal and tangential force and displacement. The solutions were presented in the form of instantaneous compliances. However, due to the dependence on both the initial state and the entire loading history, the instantaneous compliances cannot be integrated *a priori*. Thornton and co-workers (Thornton and Yin, 1991) suggested that several loading sequences can be identified with the variations of both normal and tangential forces in this procedure. Therefore, they adopted an incremental approach in which the updated normal force and the contact area is followed by calculating the incremental tangential force ΔF^t as:

$$\Delta F^t = 8G^* r_a \eta \Delta \alpha_t \pm \mu(1-\eta)\Delta F^n \tag{2.25}$$

in which

$$G^* = \left(\frac{2-\upsilon_i}{G_i} + \frac{2-\upsilon_j}{G_j} \right)^{-1} \tag{2.26}$$

where ΔF^n is the incremental normal force; G_i and G_j are the shear moduli of sphere *i* and *j*; the parameter η can be defined as:

$$\eta = 1 \text{, when } \left|\Delta \alpha_t\right| < \frac{\mu \Delta F^n}{8 G^* r_a} \tag{2.27}$$

It can be seen that, at this stage, the incremental tangential force entirely depends on the contact area and the tangential displacement. This is the Mindlin (1949) 'no-slip' solution. If Eq. (2.27) is not satisfied, a small relative motion, termed 'slip' occurs over an annulus of the contact area with a no slip central circular region. This assumption is often referred as micro-slip, in which θ can be defined as:

$$\eta^3 = 1 - \frac{F^t + \mu \Delta F^n}{\mu F^n} \text{, when loading} \tag{2.28}$$

$$\eta^3 = 1 - \frac{F^* - F^t + 2\mu \Delta F^n}{2\mu F^n} \text{, when unloading} \tag{2.29}$$

$$\eta^3 = 1 - \frac{F^t - F^{**} + 2\mu \Delta F^n}{2\mu F^n} \text{, when reloading} \tag{2.30}$$

The negative sign in Eq. (2.25) is only invoked during unloading. F^* and F^{**} are the reversal points for the transitions from loading-to-unloading and unloading-to-reloading, which should be updated to consider the effect of varying normal force in each time step. A similar damping effect as the dashpot can also be applied to the normal and tangential direction to account for the energy dissipation. When the tangential force is equal to the maximum tangential force defined by the Coulomb's law of friction, the sliding behaviour will occur on the contact area

and the tangential force can be determined by Eq. (2.19). Due to the complexity of the Hertz and Mindlin and Deresiewicz theories, several simplified models have also been developed and extensively used in DEM (Walton and Braun, 1986; Walton, 1993; Langston *et al.* 1994, 1995; Vu-Quoc and Zhang, 1999). Plastic deformation during contact has also been considered recently by Thornton (1997) and Vu-Quoc and Zhang (2004).

The Hertz (Johnson, 1985) and Mindlin and Deresiewicz (1953) theories utilise physically realistic particle properties, such as Young's modulus and Poisson's ratio to evaluate the contact interactions. It is easier to link the particle properties to the dynamic behaviour of particles during powder handling processes, compared with the spring-dashpot contact models that have artificial contact stiffnesses. Di Renzo and Di Maio (2004) compared the accuracy of different contact models for collision processes. Three models were chosen: a linear model, based on a spring relationship; a non-linear model, based on the Hertz theory (Johnson, 1985) for the normal force-displacement relationship and the Mindlin (1949) no-slip solution for the tangential force-displacement relationship; a non-linear model with hysteresis, based on the complete theories of Hertz and Mindlin and Deresiewicz (1953). They concluded that it is important to account for the non-linearity in the contact model and micro-slip effects in order to obtain the correct evolution of the contact forces, velocities and displacements.

2.5.1.4. Adhesive forces

Particles can adhere to each other during powder handling processes, especially when fine particles are in contact. The main molecular attraction/surface energy component in adhesion is the van der Wall force. Between molecules it is proportional to z^{-6}, where z is the separation

distance. Hence, the van der Waal force decays very rapidly when the separation distance between two contacting surfaces increases and becomes negligible when the separation distance is larger than a few nanometres (Zhu *et al.*, 2007a). So, in DEM, the van der Waal force is usually considered as an adhesive force during contact. Two common models, JKR (Johnson *et al.*, 1971) and DMT (Derjaguin *et al.*, 1975), were developed to consider the adhesive effect based on the classic Hertz theory. The JKR model combines the adhesive force with the Hertz theory. The adhesive force is assumed to act within the contact area and contributes to the deformation at the contact area. Therefore, it predicts a larger contact area that predicted by the Hertz theory. In contrast, the DMT model considers the adhesive force and Hertz theory separately. It is assumed that the adhesive force cannot affect the contact deformation in the contact area. The contact area is determined by the Hertz theory and the adhesive force is only considered outside the contact area where the separation distance between surfaces is small. Cappella and Dietler (1999) used Atomic force microscopy (AFM) to study the interaction force between the tip of the AFM and the sample. It was found that the JKR model is suitable for highly adhesive systems with low stiffness and large tip radii while the DMT model is applicable for systems with low adhesion and small tip radii. Thornton and Yin (1991) suggested that the JKR and DMT models are both approximations to the general solution that must account for both the adhesive forces acting outside the contact area and within the contact area. Furthermore, complex adhesive models for elastic tangential contact and the elastic-perfectly plastic contact were also developed by Thornton and his co-works (Thornton, 1991; Thornton and Yin, 1991; Thornton and Ning, 1998).

2.5.2. DEM-CFD method

Particle flow is often influenced by the fluid flow during various powder handling processes. The interactions between the particle and the fluid can significantly alter the performance of powder handling processes, especially when the particles are sensitive to the fluid (Guo *et al.*, 2009). In DEM-CFD, a two-way coupling method is usually used to determine the particle-fluid interaction (Tsuji *et al.*, 1993; Xu and Yu, 1997; Kafui *et al.*, 2002).

2.5.2.1. The particle-fluid interaction

In general, the dynamics of the particle-fluid system is governed by classical Newtonian mechanics. When the system comprises a large number of particles in a fluid field, the dynamics of the system becomes too complicated to be modelled by direct analytical solutions. Numerical methods based on local averages (Anderson and Jackson, 1967) are usually adopted to describe the motion of the system. The fluid field is usually divided into cells and the cell size is usually larger than the particle size in DEM-CFD. Then the particle-fluid interaction acting on the particle can be determined in each fluid cell as (Anderson and Jackson, 1967; Kafui *et al.*, 2002):

$$\mathbf{F}_i^f = \psi_i \nabla \cdot \boldsymbol{\xi}_f + \mathbf{F}_{di}^{'} \tag{2.31}$$

where ψ_i is the volume of the particle *i*; $\boldsymbol{\xi}_f$ is the total local average stress tensor; $\mathbf{F}_{di}^{'}$ is the skin friction and drag component to the particle-fluid interaction. The total local average stress tensor can be defined as:

$$\boldsymbol{\xi}_f = -p\mathbf{\Gamma} + \boldsymbol{\tau}_f \tag{2.32}$$

where p is the fluid pressure; Γ is the identity tensor; $\boldsymbol{\tau}_f$ is the viscous stress tensor. The skin friction and drag force component $\mathbf{F}_{di}^{'}$ comprise (1) the effective drag force due to the relative motion between the fluid and the particle and (2) the virtual mass force and the Basset force (Li *et al.*, 1999) due to the acceleration of the particle with respect to the fluid. The virtual mass force and the Basset force become insignificant when the fluid density is much smaller than the particle density (Kafui *et al.*, 2002; Zhu *et al.*, 2007a). According to Anderson and Jackson (1967), the effective drag force should be related to the local porosity or void fraction of the fluid cell. Then the particle-fluid interaction can be written as:

$$\mathbf{F}_i^f = -\psi_i \nabla p + \psi_i \nabla \cdot \boldsymbol{\tau}_f + \kappa \mathbf{F}_{di} \tag{2.33}$$

where κ is the local void fraction of the fluid cell. The drag force for an isolated particle moving in a fluid depends on the relative velocity between the fluid and the particle. However, when the particle is surrounded by other particles in a fluid, the void fraction at the local area should also be considered to correct the drag force (Di Felice, 1994; Xu and Yu, 1997; Kafui *et al.*, 2002; Li and Kuiper, 2002). In addition, the lift forces, including Saffman force and Magus force, can also contribute to the particle-fluid interaction (Xiong *et al.*, 2005; Zhu *et al.*, 2007a). The Saffman lift force is caused by the pressure gradient induced by the relative shear velocity while the Magus lift force is induced by the rotational velocity difference. The lift forces are usually perpendicular to the fluid flow direction and different from the drag force that is parallel to the fluid flow direction.

2.5.2.2. The fluid flow

The motion of the fluid is governed by the continuity and momentum equations in DEM-CFD. In dry powder handling processes, the fluid is usually treated as a gas, which is an ideal

compressible fluid. Then the continuity and momentum equations on the local average variables can be written (Kafui *et al.*, 2002):

$$\frac{\partial(\kappa\rho_f)}{\partial t} + \nabla\cdot(\kappa\rho_f \mathbf{u}) = 0 \tag{2.34}$$

$$\frac{\partial(\kappa\rho_f \mathbf{u})}{\partial t} + \nabla\cdot(\kappa\rho_f \mathbf{u}\mathbf{u}) = \nabla\cdot\xi_f - \mathbf{F}^f + \kappa\rho_f \mathbf{g} \tag{2.35}$$

where $\mathbf{u}$ and ρ_f are the fluid velocity and density, respectively. The particle-fluid interaction $\mathbf{F}^f$ on the fluid cell is defined as:

$$\mathbf{F}^f = \frac{\sum_i^{n_f} \mathbf{F}_i^f}{\psi_c} \tag{2.36}$$

where n_f is the number of particles inside the fluid cell; ψ_c is the volume of the fluid cell. It can be seen that the particle-fluid interaction $\mathbf{F}^f$ on the fluid cell is a summation of fluid force, acting on particles inside the fluid cell, divided by the volume of the fluid cell.

In this method, the fluid cell is larger than the particle size and the particle-fluid interaction acting on each particle inside the fluid cell is locally averaged, especially for spherical particles. So this method cannot provide specific information at the interface between the particle and the fluid, such as the pressure distribution and the body force field of the fluid around the particle surface. To solve the body force field at the particle-fluid interface, various alternative methods have been proposed, such as DEM-CFD coupled with the immersed boundary method (Guo *et al.*, 2013), DEM coupled with lattice Boltzmann method (Feng *et al.*, 2007), and DEM coupled with the smoothed particle hydrodynamics (Potapov *et al.*, 2001; Cleary *et al.*, 2006). In these methods, the particle surface is treated as a solid boundary for the smaller fluid elements. The particle-fluid interaction at the particle-fluid

interface is a function of the relative velocity between the particle and the fluid and the volume fraction at the local area, so that the body force field at the particle-fluid interface can be solved and represented by the fluid elements around the particle surface.

2.5.3. DEM-CFD applications

DEM-CFD has been extensively applied to investigate the dynamic behaviour of particle systems in various powder handling processes. Zhu *et al.* (2008a) categorised the DEM-CFD applications of the particulate system into three groups: particle packing, particle flow and particle-fluid flow/transport. The particle packing includes particle deposition (Zhang *et al.*, 2001; Munjiza and Latham, 2004; An *et al.*, 2005), pile formation (Luding, 1997; Zhou *et al.*, 2003), compaction (Kong and Lannutti, 2000; Thornton *et al.*, 2004; Martin *et al.*, 2006; Chung and Ooi, 2007) etc. The study of particle packing focuses on the macroscopic properties, e.g. packing density and packing pattern, and micro-structural properties, e.g. coordination number, radial distribution function, force network and stress distribution. The particle flow concerns the flow pattern, convection, segregation, etc, which involves hopper flow (Potapov and Campbell, 1996; Cleary and Sawley, 2002; Parisi *et al.*, 2004; Ketterhangen *et al.*, 2007), mixing/blending (Stewart *et al.*, 2001; Kuo *et al.*, 2002; Chaudhuri *et al.*, 2006), milling (Rajamani *et al.*, 2000; Cleary, 2001; Morrison *et al.*, 2004), die filling (Wu *et al.*, 2003; Coube *et al.*, 2005; Wu and Cocks, 2006; Wu, 2008; Bierwisch *et al.*, 2009; Guo *et al.*, 2009, 2010, 2011; Nwose *et al.*, 2012). Particle-fluid flow concentrates on the flow regimes and the dynamic behaviour of particle in fluidization (Tsuji *et al.*, 1993, 2008; Xu an Yu, 1997; Xu *et al.*, 2000; Kafui *et al.*, 2002; Li and Kuipers, 2007; Gui *et al.*, 2008) and

pneumatic conveying processes (Xiang and McGlinchey, 2004; Lim *et al.*, 2006; Kuang *et al.*, 2008).

The utilization of DEM-CFD can provide a better multi-scale understanding of powder handling processes. For instance, Ketterhagen *et al.* (2009) suggested that process modelling in the pharmaceutical industry using DEM can offer insight into the effects of particle properties and operating conditions on the performance of pharmaceutical processes.

2.5.4. DEM-CFD analysis of contact electrification and electrostatic interactions

DEM-CFD has attracted interesting attention for research on contact electrification and electrostatic interactions during powder handling processes. In DEM-CFD, the contact electrification and the electrostatic interactions can be analyzed separately, which can establish the fundamental understanding of different electrostatic phenomena. The combined effects of contact electrification and electrostatic interactions can also be considered and compared with experimental work, and thus model the problem more realistically.

2.5.4.1. Electrification

DEM-CFD can be used to model contact electrification at different geometrical scales, including charge transfer and distribution on the particle surface and charge transfer in the particle system.

In order to determine the charge distribution on a particle surface, the surface is usually divided into meshes or elements so that the charge concentration in each element can be determined and subsequently the charge distribution may be obtained. Duff and Lacks (2008) randomly generated points on a spherical particle and assumed that high energy electrons are trapped at these points. A hard-sphere model was then used to simulate the motion of the particles with initial random velocities. When the points on one particle are within the contact area between particles, the trapped electrons will be transferred to the area with lower energy states on the other particle. Although the initial surface charge density is the same for particles with different sizes, it was shown that larger particles were charged positively while smaller particles became negatively charged. In powder handling process, the contacts between objects depend on the operating conditions (Ireland, 2010a). Random generation of energy points may not be able to precisely represent the charge distribution on particles. In Ireland's work (2012), the charge transfer between a 2-D elliptic particle and a tilted surface during impact was modelled using DEM. The surface of each particle was divided into segments and the charge was only transferred onto the segments inside the contact area because of the insulting nature of the particle. The roundness ratio was defined as the ratio of radii between the major axis and the minor axis. It was shown that for the contact electrification of an elliptic particle impacting (bouncing) on a surface, the particle with a lower roundness ratio lead to a larger contact area. In addition, the transferred charge was larger with a larger contact area, which meant that the contact and charge transfer process could be affected by particle shape.

The charging behaviour of the particles during powder handling processes has also investigated. Watano *et al.* (2003) implemented a simplified electrification model in DEM

and explored the contact electrification in pneumatic conveying processes. In their model, the transferred charge between the particle and the pneumatic conveying during each collision Δq is assumed to be proportional to the maximum contact area $S(v)$, which is a function of the impact velocity v:

$$\Delta q = \sigma S(v) \tag{2.37}$$

where σ is a constant that is related to the charge density. It is found that the charge of particles during pneumatic conveying process increases with the number of collision and the air velocity. However, the saturation of the charge on each particle was not considered, which may result in an overestimation of the maximum charge that a particle can acquire. Yoshida *et al.* (2003) analyzed the charge accumulation of polymer particles in a vibrating container with an electrification model in which the impact charge is a function of the contact area and the initial charge on the particle. The surface of a particle is divided into a number of meshes and the transferred charge stays in the contact mesh. It is observed that the charge of the particle reaches an equilibrium state during vibration and the number of the meshes does not affect the charge of the particles if the number of the sites is larger enough. However, the charge distribution on the particle surface using meshes is not examined in this study.

2.5.4.2. Electrostatic interactions

The presence of charge on particles induces electrostatic interactions. In numerical methods, the electrostatic interactions between particles can be determined explicitly or implicitly (Esselink, 1995; Kolikov *et al.*, 2012). The explicit method generally determines the electrostatic force directly based on the distance between objects and the charge of the objects, while the implicit method first calculates the electric potential for the given charge density

distribution in the electric field, then determines the electric strength and the subsequent electrostatic interactions.

Using the explicit method, the electrostatic interactions are generally determined based on the Coulomb's law (Eq. (2.9)). If the distance between particles is large enough, the electrostatic force can be adequately and accurately determined by the total charge of particles that is calculated by summing up elementary point charges on each particle (Kolikov *et al.*, 2012). If the separation distance between the charged objects is relatively small compared to the size of the charged objects, the charged objects cannot be considered as point charges because of the polarization of the elementary charge on the surface of the object. So the explicit method should be applied to the elementary charge on the surface of the object rather than the object.

However, the efficiency of the explicit method is limited by the number of particles (point charges). Due to the long-range nature, theoretically, electrostatic interactions between all particles in a system should be considered, which is very computer-intensive with a computational time up to $O(N^2)$ for a system of N particles (Hoffmann, 2006). Since the electrostatic force generally decreases with increasing separation distance, r, to a power of -2 (Eq. (2.9)), and it becomes very weak when the separation distance is large, a direct truncation (DT) method has been introduced in order to improve the computational efficiency. In the DT method, a cut-off distance is specified and only electrostatic interaction between particles of a separation distance less than the cut-off value is considered. The computation efficiency of the DT method depends upon the cut-off distance; the shorter the cut-off distance, the faster the computation. The DT method is a simple approach that can significantly reduce the computational time. However, the DT method may cause some artificial effects or introduce

computational errors due to the exclusion of long-range electrostatic interactions (Brooks, et al., 1985; Brooks, 1987; Takahashi et al., 2010).

However, the implicit method can be used to consider the entire particle system and the electric field. The potential distribution of an electric field is first calculated from the charge distribution by solving Poisson's equation that is derived from Guess' law and energy conservation (Dawson, 1983; Hockney and Eastwood, 1988; Esselink, 1995) as follows:

$$\nabla^2 \phi = -\frac{\sigma}{\varepsilon_0} \tag{2.38}$$

where ϕ is the electric potential; σ is the charge density. The electric potential distribution is then differentiated to obtain the electric field strength and by multiplying the electrostatic charge with the electric field strength, the electrostatic forces are obtained:

$$\mathbf{F}^e = q\mathbf{E} = -q\nabla\phi \tag{2.39}$$

where q is the charge of the particle; $\mathbf{E}$ is the electric field strength. The indirect method with an electric potential is commonly used in molecular dynamics, plasma and astrophysics simulations for the applications in which the electric field and the charge distribution are of primary concern (Esselink, 1995).

In practice, the electric field or the calculation domain should be divided into meshes and then the charge of particles can be mapped onto their nodes to obtain the charge (density) distribution. This is the so-called particle-mesh (PM) method (Dawson, 1983; Hockney and Eastwood, 1988). However, in this method, the interaction between particles is calculated based on the mesh discretisation and the particle distribution, even for the short-range neighbourhood. So the interactions between particles in the local vicinity (e.g. in the same

mesh) cannot be determined accurately due to the extrapolation of the charge distribution onto each mesh. In order to obtain a more accurate calculation, on the basis of the PM method, the particle-particle and particle-mesh (PP-PM) method (Dawson, 1983; Hockney and Eastwood, 1988; Shimada *et al.*, 1993; Luty and VanGunsteren, 1996) has been derived. In this method, the electrostatic interaction between particles within the cut-off distance is calculated directly while the PM method is employed for particles located outside the cut-off distance. In terms of the computational complexity, under periodic boundary conditions, the PP-PM method is superior to the Ewald method (Esselink, 1995), in which the short-range component is summed in real space and the long-range component is summed in Fourier space in MD and plasma simulations. In order to reduce the computational complexity in calculating the charge and potential distribution, some advanced method such as the multipole expansion method can also be employed (Hoffmann, 2006; Liu *et al.*, 2010).

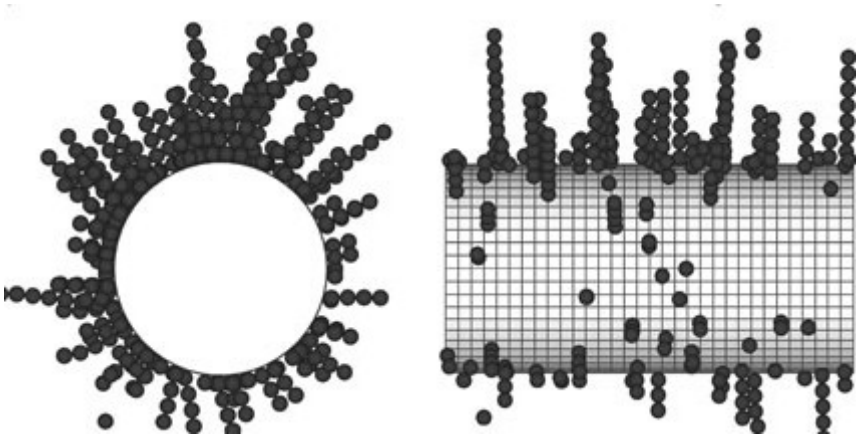

Figure 2.9 A snapshot of DEM simulations of particle deposition on the cylinder (Liu *et al.*, 2010).

DEM has been advanced to model charged particle systems (Liu *et al.*, 2010; Pei *et al.*, 2010; Hassani *et al.*, 2013). Hassani *et al.* (2013) investigated the effects of electrostatic forces on the hydrodynamics of gas-solid fluidized beds using DEM-CFD. The particle size is in the

range of millimetres and the charge of the particle is maintained constant. The Coulomb force was used to compute the long-range electrostatic interaction. The DT method was applied at the cut-off distance, for which the electrostatic force became less than 5% of the gravitational force on each particle. It was found that, for mono-charged particles, the bubble size decreased and the fluidized bed tended to be more homogeneous; for bi-charged particles, the fluidized bed tended to form chains of particles. Pei *et al.* (2010) developed a coupled discrete element method with computational fluid dynamics (DEM-CFD) with electrostatic interactions using the DT method and simulated the deposition of bi-charged micro particles in a container using a cut-off distance of 10 times the particle radius. Due to the electrostatic forces between particles, the formation and breakage of agglomerates were observed in various deposition stages (see Section 4.4). Liu *et al.* (2010) modelled the capture of particles onto a macroscopic electrode in an induced electric field, in which the dynamics of particles was analyzed using DEM and the electric field near surfaces within a distance of 1.05-1.2 times the particle radius was computed with a boundary element method (BEM). The electric field induced by distant particle charges was considered using an adaptive multipole expansion method. The numerical simulations confirmed the formation of "chain-like" aggregates on the macroscopic electrode (Figure 2.9). However, because of the computational complexity of BEM in calculating the charge distribution on the surface of spheres, the computational time will increase significantly if more particles are involved. In the previous DEM studies for charged particles, the DT method was generally employed because of its computational efficiency. Artefacts and computational errors may be introduced as a result of neglecting long-range electrostatic forces in DEM-CFD.

2.5.4.3. The combined effects

Contact electrification and electrostatic interactions occur simultaneously during powder handling processes. In numerical methods, the combined effects of contact electrification and electrostatic interactions can be considered with the contact electrification models and electrostatic force models.

Hogue *et al.* (2008) analyzed the electrification of particles rolling down an inclined plane using a time-dependent electrification model:

$$q(t) = q_a\left(1 - e^{-k_c t}\right) \tag{2.40}$$

where $q(t)$ is the charge of the particle at time t, q_a is the saturation charge that is calculated from the air breakdown field induced by a sufficiently high surface charge density and k_c is a charging coefficient. Eq. (2.40) indicates that the charge on a particle is a function of the saturation charge q_a and time t. The electrostatic interactions between particles are modelled with unscreened and screened Coulomb force models. The former is a direct use of Coulomb's law (Eq. (2.9)) by treating the charged particles as point charges, while the latter introduces an additional term to consider the polarization effects of particles close to a reference particle. A screening radius is also applied to define a spherical region for calculating the charge concentration and determining the induced polarization effects. They showed that, with the unscreened force model, particles spread to a larger angle on the inclined plane compared to that determined using the screened force model.

Šupuk *et al.* (2011) experimentally investigated the charging process of α-lactose monohydrate, hydroxypropyl cellulose and alumina in a horizontally shaking capsule made of

stainless steel, PTFE, PMMA (Perspex) or glass. In addition, DEM was used to simulate the charging process; they used Eq. (2.40) to model the electrification process and also considered the long-range Coulomb force between particles. It was found that the temporal trend of the charging process followed a first-order (exponential) rate process both in the experiments and the simulations. If the electrostatic force was ignored in DEM, the predicted equilibrium charge was much higher than the experimental value. When the electrostatic force was considered within the electrification process in DEM, it provided an improved prediction of the charging accumulation, comparing with the experimental results.

The time-dependent electrification model (Eq. (2.40)) can be derived from the contact frequency (Zhu *et al.*, 2007b), which can be used for collisional systems or processes dominated by particle collisions with 'regular' frequency. It is not applicable for systems or processes involving complicated particle dynamics and enduring random contacts.

2.6. Other numerical methods for contact electrification and electrostatic interactions

Contact electrification and electrostatic interactions have also been modelled using different numerical methods, such as molecular dynamics (MD), Monte Carlo (MC), CFD, etc.

At the electronic interface, Shirakawa *et al.* (2010) calculated the electron transfer between a metal and a polymer (PTFE) using a quantum chemical calculation that was based on the exchange correlation potential of electrons. The surface structure of the metal and the polymer are modelled by a few layers of molecule clusters (Figure 2.10). It was found that the electron from the metal can be transferred to the unoccupied states (surface state and conduction band)

of PTFE, depending on the work function of the metal. The electronic structure at several layers of molecules from the PTFE surface is changed due to the charge transfer.

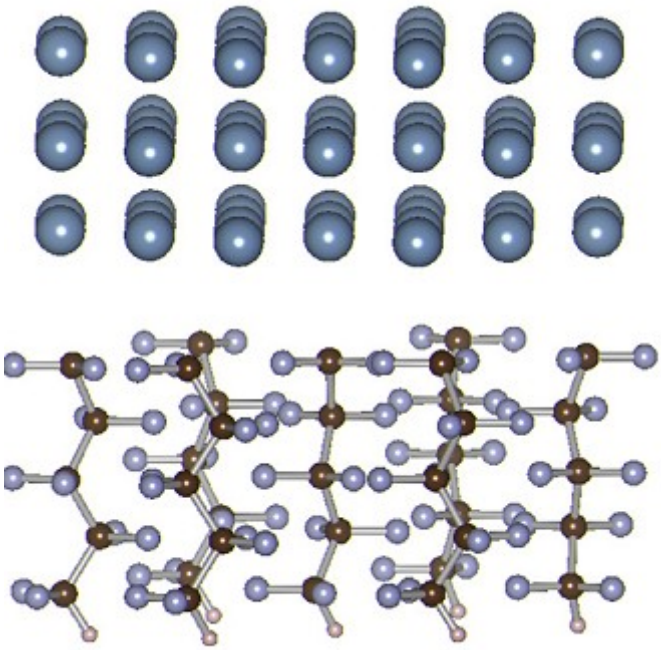

Figure 2.10 Interface model of aluminium (upper) and PTFE (lower) (Shirakawa *et al.* 2010).

Wu *et al.* (2005, 2008) modelled the self-assembly of similarly charged particles using a 2D Monte Carlo (MC) method in which the particle system is treated as a canonical ensemble. A dispersed structure is observed in the particle system. The structure varied with the area fraction (the area occupied by particles divided by the total system area). This numerical analysis showed good agreements with the experimental investigation, especially at low particle area fractions.

Rokkam *et al.* (2013) investigated the electrostatics in gas-solid fluidization using a CFD electrostatic model. The hydrodynamics of a gas–particle fluidized-bed was modelled by an Euler-Euler multi-fluid CFD model, in which the gas phase and the particle phase (particles

and walls) were treated as different fluid phases. The electrostatic force is a function of particle volume fraction, particle charge and the gradient of the electric potential which can be solved by Poisson equation (Eq. 2.38). Particle-phase segregation due to the electrostatic interactions was observed in two fluidization regimes: bubbling and slugging. The walls were coated by charged particles which induced higher electric fields at the regions close to the walls (Figure 2.11).

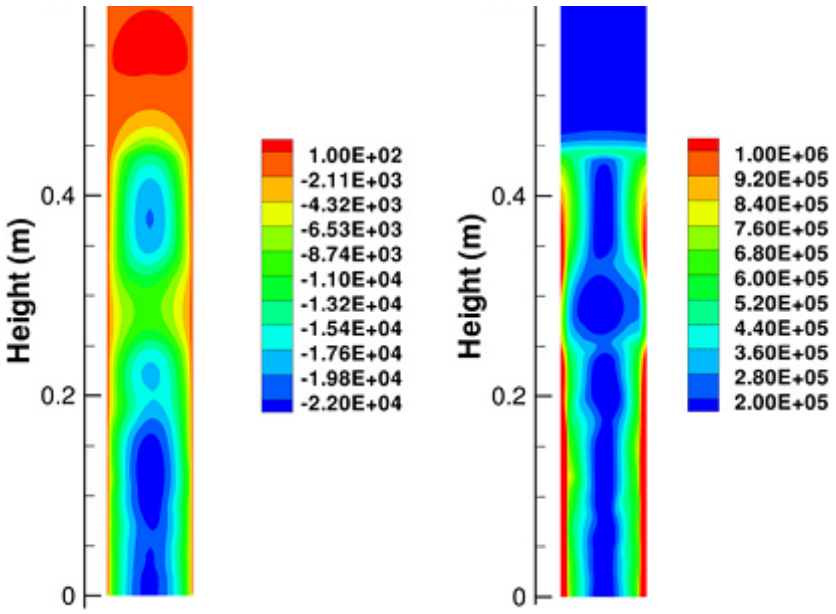

(a) (b)

Figure 2.11 Instantaneous contours in the bubbling fluidized-bed: (a) electric potential (V) and (b) radial component of electric field (V/m) (Rokkam *et al.* 2013).

Various numerical methods can be used to analyze the contact electrification and electrostatics at different scales and conditions. However, the DEM-CFD method can directly link particle properties to contact electrification and electrostatic interactions during powder handling processes, which provides a deeper multi-scale understanding on particle systems.

2.7. Summary

Contact electrification and electrostatic interactions can significantly influence powder handling processes. The mechanisms of contact electrification and electrostatic interactions involving particles are rather complex and not well understood. Due to the complexity of powder handling processes, the effects of contact electrification and electrostatic interaction are extremely difficult to investigate experimentally. In addition, the experimental approaches are limited in providing detailed information on the dynamics of particles in the processes. On the other hand, DEM-CFD is a robust method for analysing the link between the dynamic behaviour of particles and the performance of powder handling processes. Therefore, it is feasible and suitable to investigate the mechanisms and influence of contact electrification and electrostatic interactions on powder handling processes using DEM-CFD.

CHAPTER 3 CONTACT ELECTRIFICATION FOR SPHERICAL PARTICLES

3.1. Introduction

Contact electrification can generally be recognised as a successive charging process, which can be modelled by a first-order condenser model, as discussed in Chapter 2. In this chapter, a successive condenser model is developed and implemented in the DEM-CFD model developed by Kafui *et al.* (2002) for analysing contact charging processes. The model is validated using the experimental data reported in the literature. Using the developed model, the effect of particle size on contact electrification during successive impacts is also analyzed. The contact electrification during fluidization is also investigated. Some of the results presented in this chapter have been published in Pei *et al.* (2012, 2013b).

3.2. Implementation of electrification into DEM

3.2.1. Contact electrification model

When a contact occurs, the charge can be transferred from one surface to another due to the total potential difference. To compute the charge transfer in such a collision, a successive condenser model will be introduced for which the total potential difference between the contacting surfaces *i* and *j* can be expressed as (Matsusaka *et al.*, 2000; Matsuska *et al.*, 2010):

$$\Delta V = V_c - V' = V_i - V_j - V' \tag{3.1}$$

where ΔV is the total potential difference; V_c (=V_i - V_j) is the contact potential difference (CPD) between the surfaces; V' is the induced potential difference; V_i and V_j are the work function potential of material *i* and *j*, respectively.

Assuming that the electrostatic field distribution is uniform without image effects, Matsuyama *et al.* (1995a) showed that the induced potential difference for a uniformly charged spherical particle at a given separation distance between a metal plate and the particle can be approximated as:

$$V' = k_0 q = \frac{z}{4\pi\varepsilon_0 r_p^2} q \tag{3.2}$$

where

$$k_0 = \frac{z}{4\pi\varepsilon_0 r_p^2} = \frac{z}{\varepsilon_0} A_p^{-1} \tag{3.3}$$

r_p and A_p are the radius and surface area of the spherical particle, ε_0 is the permittivity of a vacuum (8.854×10^{-12} F·m^{-1}), z is the contact gap for tunnel relaxation of the order of a few nano-meters to hundreds of nano-meters (Lowell and Roseinnes, 1980). The induced electric field can further polarize the metal plate and cause the image effects. If the image effects are considered, the induced potential difference can be affected by a factor of 1 - 10 as shown in Eq. (2.7) in Chapter 2, depending on the properties of the particle and the metal plate and the contact conditions. In the current study, as a first approximation, this image effects is ignored

If two charged spheres of insulating materials are considered, then the induced potential difference between the two charged spheres at a given separation distance can be determined as:

$$V' = \frac{z}{4\pi\varepsilon_0}\left(\frac{q_j}{r_{pj}^2} - \frac{q_i}{r_{pi}^2}\right) \tag{3.4}$$

where q_i and q_j are the charge of spherical particles i and j; r_{pi} and r_{pj} are the radii of the spherical particles i and j respectively. The image effects between the charged spheres are ignored.

Based on the condenser model, the CPD ($V_c = V_i - V_j$) is the driving force for electron transfer between contacting surfaces. Matsusaka *et al.* (2000) showed that, in each collision, the transferred charge is proportional to the maximum contact area, so that for the m^{th} collision, the transferred charge can be determined by:

$$\Delta q_m = k_s S_m \Delta V_m \tag{3.5}$$

where S is the maximum contact area during the collision, k_s is the charging constant during contact electrification and is of the order of 10^{-4} $C \cdot m^{-2} \cdot V^{-1}$ (Matsusaka *et al.*, 2000;.Matsuyama and Yamamoto, 2006; Watanabe *et al.*, 2007). During a collision, the charge will be transferred from material i to material j. Hence after each collision, the charge on these materials will become $q_i - \Delta q$ and $q_j + \Delta q$, respectively. Therefore, the charging rate between two consecutive contacts can be written as:

$$\frac{\Delta q}{\Delta n} = k_s S \Delta V \tag{3.6a}$$

where, according to Eq. (3.6a), Δq is the transferred charge between two consecutive contacts; Δn is equal to 1 for two consecutive contacts. For a number of successive contacts (when n is relative large), Δn (=1) can be considered as an infinitesimal step of a continuous charging process. Hence, the charging process is governed by the following differential equation:

$$\frac{dq}{dn} = k_s S \Delta V \tag{3.6b}$$

In Eqs. (3.6a)-(3.6b), n is the number of collisions. It can be seen that, in each collision, the transferred charge is a function of the maximum contact area and the total potential difference.

The condenser model, which is based on the contact interaction and contact potentials of the charged particles, is implemented (Appendix D.1) in the DEM-CFD code developed by Kafui *et al.* (2002). For DEM-CFD simulations with contact electrification, the work function of each material is assigned to the particles and also to the physical boundaries (i.e. walls, surfaces). During a collision period, the maximum contact area is recorded. Once a contact is broken (i.e., the contacting particles separate), Eqs. (3.1)-(3.5) are used to calculate the current transferred charge. It is also assumed that the transferred charge instantaneously distributes uniformly on the particle surface and will affect subsequent contact charging processes. The transferred charge on highly insulating particles can be retained for several minutes to several hours (Kornfeld, 1976), which is much longer than most powder handling processes that involve intensive particle collisions. Therefore, the charge relaxation and dissipation are ignored in this study. Since the purpose of this chapter is to explore the contact electrification process, the electrostatic interactions between charged objects (Pei *et al.*, 2010) are not considered in the simulations reported in this chapter. The combined effects of the contact electrification and electrostatic interactions are discussed in Chapter 5.

3.2.2. Model validation

Successive normal impacts of an elastic spherical particle with an elastic substrate were analyzed using the developed DEM-CFD model with contact electrification. The model set-up is identical to the experimental one reported in Matsusaka *et al.* (2000) as illustrated in Figure

3.1. An insulating particle impacts with a stationary and grounded conductive surface successively at initial normal impact velocities, v_0 , in the range 0.5 - 4.0 m·s^{-1} and with different initial net charges q_0 (-5 nC, 0 nC and 5 nC). The material parameters for the particles and substrate are the same as those reported in Matsusaka *et al.* (2000) and are given in Table 3.1. The transferred charge in each collision and the accumulation of the charge during successive process are determined. The transferred charge to the substrate is assumed to dissipate instantaneously so that the net charge remains zero. Hence, the transferred charge to a particle during each impact is given in a differential form as:

$$\frac{dq}{dn} = k_s S\left(V_s - V_p - k_0 q\right) \tag{3.7}$$

where V_s and V_p are work functions potentials of the surface and the spherical particle, respectively. In the present study, V_s is set to 4.70 V and V_p to 4.52 V, which are typical values for steel and an organic polymer (Cross, 1987). The value of the parameter k_s is set to 1×10^{-4} C·m^{-2}·V^{-1}, which is the typical value for the charging constant during contact electrification between polymers and metals as shown by many studies (Matsusak *et al.*, 2000;.Matsuyama and Yamamoto, 2006; Watanabe *et al.*, 2007). By fitting the experimental data of Matsusaka *et al.* (2000) with Eq. (3.7) and $q_0 = 0$, the separation distance z is set to 260 nm and the parameter k_0 is 1.0×10^{7} V·C^{-1} in this study.

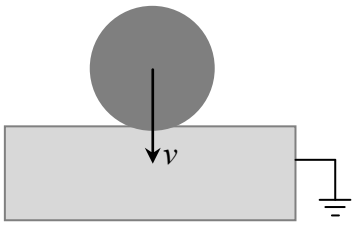

Figure 3.1 The model set-up for impact of a sphere with a substrate.

Table 3.1 Material parameters

	Particle	Substrate
Elastic modulus, Y	$2.0\text{x}10^6$ Pa	$210\text{x}10^9$ Pa
Poisson's ratio, υ	0.5	0.3
Density, ρ	890 kg·m^{-3}	7800 kg·m^{-3}
Diameter, d_p	5 ~ 31 mm	-
Material type	Rubber	Steel

For successive collisions, the accumulation of charge can be derived from Eq. (3.7) as:

$$q = q_0 e^{-k_s k_0 Sn} + q_\infty \left(1 - e^{-k_s k_0 Sn}\right), \ (n = 0, q = q_0) \tag{3.8}$$

where

$$q_\infty = \frac{V_s - V_p}{k_0} \tag{3.9}$$

q_0 is the initial charge and q_∞ is the equilibrium charge.

From Eqs. (3.7) and (3.8), the charging coefficient, k_c, can be written as:

$$k_c = k_s S k_0 \tag{3.10}$$

Eq. (3.8) can then be re-written as:

$$q = q_0 e^{-k_c n} + q_\infty (1 - e^{-k_c n}), \ (n = 0, q = q_0) \tag{3.11}$$

Figure 3.2 shows the variation of transferred charge as a function of the maximum contact area for an initial charge of $q_0 = 0$ nC; the experimental data of Matsusaka *et al.* (2000) are also superimposed. It is clear that the numerical results are in excellent agreement with the experimental data. It can also be seen that the transferred charge is linearly proportional to the maximum contact area.

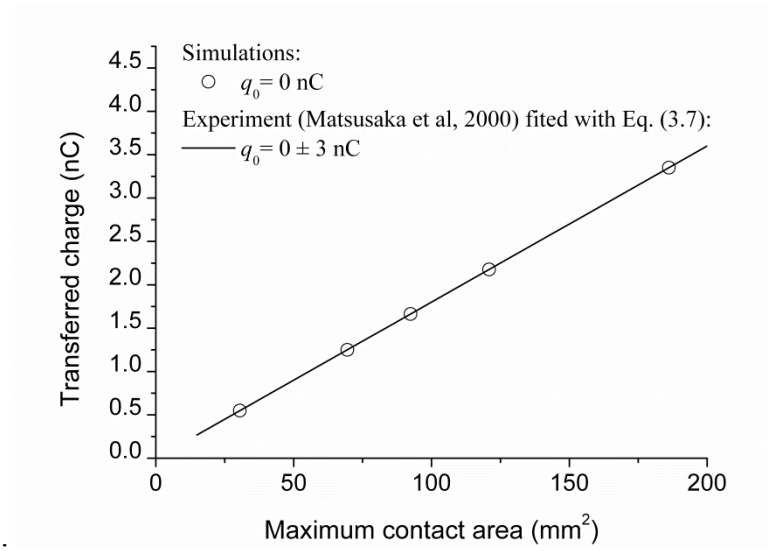

Figure 3.2 The variation of transferred charge with maximum contact area.

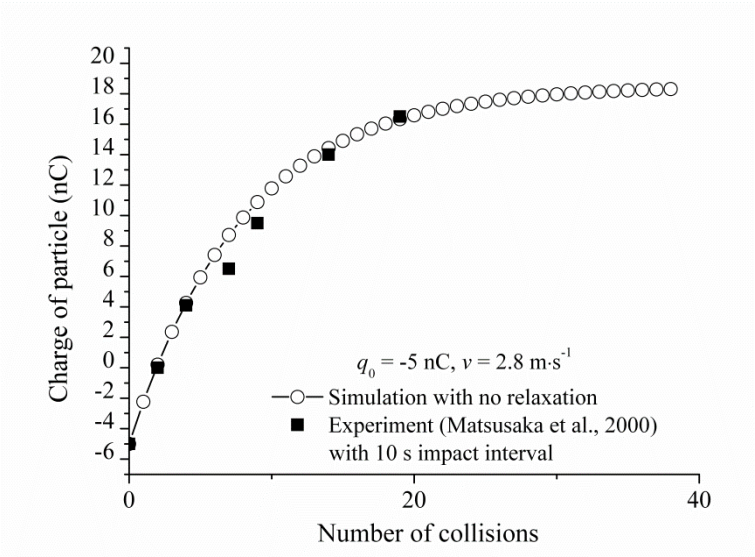

Figure 3.3 The accumulation of electrostatic charge as a function of the number of impacts.

Figure 3.3 presents the accumulation of electrostatic charge as a function of the number of impacts for an initial impact velocity of 2.8 m·s^{-1}. It is clear that the acquired charge increases exponentially with the increase in the number of impacts and eventually reaches an equilibrium state with a maximum value. The experimental results for an impact interval of

10s obtained by Matsusaka et al. (2000) are also superimposed in Figure 3.3 as shown by solid symbols. It is clear that the numerical results are in close agreement with the experimental data.

3.2.3. Effect of particle size on contact electrification

Contact electrification during the impact of spherical particles of various sizes with a grounded conductive substrate is analyzed using the DEM-CFD model, in order to investigate the effects of particle size on contact charging. The model setup is similar to that shown in Figure 3.1. Particles with sizes ranging from 5 - 31 mm are considered. The material properties of the particles and the substrate are also identical to those given in Table 3.1. The initial impact velocity is set to 2.8 $m \cdot s^{-1}$ and the initial charge of the particles is assumed to be 0 nC. The particle of a specified initial impact velocity is set to impact with the substrate successively under gravity, and the charge transfer process during the successive impacts is analyzed.

Figure 3.4 shows the accumulated charge as a function of the number of collisions for particles with various sizes. It can be seen that, for all cases considered, as the number of collisions increases, the charge accumulated on the particles increases until an equilibrium value is reached. In addition, the simulations are in excellent agreement with theoretical calculations as shown in Figure 3.4 in solid lines, in which the changing coefficient k_c is equal to 0.132 for the various diameters at the same impact velocity. In other words, the charges on the particles with various sizes are accumulated at the same charging coefficient and can achieve the equilibrium state in the same characteristic time.

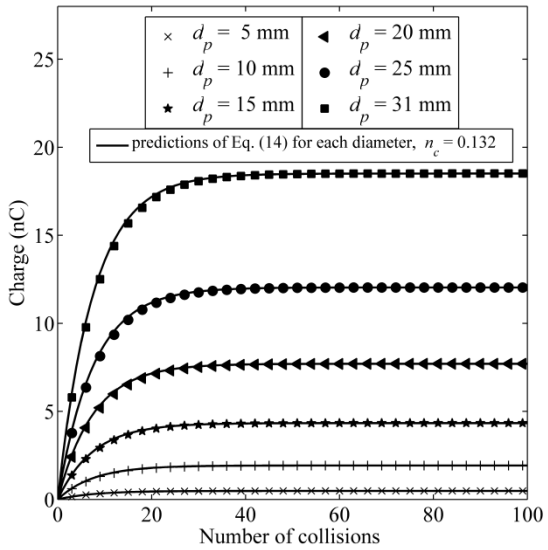

Figure 3.4 The accumulation of electrostatic charge on particles of various diameters (d_p).

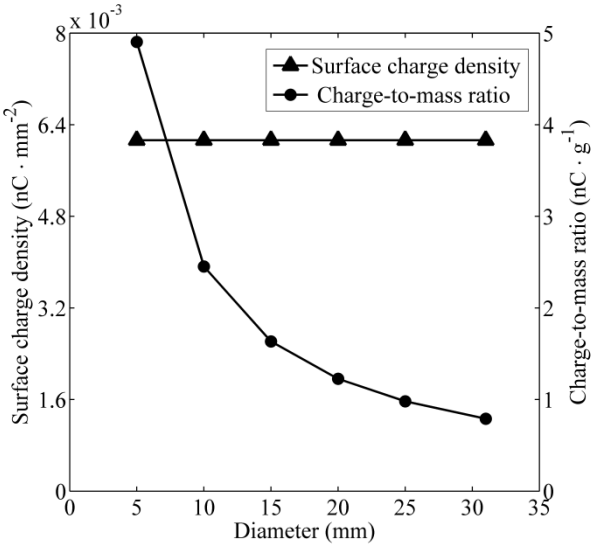

Figure 3.5 The variation of surface charge density and charge-to-mass ratio with the particle size.

The surface charge density and charge-to-mass ratio are frequently used to indicate the relative charge level with reference to the surface area and the mass of particles. In this study, the surface charge density is defined as the net charge on a particle divided by the surface area

of the particle, and the charge-to-mass ratio as the net charge of the particle divided by the mass of the particle. Figure 3.5 shows the surface charge density and the charge-to-mass ratio at the equilibrium state as a function of the particle size. It is clear that, although the charge-to-mass ratio decreases with increasing particle size, the surface charge density is essentially identical for particles of different sizes.

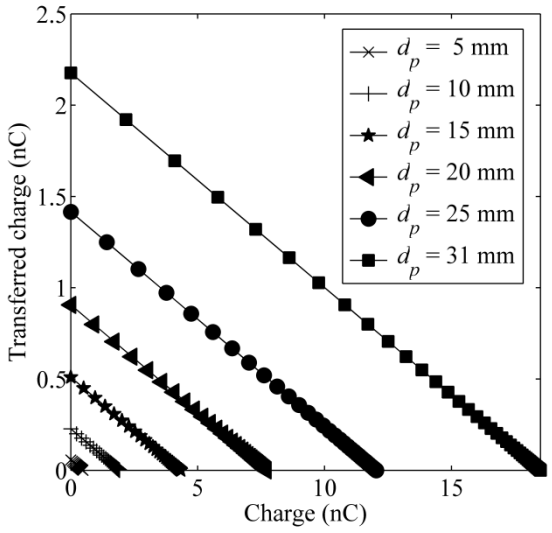

Figure 3.6 Transferred charge in each collision as a function of net charge.

Figure 3.6 presents the transferred charge in each collision, Δq, as a function of net charge q. It is clear that the transferred charge decreases linearly as the net charge accumulated on the surface of the particle increases. The gradient is equal to the charging coefficient during collisions. It can be seen that, for particles of different sizes, the charge coefficients are essentially identical since the lines for various sized particles are parallel to each other. This indicates that, for the same initial impact velocity, the charging coefficient is constant regardless of the particle size.

3.3. Contact electrification of spherical particles during fluidization

3.3.1. Model setup

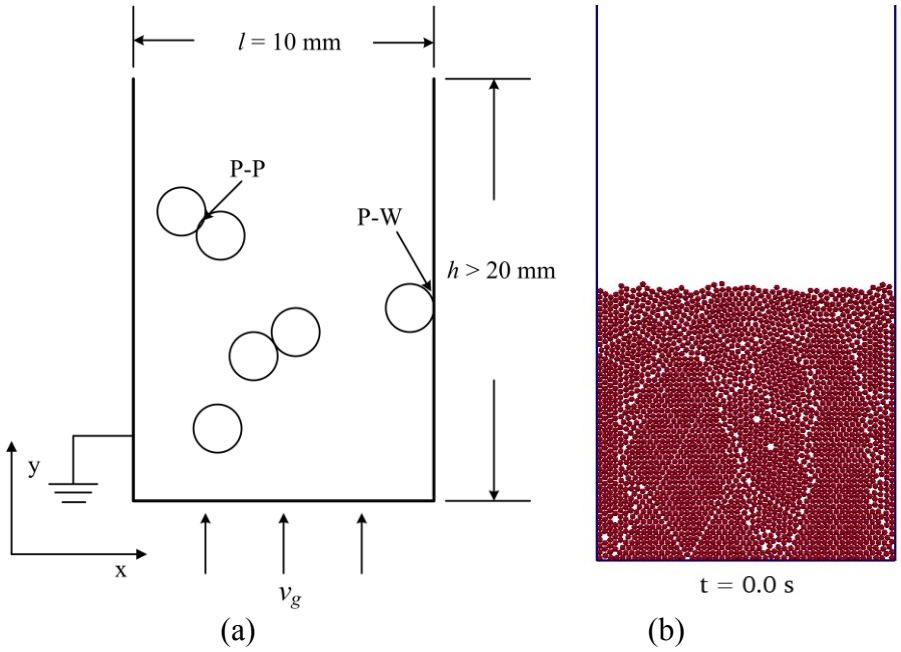

Figure 3.7 Illustration of the model set-up for contact electrification during fluidization.

During fluidization, particles can become charged as a result of intensive collisions between particles and surfaces. In order to investigate charge acquisition and accumulation, and the charge distribution of a particle system during fluidization, the current DEM-CFD model with electrification (Section 3.2) is employed to analyze gas fluidization in 2D with the geometrical set up illustrated in Figure 3.7. In the numerical simulations, 2500 spherical particles with a diameter of 200 μm were used. The Young's modulus, Poisson's ratio and density are 8.7×10^9 Pa, 0.3 and 1.5×10^3 kg·m^{-3}, respectively. The material properties of the walls were identical to those used for the substrate given in Table 1. The work functions of the particle and the walls are 4.52 and 4.70 V, respectively. Air is used as the gas for

fluidization gas and has an average molar weight of 2.88×10^{-2} kg·mol^{-1} and a shear viscosity of 1.8×10^{-5} kg·m^{-1}·s^{-1}. The initial air pressure is set to one atmospheric pressure and the temperature of the fluidized bed is maintained constant.

The 2D granular bed was generated by randomly depositing particles into the bottom of the fluidized bed until the total kinetic energy became negligible (i.e. the minimum particle velocity is smaller than 10^{-6} m·s^{-1}), as shown in Figure 3.7b. Thereafter, air with a constant superficial velocity was introduced from the bottom of the fluidized bed. Three superficial gas velocities (100, 200 and 250 mm·s^{-1}) were employed to explore the influence on contact electrification. No-slip boundaries were assumed at the side walls, and the upper boundary was set as a continuous outflow. The internal domain is divided into 20 × 80 CFD cells along x and y directions. It was also assumed that the acquired charge on the earthed conductive walls dissipated instantaneously so that the net charge remained zero. The actual electrification process during fluidization can take more than 10 min of physical time to reach an equilibrium state (Guardiola *et al.*, 1996). It is extremely computer-intensive to simulate this process with the actual charging constant of the order of 10^{-4} C·m^{-2}·V^{-1} using DEM-CFD. In order to complete the simulations of the entire charge accumulating process (i.e. from zero charge to equilibrium charge) in a reasonable timescale and demonstrate the performance of the model, the charging constant k_s was assumed to be 0.2 C·m^{-2}·V^{-1}, which enabled the overall contact electrification behaviour to be analyzed numerically, even though the charge transfer process is accelerated with a high charge rate.

3.3.2. Results

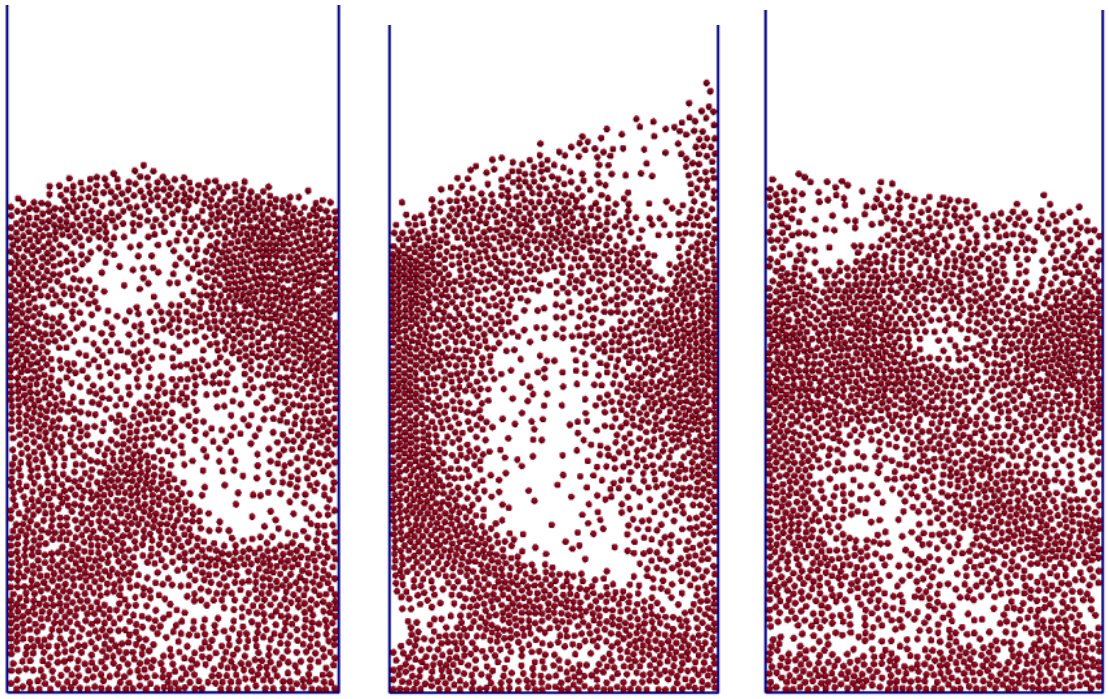

(a) t = 0.2 s (b) t = 0.6 s (c) t =1.0 s

Figure 3.8 Particle profiles during fluidization at various time instants (v_g = 200 mm·s^{-1}).

Figure 3.8 shows typical particle profiles during fluidization at various times with a superficial gas velocity of 200 mm·s^{-1}. The gas bubbles rise from the bottom and travel through the granular bed, causing collisions and mixing of the fluidized particles. Eventually, the granular bed becomes fully fluidized and the gas bubbles continue flowing though the granular bed.

The charge density distribution is obtained to show the charge level in different regions in the fluidized bed. To calculate the charge density distribution, the fluidized bed as shown in Figure 3.7 was first divided into 20×20 grids. The charge density in each grid was then determined as the total charge of particles in the grid divided by the area of the same grid.

Figure 3.9 shows the corresponding charge density distributions. It is clear that, at the early stage of the fluidization, regions near the walls have higher charge densities as particles in these regions acquire more charges than particles in the centre of the bed, due to frequent collisions with the walls (Figure 3.9a). As the fluidization proceeds, mixing and collisions of charged particles occur, and then an increasing number of particles in the centre of the bed gain higher charges. Consequently, regions with higher charges gradually extend into the centre of the fluidized bed (Figure 3.9b). As each particle in the fluidized bed reaches its equilibrium charge, the whole system reaches a saturated state (Figure 3.9c), and further charge transfer does not occur.

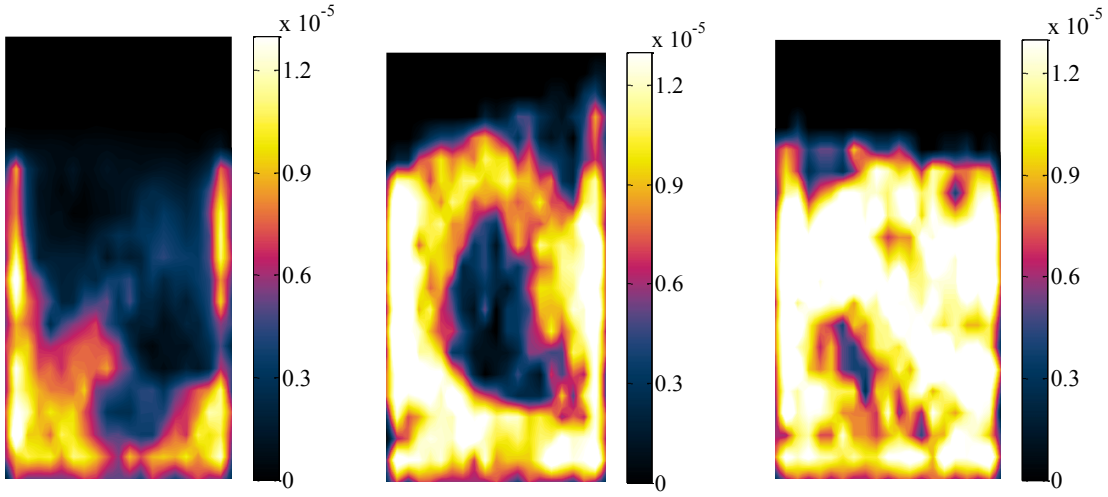

(a) t = 0.2 s (b) t = 0.6 s (c) t = 1.0 s

Figure 3.9 Charge density distribution (C·m^{-2}) at defined times (v_g = 200 mm·s^{-1}).

Figure 3.10 shows the particle profiles at t = 0.6 s for various superficial gas velocities. It is clear that the bubble size and the height of the granular bed are different at different superficial gas velocities. More specifically, the bubble size and the height of the granular bed increase with increasing superficial gas velocity. Thus the particles in the fluidized bed with higher superficial gas velocities will be more dispersed and mixed.

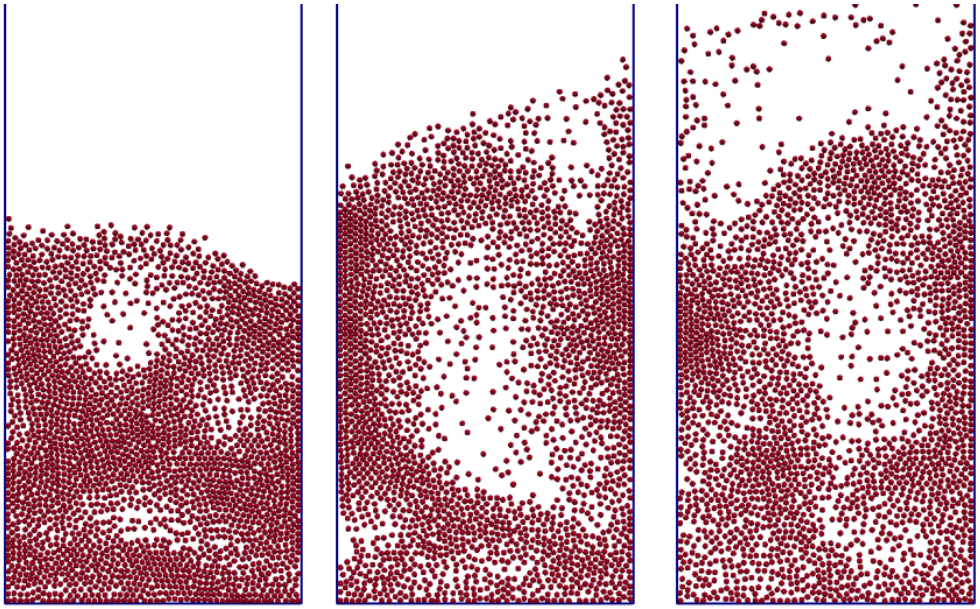

(a) v_g= 100 mm·s^{-1} (b) v_g = 200 mm·s^{-1} (c) v_g = 250 mm·s^{-1}

Figure 3.10 Particle profiles at t = 0.6 s for various superficial gas velocities.

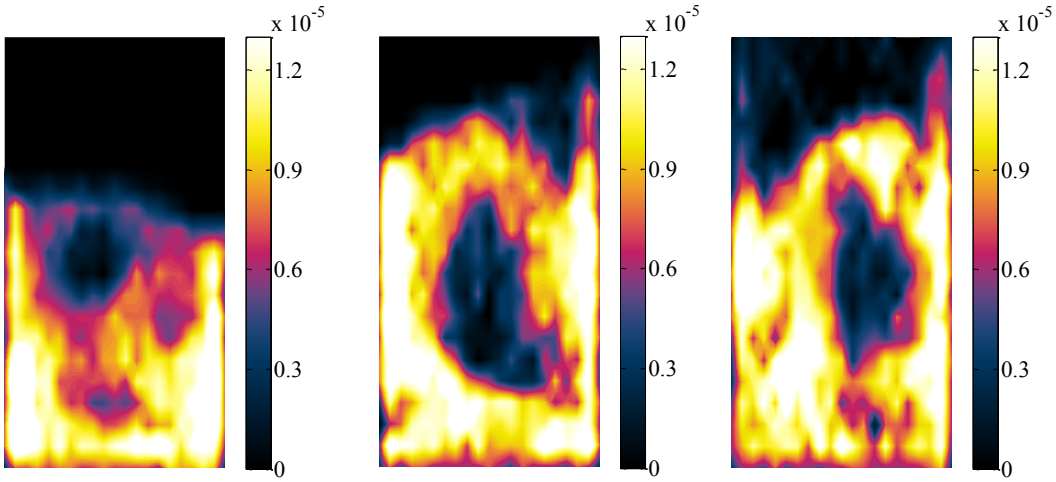

(a) v_g= 100 mm·s^{-1} (b) v_g = 200 mm·s^{-1} (c) v_g = 250 mm·s^{-1}

Figure 3.11 Charge density distributions (C·m^{-2}) at t = 0.6 s for various superficial gas velocities.

Figure 3.11 shows the corresponding charge density distributions at t = 0.6 s for fluidization with different superficial gas velocities. The charge density distribution varies with the

superficial gas velocities. At a low gas velocity (i.e. 100 mm·s^{-1}), the charge density of the granular bed mainly concentrates at the region near the walls (Figure. 3.11a), which means that the mixing and charge transfer in the granular bed is slower. However, higher gas velocities (Figures. 3.11b and 3.11c) result in a greater and more uniform charge density, despite the voidage caused by the gas bubbles.

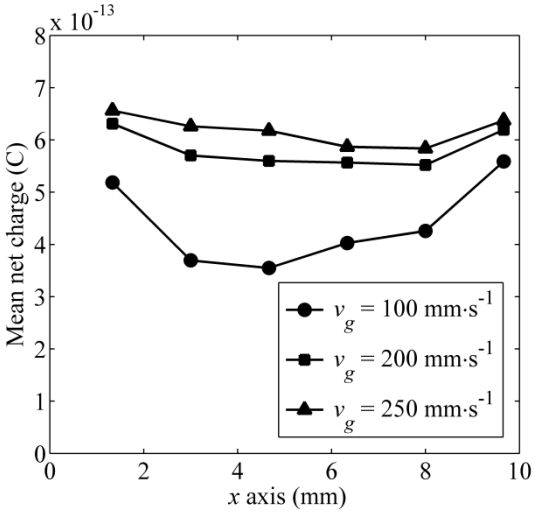

Figure 3.12 Mean net charge distribution along the x-axis at t = 0.6 s.

The granular bed was divided into 6 regions along the x axis and then the mean charge of particles in each region was calculated. Figure 3.12 shows the mean net charge of particles along the x axis at t = 0.6 s. It is clear that for all superficial gas velocities, the average net charge in the side regions is greater than that in the central region, as observed in Figures 3.9 and 3.11. However, the higher superficial velocity provides a more uniform distribution and greater average net charge, which means faster charge accumulating process in the entire fluidized bed.

As shown in Eqs. (3.6) and (3.11), the charge accumulating process of each particle can be approximated as using first-order kinetics. So the total net charge of the fluidized bed can also be defined as:

$$Q = Q_0 e^{-k_g t} + Q_\infty \left(1 - e^{-k_g t}\right) \tag{3.12}$$

where, Q_0 is the initial total net charge of the fluidized bed and is zero in this study; Q_∞ is the equilibrium charge of the fluidized; and k_g is the charging coefficient of the fluidization.

Figure 3.13 shows the charge accumulating of particles in the fluidized bed. The solid lines are the fitting lines of Eq. (3.12) to the corresponding data. The total net charge of the particles accumulates until saturation is achieved, which is similar to published experimental observations (Guardiola *et al.*, 1996). It is clear the charge accumulation follows an exponential trend during the fluidization. The equilibrium charge of the fluidized bed is 1.925 nC, which is the total of particle equilibrium charge which can also be given by Eq. (3.12).

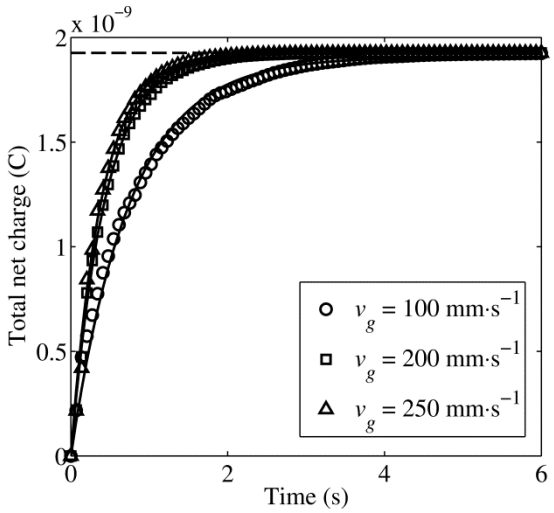

Figure 3.13 The charge accumulation in the fluidization.

However, the charging coefficient of the fluidized bed is also related to the gas velocity as shown in Figure 3.13. The minimum fluidization velocity u_{mf} can be calculated as (Seville *et al.*, 1997):

$$\frac{\rho_f d_p^3 (\rho_p - \rho_f) g}{\mu_s^2} = 150 \frac{(1-\kappa_{mf})}{\kappa_{mf}^3} \frac{\rho_f d_p}{\mu_s} u_{mf} + \frac{1.75}{\kappa_{mf}^3} \frac{\rho_f^2 d_p^2}{\mu_s^2} u_{mf}^2 \tag{3.12}$$

where d_p is the diameter of the spherical particle; κ_{mf} is the voidage of the fluidized bed at the minimum fluidization. When $\kappa_{mf} = 0.4 \sim 0.5$, according to Wen and Yu (1966), Eq. (6.12) can be rewritten as:

$$Ar = 1650 \,\mathrm{Re}_{mf} + 24.5 \,\mathrm{Re}_{mf}^2 \tag{3.13}$$

where,

$$Ar = \frac{\rho_f d_p^3 (\rho_p - \rho_f) g}{\mu_s^2} \tag{3.14}$$

$$\mathrm{Re} = \frac{\rho_f d_p}{\mu_s} u_{mf} \tag{3.15}$$

When $1650 \,\mathrm{Re}_{mf} >> 24.5 \,\mathrm{Re}_{mf}^2$, Eq. (3.13) can be written as:

$$Ar = 1650 \,\mathrm{Re} \tag{3.16}$$

$$\frac{\rho_f d_p^3 (\rho_p - \rho_f) g}{\mu_s^2} = 1650 \frac{\rho_f d_p}{\mu_s} u_{mf} \tag{3.17}$$

$$u_{mf} = \frac{d_p^2 (\rho_p - \rho_f) g}{1650 \mu_s} \tag{3.18}$$

where d_p is the diameter of the particle; ρ_p and ρ_f are the density of the particle and the gas respectively; g is the gravitational acceleration; μ_s is the viscosity of the gas. From Eq. (3.18), the minimum fluidization velocity is 20 mm·s^{-1}, where $1650 \,\mathrm{Re}_{mf} >> 24.5 \,\mathrm{Re}_{mf}^2$. Then the excessive gas velocity of the fluidization can be defined as the velocity difference between the

superficial gas velocity and the minimum fluidization velocity, $u_e = v_g - u_{mf}$. The charging coefficients of the fluidized bed at various excessive gas velocities are shown in Table 2. It is clear that the charging coefficient of the fluidized bed increases with increasing excessive gas velocity, indicating that a higher superficial gas velocity leads to a larger charging coefficient and a faster charge accumulating process.

Table 3.2 Excessive gas velocities and charging coefficients of various cases

v_g (mm·s^{-1})	u_e (mm·s^{-1})	k_g (s^{-1})
100	80	1.34
200	180	2.32
250	230	2.60

3.4. Discussions

3.4.1. The effect of particle size on contact electrification during the impact with a substrate

Equations (3.8) and (3.9) show that charge accumulation follows an exponential relationship with successive collisions and that the equilibrium charge is only related to geometrical properties of the particles (i.e. the diameter of the particles) and the CPD. Therefore, for particles of different sizes, a similar exponential trend is obtained for the charging process. From Eq. (3.3), it can be seen that the equilibrium charge is proportional to the particle diameter to a power of 2, which is intermediate between a power of 1 to 3 as analyzed by other researchers (Masuda *et al.*, 1976; Matsuyama and Yamamoto, 1997). However, the charge-to-mass ratio of a particle is inversely proportional to the particle size (Matsuyama and

Yamamoto, 1997; Chen *et al.*, 2003). Specifically, it is found that a smaller particle has a smaller equilibrium charge but a higher charge-to-mass ratio, which means that the electrostatics can play an important role in powder processes involving fine particles, since the electrostatic force will be more significant compared to the gravitational force.

Since the equilibrium charge is proportional to the square of the particle diameter it is also proportional to the surface area of the particle. Therefore, the surface charge density of the particles is independent of the particle size as shown in Figure 3.5. This is also observed experimentally and numerically by many others (Bailey, 1984; Hogue *et al.*, 2008). However, it should be noted that this method is only applicable to a uniformly distributed surface charge. If the charge distribution is non-uniform, the electrostatic field induced by the net charge will depend on the surface curvature, i.e. the particle size and shape (Bailey, 1984) and eventually affect the equilibrium charge.

According to Hertz theory (Johnson, 1985; Li *et al.*, 2000; Guo *et al.*, 2009), S in Eq. (3.10) is proportional to $v_0^{4/5}$ and r_p^2 and, in addition, k_0 is proportional to r_p^{-2}. Therefore, k_c is only related to the impact velocity, which is the same for simulations with different particle sizes. Consequently, the charging rates are identical for particles of different sizes. Consequently, particles with various sizes can accumulate charge on their surface at the same charging rate.

3.4.2. Contact electrification during fluidization

During fluidization, a granular bed initially shows a non-uniform charge density distribution and eventually achieves an equilibrium state. According to the condenser model, charge

transfer can occur both between particles and between particles and the wall. At the beginning of fluidization, there will be no charge transfer between particles, since the particles are of the same size and material. The charges on the particles are generated primarily from the collisions between particles and walls (LaMarche *et al.*, 2009). Therefore, the charge is mainly concentrated in the regions near the base and side walls (see Figure. 3.9a). As the fluidization process continues, particles start to possess different net charges, which will lead to charge transfer between them during collisions. Since in the current work, the walls were grounded and conductive, they were treated as being always neutral after each collision. Thus, the charge continues to be generated and to transfer between particles and walls. At the same time, the particles are mixed during fluidization, which can affect the charge distribution. Eventually, all particles will achieve their equilibrium charge and the charge of the granular bed becomes saturated. The charging process shows an exponential trend during the fluidization as observed experimentally (Guardiola *et al.*, 1996).

Contact electrification during fluidization also depends on the superficial gas velocity. At a high gas velocity, particles collide at high impact velocities and more charges are transferred in each collision. Furthermore, a high gas velocity also promotes fast mixing of charged particles and particle-particle collisions. Consequently, the net charge of particles can reach their equilibrium value quicker and the whole system can reach its saturated state earlier, when compared to that at low gas superficial velocities (Figure. 3.13 & Table 3.2).

3.4.3. Charge relaxation during contact electrification

It is worth mentioning that the experimental data shown in Figure 3.3 is for an impact interval of 10 s, which is the smallest interval used by Matsusaka *et al.* (2000). As the interval is relatively small, charge relaxation and dissipation during the intervals between successive impacts is inhibited, so that it can be ignored as assumed in our DEM-CFD model. It is also noticeable in Figure 3.3 that a slightly higher charge is obtained in the DEM simulations, compared to the experimental results. This is because some charge relaxation and dissipation is inevitable in the physical experiments, which results in a slightly lower charge, even though the impact interval is relatively small. If the impact interval is increased (for instance, 20 or 30 s), the charge relaxation will prevail and more charges will be dissipated. As a consequence, less charge will be acquired by the particles as observed by Matsusaka *et al.* (2000). For those cases, DEM-CFD modelling without consideration of charge relaxation and dissipation would significantly overestimate the charge acquired by a particle. Thus, further work is needed to incorporate charge relaxation and dissipation into the DEM-CFD model in order to simulate electrification more rigorously. Nevertheless, the results shown in Figures 3.2 and 3.3 clearly demonstrated that the present DEM-CFD model can accurately predict contact electrification if the charge relaxation is negligible, such as in rapid granular flows and particle collision dominated powder handling processes.

3.5. Summary

DEM-CFD with a condenser model for modelling contact electrification has been developed. It was validated using published experimental data, indicating that the method is a feasible

tool to explore the dynamic charging behaviour of particles during powder processing. It was also demonstrated that, during each collision of an insulated particle with a conductive substrate, the transferred charge is proportional to the maximum contact area. In successive impacts, the accumulation of charge on the particle is an exponential function of the number of collisions and eventually reaches an equilibrium state.

The DEM-CFD method was then used to analyze the contact electrification of particles with various sizes during the impact with a conductive substrate. It is found that larger particles can achieve a higher equilibrium charge but a lower charge-to-mass ratio. However, particles with various sizes will eventually have the same surface charge density.

Contact electrification during fluidization was also analyzed using the DEM-CFD method. It was shown that the charge is initially generated in the regions near the walls and then propagates into the entire granular bed, induced by particle mixing and particle-particle collisions. Eventually, the charge accumulation can achieve an equilibrium state, which also follows an exponential trend as observed experimentally. The superficial gas velocity can affect the charge transfer and mixing behaviour of the particles and a higher superficial gas velocity generally results in more rapid charge accumulation.

CHAPTER 4 MODELLING ELECTROSTATIC INTERACTIONS USING DEM-CFD

4.1. Introduction

In this chapter, the algorithm for calculating the electrostatic interactions, which are long-range in nature, in DEM is introduced. Using DEM-CFD with electrostatic interactions, deposition of mono-charged particles and bi-charged particles are investigated. The micro-structure and dynamic behaviour of the particle system are analyzed. Some of the results presented in this chapter have been published in Pei *et al.* (2010).

4.2. Electrostatic interaction models

4.2.1. Basic principles

In general, the electrostatic interaction between point charges is governed by Coulomb's law. As a first approximation in this study, the charge is assumed to be distributed uniformly on the surface of a spherical particle and cannot be polarized. Then the electrostatic interaction between charged particles (Figure 4.1) is governed by Coulomb's law as:

$$\mathbf{F}_{21}^{\mathrm{e}} = \frac{1}{4\pi\varepsilon_0\varepsilon_r}\frac{q_1 q_2}{r_{21}^2}\mathbf{n}_{21} \tag{4.1}$$

where $\mathbf{F}_{21}^{\mathrm{e}}$ is the electrostatic force from q_2 to q_1, ε_0 is the permittivity of a vacuum (8.854×10^{-12} F·m^{-1}), ε_r is the relative permittivity of the medium in the vicinity of the particles, q_1 and q_2

are charges on each particle, r_{21} is the distance between the centres of the two particles and $\mathbf{n}_{21}$ is the unit vector from q_2 to q_1.

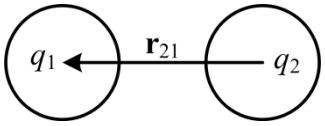

Figure 4.1 The electrostatic interaction between two charged particles.

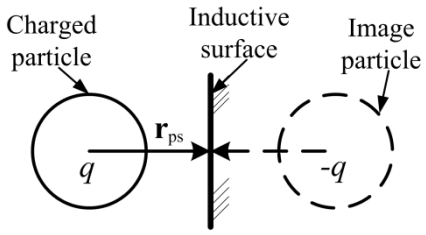

Figure 4.2 The image force between the particle and inductive surface.

When a charged particle approaches an inductive (polarisable) surface (normally made of conductive or polarisable materials) (Figure 4.2), a re-distribution of the charge on the surface is induced. The charge on the particle and the induced charge on the surface cause the so-called image (charge) force (Seville *et al.*, 1996). The image force can be calculated as:

$$\mathbf{F}_{ps}^{I} = \frac{1}{4\pi\varepsilon_0\varepsilon_r}\frac{qq}{(2r_{ps})^2}\mathbf{n}_{ps} \tag{4.2}$$

where $\mathbf{F}_{ps}^{I}$ is the image force between the particle and inductive surface, q is the value of the charge on the particle, r_{ps} is the distance between the centre of the particle and the inductive surface and $\mathbf{n}_{ps}$ is the unit vector. It can be seen that the Coulomb force and the image force share the same mathematic form due to the same long-range nature.

4.2.2. Particle impact with electrostatic interactions

The influence of the electrostatic interaction can be significant compared with the gravitational and the contact forces between particles. According to Eq. (4.1), the Coulomb force can be predicted based on the distance between particles. The charge and the mechanical properties of the particles in Table 1 are typical values for pharmaceutical powders, e.g. lactose (Watanabe *et al.*, 2007; Nwose *et al.*, 2012). The gravitational force on a particle can also be calculated as shown in Figure 4.3. It can be seen that when the distance between the particles is sufficiently large, e.g. 10 particle diameters in this case, the value of the Coulomb force is much smaller than that associated with gravity.

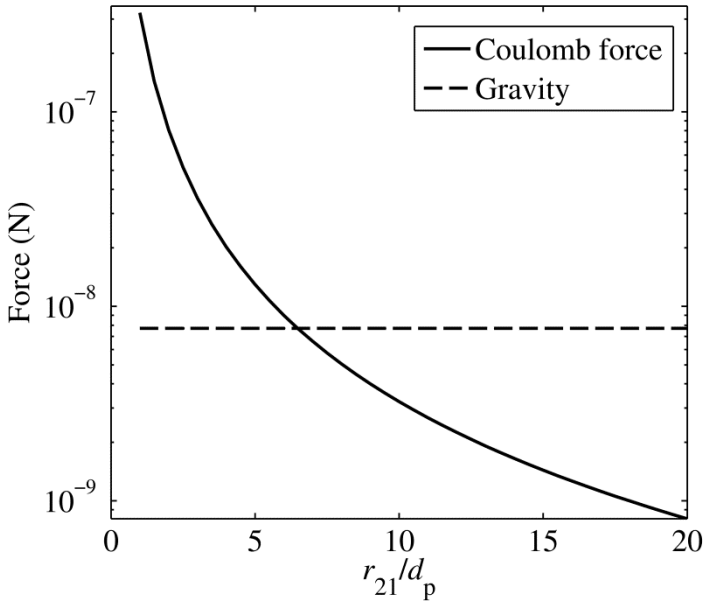

Figure 4.3 A comparison between the Coulomb and gravitational forces.

To verify the implementation of the electrostatic interaction in DEM codes and compare the electrostatic force with the mechanical contact force, DEM models with and without

oppositely charged particles were implemented under the same conditions. The oppositely charged particles are initially static with a distance of 1.2×10^{-4} m between their centres. For the case without charge, particles are positioned just in contact. A relative contact velocity of 8.3×10^{-2} m·s^{-1} was specified (Figure 4.4). The same mechanical properties for the particles given in Table 4.1 were used.

Table 4.1 Properties of particles

Parameters	Value
Diameter (μm)	100
Density (kg·m^{-3})	1.5×10^{3}
Elastic module (GPa)	8.7
Poisson's ratio	0.3
Charge (C)	6.0×10^{-13}
Coefficient of friction	0.3

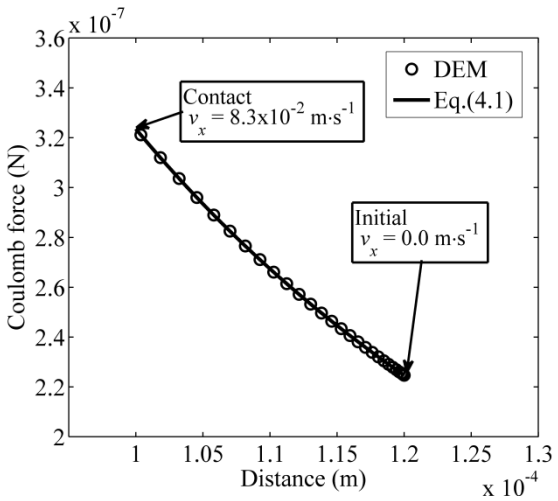

Figure 4.4 The relationship between Coulomb force and distance.

Figure 4.4 shows the relationship between the Coulomb force and the distance between the centres of the particles obtained using Eq. (4.1). Figure 4.5 shows the time histories of the

normal contact forces. For both cases, the contact force increases during the loading stage when the particles approach each other. After the contact force reaches the maximum value, it starts to decrease as the particles are separating from each other. It is clear that the contact forces for both cases are similar. This is because the electrostatic force is very small compared to the mechanical contact force (the maximum Coulomb force is 3.24×10^{-7} N, while the normal contact force is 2.93×10^{-4} N) during the contact. However, the electrostatic force is not negligible, as the electrostatic force can be effective in a longer range for a longer time (Figures 4.4 and 4.6). This phenomenon indicates that the long-range electrostatic force can cause relatively a larger impact force and potentially affect the flow behaviour of particles.

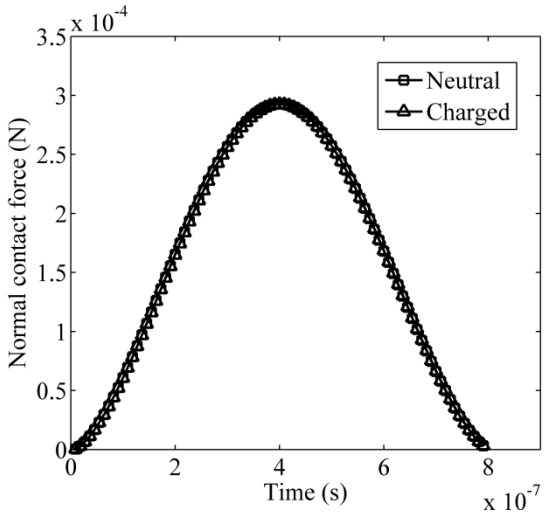

Figure 4.5 The normal contact force as a function of the time for neutral and charged cases.

Figure 4.6 shows the evolution of the electrostatic force during the impacts of two oppositely charged particles with Rayleigh damping (Mohammad *et al.*, 1995). Full Rayleigh damping involves global damping and contact damping. However, only contact damping is considered in this analysis. The contact damping ratio for this particle-particle interaction is set to 0.016 which gives a restitution coefficient of about 0.95 (Hu *et al.*, 2011). It can be seen that after

each impact, the minimum Coulomb force becomes larger, which indicates that the distance and the potential energy between the two particles becomes smaller. Due to the dissipation of the energy, the two particles can eventually adhere together.

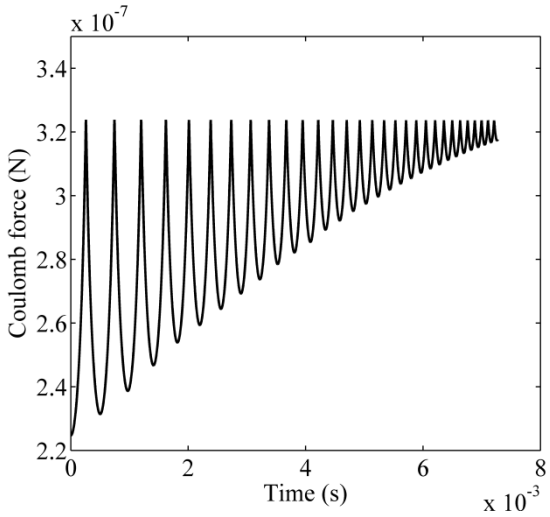

Figure 4.6 The Coulomb force as a function of time with contact damping for the charged case.

The particle impact simulations illustrate the dynamic behaviour of particles subjected to electrostatic interactions. The electrostatic force, specifically the attractive force, because of the long-range nature, can lead to intensive contacts and eventually to the agglomeration of particles, which can subsequently affect the flow behaviour of particles during powder handling processes.

4.2.3. Direct truncation (DT) and Hybrid particle – cell (HPC) algorithms

To calculate the electrostatic interactions, both the DT and HPC methods are considered and implemented (Appendix D.2) in our in-house DEM-CFD code. To simplify the incorporation

of electrostatic interactions, it is assumed that (1) electrostatic charge on each particle is treated as a concentrated point charge at the centre of the particle; (2) the induced electrostatic forces are governed by Coulomb's law; and (3) image and polarization effects between a pair of interacting particles are ignored. In this study, the image force between the particles and the physical boundaries (walls and surfaces) can be selected or ignored with respect to different analyzes.

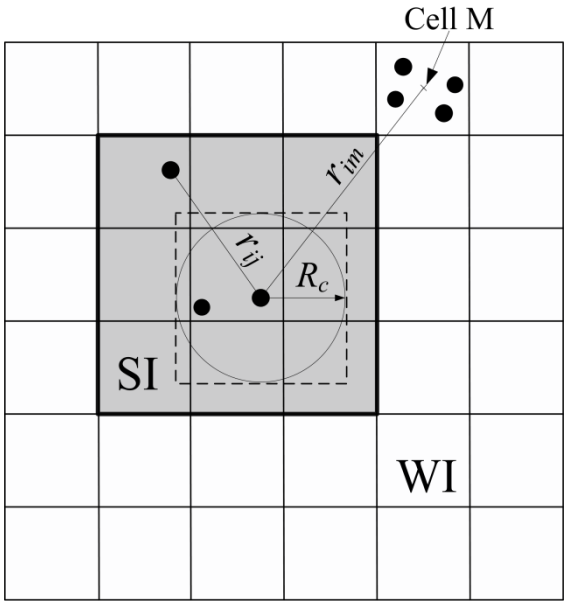

Figure 4.7 A 2D illustration of the cell list method

For both the DT and HPC methods, a cell list is used to group and detect charged particles and their long-range electrostatic interactions in the computational domain, as illustrated in Figure 4.7. The domain is first divided into cells with a size greater than the diameter of the particle (For the HPC method, a sensitivity study shows that the cell size in the range of 2 - 16 particle diameters can provide consistent results). All particles are then sorted into their corresponding cells based on the relative positions of the particles to the cells. As a result, each cell has its own particle list. A cut-off distance, R_c, is then introduced to define the

maximum range of the electrostatic interactions. The total electrostatic force acting on particle *i*, $\mathbf{F}_i^e$, is determined as:

$$\mathbf{F}_i^e = \sum_{j=1}^{N} \mathbf{F}_{ij}^e \tag{4.3}$$

where $\mathbf{F}_{ij}^e$ is the electrostatic force between particles *i* and *j*, *N* is the total number of particles.

In the DT method, $\mathbf{F}_{ij}^e$ is given as:

$$\mathbf{F}_{ij}^e = \frac{q_i q_j}{4\pi\varepsilon_0 r_{ij}^2}\mathbf{n}_{ij} \qquad r_{ij} \le R_c \tag{4.4a}$$

$$\mathbf{F}_{ij}^e = 0 \qquad r_{ij} > R_c \tag{4.4b}$$

where q_i and q_j are the net charges on the particles *i* and *j*; *n* is the number of particles; r_{ij} is the distance between the particles *i* and *j*; $\mathbf{u}_{ij}$ is the unit vector from particle *j* to particle *i*; ε_0 is the permittivity of a vacuum (8.854×10^{-12} F·m^{-1}). Equations (4.3) and (4.4) indicate that, in the DT method, only the electrostatic force between particles located within the cut-off distance is considered, while electrostatic interactions between particles with a separation distance greater than the cut-off distance are ignored. This is similar to most published DEM models involving electrostatic interactions (Hogue *et al.*, 2008; Pei *et al.*, 2010).

In the HPC method, electrostatic interactions between all particles are considered in the following manner: for particle *i*, its electrostatic domain is divided into two regions using the specified cut-off distance R_c: a strong interaction (SI) region and a weak interaction (WI) region. The SI region is defined as the area of the cells that envelops the circumscribed square/cube (the shaded area in Figure 4.7) of the cut-off circle/sphere, while the cells outside the SI region constitute the WI region. The electrostatic force between particle *i* and any

particle *j* located in the SI region is calculated directly using Eq. (4.4a). To determine the electrostatic interaction between particle *i* and those located in the WI region, the total net charge in each cell in the WI region is first calculated using:

$$Q_M = \sum_{k=1}^{n_M} q_k \tag{4.5}$$

where n_M is the total number of particles in the cell *M*, Q_M and q_k are the total charge of particles in the cell *M* and the charge of particle *k*, respectively. The electrostatic force between particle *i* and those in the cell *M*, $\mathbf{F}_{iM}$, is then approximated as:

$$\mathbf{F}_{iM}^e = \frac{q_i Q_M}{4\pi\varepsilon_0 r_{iM}^2}\mathbf{n}_{iM} \tag{4.6}$$

where r_{iM} is the distance between the particle centre and the centre of the cell *M*; $\mathbf{n}_{im}$ is the unit vector from cell *M* to particle *i*. Eq.(4.6) is used to calculate the electrostatic force between particle *i* and particles in the cells located in the WI region. In this way, the electrostatic interactions between all particles are considered and the total electrostatic force acting on particle *i* is then determined by

$$\mathbf{F}_i^e = \sum_{j=1}^{n_s} \mathbf{F}_{ij}^e + \sum_{M=1}^{N_M} \mathbf{F}_{iM}^e \tag{4.7}$$

where n_s is the number of neighbouring particles in the SI region and N_M is the number of cells in the WI region.

Since a cut-off distance, R_c, is introduced in both the DT and the HPC models, their accuracy may depend on its value so that the accuracy of the electrostatic forces between particles may increase with increasing values of R_c. However, the computational cost will also be increased. In order to explore the sensitivity of R_c values on the performance of these two methods,

deposition of mono-charged particles in a container in air, similar to those presented by Yu *et al.* (2009), is modelled with various R_c values as described below.

4.3. Deposition of mono-charged particles

4.3.1. Model setup

In this section, the deposition of mono-charged particles is modelled using the developed DEM-CFD code. Mono-charged particles are referred to as those with the same value and polarity of the electrostatic charge. The DT and HPC methods for the electrostatic interactions between particles are employed and compared. The structure and the dynamics of the particle system during the deposition are analyzed.

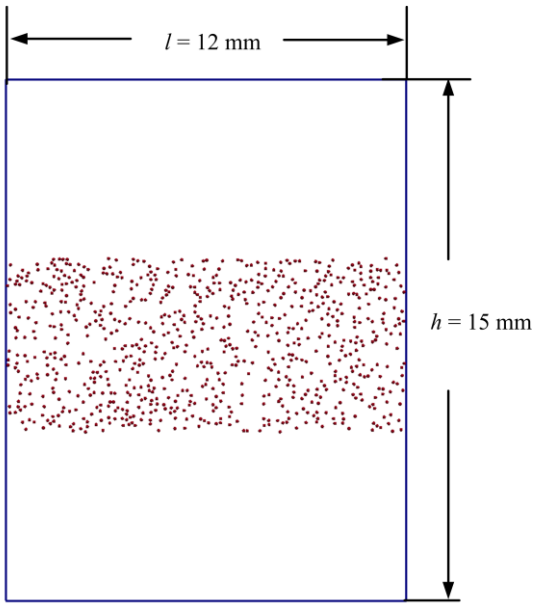

Figure 4.8 DEM model for deposition of mono-charged particles.

A 2D DEM-CFD model is constructed to simulate the deposition of mono-charged particles in a container of size 12×15 mm in air, as shown in Figure 4.8. Initially, 800 mono-charged particles are randomly generated in a central horizontal section of the container. The gravitational force and electrostatic interactions between particles are applied throughout the deposition process. The image force between the particle and the wall is ignored. When the simulation is initiated, particles start to pack under the action of gravity and electrostatic forces. The charge on each particle was maintained at a constant value and charge transfer was not considered. The material parameters for the particles and the container are given in Table 4.2. Generally Rayleigh damping (Mohammad *et al.*, 1995), which involves global damping, and contact damping are used in DEM simulations. In this analysis, only contact damping is considered. The damping ratio for particle-particle interactions was set to 0.016, and the damping ratio for particle-wall interactions was set to 0.032, which gives values of the restitution coefficient in the range of 0.90-0.95 (Hu *et al.*, 2011)

The motion of air is modelled using the CFD scheme. The entire domain is divided into fluid cells with a size of 8 particle radii. The air has a temperature of 293 K and a shear viscosity of 1.8×10^{-5} kg·m^{-1}·s^{-1}. The initial air pressure is set to the atmospheric value (0.1 MPa). The average molar mass of air is 2.88×10^{-2} kg·mol^{-1}. The surfaces of the container are impermeable to air. No-slip boundary conditions are assumed for the flow of the air adjacent to sides and base of the container. The upper boundary is set as free outflow. The flow of air is induced by the deposition of the particles due to the interaction between the air and the particles.

Table 4.2 Material properties of particles and container walls.

	Particle	Container
Diameter, d_p (μm)	100	-
Elastic module, Y (GPa),	8.9	210
Poisson ratio, v	0.3	0.3
Density, ρ_p (Kg·m^{-3})	1500	7800
Charge, q (C),	2.6×10^{-13}	-

Both the DT and HPC methods are employed to compute the electrostatic interactions. The cut-off distance, R_c, is set to $5d_p$, $15d_p$ and $25d_p$, where d_p is the particle diameter, for both the DT and HPC methods, in order examine their sensitivity to this parameter. For the HPC method, the entire domain is divided into cells with a size of $4d_p$ in order to calculate the electrostatic interactions in the WI region. The evolution of the granular temperature (GT) during deposition and the bed height and also the steady-state radial distribution function (RDF) of the granular bed are analyzed and reported in the next section.

4.3.2. Deposition behaviour of mono-charged particles

Figure 4.9 shows the particle profiles at various time instants during deposition obtained using the HPC method with $R_c = 15d_p$. At the beginning of the deposition, as shown in Figure 4.9a, the charged particles repel each other and move towards the container walls due to the strong repulsive electrostatic forces between mono-charged particles. At the same time, the gravitational force causes particles to pack toward the bottom of the container (Figure 4.9b). Consequently, there is a strong particle oscillation in the granular bed as the gravitational force and the repulsive electrostatic force tend to balance each other. As the initial kinetic energy is gradually dissipated, through the contact damping and the friction between the

particles and wall, particles start to oscillate around their own equilibrium positions and the kinetic energy of the system fluctuates about a constant value. A dispersed structure of the granular bed as shown in Figure 4.9c is eventually obtained. In addition, it can be seen that a denser structure is obtained at the bottom of the bed compared to that at the top. This is attributed to the fact that the particles in the lower region of the particle bed need to stay closer with a smaller interparticle distance and a larger electrostatic repulsive force to support the resultant electrostatic forces from the particles in the upper region. This phenomenon is in broad agreement with the experimental observations of Wu *et al.* (2008), as shown in Figure 4.10.

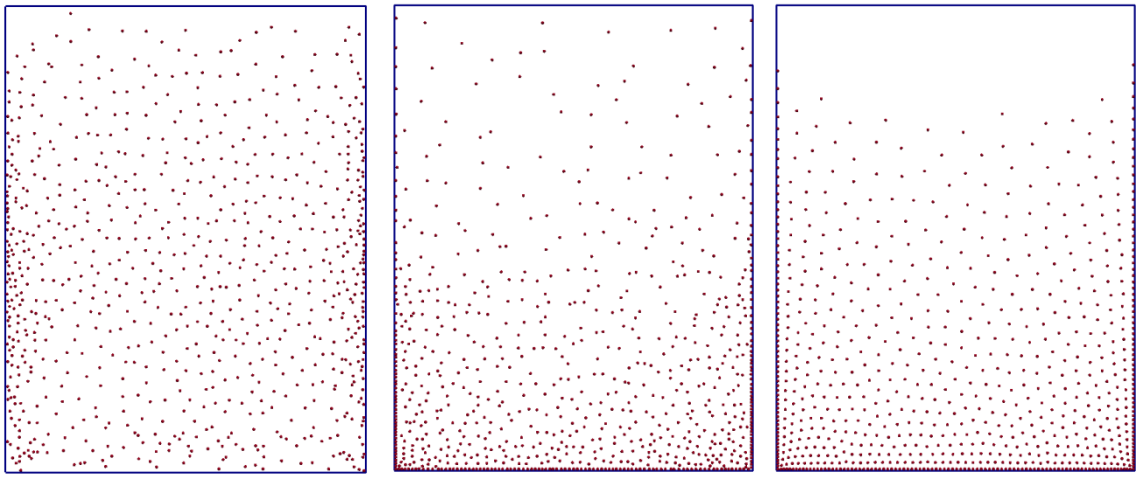

(a) $t = 0.017$ s (b) $t = 0.085$ s (c) $t = 0.34$ s

Figure 4.9 Particle profiles at various time instants obtained with the HPC method ($R_c = 15d_p$).

Figure 4.11 shows the equilibrium states of the granular bed obtained using the DT method with various cut-off distances. It is observed that the height of the granular bed increases as the cut-off distance increases. The corresponding packing patterns obtained using the HPC method are shown in Figure 4.12. In contrast to those observed in Figure 4.11, the packing

patterns obtained with various cut-off distances with the HPC method are essentially identical. The packing structure obtained using the HPC method is independent of the cut-off distance specified, while the results obtained using the DT method are very sensitive to the specified cut-off distance. This is a numerical effect of the DT method, which is not physically realistic.

Figure 4.10 Packing profile of charged particles obtained experimentally by Wu *et al.* (2008).

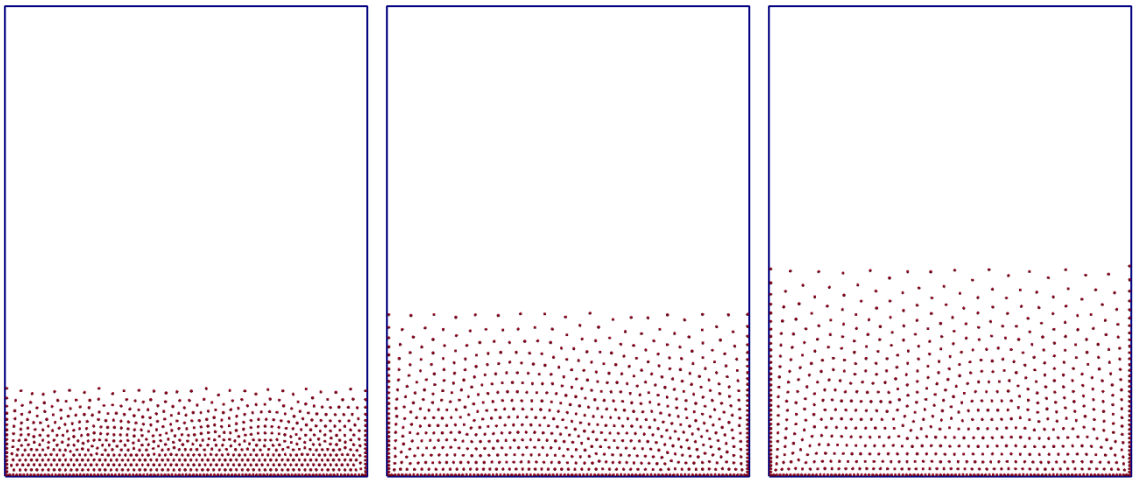

(a) $R_c = 5d_p$ (b) $R_c = 15\ d_p$ (c) $R_c = 25\ d_p$

Figure 4.11 Equilibrium packing patterns obtained using the DT method with different R_c.

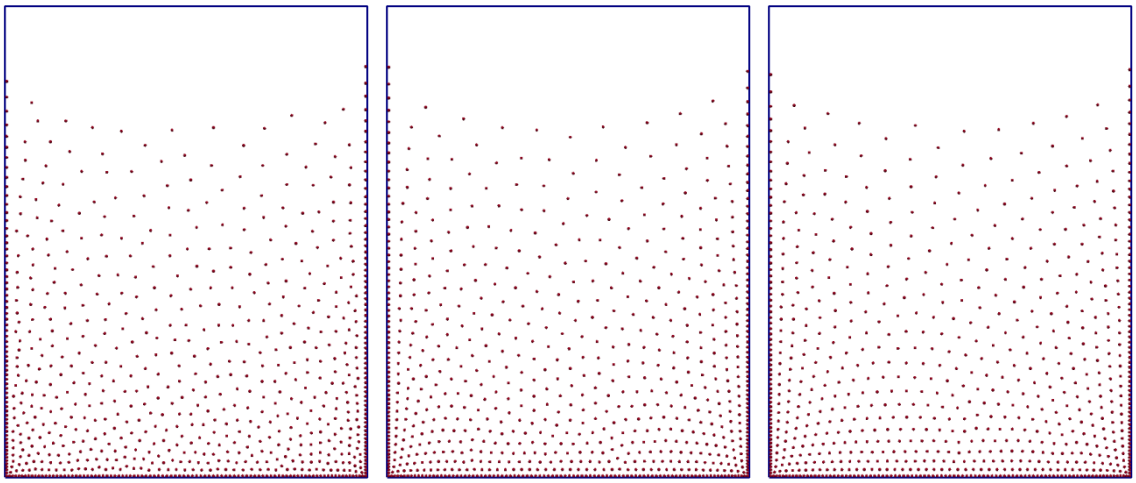

(a) $R_c = 5d_p$ (b) $R_c = 15d_p$ (c) $R_c = 25d_p$

Figure 4.12 Equilibrium packing patterns obtained using the HPC method with different R_c.

4.3.3. Radial distribution function

The radial distribution function (RDF), $g(r)$, is introduced to analyze the packing patterns shown in Figures 4.11 & 4.12. The RDF defines the variation of the number density of particles within the distance from a reference particle and can effectively describe the radial scattering pattern of a particle system (Wu *et al.*, 2005). The RDF of a two-dimensional inhomogeneous system is defined as:

$$g(r) = \frac{n(r)}{2\pi r \sigma_n \Delta r} \tag{4.8}$$

where r is the distance from the reference particle; $n(r)$ is the mean number of particles within an annulus of width Δr at distance r; σ_n is the mean number density of particles. It can be seen that the RDF gives the normalized number density of particles within the region between r and $r + \Delta r$ from the reference particle. In the current study, the RDF is determined with r varying from d_p to $30d_p$ with an interval of $0.2d_p$ and Δr is set to $0.01d_p$, which is similar to the values used by Wu *et al.* (2005).

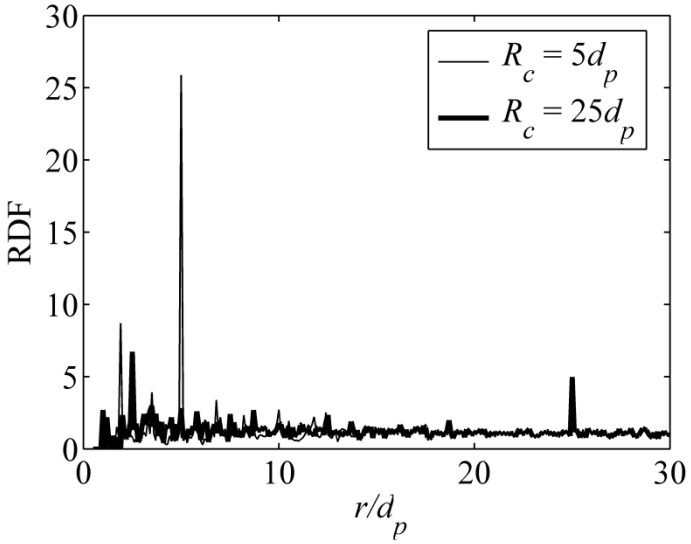

Figure 4.13 RDF profiles obtained using the DT method with different R_c.

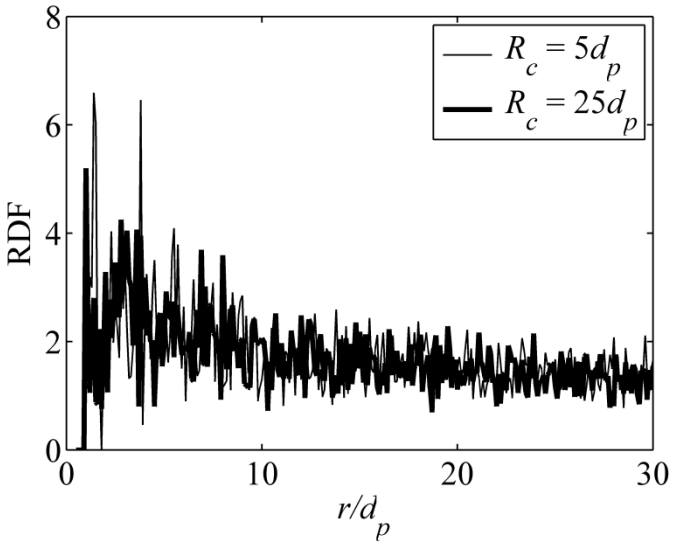

Figure 4.14 RDF profiles obtained using the HPC method with different R_c.

Figures 4.13 and 4.14 show the RDFs for $R_c = 5d_p$ and $25d_p$ using the DT and HPC methods; the data for $R_c = 15d_p$ are very similar to those for $R_c = 25d_p$ and are consequently not shown. The DT method results in two peaks that correspond to $R_c = 5d_p$ and $25d_p$, which indicates that an artificial dense layer is developed at the specified cut-off distance. However, the RDF

profiles obtained using the HPC method are essentially identical when different cut-off distances are specified, which is more realistic.

4.3.4. Granular temperature

The granular temperature (GT) describes the internal thermal energy of a chaotic particle system (Goldhirsch, 2008; Müller *et al.*, 2008). It reflects the fluctuation of particle kinetic energy of a particle system, which can be defined as:

$$T_g = \frac{1}{D_n}\left\langle \left(\mathbf{v} - \bar{\mathbf{v}}\right)^2 \right\rangle \tag{4.9a}$$

where the angle bracket <> indicates ensemble average; **v** is the velocity of each particle; $\bar{\mathbf{v}}$ is the average velocity of all particles in the system; D_n denotes the spatial dimension.

For a 2D particle system, the average GT is defined as (Müller *et al.*, 2008):

$$T_g = \frac{1}{2N}\sum_{i=1}^{N}\left(v_x^i - \bar{v}_x\right)^2 + \frac{1}{2N}\sum_{i=1}^{N}\left(v_y^i - \bar{v}_y\right)^2 \tag{4.9b}$$

where v_x^i and v_y^i are the velocity components of particle *i* in *x* and *y* directions; $\bar{v}_x$ and $\bar{v}_y$ are the average velocity components of all particles in *x* and *y* directions, *N* is the number of particles.

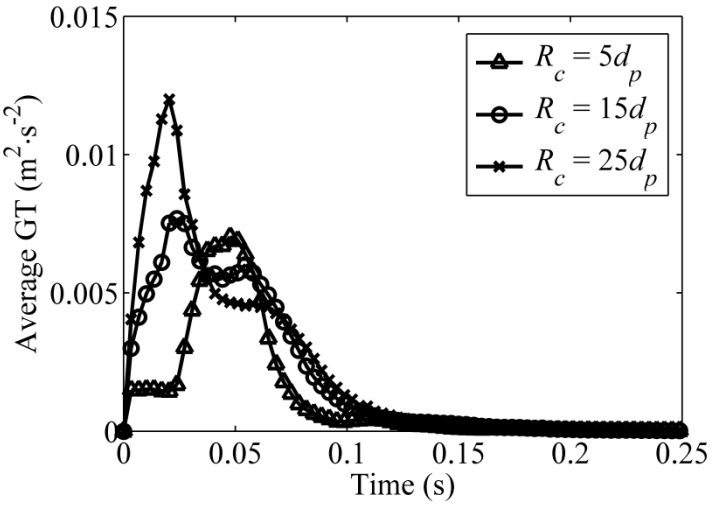

Figure 4.15 The evolutions of granular temperatures obtained using the DT method for different values of R_c.

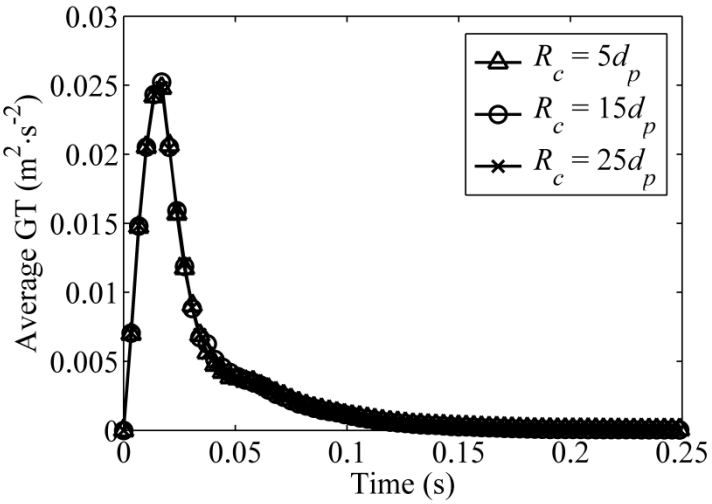

Figure 4.16 The evolutions of granular temperatures obtained using the HPC method for different values of R_c.

Figure 4.15 shows the evolution of GTs obtained using the DT method with different values of R_c. It is clear that the GT increases initially as the particles are released to move under gravitational and electrostatic forces. It reaches a maximum value and then starts to decrease, indicating that the system is "cooling down" as the kinetic energy starts to be dissipated

through the contacts between particles and walls, and the interaction between particles and the air. However, the maximum value increases with increasing R_c with a corresponding reduction in the rate of cooling. In addition, for the shortest cut-off distance (*i.e.* $R_c = 5d_p$), there is a dwell period during the heating stage, at which the GT remains unchanged. The corresponding GTs obtained using the HPC method are presented in Figure 4.16. It can be seen that they are independent of the value of R_c, which should be the case. In addition, compared to the GTs obtained using the DT method (Figure 4.15), the maximum value is larger about a factor of two.

4.4. Deposition of bi-charged particles

4.4.1. Model setup

In this section, the deposition of bi-charged particles is modelled using the developed DEM-CFD code. The bi-charged particles are also referred to as bipolarized particles that are of different signs of electrostatic charge. In Section 4.3, for mono-charged particles, the HPC and DT methods are both used for comparison. However, if bi-charged particles are used as in Section 4.4, using Eq. (4.5) will neutralize the charge in each cell without considering the superposition of the electrostatic forces and eventually show a similar result as the DT method (Appendix A). Hence, for bi-charged particles, only the DT method is used. To investigate the microstructure of a bi-charged particle system and its flow behaviour, the coordination number and the flow indices including deposition ratio and deposition rate are analyzed and discussed.

A similar deposition process as Section 4.3 is implemented. Bi-charged particles are considered in order to explore the flow behaviour of powders during a deposition process. The initial configuration of a 2D model is shown in Figure 4.17, in which charged particles are randomly positioned in the region $w \times l$ within the container and deposited from a height h_0. The calculation is terminated when the final state is relatively stable with a negligible kinetic energy.

The flow of air is modelled using the CFD scheme. The entire domain is divided into fluid cells with a side length of 5 particle diameters. The properties of the air and the boundary conditions of the CFD domain are identical to those given in Section 4.3.1.

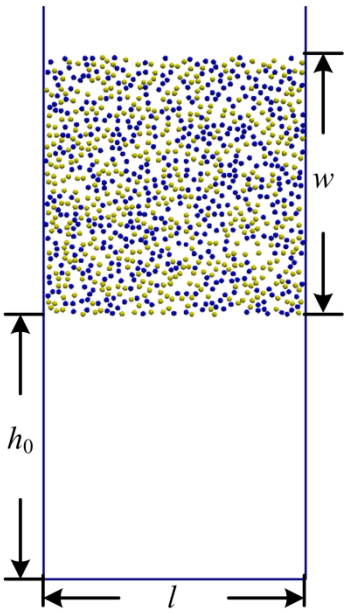

Figure 4.17 The computational setup of the deposition of bi-charged particles: w = 5 mm, h_0 = 5 mm, l = 5 mm.

The magnitude of the electrostatic, F^e, relative to the gravitational force, mg, for mono-dispersed particles, is expressed as a dimensionless ratio, ξ:

$$\xi = \frac{F^{\mathrm{e}}}{mg} = \frac{\dfrac{1}{4\pi\varepsilon_0}\dfrac{q^2}{d_{\mathrm{p}}^2}}{\dfrac{4}{3}\pi r_{\mathrm{p}}^3 \rho_p g} = \frac{3q^2}{64\pi^2\varepsilon_0\rho_p g r_{\mathrm{p}}^5} \tag{4.10}$$

where r_{p}, and d_{p} are the radius and diameter of the particle; q and ρ_p are the charge and density of the particle.

The dimensionless ratios of 0.0, 7.88 and 42.0 are considered. The properties of the particles and containers are given in Table 4.3. For bi-charged particles, each system contains 500 positively charged particles and 500 negatively charged particles coloured in dark (blue) and light (yellow), respectively.

Table 4.3 Properties of particles and walls

Parameters	Particles	Walls
Diameter (μm)	100	~
Density (kg·m^{-3})	1.5×10^3	7.9×10^3
Elastic module (GPa)	8.7	210
Poisson's ratio	0.3	0.3
Coefficient of friction	0.3	0.3

4.4.2. The deposition of particles

Figure 4.18 shows the deposition process of neutral particles (*i.e.* without any electrostatic interaction). It can be seen that at the initial stage (Figure 4.18a), particles are randomly generated in the defined area without any contacts. Then the deposition starts and particles flow smoothly until they reach the base as shown in Figure 4.18b. Eventually the particles are

deposited on the base (Figure 4.18c). Similar phenomena are observed for the deposition of neutral particles in a vacuum.

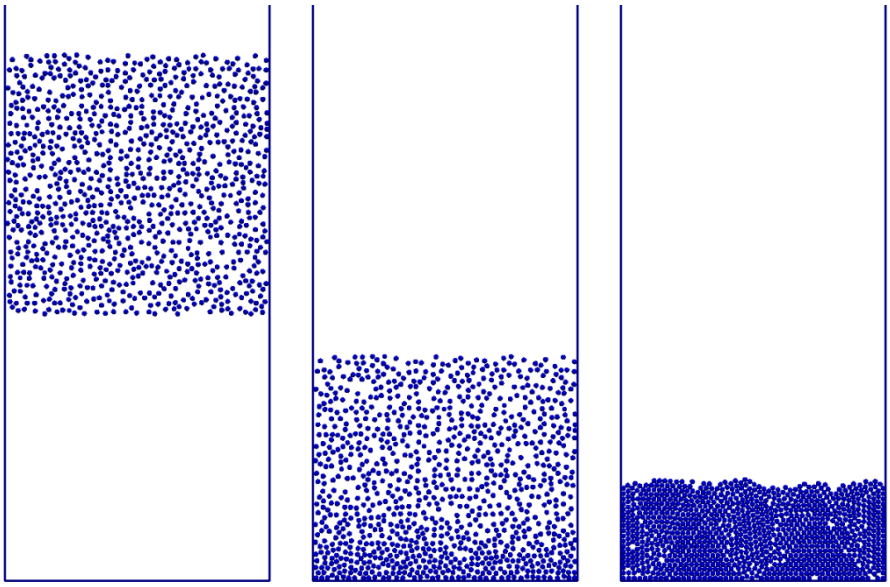

(a) $t = 0.0$ s (b) $t = 0.034$ s (c) $t = 0.1$ s

Figure 4.18 The deposition of neutral particles in air ($\xi = 0.0$).

Figure 4.19 shows the deposition process for charged particles, in which the image forces between particles and walls are considered. Similarly to Figure 4.18a, the bi-charged particles are randomly generated in the defined area without contacts. However, as the deposition starts, particles with opposite charges attract each other and form agglomerates during the deposition process (Figure 4.19b). Meanwhile, because of the image force, particles are attracted to the conductive walls and retained on the wall surface. As the agglomerates of charged particles reach the base of the container, the impact between them and the base results in breakage of the agglomerates, which can be seen in Figure 4.19c and 4.19d. Most particles, except particles sticking on the side walls, eventual settle and pack on the base (Figure 4.19e and 4.19f). Other groups of charged particles show similar phenomena during deposition (Figure 4.20). For simulations without image forces, particles are assumed only to have electrostatic

interactions with each other but without the attractive force with the walls. Consequently, agglomeration of charged particles occurs during deposition, but there are no particles sticking on the side walls (see Figure 4.20a and 4.20c). It is clear that the deposition processes of charged particles are different from those of neutral particles. The formation and breakage of agglomerates occur in the deposition of bi-charged particles.

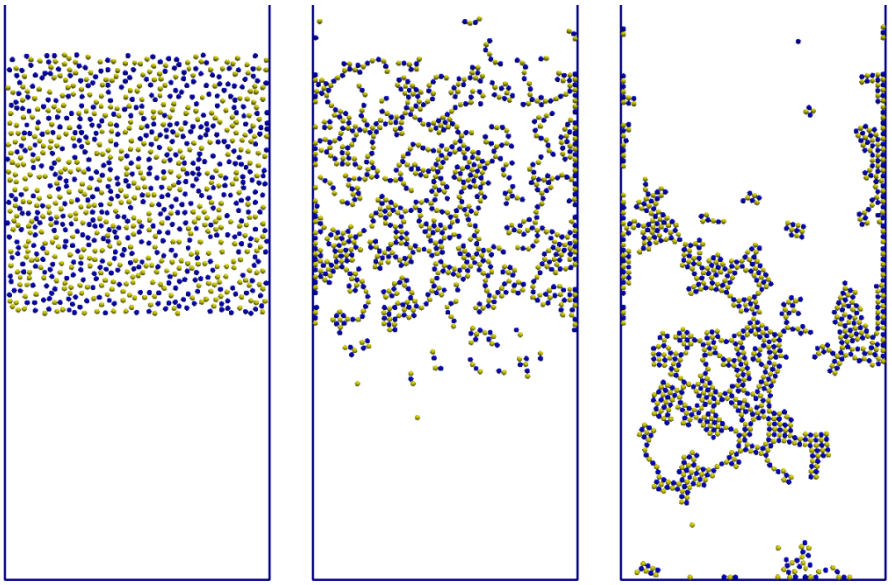

(a) t = 0.0 s (b) t = 0.0085 s (c) t =0.032 s

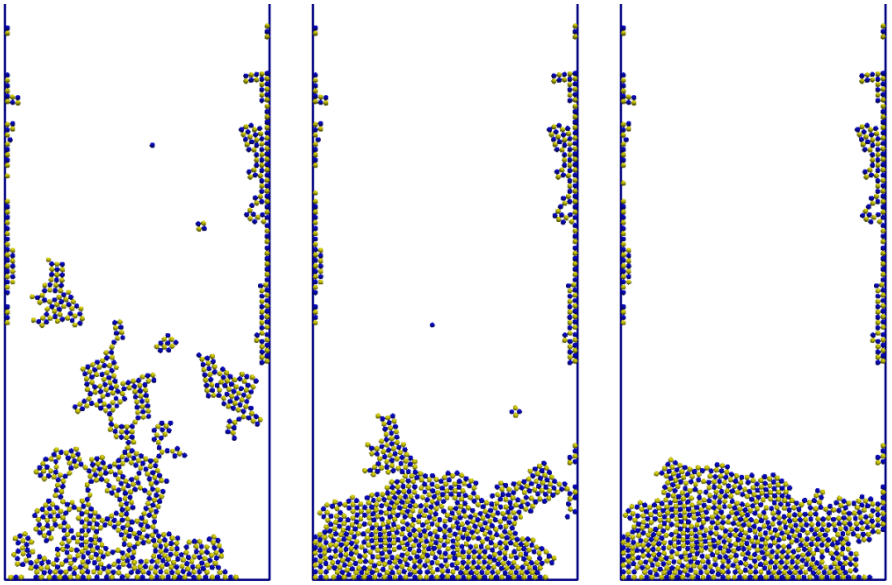

(d) t = 0.044 s (e) t = 0.06 s (f) t = 0.1 s

Figure 4.19 The deposition of charged particles in air (ξ = 42.0).

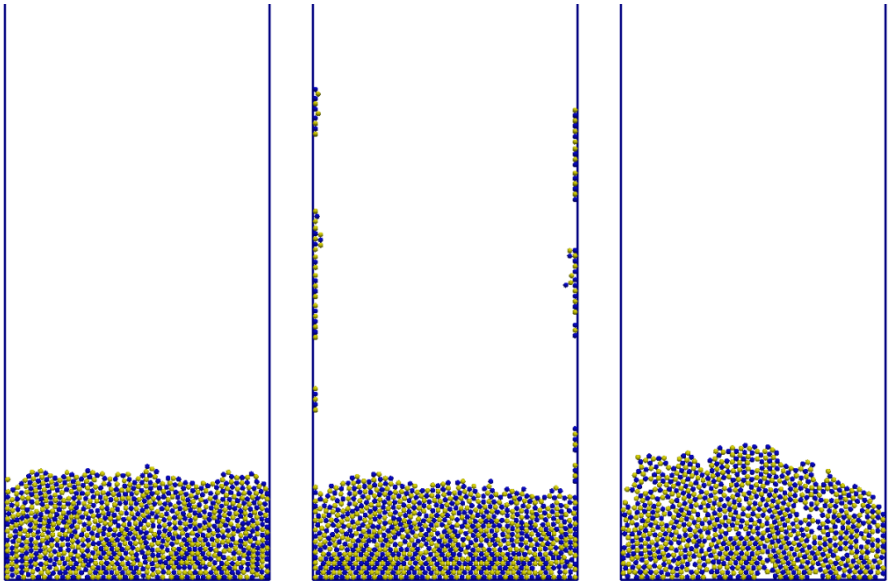

(a) (b) (c)

Figure 4.20 The deposited granular bed of various charged particles: (a) $\xi = 42.0$, without image force (b) $\xi = 7.88$, with image force (b) $\xi = 7.88$, without image force).

4.4.3. Coordination number

The coordination number (CN) is introduced to characterise the microstructure of the particle systems, especially for agglomerates (Liu *et al.*, 1999; Lim and McDowell, 2007). In the current study, the coordination number is defined as:

$$Z = \frac{C}{N} \tag{4.11}$$

where C is the total number of contacts on all particles; and N is the total number of particles. Hence, the coordination number Z is the mean number of contacts per particle, which can be used to evaluate the packing density of particle systems.

Figure 4.21 shows the evolution of the coordination number during a deposition process. For particles without charges, there are no contacts at the initial deposition stage until particles

begin to reach the base of the container (Figure 4.18b). Then the coordination number keeps increasing and achieves a stable value when all particles are deposited on the base. In contrast, the evolution of the CN for bi-charged particles shows a different pattern. The CN starts to increase at the initial stage for the bi-charged particles and then deceases when the agglomerates reach the base, as shown in Figure 4.19c and 4.29d. After all the particles settle on the base, the coordination number gradually increases to a stable value. The particles with different charges (ξ = 7.88 and 42.0) give the similar pattern, although the particles with smaller charges have a smaller coordination number at the initial stage. Comparing Figures 4.21a with 4.21b, it can be seen that the deposition of particles in vacuum and air have similar patterns. However, the evolution of the CN for particles in air is slower than that in a vacuum. For instance, the CN for ξ = 42.0 in a vacuum starts to decrease due to the breakage of agglomerates at the base at about 0.02 s whilst the CN for ξ = 42.0 in air starts to decrease at about 0.04 s.

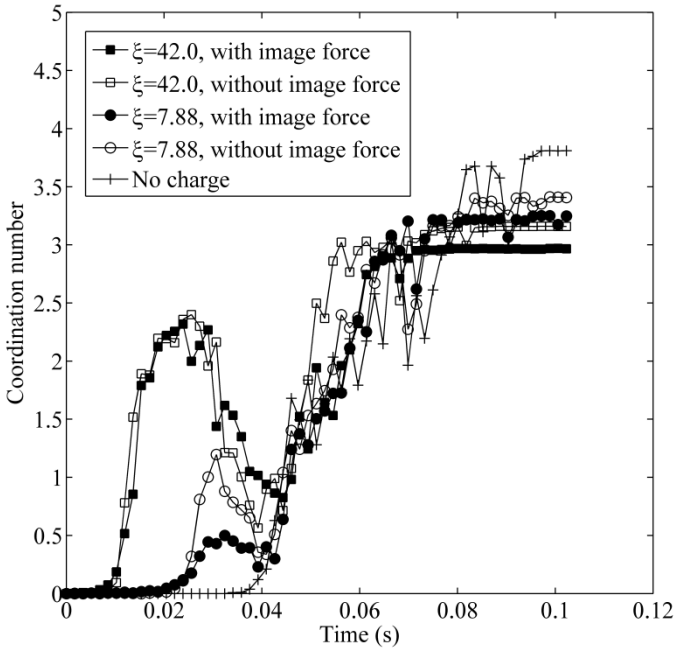

(a) In a vaccum

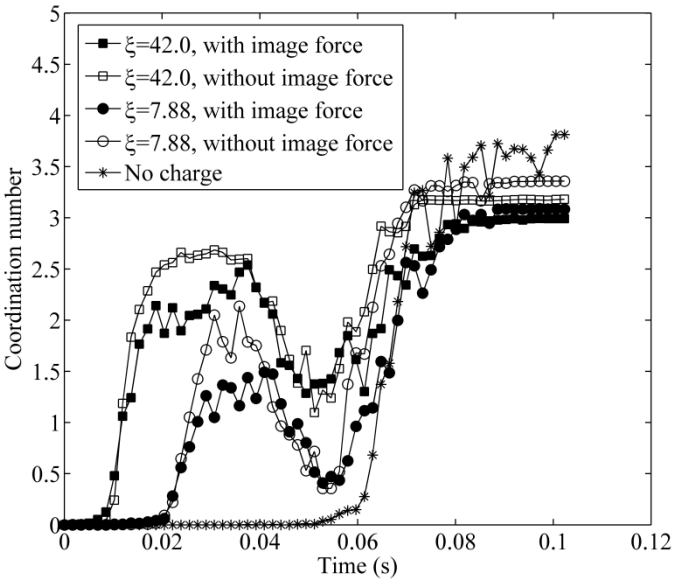

(b) In a air

Figure 4.21 The evolution of coordination number during the deposition process.

4.4.4. Deposition ratio

The deposition ratio (DR) is introduced to examine the flow of particles. It is defined as the ratio of the mass of particles below the height h_0 to the total mass of the particles.

Figure 4.22 presents the evolution of the DR of various particles without image forces in vacuum and air. For all cases, the DR reaches a hundred percent at a specific time, termed the deposition time. It can be seen that the deposition time in vacuum is shorter than that in air for particles with and without charge. It is clear that the existence of air can prolong the deposition time. In addition, the difference between the deposition time in vacuum and in air for particles with higher charges is smaller than that for particles with lower charges, which indicates that the electrostatic force can also affect the deposition process.

Figure 4.23 shows the deposition ratio for various cases in air with and without the image force. It is clear that the deposition ratios of the groups without the image force can reach a hundred percent, while the deposition ratio of the groups with the image force is smaller. According to Figures 4.19f and 4.20b, the image force can cause charged particles to stick to the walls, which significantly decreases the DR. Consequently, the particle system with higher charges (ξ = 42.0) tends to have a smaller deposition ratio, compared to the one with lower charges (ξ = 7.88).

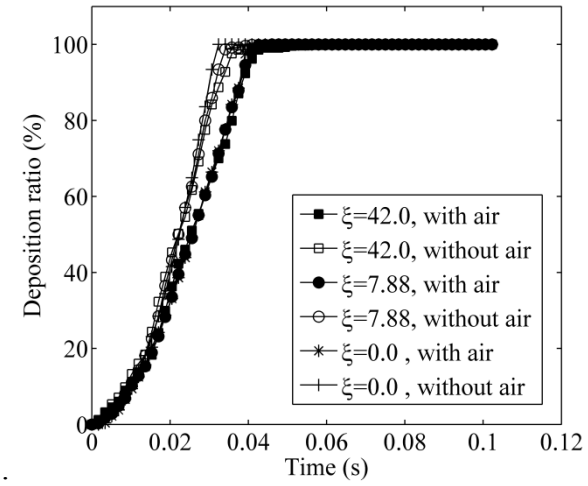

Figure 4.22 Deposition ratios for bi-charged particles in air and vacuum without image force.

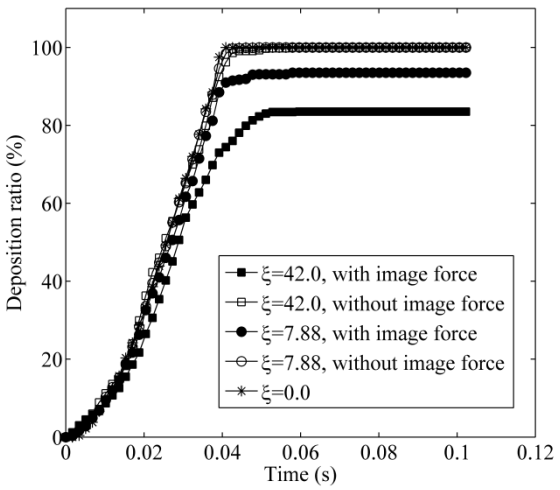

Figure 4.23 Deposition ratio for bi-charged particles in air with and without image force.

The mean deposition rate can be used to identify the flowability of the particles during deposition, which is defined as:

$$\overline{m} = \frac{m_h}{t} \tag{5}$$

where $\overline{m}$ is the mean deposition rate, m_h is the mass of particles below the height h_0, and t is the deposition time, *i.e.* from the start of deposition to the point that the deposition has just completed.

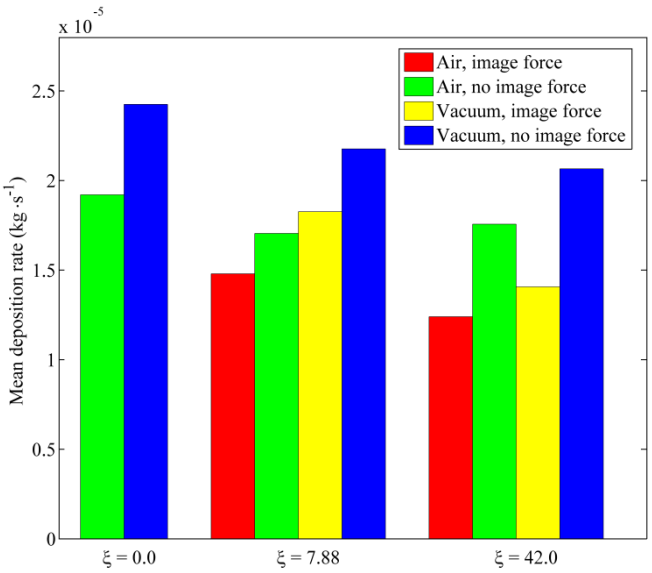

Figure 4.24 Average deposition rates of various cases.

Figure 4.24 presents the mean values of the DR for various cases. The DRs of particles without charge are larger than those for bi-charged particles in a vacuum and in air respectively. Furthermore, the difference between deposition rates in a vacuum and in air for particles with higher charge is smaller than that for particles with lower charge. In addition, the image force can lead to a smaller mean DR, especially for the highly bi-charged case (ξ =

42.0). These results correspond closely with the results shown in Figures 4.22 and 4.23, indicating that both the air and the electrostatic interactions affect the deposition process.

4.5. Discussions

4.5.1. Deposition of mono-charged particles

Figures 4.11-4.16 show that, even for the same deposition process with mono-charged particles, using the DT method, the height of the granular bed increases with increasing cut-off distance. There is a strong correlation between the peak in the RDF and the cut-off distance, and the evolution of the granular temperature is very sensitive to the specified cut-off distance. These observations of cut-off effects are physically unrealistic, as the cut-off distance is only a simulation parameter that should not have such a significant impact on the microstructure of the deposited particle system and thermal behaviour. These unrealistic features were attributed to the fact that the repulsive electrostatic forces between particles with a separation distance longer than the cut-off distance are completely ignored in the DT method. As a consequence, particles experience weaker electrostatic forces with a smaller cut-off distance. To counter-balance the gravitational force on the particles, smaller inter-particle distances and larger electrostatic forces are necessary. Therefore, a more compact packing structure is induced as observed in Figure 4.11.

In 2D simulations using the DT method, the circle at the cut-off distance of each particle acts as a critical and equilibrium boundary for the combined effects of gravitational and electrostatic repulsive forces. Particles under gravity tend to deposit onto the base of the

container and pack together while the electrostatic repulsive force between mono-charged particles will dilate the particle system. For each pair of particles, when the electrostatic force is larger than the gravitational force, particles move away from each other until their separation distance reaches the cut-off value. As the particles move further away from each other (*i.e.* beyond the cut-off distance), the electrostatic force between them is ignored and the particles start to pack together because of the gravitational force. Once the distance between the particles is smaller than the cut-off value, the electrostatic force is activated again. Thus each pair of particles vibrates around the cut-off distance and eventually achieves the equilibrium state due to the contact damping and friction between the particles and walls. Therefore, a strong peak at the cut-off distance is induced in the RDF profile. However, when the cut-off distance is larger, the electrostatic force at the corresponding cut-off distance becomes weaker and the corresponding value of the RDF is much smaller. This artificial effect has also been observed in MD and Monte Carlo simulations (Brooks, *et al.*, 1985; Brooks, 1987; Takahashi *et al.*, 2010), showing that artificial layers located at the cut-off distances were observed when the truncation method was used to describe the thermodynamics of aqueous ionic solutions.

It has been shown that the GT obtained using the DT method is much lower than that using the HPC method due to the neglect of the electrostatic potential from the long-range region. Since only the electrostatic forces within the cut-off distance are considered in the DT method, the particles in the simulations with smaller cut-off distances experience a smaller electrostatic repulsive force at the initial stage and possess smaller electrostatic energy, which leads to a smaller acceleration and a smaller velocity difference (*i.e.* GT). Initially, particles are accelerated to move away from each other because of the electrostatic repulsion and this

results in an increase of the GT. As the separation distance becomes longer than the cut-off value, the electrostatic force and the subsequent acceleration are ignored in the simulation and consequently the GT remains unchanged. When the particles reach the base of the container and consolidate under gravity, the distance between particles becomes smaller than the cut-off distance again. The GT starts to increase and eventually achieves the maximum value. Moreover, when the cut-off distance is longer, the ignored electrostatic interactions becomes less significant and the influence on the GT is also smaller.

In the HPC method, all potential electrostatic interactions are considered. Even though an approximation is made to calculate the electrostatic forces in the WI region (*i.e.* with a separation distance longer than the cut-off value) using the cumulative net charge in a cell (Eqs. 4.5-4.7) instead of a direct calculation of particle-particle interactions, the results illustrated that this approximation is appropriate and produces more realistic results than the DT method. In particular, it is demonstrated that the HPC method is insensitive to the cut-off distance specified (Figures 4.12, 4.14 and 4.16).

The cut-off distance can also affect the computational time for the DT and HPC methods. To compare the difference between these two methods, the computational time for simulations with different cut-off distances were obtained at the same physical time of 0.68 s as given in Table 4.4. The computational time with the DT method is more sensitive to the cut-off distance than the HPC method. For the DT method, it takes 19.9 to 40.7 h when the cut-off distance varies from $5d_p$ to $25d_p$. However, for the HPC simulations with different cut-off distances similar computational times are required. This is due to the consideration of electrostatic interaction in both the SI and WI regions. In these two regions, similar

computations are implemented to calculate the electrostatic interactions for each reference particle. Although the change of cut-off distance alters the sizes of the two regions, it will not significantly affect the total computation cost.

Table 4.4 Computation time (Unit: hour) required with the DT and HPC methods for a simulation of physical time of 0.68 s

R_c	$5d_p$	$15d_p$	$25d_p$
DT	19.9	30.4	40.7
HPC	101.0	112.1	107.0

It should be noted that the accuracy of the HPC method is still limited. The electrostatic force is a function of the charge of objects and the distance between them. From Figure 4.7 and Eq. (4.5), it can be seen that the charge of a cell is a simple summation of the charge of the particles without considering the distance between each particle and the centre of the cell. Consequently, the electrostatic force between the reference particle and the cell cannot accurately represent the actual force between the reference particle and those in the cell. To obtain a high order of accuracy, a multipole expansion method (Esselink, 1995) can be used to approximate the charge of the particles onto the centre of the corresponding cell. Moreover, the image and polarization effects that affect the electrostatic interactions between closely positioned particles should also be considered in the future.

4.5.2. Deposition of bi-charged particles

The agglomerates formed by the bi-charged particles in Figure 4.19 show a crystalline structure. This is caused by the mutual attractive and repulsive force induced by the positive

and negative charge on the particles. In the experiments performed by Grzybowski *et al.* (2003), bi-charged spheres with different materials can form similar crystalline patterns when they are charged by contact electrification. The experimental and the simulation results are shown in Figure 4.25 which exemplifies the excellent agreement.

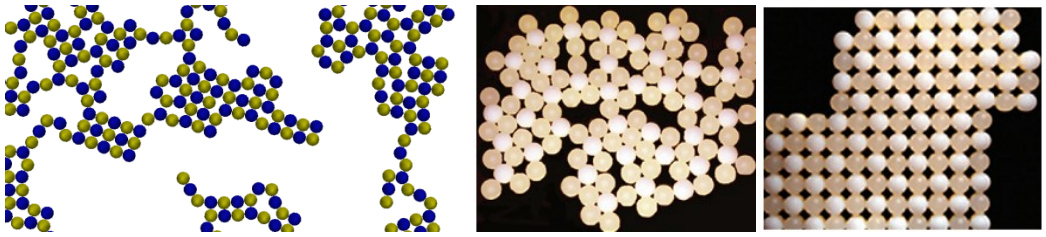

(a) DEM (b) Experiments (Grzybowski et al, 2003)

Figure 4.25 Comparison between simulations and experiments.

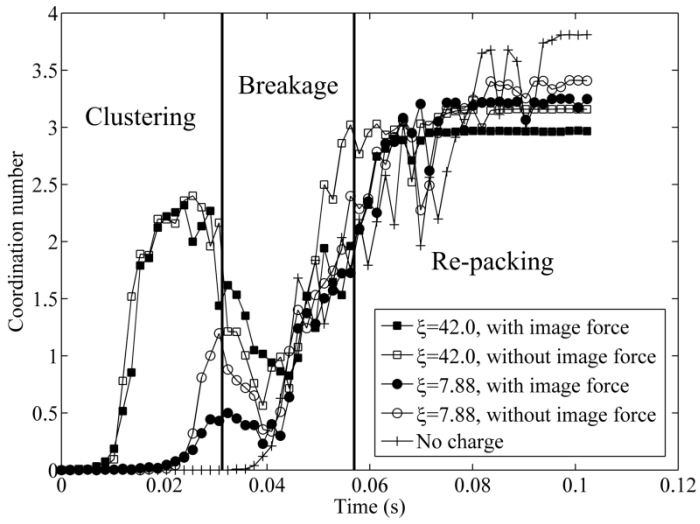

Figure 4.26 Three stages of the deposition process.

According to Figure 4.21, the deposition process of the bi-charged particles can be divided into three stages: clustering, impact breakage and re-packing as shown in Figure 4.26. At the beginning of deposition, particles can agglomerate due to the long-range electrostatic forces, as shown in Figure 4.19b and the highly charged particles have a larger number of contacts

due to the larger attractive force. When particles reach the base of the container, the breakage of clusters is observed as shown in Figure 4.19c, because the impact force is normally greater than the electrostatic force as discussed in Section 4.1.2. As a consequence of the energy dissipation during impact, particles gradually settle down at the base (Figure 4.19d) after the coordination number reaches the minimum value. Thereafter, re-clustering and packing take place and consequently the coordination number increases again (Figures 4.19e and 4.19f).

The presence of air and electrostatics can both affect the deposition process. The influence of air on particle behaviour mainly depends on the air sensitivity of particles (Yu *et al.*, 2009). When there is an electrostatic force during deposition, particles in the upper layer can be repulsed by particles with the same charge in a lower layer and retard the overall deposition velocity of the particles in the upper layer. In addition, the formation of agglomerates caused by the electrostatic interactions can lead to significant damping of the kinetic energy and eventually decrease the flowability of particles. The combined effect of air and electrostatics is more complicated. Both the air-drag and electrostatic forces can reduce the flowability of particles. However, the agglomerate formed by the electrostatic force can decrease the air sensitivity of particles as discussed above. Further simulations and validations will be needed to fully understand this combined effect.

4.6. Summary

To model charged particle systems with DEM-CFD, long-range electrostatic interactions were considered and implemented. The DT and HPC methods were used to compute the long-range

electrostatic interactions. The deposition processes of mono-charged and bi-charge particles were simulated and analyzed using the developed DEM-CFD method.

In the deposition of mono-charged particles, a simple direct truncation (DT) method and a hybrid particle cell method (HPC), both using a cut-off distance to improve the computation efficiency, are implemented into the DEM-CFD code. The sensitivity of both methods to the cut-off distance is examined. It was found that the DT method is very sensitive to the cut-off distance and the neglect of the weak electrostatic interactions between mono-charged particles with a separation distance longer than the cut-off value introduces significant errors and artificial phenomena were observed. As an alternative, these weak interactions are approximated using the particle-cell approach in the HPC method. It has been shown that this method is not sensitive to the cut-off distance and more accurate and consistent results are obtained for the deposition of mono-charged systems, compared to the DT method.

In the deposition of mono-charged particles, the repulsive electrostatic forces disperse the particles in the granular bed. The particle concentration gradually decreases from the base to the top of the granular bed because of the combined effects of gravity and electrostatic repulsion, which results in a complex particle distribution as shown in the RDF. The internal energy of the particle system indicated by the GT presents a typical ‘cooling’ process, in which the GT increases as initiated by the electrostatic force and then decreases after particles settle in the container.

During the deposition of bi-charged particles, the electrostatic forces, including attractive and repulsive forces, cause crystalline agglomerations of particles to form. Therefore, the

deposition process can be divided into three stages: clustering, breakage and re-packing, which show different characteristics of agglomeration in the granular bed. The air and electrostatics can both reduce the flowablity of particles during deposition. However, the agglomerate formed by the bi-charged particles can decrease the air sensitivity of particles and the difference between deposition rates in a vacuum and in air for particles with higher charge is smaller than that for particles with lower charge.

The simulations are compared qualitatively with the experiments reported in the literature, and close agreement is obtained, especially in terms of the distribution of the particles and the micro-structure of the particle system. Further studies should consider the influence of the polarization of the charge and non-uniform charge distribution on particle surfaces on electrostatic behaviour during powder handling processes.

CHAPTER 5 CONTACT ELECTRIFICAITON AND ELECTROSTATIC INTERACTIONS IN FLUIDIZATION

5.1. Introduction

In this chapter, the combined effects of contact electrification and electrostatic interactions in fluidization are investigated. Charging behaviour is analyzed using the contact electrification model and electrostatic interactions between charged particles are analyzed using Coulomb's law. The micro-structure and the performance of the fluidization affected by the induced electrostatic interactions are further examined.

5.2. Model setup

A 2D DEM-CFD model is set up to simulate the contact electrification and electrostatic interactions during fluidization as shown in Figure 5.1. In the simulation, 2500 particles with diameter of 100 μm are used and the properties of the particles and the container are given in Table 5.1. Initially the particles are randomly generated and deposited onto the base of the column with a size of $l \times h$ until the granular bed becomes stable (i.e. maximum particle velocity is smaller than 10^{-6} m·s^{-1}).

The air is then introduced through the base of the column with a superficial gas velocities v_g = 25 ~ 100 mm·s^{-1}. The air is treated as a continuous compressible fluid. The internal domain is divided into 10 × 80 CFD cells. No-slip boundaries are assumed at the side walls, and the

upper boundary is set as a continuous outflow. The air has an average molar weight of 2.88×10^{-2} kg·mol^{-1} and a shear viscosity of 1.8×10^{-5} Pa·s. The initial air pressure is set to one atmospheric pressure and the temperature of the fluidized bed is maintained constant.

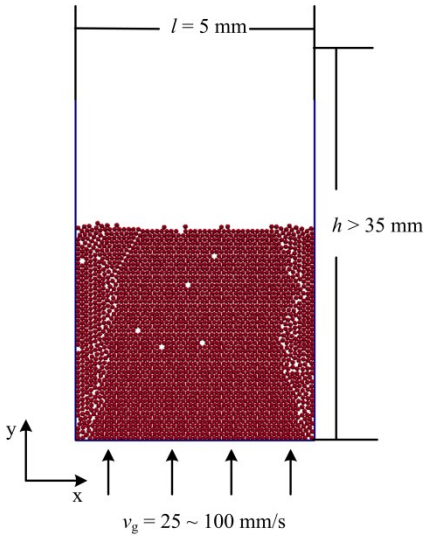

Figure 5.1 Model setup.

Table 5.1 properties of the particle and container

	Particle	Container
Elastic module, Y (GPa),	8.9	210
Poisson ratio, υ	0.3	0.3
Density, ρ_p (kg·m^{-3})	1500	7800

Contact electrification and electrostatic interactions (Appendices C and D) are both considered during the fluidization. The contact electrification model introduced in Chapter 3 is used to model the charge transfer between particles and between the particles and the wall. Two types of particles with different work function potentials (5.9 and 4.1 V) are used. The container is assumed to be a conductive material with a work function potential of 3.5 V and the net charge of the container can dissipate instantaneously and remain zero. The charging

constant k_s is set to 1×10^{-4} C·m^{-2}·V^{-1}. The induced electrostatic force between particles and the image force between the particle and the wall are governed by Eqs. 4.1 and 4.2, respectively. The direct truncation method is applied and the cut-off distance is set to 10 particle radii. Fluidization with neutral particles, i.e. the electrification and electrostatics are not applied, are also modelled for comparison.

5.3. Results

5.3.1. The particle profiles

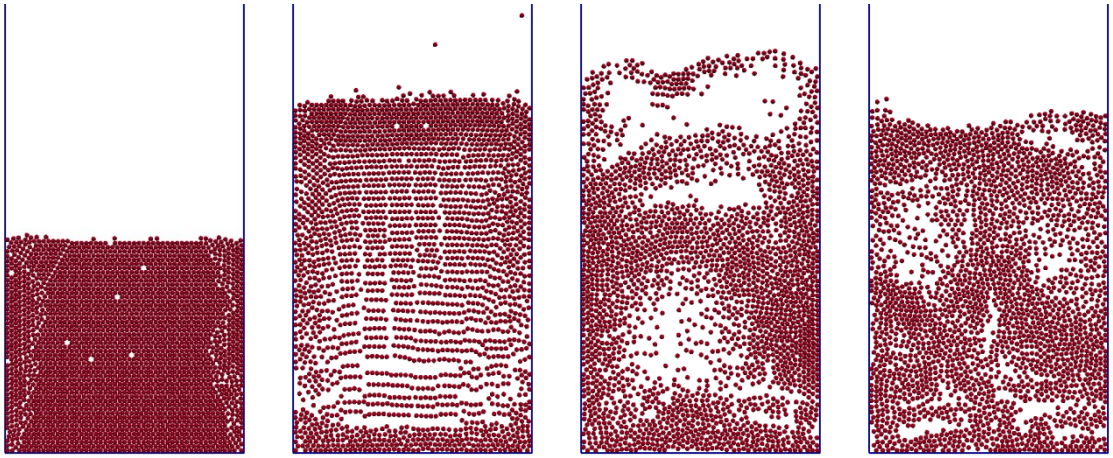

(a) t = 0.0 s (b) t = 0.068 s (c) t = 0.17 s (d) t = 0.34 s

Figure 5.2 Fluidization of neutral particles with v_g = 50 mm·s^{-1}.

Figure 5.2 shows the fluidization process of neutral particles with a superficial gas velocity of 50 mm·s^{-1}. Initially, the granular bed is settled on the base of the container as shown in Figure 5.2a. When the gas is injected from the base, the particles are lifted by the gas and move upwards (Figure 5.2b). The granular bed is gradually fluidized. The particles are dispersed and bubbles of gas continually form and move from the base to the top. As it is assumed that

the particle cannot get charged, similar bubbling behaviour as shown in Figure 5.2c and 5.2d continue throughout the entire fluidization process.

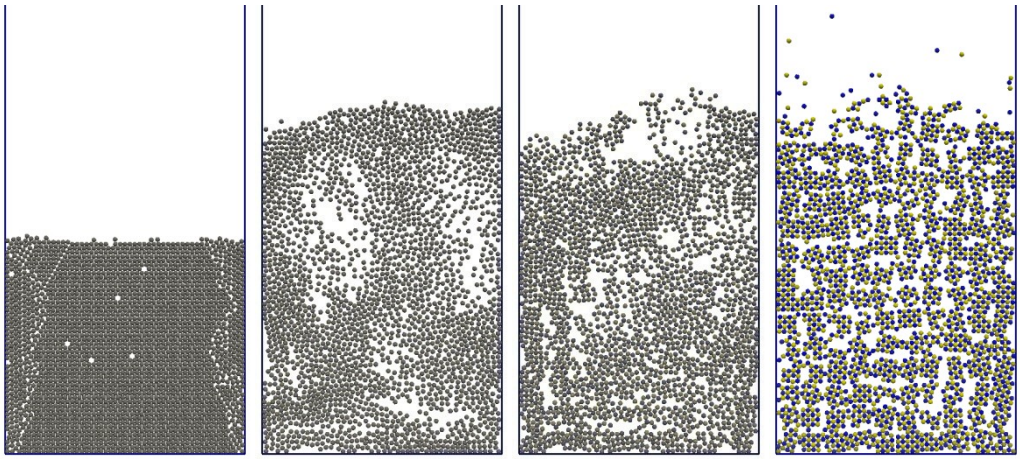

(a) t = 0.0 s (b) t = 0.34 s (c) t = 1.02 s (d) t =2.05 s

Figure 5.3 Fluidization of chargeable particles with v_g = 50 mm·s^{-1}.

Figure 5.3 presents the fluidization process of chargeable particles influenced by contact electrification and electrostatics with a superficial gas velocity of 50 mm·s^{-1}. From Figure 5.3a and 5.3b, it can be seen that at the early stage of the fluidization, the fluidized bed shows similar fluidizing phenomena as that with neutral particles as shown in Figure 5.2d. However, while the net charges on particles accumulate, bi-charged particles tend to move towards each other to form crystalline agglomerates and the gas bubbles becomes smaller (Figure 5.3c), compared to Figure 5.3b. As the electrostatic interaction becomes stronger and the charge accumulates, the gas cannot easily disrupt the agglomerates of bi-charged particles (Figure 5.3d, positive in dark colour and negative in light colour). Consequently, the dispersed fluidized bed transforms into a collection of agglomerates and the gas can only flow through the channels formed between the agglomerates, rather than bubbling (Figure 5.3d).

5.3.2. The charge distribution

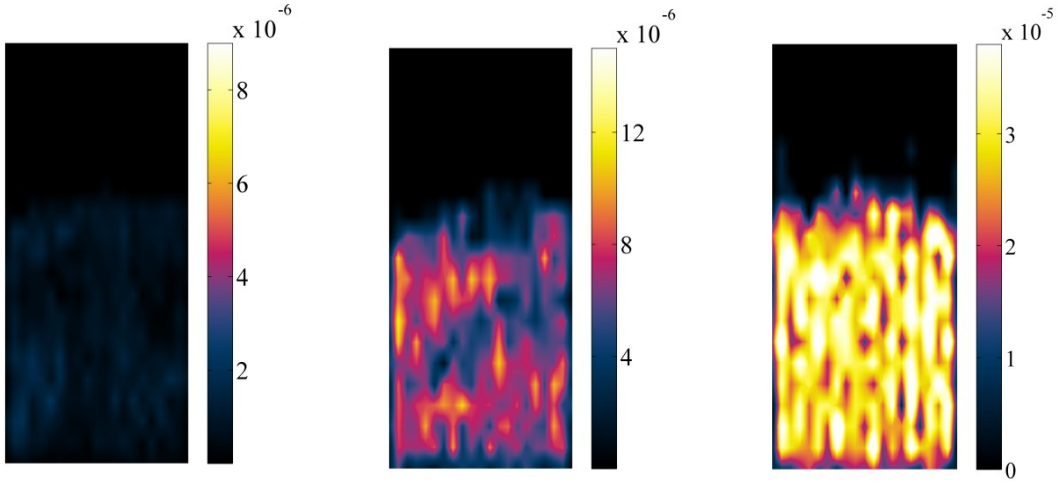

(a) t = 0.34 (b) t = 1.02 s (c) t =2.05 s

Figure 5.4 Positive charge density distribution (C·m^{-2}) of the charged fluidized bed with v_g = 50 mm·s^{-1}.

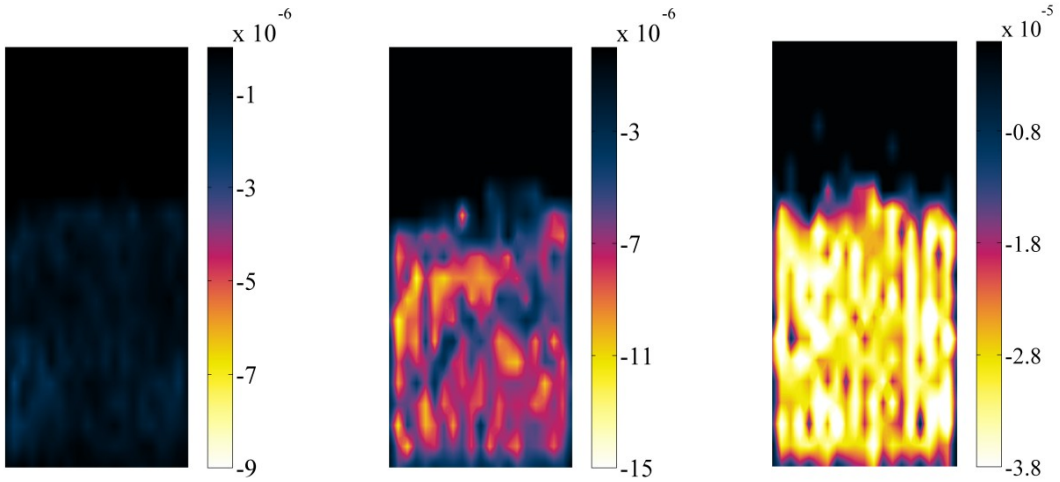

(a) t = 0.34 (b) t = 1.02 s (c) t =2.05 s

Figure 5.5 Negative charge density distribution (C·m^{-2}) of the charged fluidized bed with v_g = 50 mm·s^{-1}.

Charge density distribution as discussed in Chapter 3 can also be used to analyze the charge accumulation and distribution during fluidization. The fluidized bed is divided into 20×20 grids. In this study, particles with the low work function potential are charged positively and

particles with the high work function potential are charged negatively as observed in Figure 5.3. The positive and negative charge can be analyzed separately to examine the charge distribution. Therefore, the positive charge density distribution only considers the total positive charge of the fluidized bed and the negative charge density distribution is only for the negative charge.

Figures 5.4 and 5.5 show the corresponding positive and negative charge density distributions of the fluidized bed with a superficial gas velocity of 50 $mm \cdot s^{-1}$. Both positive and negative charge density distributions present similar patterns and accumulations during the fluidization. At the early stage of the fluidization, the particles start to accumulate charge. However, the charge density is relatively low (Figures 5.4a and 5.5a), and thus the granular bed can still be fluidized (Figure 5.3b). As the granular bed is fluidized, the charge density increases (Figures 5.4b and 5.5b). In addition, the positive and negative charges are concentrated in the same areas in the fluidized bed (Figures 5.4c and 5.5c), which indicates that the positive and negative charges induce strong electrostatic interactions to form agglomerates of particles (Figure 5.3d).

Figure 5.6 shows the fluidized beds of charged particles with various superficial gas velocities at t = 3.4 s. It is clear that the structures and the height of fluidized beds for chargeable particles vary with the superficial gas velocities. With a smaller gas velocity of v_g = 25 and 50 $mm \cdot s^{-1}$, the granular beds have larger agglomerates and the gas cannot disrupt the agglomerates and flows through the channels between agglomerates. On the contrary, the gas with a larger velocity of 100 $mm \cdot s^{-1}$ can lead to impacts between agglomerates and also

breakage. Therefore, due to the breakage and fluidization, the heights of fluidized beds increase with the superficial gas velocities.

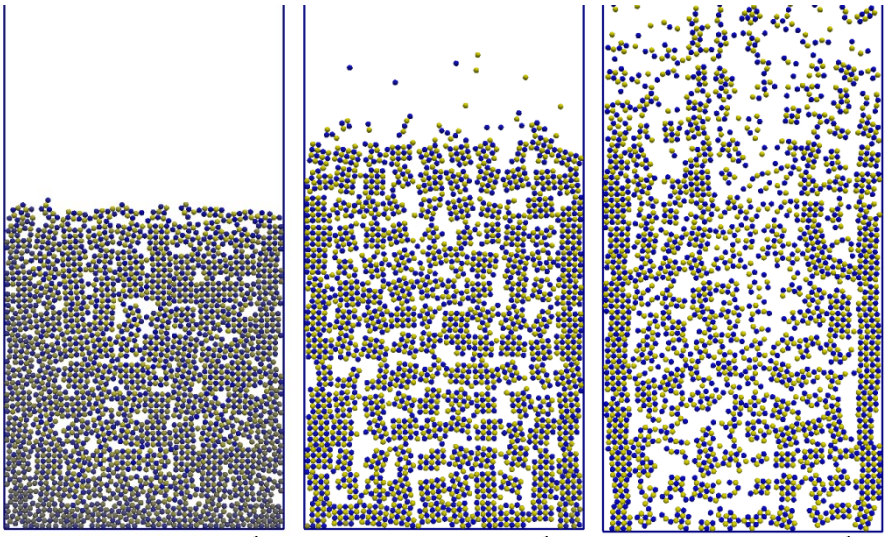

(a) v_g = 25 mm·s^{-1} (b) v_g = 50 mm·s^{-1} (c) v_g = 100 mm·s^{-1}

Figure 5.6 The fluidized beds of chargeable particles with various gas velocities at the same time instant (t = 3.4 s).

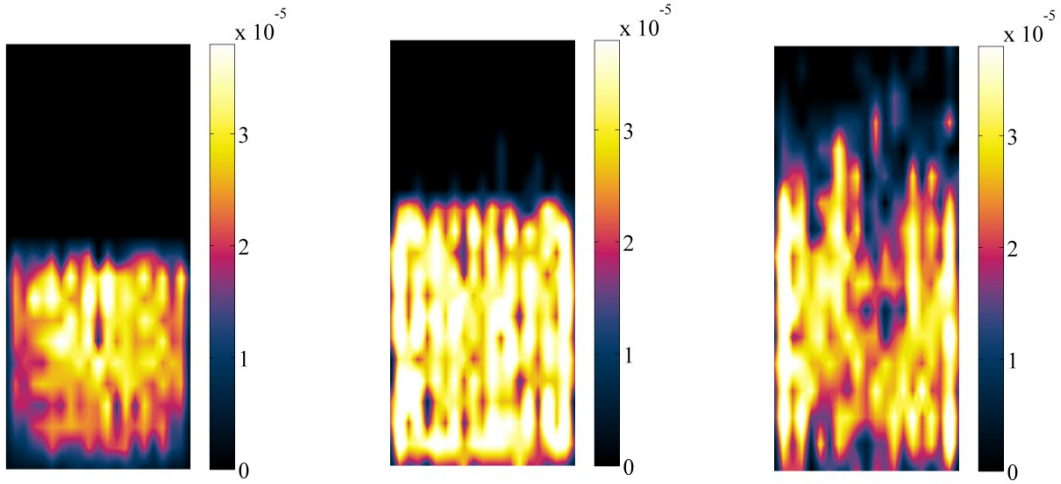

(a) v_g = 25 mm·s^{-1} (b) v_g = 50 mm·s^{-1} (c) v_g = 100 mm·s^{-1}

Figure 5.7 The positive charge density distribution (C·m^{-2}) of chargeable particles with various gas velocities (t = 3.4 s).

Figure 5.7 shows the corresponding positive charge density distribution of charged particles with various gas velocities at 3.4 s. The fluidized beds with different gas velocities present

different charge density patterns. At a smaller gas velocity (25 mm·s^{-1}), the charge density is smaller and concentrated at the top-centre of the granular bed. When the superficial gas velocity is 50 mm·s^{-1}, the charge is distributed over the entire granular bed densely, which means that the agglomerates are relatively stable as shown in Figure 5.7b. As the gas velocity is much larger, the charge is distributed sparsely in the fluidized bed since the particles and agglomerates are moving with the gas flow (Figure 5.7c). These phenomena indicate that the superficial gas velocity can affect the contact electrification process, and the subsequent dynamics of particles and agglomerates caused by electrostatic interactions. The negative charge density distribution is very similar as the positive charge density distribution.

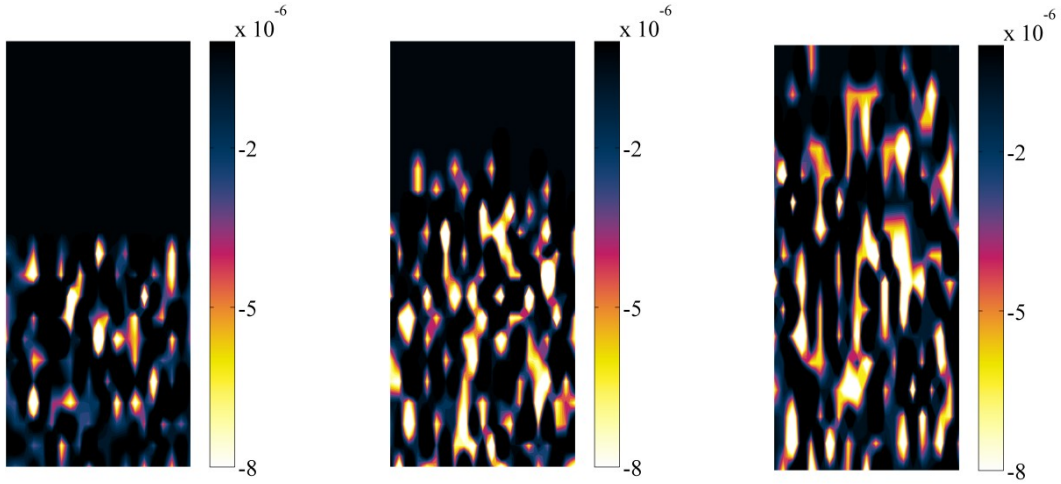

(a) v_g = 25 mm·s^{-1} (b) v_g = 50 mm·s^{-1} (c) v_g = 100 mm·s^{-1}

Figure 5.8 The total net charge distribution (C·m^{-2}) of chargeable particles with various gas velocities (t = 3.4 s).

The net charge is defined as the summation of the positive and negative charges, which represents the polarity and the total charge of the fluidized bed. The net charge density can be calculated as the net charge of particles in each grid divided by the area of the grid.

Figure 5.8 presents the corresponding net charge density distribution of charged fluidized beds with various gas velocities at 3.4 s. It can be seen that the net charges of fluidized beds with various gas velocities are negative. A larger gas velocity causes a more dispersed and sparse net charge distribution. By comparing with Figure 5.7, the value of net charge density is much smaller than the corresponding positive charge density of the fluidized bed.

5.3.3. The charge accumulation

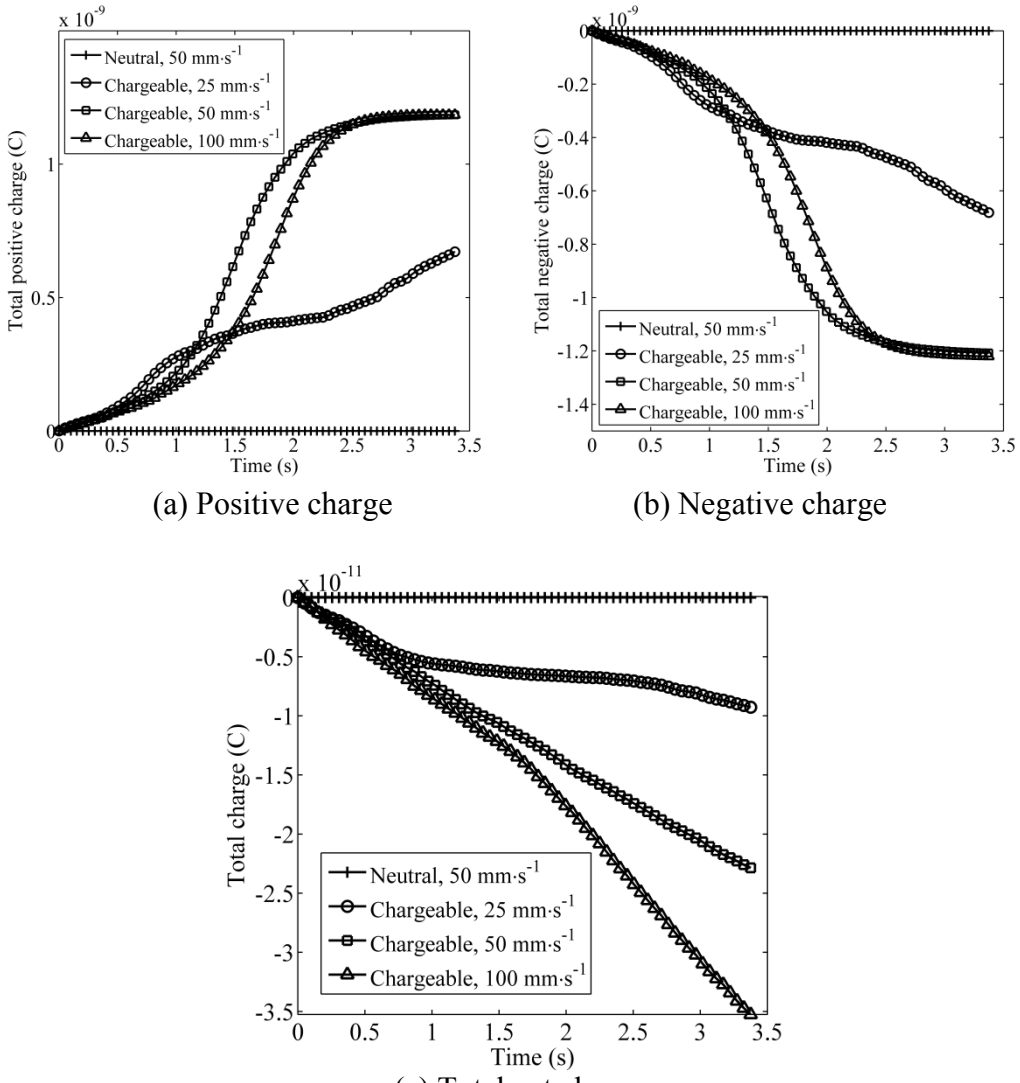

(a) Positive charge (b) Negative charge

(c) Total net charge

Figure 5.9 The charge accumulation during fluidization.

Figure 5.9 presents the charge accumulation of particles caused by contact electrification during fluidization. It is clear that for the fluidization with neutral particles, the net charge of particles remains zero, which indicates all particles are uncharged. The fluidizations with chargeable particles show different charging processes due to contact electrification. As shown in Figure 5.9a, initially, the positive charge of the fluidized bed with smaller gas velocity of 25 mm·s^{-1} increase faster than that with larger gas velocity (50 and 100 mm·s^{-1}). However, after a period of fluidization, the accumulation of positive charge of the groups with larger gas velocities becomes faster and exceeds the group with smaller gas velocity. The total negative charges in Figure 5.9b shows similar trends. The total net charges in all cases with contact electrification are negative (Figure 5.9c). In addition, the total net charge increases faster with a larger superficial gas velocity.

5.3.4. The performance of fluidization

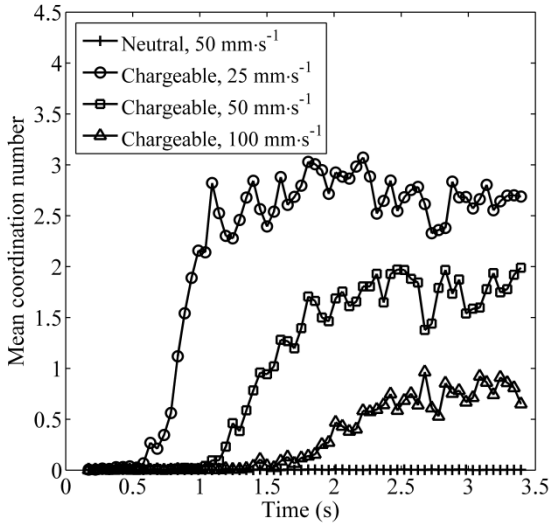

Figure 5.10 Mean coordination number during fluidization.

Figure 5.10 shows the mean coordination number of the fluidized bed during fluidization. For the fluidized bed without contact electrification, the coordination number is nearly zero, which indicates that the granular bed is fully dispersed and fluidized at the superficial gas velocity of 50 mm·s^{-1}. However, for the fluidized bed affected by contact electrification and electrostatic interactions, the coordination number gradually increases during fluidization. Moreover, when a small gas velocity is used, a faster increase and a larger coordination number are induced, implying that the particles retain a larger number of contacts during fluidization at a smaller superficial gas velocity.

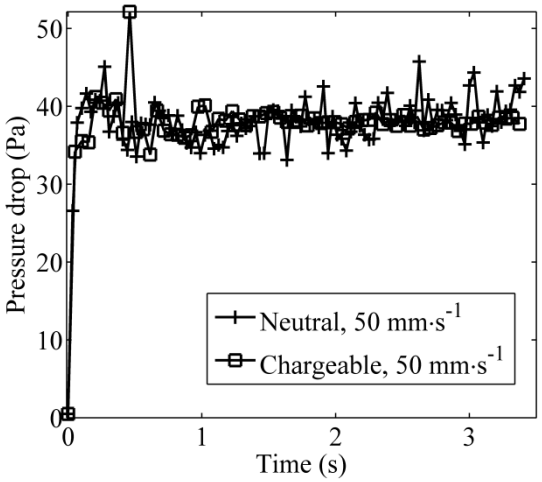

Figure 5.11 A comparison of the pressure drop between fluidizations with neutral and chargeable particles with v_g = 50 mm·s^{-1}.

The pressure drop of the fluidization, which can be used to identify the quality of the fluidization, is defined as the pressure different between the pressure of the input gas at the base of the fluidized bed and the pressure of the outflow gas at the top of the fluidized bed.

Figure 5.11 shows the pressure drops of fluidized bed with the neutral and chargeable particles at a superficial gas velocity of 50 mm·s^{-1}. It can be seen that, for both cases, the pressure drop increases rapidly to a plateau once the gas is injected. However, the pressure drop of the fluidized bed with neutral particles continues to fluctuate as the neutral particles are moving upwards and downwards in the fluidization. However, the pressure drop of the fluidized bed with chargeable particles becomes relatively steady, which indicates that the movement of the particles with the gas is relatively small.

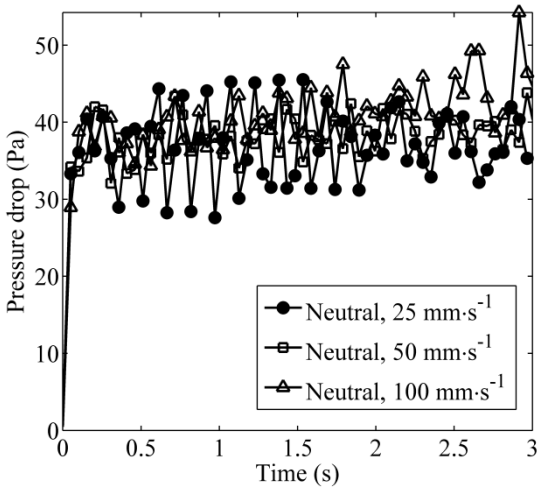

Figure 5.12 The pressure drops of fluidized beds with neutral particles at various gas velocities.

Figure 5.12 shows the pressure drop of the fluidized beds with neutral particles at various gas velocities. The evolution of the pressure drop for all cases shows a similar trend during fluidization. The pressure drop initially increases rapidly and then achieves a plateau. The pressure drop keeps fluctuating due to the movement of the neutral particles.

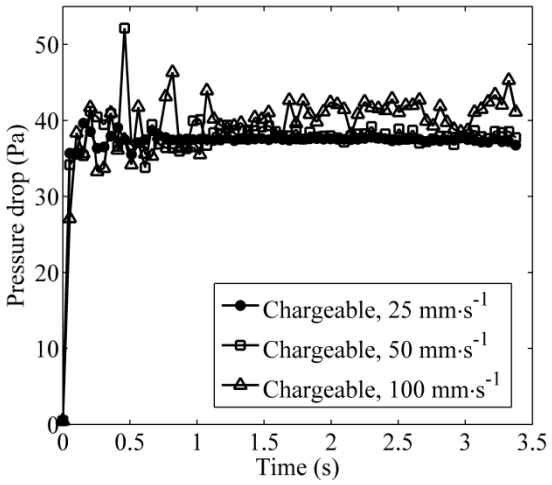

Figure 5.13 The pressure drops of fluidized beds with chargeable particles at various gas velocities.

Figure 5.13 shows the pressure drops of fluidized beds with chargeable particles at various gas velocities. For all case, the pressure drop shows a similar trend to that shown in Figure 5.11. For the cases with smaller gas velocities (25 and 50 mm·s^{-1}), the pressure drop rapidly increases to a plateau. However, the case with a higher gas velocity of 100 mm·s^{-1} shows a fluctuating pressure drop during the fluidization, indicating that particles are moving with the gas at this gas velocity.

5.4. Discussions

5.4.1. The charging process during fluidization

Since two types of particles with different work function potentials are used, both positive and negative charges are observed in the fluidized bed affected by contact electrification and electrostatic interactions. During a contact, the particles with a higher work function will be

charged negatively and those with a lower work function are positive. At the initial stage of fluidization, the fluidized bed with a smaller gas velocity is less dispersed and has more contacts between particles than the fluidized bed with a larger gas velocity, which leads to a faster increase in the total positive (negative) charge. However, as the charge accumulates on the particles, the electrostatic interactions become stronger and force particles to form agglomerates. The interactions become so strong that the gas with a small velocity (25 $mm \cdot s^{-1}$) cannot disrupt the agglomerates (Figures 5.6a and 5.10). Due to the agglomeration, fewer collisions occur between particles and the charge transfer is also reduced for particles within the agglomerate. Thereafter, the positive (negative) charge accumulation becomes slower for the case with smaller gas velocity (25 $mm \cdot s^{-1}$) than those with larger gas velocities which can still break the agglomerates and fluidize the granular bed. The charging process during fluidization with bi-charged particles varies with the particle properties (e.g. work functions) and the operating conditions (e.g. gas velocity) due to the combined effects of the contact electrification and electrostatic interactions. However, for fluidization with mono-charged particles without considering the electrostatic interactions (Chapter 3), the charging process shows an exponential trend. Therefore, the sensitivity of the charging process to the combined effects of the contact electrification and electrostatics requires further investigation.

5.4.2. Agglomeration during fluidization

The bi-charged particles can form agglomerates during fluidization. The size and the breakage of the agglomerates are determined by the superficial gas velocity. A larger gas velocity can lead to a larger impact velocity between agglomerates and result in the disruption of the agglomerates as shown in Figure 5.6. Hence, the corresponding coordination number is

smaller with a larger gas velocity as shown in Figure 5.10 indicating that a smaller number of particles adhere to each other. Moreover, the size of the agglomerate with a larger gas velocity will be smaller.

5.4.3. The performance of fluidization

Contact electrification and the induced electrostatic interaction can affect the overall performance of the fluidization. As can be seen from Figure 5.2, a superficial gas velocity of 50 $mm \cdot s^{-1}$ can fully fluidize the granular bed. However, the particles affected by contact electrification and the induced electrostatic interaction cannot be fully fluidized as shown in Figure 5.3 and Figure 5.6b. The phenomena are also reflected by the fluctuation of the pressure drop. When particles are fluidized and moving with the gas bubbles, the pressure drop that is induced for accelerating and moving the particles can be fluctuating. However, for charged particles with a smaller gas velocity, the agglomerates are too large to be lifted by the gas. As a result, the gas can only flow through the channels formed by the agglomerates, which leads to a steady gas flow and a steady pressure drop rather than a fluctuation. The larger gas velocity (100 $mm \cdot s^{-1}$) can disrupt the agglomerates and fluidize the granular bed, which needs extra energy and cause a large pressure drop as shown in Figure 5.13.

5.4.4. The charge distribution

The charge distribution can also be affected by different fluidization behaviours with different gas velocities. A small gas velocity (25 $mm \cdot s^{-1}$) cannot fully fluidize the particles due to the combined effects of contact electrification and electrostatics. Due to the agglomeration, the

movement of particles at the base are restricted by the electrostatic forces and the gravity of the granular bed. Therefore, the charge density at this area is much smaller as shown in Figure 5.7a. A larger gas velocity (50 $mm \cdot s^{-1}$) can maintain the fluidization longer as indicated by the coordination number in Figure 5.10, which makes the charge transfer in the fluidized bed more uniformly (Figure 5.7b). When the gas velocity is 100 $mm \cdot s^{-1}$, the gas can break the agglomerates of charged particles and drag particles and agglomerates to move. Thus, the charge distribution is much sparse in the fluidized bed.

5.4.5. The effect of the column

The material properties, especially work function, of the column can also affect the charging process during fluidization. According to Eqs (3.1) and (3.7), the total potential difference between the particle and the column surface will eventually become zero if there are sufficient contacts between the particle and the container. Since the work function potentials of the particles are higher than the work function potential of the column, the total charge of the granular bed is negative. In addition, with a larger superficial gas velocity, particles have a greater probability of making contact with the column and therefore have a larger total net charge. However, the agglomerates restrict the movement of the particles and reduce the contact number between the particle and the column. The increase of the total charge is very slow and the absolute value of the total charge is much smaller than the total positive charge as shown Figure 5.9, especially for the cases with smaller gas velocities. Moreover, it can be seen that a layer of agglomerates is generated and attracted along each side of the column because of the contact electrification and image force between the particle and the column, which will decrease and prevent further charge transfer from the container to the particle.

Therefore, it will take a much longer time (if possible) to achieve the theoretical equilibrium state of the total charge as stated by Eq. (3.8) and (3.12) in this study.

5.5. Summary

The DEM model with contact electrification and electrostatic interactions is used to simulate the electrostatic behaviour and to analyze the fluidization. Particles with two different work functions and different superficial gas velocity are considered. It is found that the fluidization process can be affected by contact electrification and electrostatic interactions. In addition, different gas velocities can produce different charging processes and agglomeration processes, which subsequently lead to different fluidizing behaviours.

Particles with different work functions are charged positively and negatively. The charged particles form agglomerates, which can compromise the fluidization process. A charged granular bed with a smaller gas velocity cannot be fluidized because of the presence of agglomerates. A larger gas velocity can break the agglomerates and drag the primary particles to move in the fluidized bed, which leads to a larger charge accumulation and a sparse charge distribution. Moreover, the particles with charges are more dense and concentrated in the granular bed when a smaller gas velocity is used.

The difference in work functions between the column and the particles can also affect the particle charging behaviour. Further analysis and discussion of these phenomena should be implemented.

CHAPTER 6 MULTI-SPHERE METHODS FOR CONTACT ELECTRIFICAITON

6.1. Introduction

Generally, real particles have complex shapes. The particle shape can affect the contact electrification process during powder handling processes. In this chapter, both symmetric and sphere-tree multi-sphere methods are used to study the contact electrification process with irregular particles.

6.2. Contact electrification and charge distribution of elongated particles

6.2.1. Introduction

In this section, contact electrification of elongated particles is modelled using the symmetric multi-sphere method. The effect of the particle shape on charge distribution and accumulation is explored during the contact electrification process in a vibrating container. Some of the results presented in this section have been published in Pei *et al.* (2013a)

6.2.2. The DEM model

In this study, elongated particle shapes are approximated using a symmetric multi-sphere model (Favier *et al.*, 1999) in which the particle is assembled with a row of primary spheres

of various sizes having negligible overlaps (i.e. smaller than 5% of the sphere radius). Thus the mass and moment of inertia of the particle can be calculated as a summation of all primary spheres. Contact detection and contact force calculation are based on each of primary spheres. The contact between particles is detected between constituent primary spheres as shown in Figure 6.1.

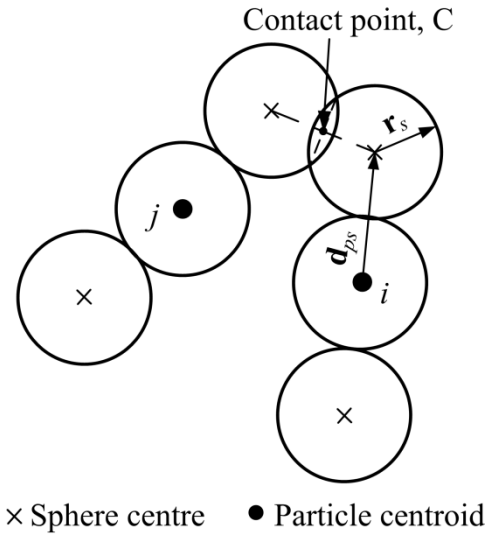

Figure 6.1 Contact detection between two particles with constituent primary spheres.

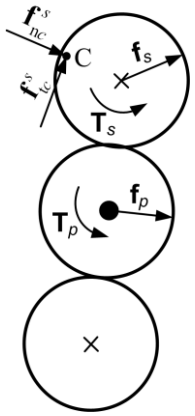

Figure 6.2 Illustration of Force calculation and integration of the multi-sphere particle *i*.

Contact forces and moments between primary spheres within different particles will be calculated as illustrated in Figure 6.2 once the contacts between these primary spheres are

determined as shown in Figure 6.1. For elastic particles, the normal contact is modelled using Hertz theory (Johnson, 1985), and that of Mindlin and Deresiewicz (1953) is employed for the tangential interaction. The contact forces and moments are integrated on each primary sphere as:

$$\mathbf{f}_s = \sum_{c=1}^{n_c} \left(\mathbf{f}_{\mathrm{nc}}^s + \mathbf{f}_{\mathrm{tc}}^s \right) \tag{6.1}$$

$$\mathbf{T}_s = \sum_{c=1}^{n_c} \left(\mathbf{r}_{sc} \times \mathbf{f}_{\mathrm{tc}}^s \right) \tag{6.2}$$

where $\mathbf{f}_{\mathrm{nc}}^s$ and $\mathbf{f}_{\mathrm{tc}}^s$ are the normal and tangential contact force at contact point c on the primary sphere s; $\mathbf{r}_{sc}$ is the vector from the centre of the primary sphere to the contact point c; n_c is the total number of contacts for the primary sphere s; $\mathbf{f}_s$ and $\mathbf{T}_s$ are the resultant force and moment of the primary sphere s, respectively.

The force and toque acting on each primary sphere are then integrated onto the particle centroid as:

$$\mathbf{f}_p = \sum_{s=1}^{n_p} \mathbf{f}_s \tag{6.3}$$

$$\mathbf{T}_p = \sum_{s=1}^{n_p} \left(\mathbf{d}_s \times \mathbf{f}_s + \mathbf{T}_s \right) \tag{6.4}$$

where $\mathbf{d}_s$ is the vector from the particle centroid to the centre of the primary sphere s; n_p is the total number of primary spheres of the particle p; $\mathbf{f}_p$ and $\mathbf{T}_p$ are the resultant force and moment of the particle. The translational and rotational motion of the particle are determined using Newton's second law of motion.

The contact electrification model (Pei *et al.*, 2013a, 2013b) was implemented to analyze the charge transfer process during collisions. According to the condenser model, the charge transfer is due to the total potential difference (Eq. (3.1)). For multi-spheres, the charge transfer process is based on the primary spheres in this study. The induced potential difference V' is assumed to be only affected by the charge on the primary spheres in contact. Therefore, according to Eq. (3.2), the induced potential difference V' between the conductive surface and the primary sphere is rewritten as:

$$V' = k_0 q_s = \frac{z}{4\pi\varepsilon_0 r_s^2} q_s \tag{6.5}$$

where

$$k_0 = \frac{z}{4\pi\varepsilon_0 r_s^2} = \frac{z}{\varepsilon_0 A_s} \tag{6.6}$$

where r_s and A_s are the radius and surface area of the primary sphere, ε_0 is the permittivity in vacuum (8.854×10^{-12} F·m^{-1}), z is the gap of tunnel relaxation and is generally of the order of a few nanometers to hundreds of nanometers (Lowell and Roseinnes, 1980). z is assumed to be 260 nm in this study.

If two charged primary spheres of insulating materials are considered, the induced potential difference between them at a given separation distance can be determined as:

$$V' = \frac{z}{4\pi\varepsilon_0}\left(\frac{q_{sj}}{r_{sj}^2} - \frac{q_{si}}{r_{si}^2}\right) \tag{6.7}$$

where q_{si} and q_{sj} are the charges of the primary spheres i and j; r_{si} and r_{sj} are the radii of primary spheres, i and j. The transferred charge on primary spheres in each contact can then be calculated by Eq. (3.6). The effects of the net charge on remote primary spheres that are not in the underlying contact are ignored (Matsuyama *et al.*, 2003). In addition, as the

particles are assumed to be perfect insulators, each primary sphere will retain the acquired charges and the charge redistribution and relaxation and electrostatic interactions are also ignored.

6.2.3. Model setup

Contact electrification of elongated particles in a vertically vibrating container (Figure 6.3) is analyzed using the developed DEM model. Initially, 50 randomly generated particles are deposited onto the base of the cubic container with a side length of 1 mm until the kinetic energy of the particle system becomes negligible (i.e. maximum velocity is less than 1×10^{-6} $m\cdot s^{-1}$). Then the container starts to vibrate in the y direction with a specified velocity profile as:

$$v_b = v_a \sin(2\pi f t) \tag{6.8}$$

where v_a is the amplitude of the vibration velocity and is set to 1.0 $m\cdot s^{-1}$; f is the frequency and is assumed to be 500 Hz in this study. The simulation was terminated once the total charge of the particles reached the equilibrium state.

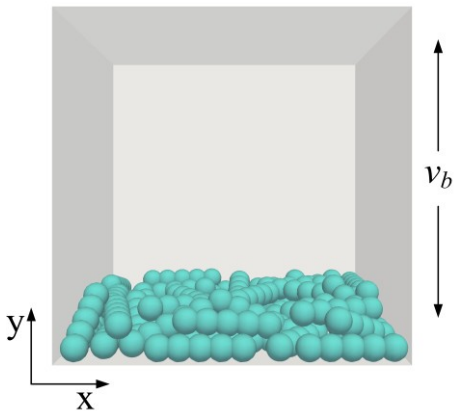

Figure 6.3 Model setup.

In this study, the elongated particles are modelled with an array of primary spheres of various sizes. 5 types of elongated particles are considered. A shape factor δ is introduced to quantify the particle shape and is defined as:

$$\delta = \frac{r_d - r_c}{\bar{r}} \tag{6.9}$$

$$\bar{r} = \frac{1}{n_g}\sum_{i=1}^{n_g} r_{si} \tag{6.10}$$

where r_d is the radius of the distal primary sphere, r_c is the radius of the central primary sphere, r_{si} is the radius of the primary sphere i and n_g is the number of size types considered, and $\bar{r}$ is the mean radius of each particle.

The shape factor can be used to characterise the particle concavity of the particle that is believed to be an important factor in determining the charge distribution during contact electrification. In other words, a negative shape factor indicates that the particle has a convex shape profile while a positive value is for a concaved profile. The shape factors and the radii of constituent primary spheres for the 5 types of particles considered are given in Table 6.1, and for each type of the particle, 3 types of sizes (n_g = 3) are chosen. The material properties of the primary spheres and the container are given in Table 6.2. Monosized spherical particles with a radius of 40 μm and same material properties are also considered for comparison.

The work function potentials of the particle, V_p, and the container, V_s, are 4.52 and 4.70 V respectively. The container is assumed to be conductive and the transferred charge will be dissipated instantaneously. The charge accumulation of the particle system and the charge distribution over each particle are analyzed in detail.

Table 6.1 A list of shaped particles

Elongated particles	r_{si} (i = 1, 2, 3, 4, 5) (μm)	$\bar{r}$ (μm)	δ
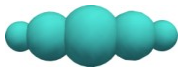	25, 40, 50, 40, 25	38.3	-0.65
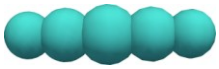	40, 45, 50, 45, 40	45	-0.22
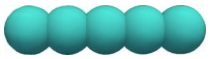	40, 40, 40, 40, 40	40	0
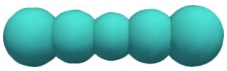	50, 45, 40, 45, 50	45	0.22
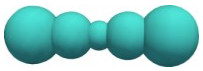	50, 40, 25, 40, 50	38.3	0.65

Table 6.2 Material parameters of the particle and the container.

	Particle	Container
Elastic modulus, Y (Pa)	8.7×10^{9}	2.1×10^{11}
Poisson's ratio, v	0.3	0.3
Density, ρ_p (kg·m^{-3})	1.5×10^{3}	7.9×10^{3}

To quantify the charge distribution over the particle, the mean charge ratio of a primary sphere i is defined as:

$$\varphi_i = \frac{\bar{q}_{si}}{\bar{q}} \tag{11}$$

where $\bar{q}_{si}$ is the mean charge of the primary spheres with the same index i; $\bar{q}$ is the mean charge of the particles.

The charge variation is defined as the charge difference between the distal primary sphere and the central primary sphere, which can be used to characterize the variation of the charge distribution on the particle. For the current particle system, the mean charge variation is determined as:

$$q_v = \frac{\sum_{i=1}^{N} \Delta q_{si}}{N} = \frac{\sum_{i=1}^{N} (\bar{q}_{di} - q_{ci})}{N} \tag{12}$$

where $\bar{q}_{di}$ is the mean charge of the two distal spheres of particle i; q_{ci} is the charge of the central sphere of particle i, N is the number of particles.

The surface charge density of a primary sphere can be defined as the charge of the primary sphere divided by its surface area, $\sigma_s = q_s/A_s$, which is used to quantify the surface charge distribution on the particle. In the current study, the mean surface charge difference can be defined as:

$$\sigma_v = \frac{\sum_{i=1}^{N} \Delta \sigma_{si}}{N} = \frac{\sum_{i=1}^{N} (\bar{\sigma}_{di} - \sigma_{ci})}{N} \tag{6.13}$$

where $\bar{\sigma}_{di}$ is the mean surface charge density of two distal primary spheres of particle i; σ_{ci} is the surface charge density of the central primary sphere of particle i.

6.2.4. Results

6.2.4.1 Particle profiles

Figure 6.4 shows a typical charge distribution on each primary sphere during vibration with particles of $\delta = 0.0$ at various time instants. The charge acquired during the deposition process is negligible as shown in Figure 6.4a. The particles vibrate with the container and gradually get charged. During vibration, the charge is accumulated on each primary sphere. Especially, at the earlier stage of the vibration (Figure 6.4b and 6.4c), the distal spheres generally accumulate more charges than the central ones. The charge on all primary spheres eventually

reaches a maximum value corresponding to the equilibrium state is reached when all particles possess their equilibrium charges (Figure 6.4d).

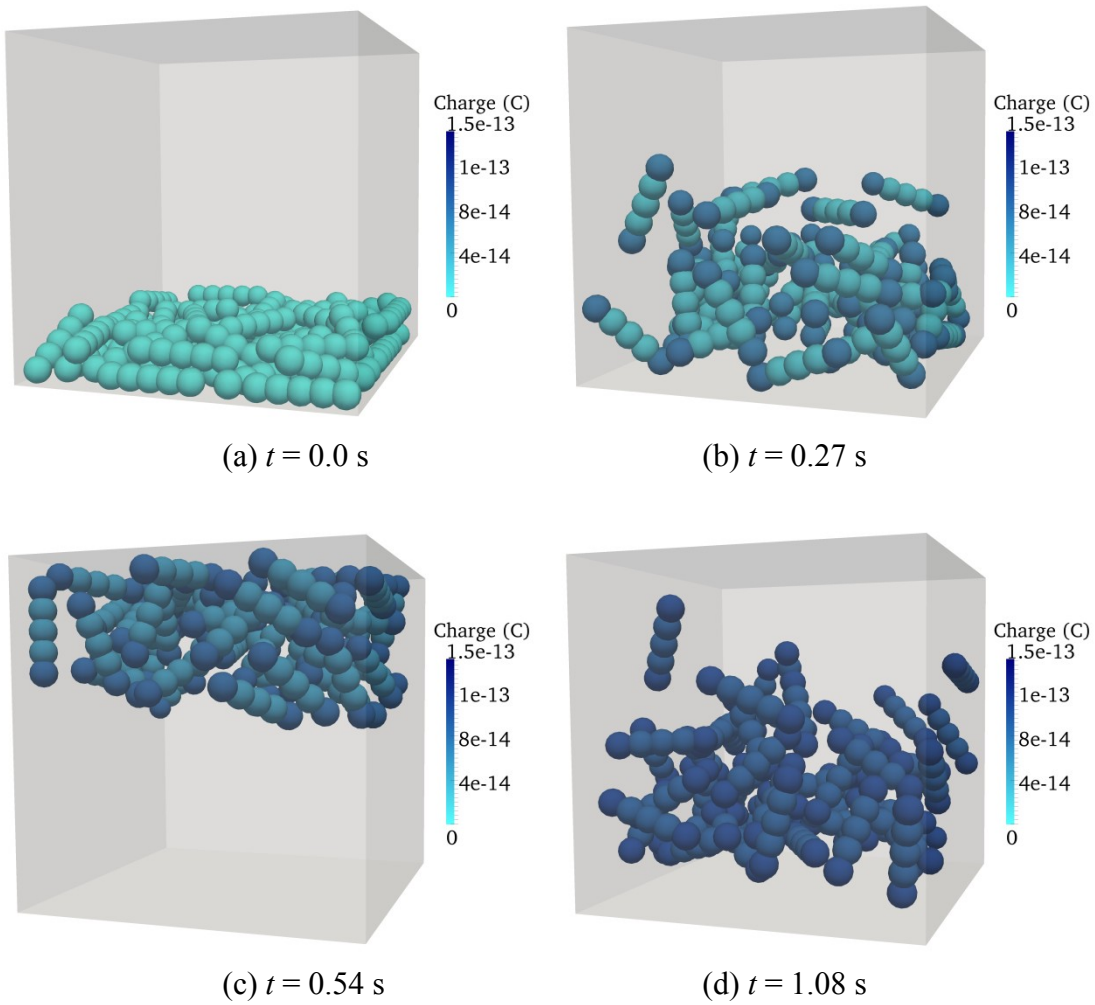

(a) $t = 0.0$ s (b) $t = 0.27$ s

(c) $t = 0.54$ s (d) $t = 1.08$ s

Figure 6.4 Charge distributions for the particles of $\delta = 0.0$ at various time instants.

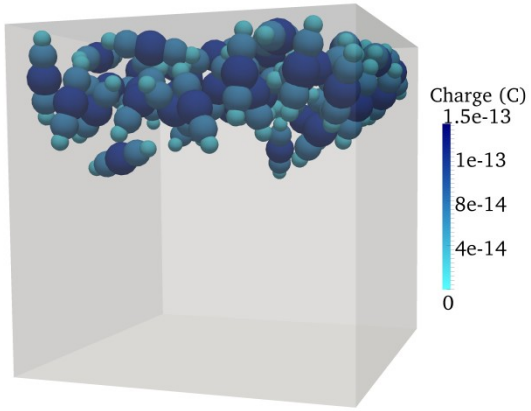

(a) δ = -0.65

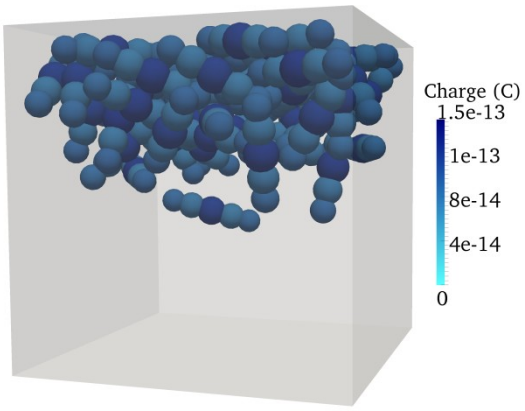

(b) δ = -0.22

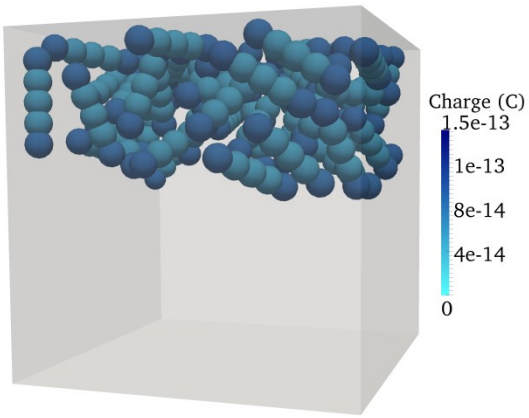

(c) δ = 0.0

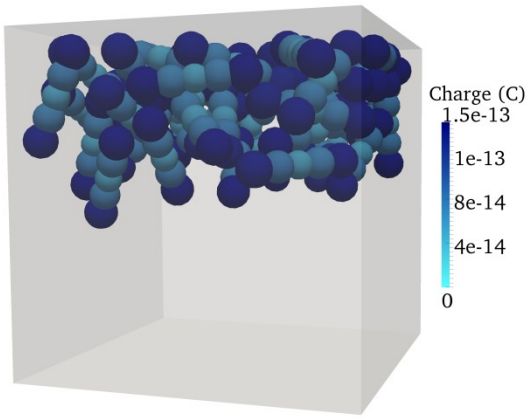

(d) δ = 0.22

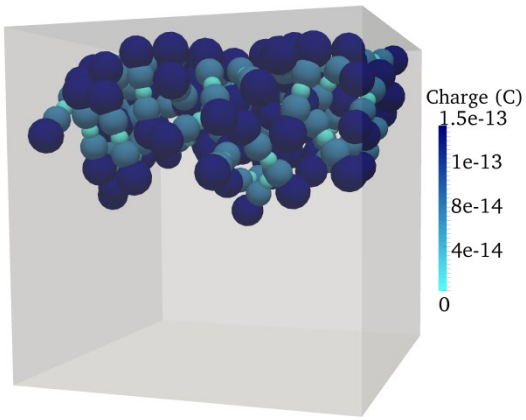

(d) δ = 0.65

Figure 6.5 Charge distributions for various shaped particles at t = 0.54 s.

Figure 6.5 shows the charge distribution over particles with different shape factors at t = 0.54 s. It is clear that the charge distribution varies with the particle shape. When the central primary sphere is larger than the distal sphere ($\delta < 0.0$), the central primary spheres acquire higher charges as shown in Figures 6.5a and 6.5b. For other cases, the distal spheres tend to have more charge than the central sphere, especially for $\delta > 0.0$.

6.2.4.2 The charge distribution and accumulation

Figure 6.6 gives the mean charge ratio over the particles of different shape factors corresponding to Figure 6.5. It can be seen that when $\delta < 0.0$, the charge ratio is larger on the central spheres than the distal spheres. For the particles of $\delta > 0.0$, the larger charge ratio occurs on the distal spheres. It is noticeable that for $\delta = 0.65$, the charge ratio of the central sphere is nearly zero. Therefore, the larger primary sphere generally possesses more net charge over the particle.

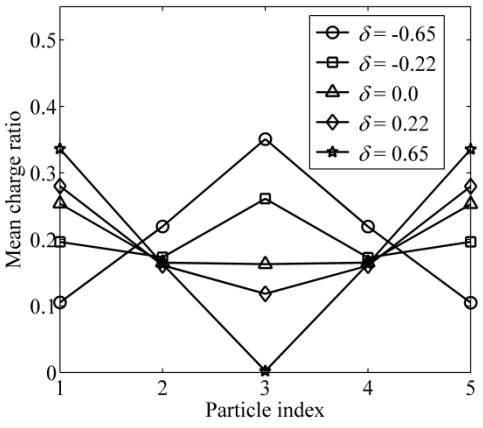

Figure 6.6 Mean charge ratio of primary spheres over the particles of different shape factors.

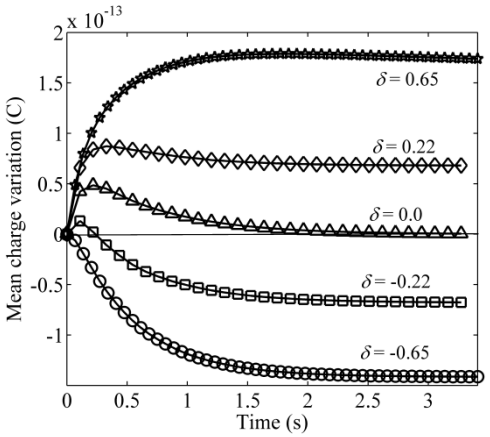

Figure 6.7 Evolutions of charge variation on various elongated particles.

The evolution of the mean charge variation on various elongated particles is shown in Figure 6.7. For particles with $\delta > 0$, the charge variation is positive, i.e., the net charge on the larger distal sphere is higher than that on the smaller central sphere. The charge variation gradually becomes larger and eventually achieves an equilibrium value during the vibration. In addition, the charge variation for $\delta = 0.65$ is larger than that for $\delta = 0.22$. In the case of $\delta = 0$, the charge variation is also positive at the earlier stage of the vibration. However, the charge variation achieves zero during the vibration. When the distal sphere is smaller than the central sphere ($\delta < 0$), the charge variation is negative, which means that the net charge is higher on the central sphere. For both cases of $\delta < 0$, the charge variations achieve equilibrium values and the value of the charge variation is larger with $\delta = -0.65$. Generally, the larger primary spheres acquire higher net charge, irrespective of their relative position. Furthermore, the charge variation becomes larger during the vibration and eventually achieves an equilibrium value.

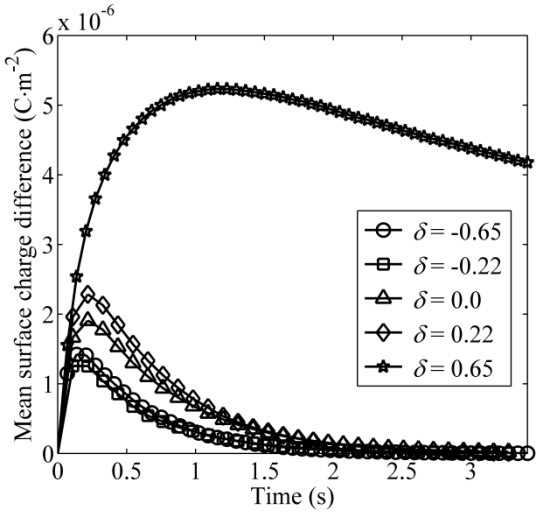

Figure 6.8 Surface charge difference for various shaped particles.

Figure 6.8 shows the mean surface charge difference for various shaped particles during the vibrating process. For all particles, the evolution of surface charge difference is similar. The surface charge difference increases initially and reaches a maximum value. Then it decreases to zero except for the particles with δ = 0.65, for which there still is a surface charge difference at the end of the vibration. In addition, a larger δ leads to a higher surface charge difference during the entire vibrating process. This indicates that the distal primary sphere has a higher surface charge density than the central sphere at the beginning and the surface charge difference is larger when δ is larger. Eventually the surface charge density becomes equal between the distal and central spheres except for the particle with δ = 0.65.

Figure 6.9 shows the charge accumulating for various shaped particles during the vibrating process. For all cases, the charge gradually accumulates on the particles and eventually achieves an equilibrium value. However, the equilibrium charge varies with the shape factor. Specifically, the particles with δ = - 0.22 and 0.22 acquire higher equilibrium charges, while the particles with δ = - 0.65 possess the lowest equilibrium charge.

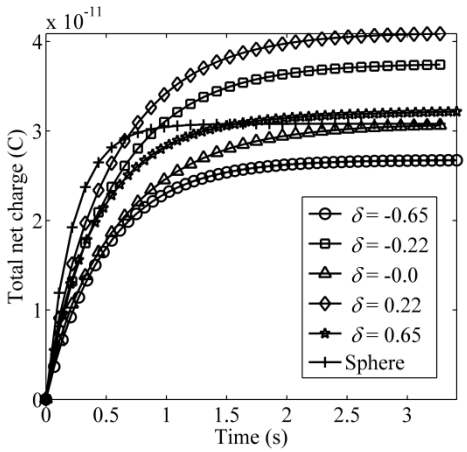

Figure 6.9 Charge accumulating processes of various shaped particles.

6.2.5. Discussions

In the current study, the charge distribution is obtained on the basis of the net charge on each primary sphere. The transferred charge on each primary sphere depends on the contact rate that is defined as the total contact number in a unit time. The contact rate on each primary sphere depends on the orientation and shape of the particle during collisions.

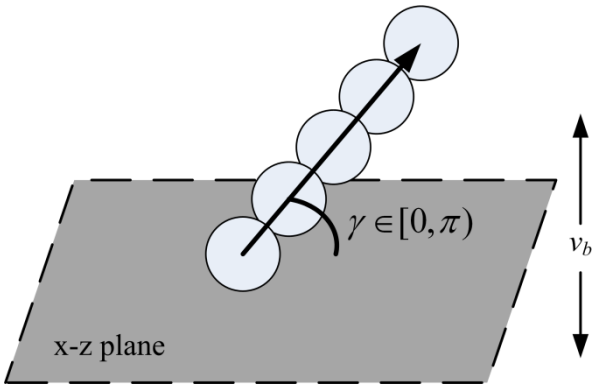

Figure 6.10 An illsutration of the orientation of the elongated particle.

An anisotropy distribution graph is used to explore particle orientation during vibration. The inclination angle between the elongated particle and the lower surface (x-z plane) during the vibration are first calculated as shown in Figure 6.10. If the x component of the vector of the elongated particles lies in the x direction, the angle is in the interval of [0, π/2]. Otherwise (in –x direction), the angle is in the interval of [π/2, π]. As the angle is restricted in an interval of [0, π], i.e. $0 \leq \gamma \leq \pi$, the interval is divided into 12 sub-intervals. For each particle, its inclination angle to the lower surface should be within one of the sub-intervals. Conversely, the number of particles in each sub-interval can be counted. Consequently, the anisotropy distribution can be defined in a polar coordinate system as 12 triangular sections from 0 to π. The angle of each triangular section is the angle of each sub-interval and length of each triangular section is the number of particles in each sub-interval. For the vibrating process, the number of particles in each section is defined as the mean number of particles in each section over all time instants, which gives the mean anisotropy distribution of particles. From Figure 6.4a, it can be seen that all particles tend to align with the bottom surface after deposition. To eliminate the effect of this initial orientation of particles, the calculation of the mean anisotropy distribution is started from the time when all particles are fully activated and start to accumulate charge (t >0.34 s). This corresponds well with Figures 6.7 and 6.9 due to relatively long vibration time (t > 3 s).

Figure 6.11 shows the mean anisotropy distribution of the particles with different shape factors. It can be seen that similar orientation patterns for all particles are observed. The orientation of most particles concentrates in the triangular sections that are parallel to the lower wall, e.g. [0, π/12] and [11π/12, π]. For instance, in Figure 6.10c (δ = 0.0), most of the particles are within the two sections of [0, π/12] and [11π/12, π]. This indicates that most of

the elongated particles tend to align perpendicular to the vibrating direction. This is because the elongated particles rotate during impacts, especially against the upper and lower walls of the container. Because particles have large aspect ratios, the elongated particles will rotate towards the impact surface. In addition, the acceleration of the container can force the particles to incline towards the impact surface as shown in Figure 6.5.

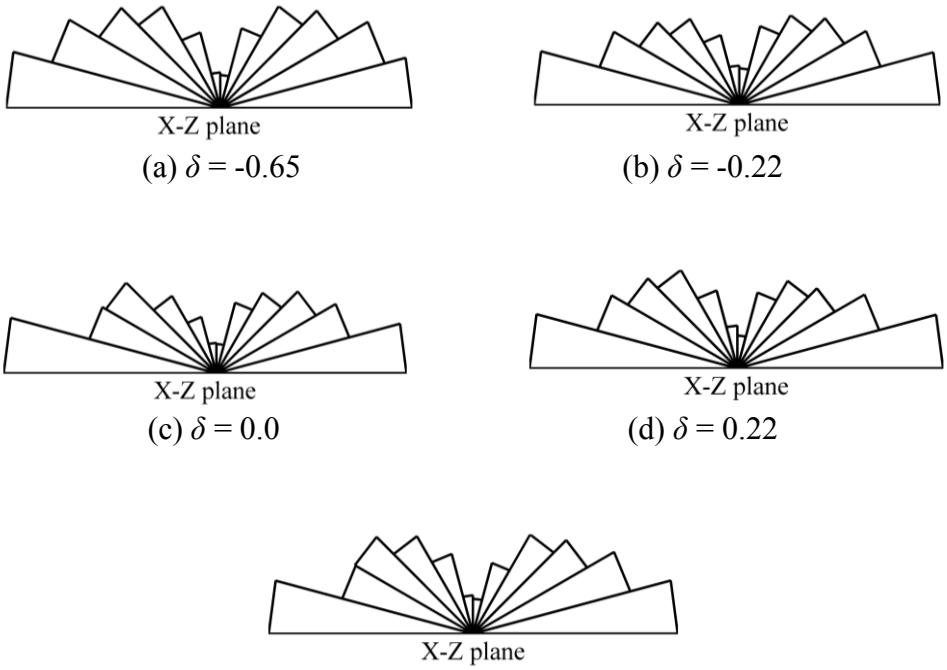

(a) δ = -0.65 (b) δ = -0.22

(c) δ = 0.0 (d) δ = 0.22

(e) δ = 0.65

Figure 6.11 Particle orientations of various particles.

To evaluate the contact rate, the total number of contacts on each primary sphere with other surfaces and particles is obtained in the DEM simulations. Then the mean contact rate of the primary sphere can be obtained as:

$$\tau_c = \frac{\bar{c}_i}{t} \tag{6.14}$$

where $\bar{c}_i$ is the mean contact number on the primary spheres with the same index i and t is the vibration time. Then the contact rate difference can be defined as the difference of mean contact rate between the distal sphere and the central sphere.

Figure 6.12 shows the mean contact rate of the distal and central spheres for various particles. It can be seen that the mean contact rate varies with the particle shape. For particles with δ = -0.65, the contact rate of the central sphere is greater than that of the distal sphere. The particle has a larger central primary sphere and tends to align with the lower surface as shown in Figure 6.11. Thus the central sphere makes more contacts with the lower surface. However, as δ increases, the contact rate of the central sphere decreases and the contact rate of the distal sphere increases, especially when the distal sphere is larger than the central sphere. For instance, the contact rate of the central sphere in the group with δ = 0.65 is nearly zero. This indicates that the larger distal spheres (as larger δ) contact with the surface and other particles more frequently.

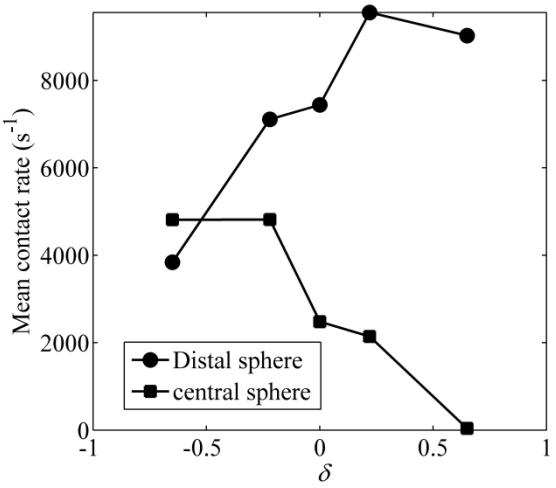

Figure 6.12 Mean contact rate during the vibration.

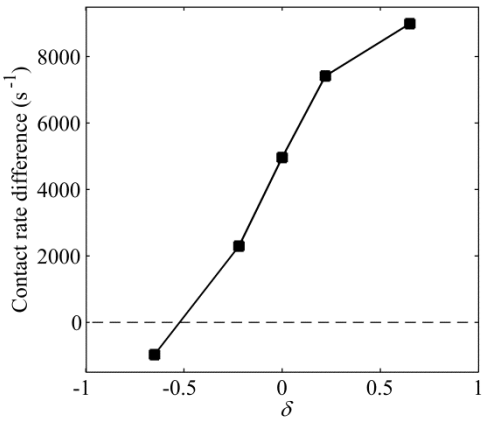

Figure 6.13 Contact rate difference of various particles.

Figure 6.13 shows the contact rate difference between the distal primary sphere and the central primary sphere of various particles. It is clear that the value increases as the shape factor increases, which is consistent with Figure 6.12.

Under similar impact conditions (i.e. the vibrating velocity and frequency), spheres with more contacts tend to accumulate a greater net charge. Consequetly, the central sphere with a larger size ($\delta < 0$) acquires a larger net charge than the distal sphere as shown in Figure 6.7. When the distal sphere is larger than the central sphere and makes more contacts with other objects, more net charge is concentrated on the distal sphere. Especially for the group of $\delta = 0.65$, the contact rate of the central sphere is nearly zero, indicating that the central sphere has a small probability of making contact with other objects and is unable to reach its equilibrium state. This eventually leads to a larger surface charge difference as shown in Figure 6.8 and a lower value of net charge for this group of particles as shown in Figure 6.9.

In the case of the surface charge density, all particles have a larger surface charge density on the distal compared to the central sphere as shown in Figure 6.8 at the earlier stage of the

vibration. However, the particles with larger distal spheres have a higher surface charge density at the distal sphere than the groups with smaller distal spheres, as a result of a greater contact rate. According to the contact electrification model (Pei *et al.*, 2013a, 2013b), the net charge on spheres will eventually achieve an equilibrium value and the surface charge density will be the same for spherical particles with different sizes and same material properties. Thus for particles with $\delta \neq 0.65$ as shown in Figure 6.8, the distal spheres will eventually have the same surface charge density as the central spheres. For the particles with $\delta = 0.65$, the contact rate of the central sphere is sufficiently small that the charge on the central sphere cannot achieve an equilibrium state. Therefore, the surface charge difference of this group is still large at the end of the vibrating process. It is clear that the shape of the particle can affect the charge acquisition and distribution.

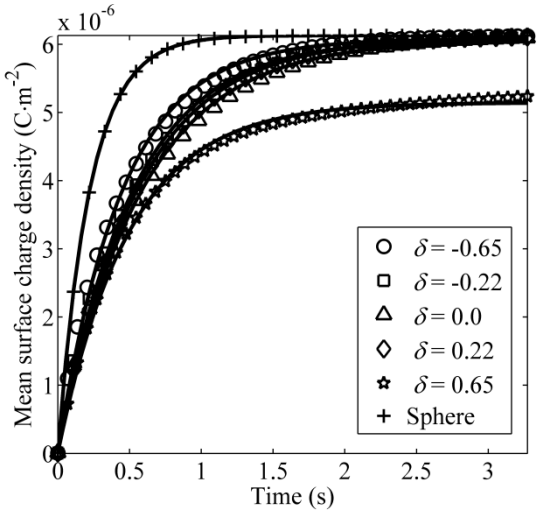

Figure 6.14 The evolution of mean surface charge density for various particle.

To study the surface charge density of a particle, a mean surface charge density can be defined as:

$$\sigma_p = \frac{1}{n_p}\sum_{s=1}^{n_p}\sigma_s \tag{6.15}$$

where n_p (= 5) is the number of primary spheres. According to Eq. (3.6), the transferred charge in each collision is linear with the net charge on the particle. Also the net charge can achieve an equilibrium value as shown in Figure 6.9. Consequently, based on first order kinetics and Eq. (3.6), the mean surface charge density during the vibration can be defined as a function of time as follows:

$$\sigma_p = \sigma_{p0}e^{-k_c t} + \sigma_{p\infty}\left(1 - e^{-k_c t}\right) \tag{6.16}$$

where σ_{p0} and $\sigma_{p\infty}$ are the initial mean surface charge density and the equilibrium mean surface charge density and k_c is the charging coefficient.

Figure 6.14 shows the mean surface charge density of various particles during the vibration process. The solid lines are the fitting lines of Eq. (6.16). It can be seen that the mean surface charge density of various particles gradually increases and eventually achieves an equilibrium value except for particles with δ = 0.65. The equilibrium value of particles with δ = 0.65 are relatively smaller, as the central primary spheres are unable to accumulate charge due to the small number of contacts. The charging process of the elongated particles can be closely represented by the exponential relationship.

Table 6.3 The charging coefficients for various particles

δ	k_c
-0.65	2.23
-0.22	1.92
0.0	1.73
0.22	1.82
0.65	2.01

The charging coefficient, k_c, can be used to determine how fast the charging process achieves equilibrium as given in Table 6.3. It can be seen that the charging rate coefficient depends on the shape factor, i.e. the particle shape. The particles with δ = - 0.65 and - 0.22 have larger charging rate coefficients than those with δ = 0 and 0.22. This is because the surface charge differences between the particles with δ = -0.65 and -0.22 are smaller and achieve zero faster than those with δ = 0 and 0.22 (Figure 6.8), indicating that the surface charge density of the particles with δ = - 0.65 and - 0.22 reach steady state faster. In addition, for the case with δ = 0.65 the charging rate coefficient is relatively larger due to the lack of charge on the central primary sphere as shown in Figure 6.8.

It should be noted that the current DEM model is based on the following assumptions : 1) for the elongated particle, the net charge is assumed to be located on the centres of primary spheres; 2) there is no relaxation across the particle and dissipating into the environment. Under realistic conditions, the charge should be distributed on the surface of a particle and may be under relaxation and dissipation, especially for conductors. As for the contact electrification model, the effects of the environmental conditions are also ignored, such as the humidity and the temperature. In addition, since the net charge is accumulated on the particle, the electrostatic interactions can affect the dynamics of the particle and the subsequent charging process. These effects should be considered further.

6.2.6. Summary

In this study, a discrete element model is developed to study the charge distribution and accumulation on elongated particles in a vibrating container. The particle shape is modelled as

a row of primary spheres using the symmetric multi-sphere approach and the charging process is computed by the contact electrification model. Five types of particles are considered.

It is found that, although the charge accumulation process for various cases shows a similar exponential relationship during the vibration and eventually achieves an equilibrium state, the particle shape affects the charge distribution and the charge accumulation on the particles. In terms of charge distribution, the net charge is greater on the larger primary sphere for each case. Although the surface charge density is always larger on the distal primary sphere, at the earlier stage of the vibration, the surface charge difference between the distal primary sphere and the central sphere increases as the shape factor increases. The surface charge density eventually becomes equal between distal and central spheres except the case of $\delta = 0.65$. The central sphere of a particle with $\delta = 0.65$ cannot achieve an equilibrium surface charge density due to the small number of contacts, which leads to a large surface charge difference between the distal and central sphere even at the end of the vibration. It is also shown that the charging rates for the particles with $\delta = 0.65$ are different from the case with $\delta = -0.65$, due to the lack of charge on the central sphere. The cases with similar shapes ($\delta = -0.22$ to 0.22) have similar charging rates.

This study indicates that particle shape plays an important role in contact electrification. The developed discrete element model can be used to study the charge acquisition, distribution and accumulation process from single particle to the entire particle system.

6.3. Contact electrification of particle with arbitrary shape

6.3.1. Introduction

In this section, contact electrification of particles with arbitrary shapes is modelled using a sphere-tree multi-sphere method. The charge distribution and accumulation of the particles in a rotating drum is analyzed.

6.3.2. The DEM model

To study the effect of the particle shape on contact electrification, the particle shape is approximated using the sphere-tree multi-sphere method (Bradshow and O'Sullivan, 2002). The geometry of the particle can be represented by a 3D object (Figure 6.15). Then the surface of the particle is meshed into triangular elements and the particle is represented using a polyhedron (Figure 6.16). The sphere-tree construction toolkit (http://isg.cs.tcd.ie/spheretree/) developed by Bradshow and O'Sullivan (2004) is used to construct the particle (multi-sphere) with multiple primary spheres of various sizes to approximate the shape of the meshed particle.

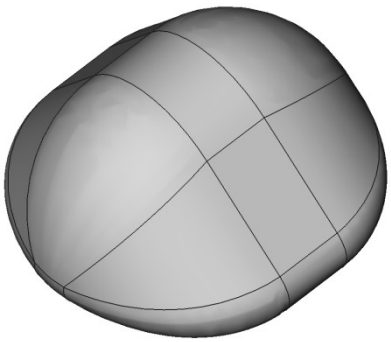

Figure 6.15 The geometry of a 3D particle.

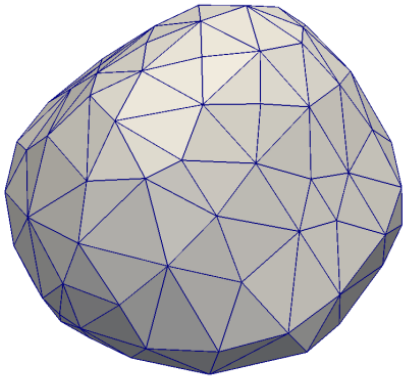

Figure 6.16 The particle represented by a polyhedron.

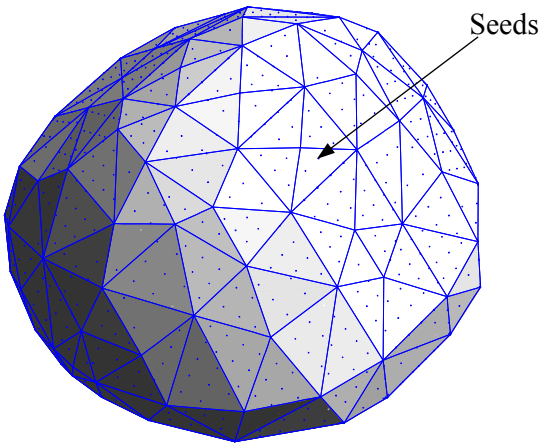

Figure 6.17 The sample seeds distributed on the surface of the particle.

The medial axis approximation method is used to generate a multi-sphere list of a number of primary spheres (Bradshow and O'Sullivan, 2004). First, the surface of the polyhedron is sampled with a number of seeds as shown in Figure 6.17. Secondly a Vornonoi diagram with connected cells is constructed such that each Voronoi cell represents the region of space that is closer to its corresponding seed than any other seeds. The boundary between the cells forms an approximation of the medial axis, which is considered as the topological skeleton of the particle shape. Then primary spheres can then be generated along the medial axis to fit the

surface seeds with optimum coverage, i.e. the smallest distance between the seeds and the surfaces of the primary spheres, as shown in Figure 6.18.

A merge optimization method is then used to control and reduce the number of primary spheres (Bradshow and O'Sullivan, 2004). In this method, each pair of neighbouring spheres are merged and approximated by a new parent sphere that should contain the same set of surface seeds covered by the child neighbouring pair. Once the set of parent spheres is generated, this method can be iterated until the desired number of primary spheres is reached as illustrated in Figure 6.19. This method is particularly useful for generating a small number of primary spheres that can be implemented into DEM simulations to save computational time. However, the accuracy for the geometric approximation of this method depends on the number of the primary spheres which can be seen by comparing Figure 6.18 with Figure 6.19. The relative error between the volumes of the multi-sphere and the polyhedron can be greater than 100% (Wang, *et al.*, 2006).

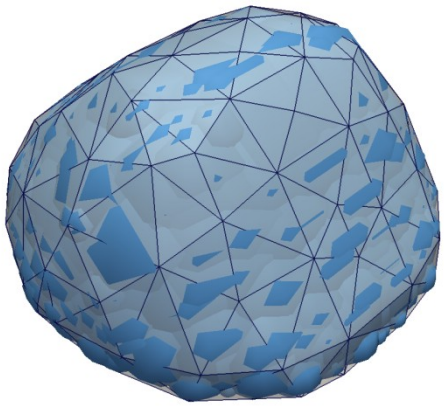

Figure 6.18 The multi-sphere generated with 500 primary spheres by the medial axis method.

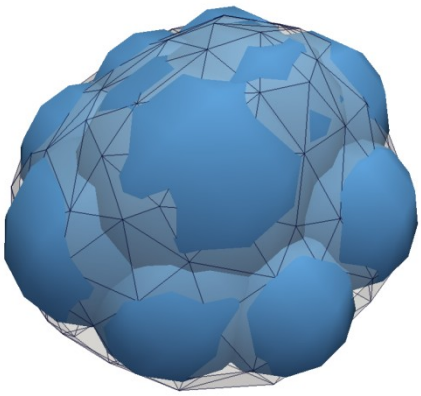

Figure 6.19 The multi-sphere generated with 10 primary spheres using merge optimization.

Due to the complex construction of primary spheres for a particle, it is difficult to determine the mass properties of the particles based on the multi-sphere model. As a first approximation, the mass properties of the particle can be calculated using the integral method developed by Mirtich (1996) with respect to triangular elements of the polyhedron. This integral method can be further reduced to three steps: line integral, projection integral and surface integral. The approach (http://www.cs.berkeley.edu/~jfc/mirtich/massProps.html) developed by Mirtich (1996) is used to calculate the mass properties of the polyhedron (particle), i.e. the location of the mass centre, the volume, and the inertia properties (principle moments of inertia and principle axes of inertia).

Each particle, once the multi-sphere (list of primary spheres) is constructed, can be imported into the DEM codes for further analysis. The connection (overlap) between primary spheres is considered as rigid. The contact detection and interaction is based on the primary spheres and then the dynamics of the irregular particles will be calculated by Newton's second law of motion, which is the same as illustrated in Section 6.2.

The contact electrification model in this DEM model is similar to the model in Section 6.2. However, as shown in Figure 6.18 and 6.19, the overlaps between primary spheres are significant. A large portion of the surface of the primary sphere is buried inside the volume of the particle and does not contribute to the actual surface of the particle, which is different from the symmetric multi-sphere method. Therefore, according to Eqs. (6.5), (6.6) and (6.7), the induced potential between the wall surface and the charged primary sphere at the contact area is modified as follows:

$$V' = k_0 q_s = \frac{z}{\varepsilon_0} A_{sp}^{-1} q_s \tag{6.17a}$$

$$k_0 = \frac{z}{\varepsilon_0} A_{sp}^{-1} \tag{6.17b}$$

If two charged primary spheres of insulating materials are considered, then the induced potential difference between the two charged primary spheres at the separation distance can be determined as:

$$V' = \frac{z}{\varepsilon_0}\left(\frac{q_{sj}}{A_{spj}} - \frac{q_{si}}{A_{spi}}\right) \tag{6.17c}$$

where q_{si} and q_{sj} are the charge of primary spheres i and j; A_{spi} and A_{spj} are the equivalent areas of the primary spheres i and j, which can be defined as:

$$A_{sp} = \frac{A_p}{n_p} \tag{6.18}$$

where A_p is the surface area of the particle; n_p is the number of the primary spheres; A_{sp} is the mean division of the particle surface area by the number of primary spheres. It can be seen that the charge transfer depends on the local polarization of the particle, which is similar to the contact electrification model in Section 6.2.

6.3.3. The model setup

The contact electrification process of particles with arbitrary shapes in a rotating drum is modelled using the developed DEM model. The model setup is shown in Figure 6.20. The cylindrical drum with a 3 mm diameter and 5 mm length is discretized into 504 triangular meshes. The contact interactions are detected and applied between particles and each triangular mesh (Kremmer and Faviour, 2001). Initially, 300 particles are deposited on the cylindrical surface of the drum until the granular bed is stable (i.e. the maximum particle velocity is smaller that 10^{-6} m·s^{-1}). Then the drum will start to rotate around the *x* axis at 30 rpm. The contact electrification model will be applied once the drum starts to rotate.

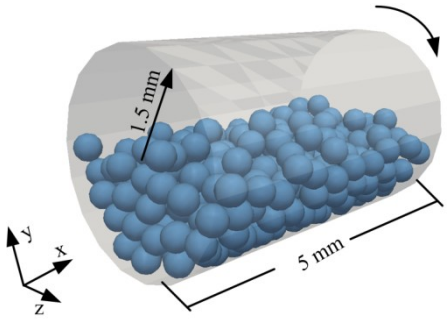

Figure 6.20 The model setup of the rotating drum.

To investigate the effects of particle shape, 4 types of multi-spheres are used in the DEM simulations. The particles represented by polyhedrons are shown in Figure 6.21. Particle I, II, III and IV consist of 440, 744, 266, 544 triangular meshes, respectively. Then the corresponding multi-sphere to each particle is generated using the medial axis approximation as illustrated in Figure 6.22. Each particle is constructed by 8 primary spheres respectively. Spherical particles (Particle V) are also used for reference and comparison.

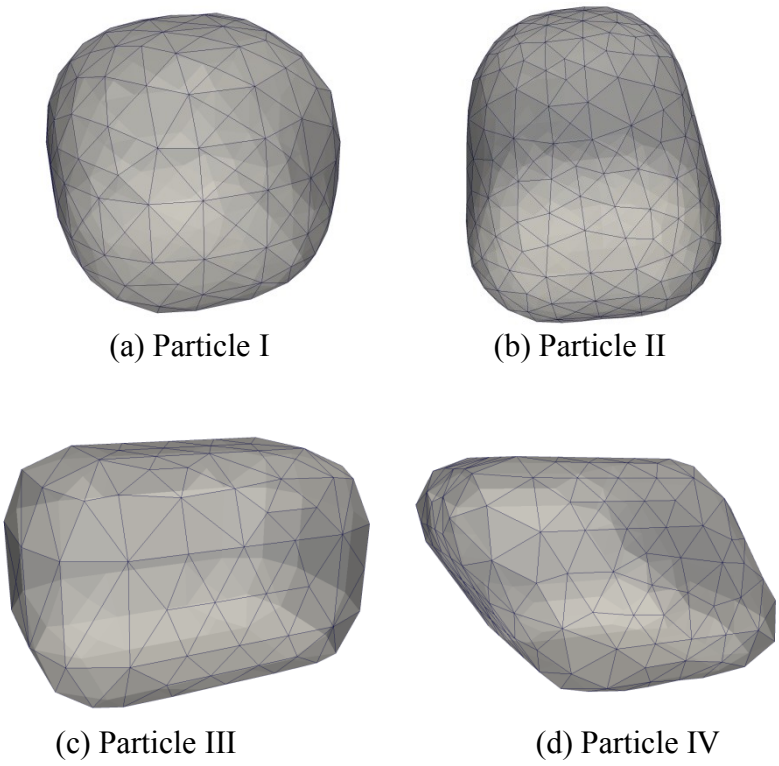

(a) Particle I (b) Particle II

(c) Particle III (d) Particle IV

Figure 6.21 Particles represented by polyhedra.

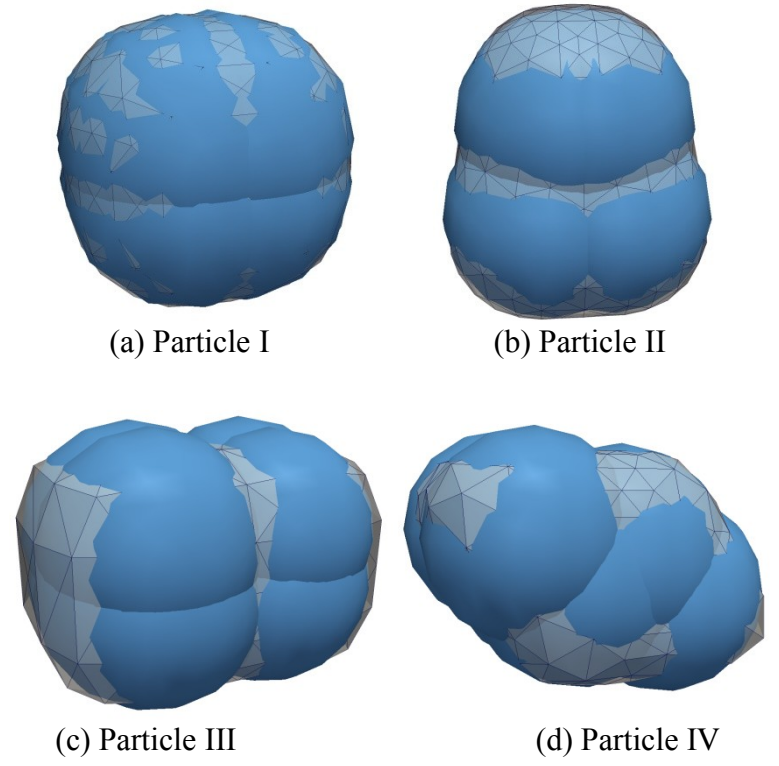

(a) Particle I (b) Particle II

(c) Particle III (d) Particle IV

Figure 6.22 The multi-spheres used in DEM simulation.

The maximum diameter of the particle, D_{max}, is defined as the largest distance between two vertices of the polyhedral particle. In this study, all particles are scaled to have the same maximum diameter of 4×10^{-4} m. The volume of each particle is calculated by the integral method (Mirtich, 1996).

The surface area is determined as the summation of the areas of all triangular meshes. The Sauter mean diameter (SMD) of the particle can be defined as (Li and Ma, 2011):

$$D_{32} = 6\frac{\psi_p}{A_p} \tag{6.19}$$

where ψ_p is the volume of the polyhedron (particle); A_p is the surface area of the polyhedron (particle). From Eq. (6.19), it can be seen that D_{32} is related to the surface-to-volume ratio and is defined as the radio between the surface area and the volume of the particle. For the same maximum diameter, a smaller value of D_{32} results in a larger surface-to-volume ratio, which means larger active surface per unit volume.

The shape of the particles are classified using the dimentionless sphericity of the particles (Wadell, 1935) defined as:

$$\varsigma = \frac{\pi^{1/3}\left(6\psi_p\right)^{2/3}}{A_p} \tag{6.20}$$

From Eqs. (6.19) and (6.20), it can be seen that, for the same maximum diamter, a larger value of D_{32} will lead to a higher spherity. The sphericity of the spherical particles is 1.0.

Table 6.4 The list of various particles

ID	Particle	D_{max} (m)	V_p (m^3)	A_p (m^2)	D_{32} (m)	ς	Fill ratio
I	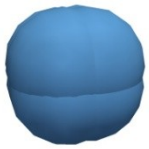	4×10^{-4}	2.79×10^{-11}	4.51×10^{-7}	3.72×10^{-4}	0.987	0.236
II	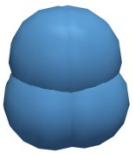	4×10^{-4}	2.38×10^{-11}	4.14×10^{-7}	3.45×10^{-4}	0.966	0.202
III	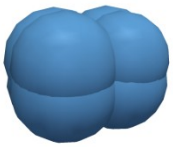	4×10^{-4}	1.84×10^{-11}	3.63×10^{-7}	3.04×10^{-4}	0.928	0.156
IV	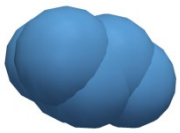	4×10^{-4}	1.38×10^{-11}	3.04×10^{-7}	2.71×10^{-4}	0.913	0.117
V	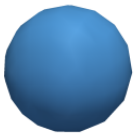	4×10^{-4}	3.35×10^{-11}	5.03×10^{-7}	4.00×10^{-4}	1.0	0.284

The geometric properties of the particles are shown in Table 6.4. The physical properties of the particles and the drum are the same as those given in Table 6.2. The work functions of the particles and the drum are 4.52 and 4.7 V, respectively. When the drum starts to rotate, the charge will be transferred between the particles and between the particle and the drum. In reality, the charge accumulation on particles takes much more time to reach saturation, which is extremly computationally expensive for DEM simulations. Consequently, the charging constant k_s is set to 0.02 $C\cdot m^{-2}\cdot V^{-1}$ in order to accelerate the charging process in the DEM smulations. The charge is assumed to be attained by the primary sphere and will not be re-distributed onto other primary spheres and dissipated to the environment. In addition, the

electrostatic interactions are also ignored in this study. The charge distribution and accumulation on the particles are then analyzed and discussed.

6.3.4. Results

6.3.4.1 The particle profiles

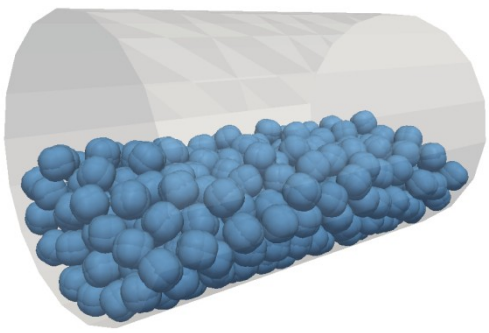

(a) Particle I (D_{32} = 3.72×10^{-4} m)

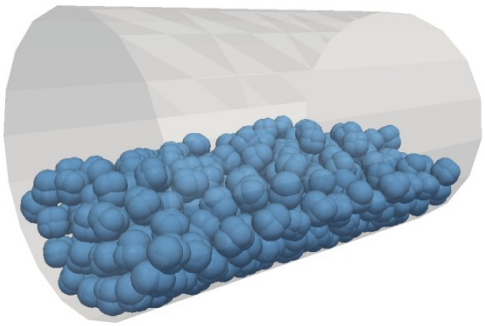

(b) Particle II (D_{32} = 3.45×10^{-4} m)

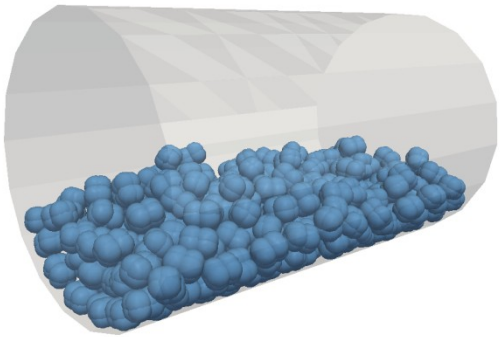

(c) Particle III (D_{32} = 3.04×10^{-4} m)

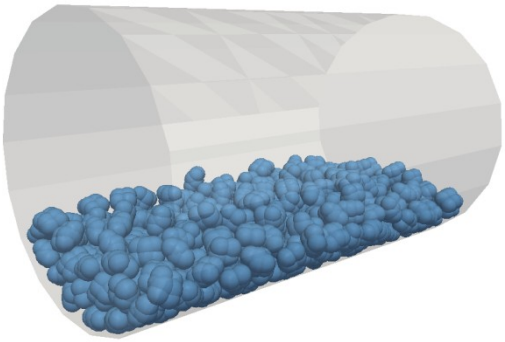

(d) Particle IV (D_{32} = 2.71×10^{-4} m)

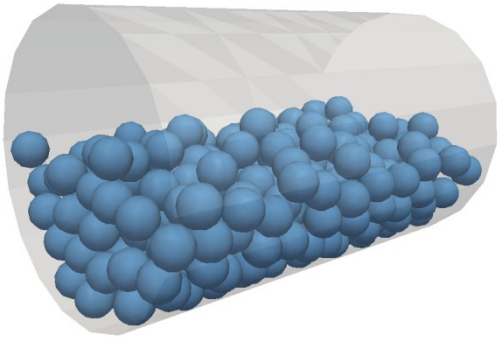

(e) Particle V (D_{32} = 4.00×10^{-4} m)

Figure 6.23 The deposited granular beds in the drum.

Figure 6.23 shows the deposited granular beds of various particles in the cylindrical drum. It can be seen that the height of the granular bed varies with the particle type. The fill ratio defined as the total volume of the particles divided by the volume of the drum is calculated and given in Table 6.4. Clearly, with a smaller particle volume, the fill ratio is smaller, which results in a lower fill height of the granular bed.

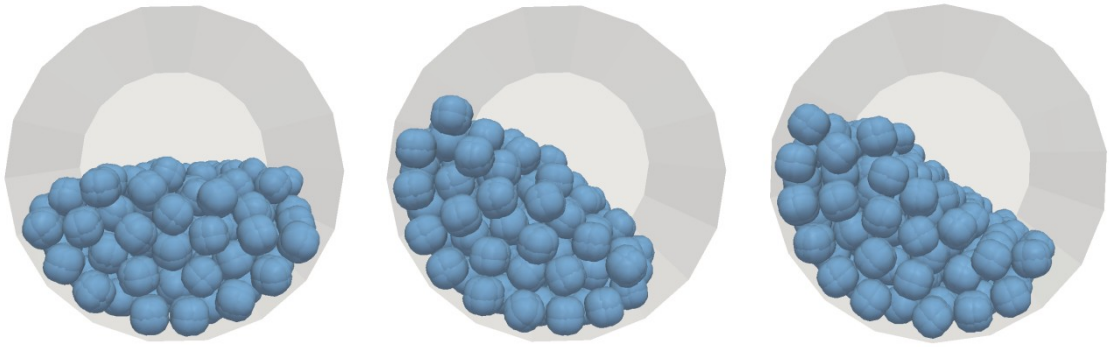

(a) $t = 0.0$ s (b) $t = 0.33$ s (c) $t = 0.63$ s

Figure 6.24 The profiles of particle I ($D_{32} = 3.72\times10^{-4}$ m) during the drum rotation.

Figure 6.24 shows the perspective view of particle I ($D_{32} = 3.72\times10^{-4}$ m) profiles during the drum rotation from the x direction. Initially (Figure 6.24a), the particles lay on the cylindrical surface of the drum. When the drum starts to rotate, the granular bed follows the movement of the cylindrical surface of the drum and forms an inclination angle with the x-z plane. As the angle increases, particles start to roll down along the inclined surface (Figure 6.24b). When the inclination angle is sufficiently large, particles at the top cascade down to the bottom of the drum (Figure 6.24c). As the drum rotation continues, this process repeats and the particles are mixing and making contact with each other. Various types of particles show similar kinematics.

6.3.4.2 The charge distribution

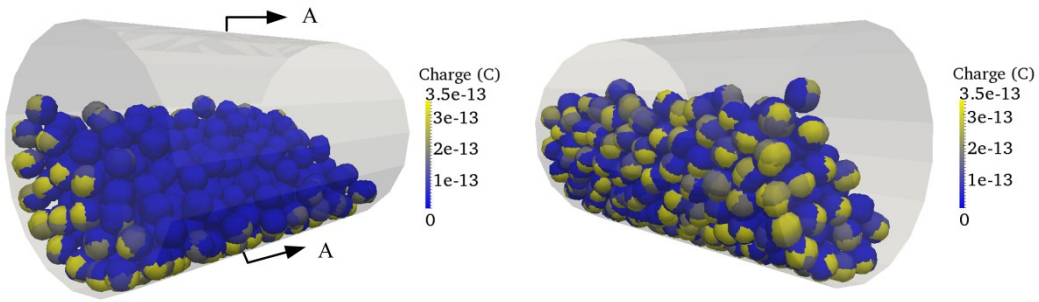

(a) front view (b) back view

Figure 6.25 The charge distribution for the particle I (D_{32} = 3.72×10^{-4} m) at t = 0.33 s.

Figure 6.25 presents the charge distribution for the particle I of D_{32} = 3.72×10^{-4} m in the rotating drum at t = 0.33 s. It can be seen that the charge distribute non-uniformly in the granular bed. At the early stage of the drum rotation, the particles at the inclined surface of the granular bed possess little charge (Figure 6.25a). On the contrary, the charges of particles close to the drum wall are much higher. This indicates that the charges are initially generated from the contact between the particles and the drum wall at the region close to the drum surface. The charge is also higher at the region near the side walls of the drum. In addition, the charge on each primary sphere varies, which means that the charge distribution of each particle is not uniform.

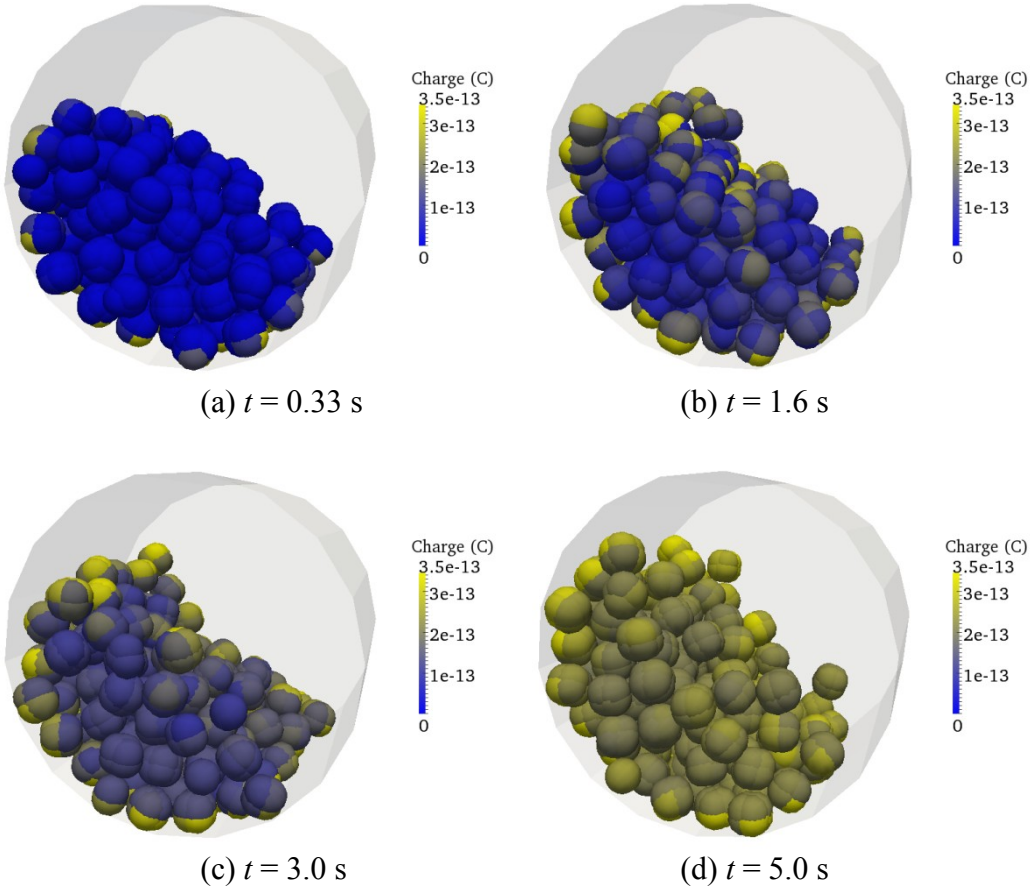

Figure 6.26 The charge evolution for the particle I (D_{32} = 3.72×10^{-4} m).

Figure 6.26 presents the charge evolution for the particle I (D_{32} = 3.72×10^{-4} m) in the granular bed during the drum rotation from the A-A view as indicated in Figure 25. It clearly shows that the charge is initially generated at the layer close to the cylindrical surface of the drum (Figure 6.26a), which is corresponding to Figure 25. As the drum rotates, the charged particles move with the drum to the top of the granular bed (Figure 6.26b) and then roll down along the inclined surface of the granular bed, which cause the particles to mix with each other and charge transfer between particles. The charge in the granular bed gradually evolves from the region near the drum walls to the inclined surface of the granular bed. The charge distribution eventually becomes uniform and the charges of the particles are saturated as indicated in Figure 6.26c.

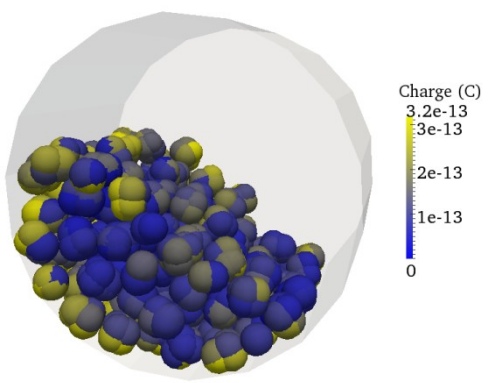

(a) Particle II (D_{32} = 3.45×10^{-4} m)

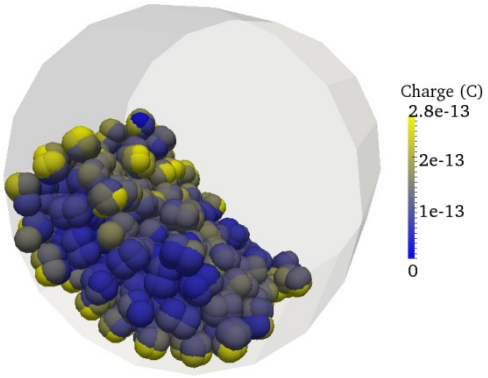

(b) Particle III (D_{32} = 3.04×10^{-4} m)

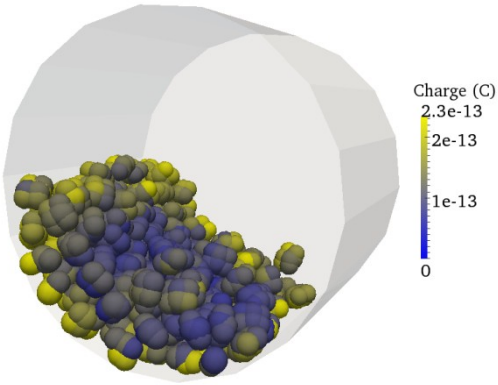

(c) Particle IV (D_{32} = 2.71×10^{-4} m)

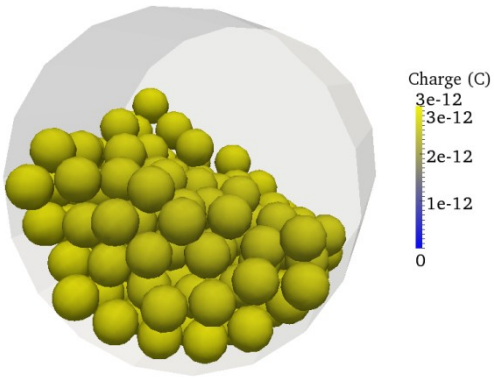

(d) Particle V (D_{32} = 4.00×10^{-4} m)

Figure 6.27 The charge distributions in the drum with various particles at t = 1.6 s.

Figure 6.27 shows the charge distribution in the drum with various particles at t = 1.6 s from the A-A view as indicated in Figure 6.25. Comparing with Figure 6.26b, the charge distribution for various shaped particles appears to be similar in the drum. The charge of the particles close to the walls of the drum is higher and the charge of the particles close to the inclined surface of the granular bed is lower except the spherical particles (Figure 6.27d). However, the saturation levels of the charges for various shaped particles are different at the same time instant. Specifically, the particles with a larger SMD accumulates less charge compared with their own equilibrium value as shown in Figures 6.27a, 6.27b and 6.27c This indicates that particle shape can affect the charging transfer rate.

The charge density distribution is further determined and mapped on the polar coordinate. The centres of all primary spheres are projected onto the *z-y* plane along *x* direction in polar coordinates as shown in Figure 6.28. As only the centres of the primary spheres are projected on the polar coordinate and a small number of particles is used, a few layers of the centres of the primary spheres are shown in Figure 6.28. To show the contour of charge density distribution continuously in the radial direction, a relatively large grid size and a small number of grids (5 layers) in radial direction was chosen. In this study, the polar coordinate with the radius of 0.0015 m is divided into 5×20 grids in the radial and circumferential directions respectively as in Figure 6.28. In each grid, the charge density can be defined as:

$$\sigma_g = \frac{\sum_{i=1}^{n_s} q_{si}}{A_g} \tag{21}$$

where A_g is the grid area; q_{si} is the charge of the primary sphere of which the centre is mapped into the corresponding grid; n_s is the number of primary spheres mapped into this grid. It can be seen that the charge density represents the charge concentration of this grid along the *x* axial direction.

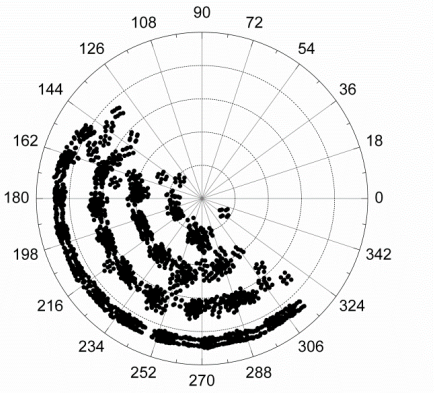

Figure 6.28 A demonstration of the polar coordinate.

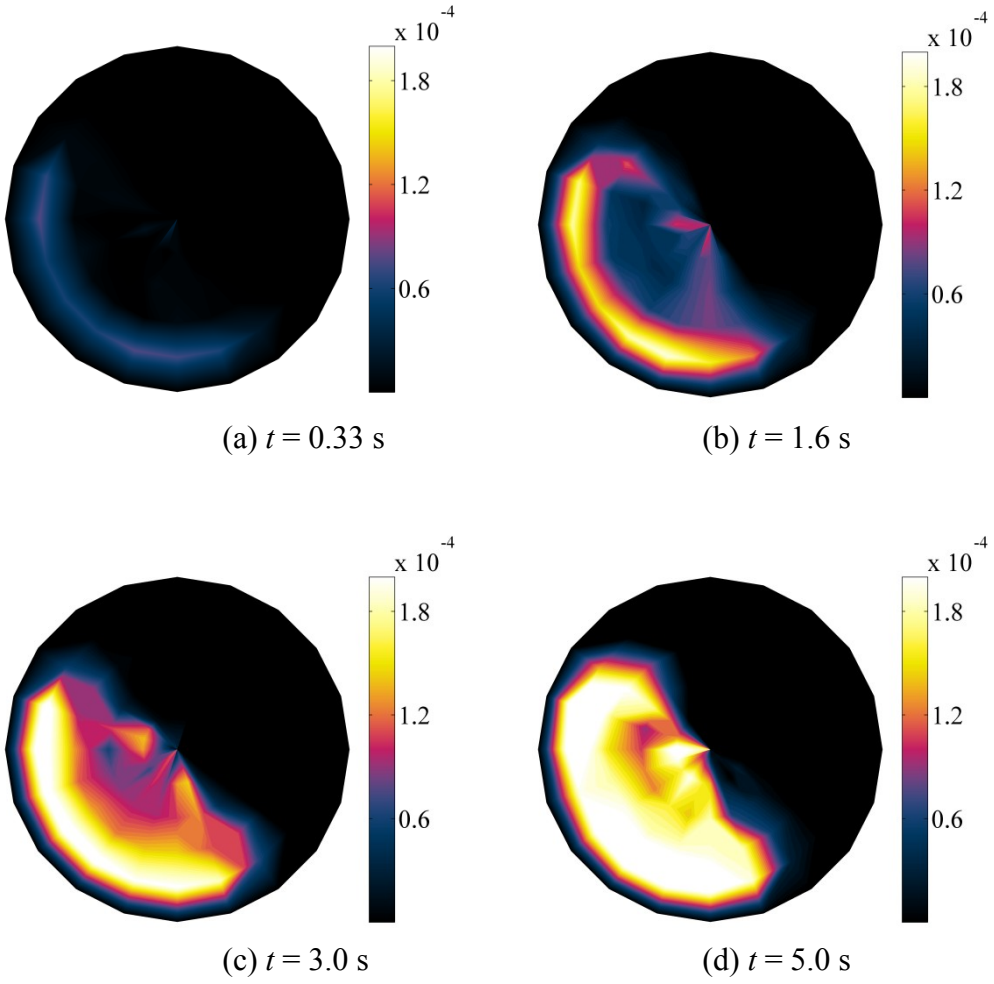

Figure 6.29 The evolution of charge density distribution ($C \cdot m^{-2}$) for the particle I (D_{32} = 3.72×10^{-4} m).

Figure 6.29 presents the evolution of the charge density distribution ($C \cdot m^{-2}$) for the particle I (D_{32} = 3.72×10^{-4} m). It is clear that the charge is initially generated from the region close to the drum wall (Figure 6.29a) and then evolves to the inclined surface of the granular bed until the charge density of the particles reaches the equilibrium value (Figures 6.29b, 6.29c and 6.29d).

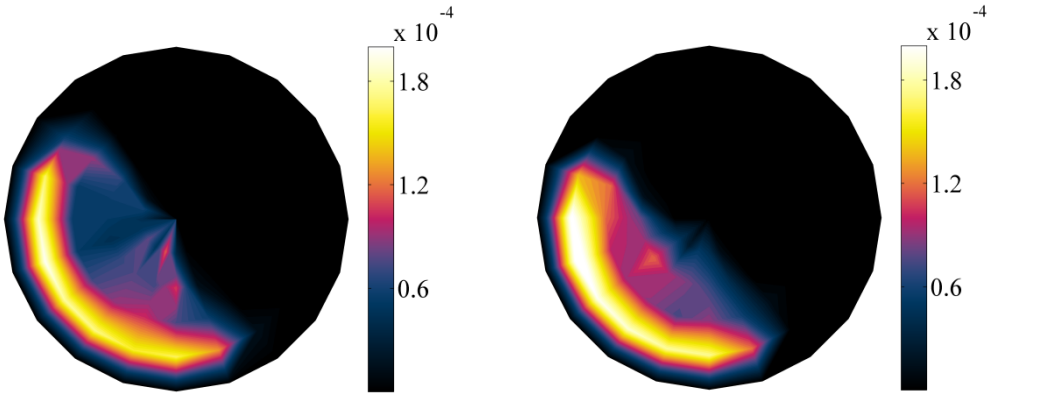

(a) Particle II (D_{32} = 3.45×10^{-4} m) (b) Particle III (D_{32} = 3.04×10^{-4} m)

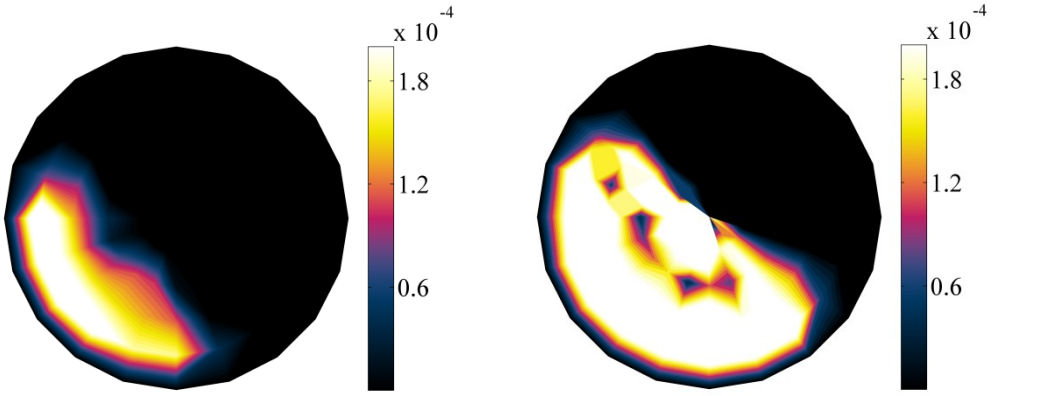

(c) Particle IV (D_{32} = 2.71×10^{-4} m) (d) Particle V (D_{32} = 4.00×10^{-4} m)

Figure 6.30 The charge density distribution (C·m^{-2}) of various particles t = 1.6 s.

Figure 6.30 shows the charge density distribution of various particles in the drum at t = 1.6 s. Particles with different shapes present different charge density distributions. For the particles with larger SMDs and larger sphericity, the charge density concentrates at the cylindrical surface of the drum and the saturation level of the charge is relatively smaller (Figures 6.29a and 6.29c). However, for the particles with a smaller SMD, a higher charge density in the entire granular bed is obtained as shown in Figure 6.29c. Exceptionally, the charge density of the spherical particles achieves is much higher than the other particles.

6.3.4.3 The charge accumulation

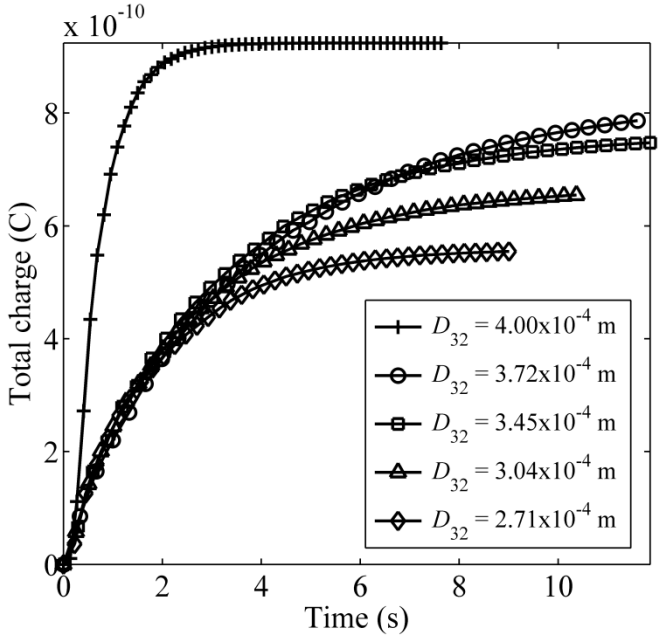

Figure 6.31 The charge accumulation of various particles.

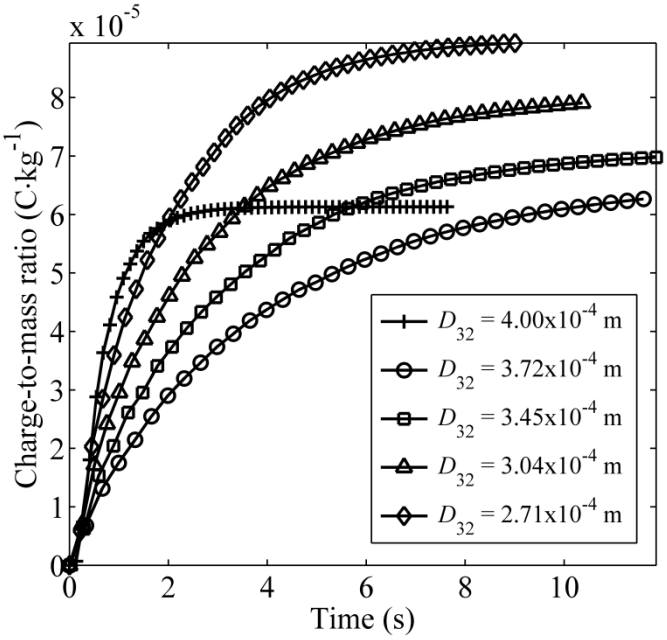

Figure 6.32 The evolution of charge-to-mass ratio for various particles.

Figure 6.31 shows the charge accumulation processes for various particles during the drum rotation. The charge gradually increases and reaches an equilibrium state. However, the equilibrium charges of particles vary with different D_{32}. Specifically, for the particles with the same D_{max}, a larger D_{32} leads to a greater equilibrium charge. Figure 6.32 shows the corresponding evolution of the charge-to-mass ratio of the various particles. It can be seen that the equilibrium charge-to-mass ratio of the particles also varies with D_{32}. However, a larger D_{32} leads to a smaller equilibrium charge-to-mass ratio.

6.3.5. Discussions

The charge distribution of various shaped particles in the rotating drum shows a similar pattern despite the different fill ratios and that the particles have the same material properties. Because of the contact potential difference between the particles and the drum, the charge is initially transferred between the particles and the drum wall as shown in Figure 6.26a. Moreover, the particles move with the drum as it rotates due to the friction between the particles and the drum until the inclination angle of the granular bed is sufficiently large that the particles at the top start to roll down to the bottom. The charged particles are mixed in the granular bed and make contacts with other particles, which promotes charge transfer. As the charge on particles accumulates, all particles are eventually charged to an equilibrium state (Figure 6.31). Hence It can be seen that the charge of the granular bed gradually increases from the region near the wall of the drum to the inclined surface of the granular bed as shown in Figure 6.26 and Figure 6.29.

The charge of particles gradually increases to the equilibrium state during the rotation of the drum. However, the equilibrium charge of particles depends on particle shape. According to Eqs. (6.17) and (3.9), the equilibrium charge of a particle is proportional to the surface area of the particle, implying that the equilibrium mean surface charge densities of particles with different D_{32} are equal.

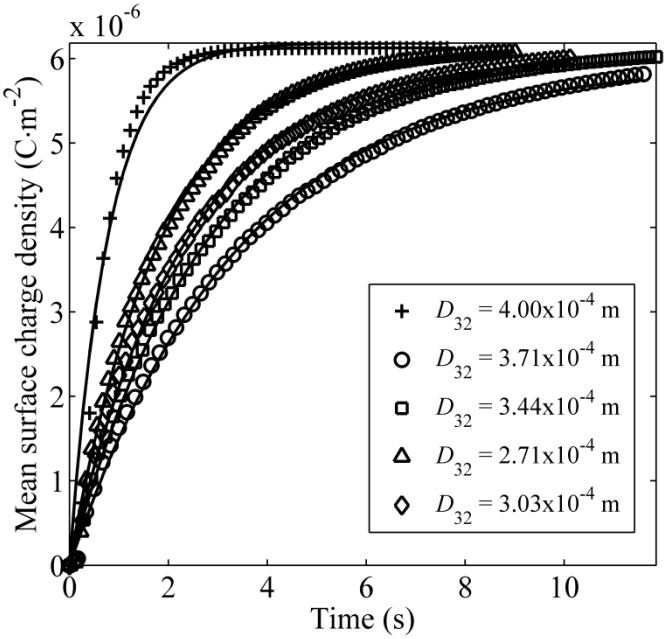

Figure 6.33 The evolution of mean surface charge density for various particles.

Figure 6.33 shows the evolution of the mean surface charge density of various particles during the drum rotation. The solid line is the fitting line of Eq. (6.16). The mean surface charge density of the particles increases exponentially to the same equilibrium state with different charging coefficients. The charging coefficients and the related SMDs and sphericity are listed in Table 6.5. Generally, for particles with the same D_{max}, a smaller D_{32} and sphericity leads to a larger charging coefficient, which means that a particle with a smaller D_{32} will become charged more rapidly than those with a larger D_{32}. Although particles have the same

maximum diameter, a smaller D_{32} leads to a smaller particle volume and a smaller fill ratio as shown in Table 6.4 and Figure 6.23. Due to the smaller fill ratio, particles with a smaller D_{32} can mix more effectively in the rotating drum. In addition, a smaller D_{32} leads to a larger surface-to-volume ratio, and relatively more contacts on the surface of the particle. Therefore, for particles with the same D_{max}, a smaller D_{32} results in a faster charge accumulation. However, the particle shape can be classified by different parameters, such as equivalent (volume) spherical diameter, which may lead to more complex electrostatic phenomena (Appendix B).

Table 6.5 The shape factors and the charging coefficients for various particles.

D_{32} (m)	ς	k_c
3.72×10^{-4}	0.987	0.29
3.45×10^{-4}	0.966	0.36
3.03×10^{-4}	0.928	0.43
2.71×10^{-4}	0.913	0.54
Sphere(4.00×10^{-4})	1.0	1.28

An exceptional case in this study is that the spherical particles (D_{32} = 4.00×10^{-4} m) have a larger charging coefficient, compared with the particles of D_{32} = 3.72×10^{-4} m, although both particles have a similar shape (D_{32} and ς). The spherical particle (D_{32} = 4.00×10^{-4} m) is treated as one sphere with a uniform charge distribution on the surface and the induced potential difference is determined by the uniform distribution as Eq. (3.2). However, the multi-sphere particle is treated as an assembly of primary spheres on which the non-uniform charge distribution is observed, as shown in Figure 6.34. Matsuyama *et al.* (2003) suggested that the induced potential difference is mainly affected by the local initial charge at the contact area while the charge at the remote (rear) side to the contact area has less effect on the

induced potential difference (Figure 6.35). Therefore, for particles approximated using multi-spheres, the induced potential difference is only determined by the charge on the local primary sphere (Eq. (6.17)). Consequently, the charging coefficients of the spherical particle (D_{32} = 4.00×10^{-4} m) and the multi-sphere particle (D_{32} = 3.72×10^{-4} m) are different. In this study, the particle shape is represented by only 8 primary spheres. A more accurate approximation, e.g. more primary spheres for one particle, needs to be considered in future study.

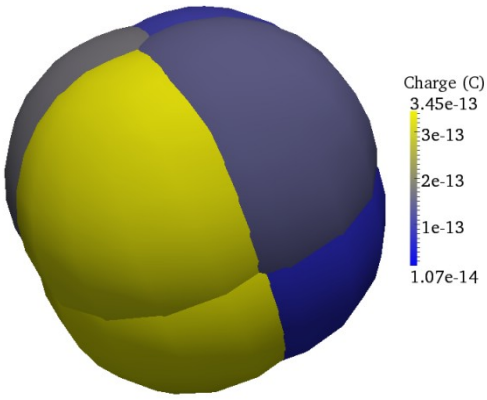

(a) Particle I (D_{32} = 3.72×10^{-4} m)

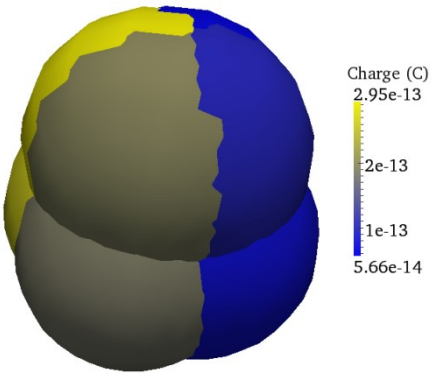

(b) Particle II (D_{32} = 3.45×10^{-4} m)

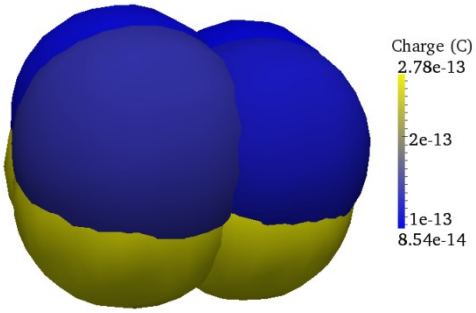

(c) Particle III (D_{32} = 3.04×10^{-4} m)

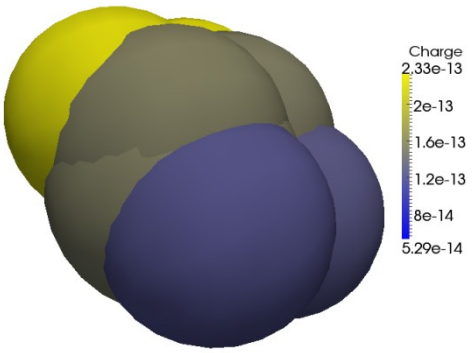

(d) Particle IV (D_{32} = 2.71×10^{-4} m)

Figure 6.34 Typical charge distribution of primary spheres on various particles.

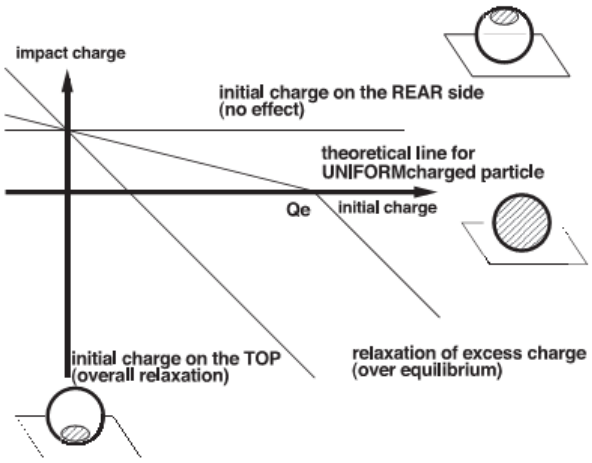

Figure 6.35 A schematic illustration of localization of initial charge on a particle (Matsuyama *et al.*, 2003).

6.3.6. Summary

In this chapter, the sphere-tree multi-sphere method and the contact electrification model are implemented into the DEM model to simulate the charging process of irregular particles. A rotating drum with irregular particles with various Sauter mean diameters are modelled. The charge distribution and accumulation of irregular particles are investigated.

For all particles, the charge transfer originated from the contact between a particle and the drum because of the contact potential difference. The charge is initially concentrated at the region near the drum wall and then propagates to the entire granular bed. A non-uniform charge distribution on the irregular particle is observed. The charge of the particles exponentially increases to the equilibrium state. However, particles with smaller SMD and sphericity have a larger charging coefficient, which leads to a faster charge accumulation. Eventually, all particles with various SMDs achieve the same surface charge density. In any

future study, more precise representation of irregular particles and the effect of charge local polarization of on charge transfer should be considered further.

CHAPTER 7 DISCUSSIONS

7.1. Introduction

In this chapter, contact electrification and electrostatic interaction models are discussed. The contact electrification process and the electrostatic behaviours during powder handling processes are summarized accordingly.

7.2. The contact electrification model

In this study, the induced potential difference between objects is treated as the linear superposition of the surface potential induced by the net charge on the contacting particles as described in Chapter 2 and 3. Physically, the induced electric field by the net charge can further cause charge re-distribution (polarization) on the objects especially with conductive materials and cause image effects between the separated objects. Strictly, the image effect is a non-linear polarization phenomenon due to the mutual electrostatic interactions between the objects. Matsuyama and Yamamoto (1995) suggested that if the higher-order polarization is ignored, the image effect can affect the induced potential difference linearly to a certain extent, e.g. by a factor of 1-10, depending on the material properties and the separation conditions. In addition, non-uniform charge distribution and charge relaxation and dissipation on the dielectric particles, especially of irregular shapes, can also affect the induced potential difference as discussed in Chapters 3 and 6.

Due to the long-range nature of electrostatic interactions, the induced potential difference between objects also depends on the external electric field (Matsusaka *et al.*, 2010). In this context, the external electric field is assumed to be generated by the charges that are not involved in the underlying contact electrification. For instance, the external electric field can be generated by the electrodes in the powder handling equipment or the charge (space charge effect) on remote particles at a distance from the underlying contact. Therefore, the induced potential difference should be considered as the summation of all electric potentials generated by the net charge, the image effect and other external electric fields.

According to the condenser model, the induced potential difference eventually balances with the contact potential difference, which leads to an equilibrium state of the charge transfer process. However, due to the complexity of the induced potential difference, it is difficult to quantify the charge transfer process accurately. It would be necessary to access the influence of different factors (image effects, space charge, particle size and shape, charge relaxation and dissipation, etc., as also discussed in Chapter 3, etc) on the charge transfer process, so that the charge transfer process can be estimated with relevant coefficients, depending on these factors.

7.3. The electrostatic interaction model

Polarization phenomena can also influence the electrostatic interactions during powder handling processes. When charged particles are close to or in contact with each other, the polarization on particle surfaces can be significant and a non-uniform charge distribution can occur on the surface of particles. Subsequently the electric field and electrostatic force between particles are altered.

Charged spherical particles are generally treated as point charges and governed by Coulomb's law in the electrostatic interaction model. It is difficult to analyze the charge distribution and polarization on a single particle. Liu *et al.* (2010) proposed that such objects can be discretized into meshes and then the charge distribution can be determined using the boundary element method (BEM). As an alternative method, in the current study, the particle is constructed by a collection of primary spheres using the multi-sphere method. The analysis of charge distribution is based on such primary spheres as shown in Sections 6.2 and 6.3. Potentially, the non-uniform charge distribution can lead to agglomeration and segregation during powder handling processes. For instance, negatively charged small particles can be agglomerated and concentrated on the highly positively charged parts of a larger carrier as demonstrated in Figure 7.1. However, this multi-sphere method for electrostatics requires further development and validation, especially charge and electric field re-distribution on primary spheres.

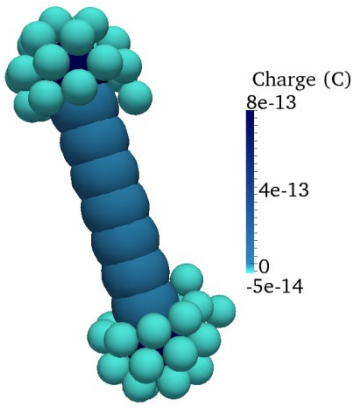

Figure 7.1 A illustration of segregation of small particles adhered on a large carrier due to electrostatic interaction.

7.4. Contact electrification and electrostatic interactions in powder handling processes

The charge generation and distribution of particles with the same material show similar scenarios in various powder handling processes (Chapters 3 and 6). The charge transfer is generally originated from the collisions between the particles and the wall surface due to the contact potential difference. Then the charge gradually increases from the region close to the wall surface to the entire particle system until it reaches the equilibrium state. This phenomenon shows close agreement with the experiments of LaMarche *et al.* (2009). The charge accumulation process follows an exponential trend, which has also been observed experimentally (Zhu *et al.*, 2007b; Liao *et al.*, 2011; Saleh *et al.*, 2011; Šupuk *et al.*, 2011).

The charge distribution and accumulation of binary mixtures are more complex than blends, especially when the electrostatic interactions are significant for the particles. The charge transfer occurs between particles and between the particle and the wall. Due to contact potential difference, the particle system becomes bi-charged. As the charge increases, particles start to form agglomerates caused by electrostatic interactions between particles. Particles can also adhere onto the wall surface due to the image effect. As discussed in Chapter 5, these phenomena can reduce the performance of the powder handling process and prevent further charge transfer between objects. Therefore, the charge accumulation does not necessarily follow an exponential trend. These phenomena has been observed by Zhu *et al.* (2007b), LaMarche *et al.* (2009), LaMarche *et al.* (2010), Sowinski *et al.* (2010).

Electrostatic interactions play an important role in powder handling processes. The repulsive force among mono-charged particles can cause dispersion of the particle system while the mutual attractive and repulsive among bi-charged particles can eventually lead to agglomeration of the particle system. Combined with electrostatics, the particle properties and operating conditions can influence the dynamics of the particle system and significantly change the performance of the powder handling processes as discussed in Chapters 4 and 5.

Smaller particles are prone to accumulate higher charge-to-mass ratios, and consequently are more sensitive to electrostatic interactions during powder handling processes (Chapter 3). According to the contact electrification model, the charge-to-mass ratio of particles is inversely proportional to the particle diameter. Therefore, particles with high charge-to-mass ratio are found adhered on the container walls as shown in Chapters 4 and 5. This explains the experimental observations (Šupuk *et al.* 2010) that API particles with smaller sizes possess higher charge-to-mass ratios and are much more prone to form agglomeration and adhesion than larger excipient particles. However, Pu *et al.* (2009) suggested that the controlled and optimised charge distribution of excipients and APIs can improve the API distribution and the blending homogeneity in pharmaceutical powders handling processes. Further analysis on the optimization mechanism and the controlling conditions needs to be performed especially with numerical methods.

Small and light particles are more sensitive to the air flow during the powder handling processes (Guo *et al.*, 2009). The electrostatics of particles and the air flow interfere with each other during powder handling processes. As discussed in Chapter 4, the air can slow down the formation of the agglomerates of bi-charged particles due to their air sensitivity. On the other

hand, the formed agglomerates of bi-charged particles become less sensitive to the air due to the aggregation. The combined effects of air and electrostatics become more complex in fluidization as shown in Chapter 5. A small gas velocity cannot fluidize bi-charged particles due to the agglomeration. Although the higher gas velocity can break agglomerates and fluidize bi-charged particles, it results in a higher charge level (net charge) that may induce a stronger electric field in the granular bed, especially close to the walls of the containers (Rokkam *et al.*, 2010; Sowinski *et al.*, 2010). The high level of charge may cause a dangerous hazard, such as ignition and explosion (Nifuku and Katoh, 2003). This indicates that electrostatic phenomena and the operations of powder handling processes are interrelated and can influence with each other.

Particle shape plays an important role in powder handling processes. For instance, it is observed that the orientation of elongated particles tends to be perpendicular to the vibration direction of a container (Chapter 6). Although the orientation of elongated particles shows a similar pattern, the surface charge distribution of particles varies with the shape factor (Eq. (6.9)). This is because primary spheres with different sizes make contact with other objects and accumulate charge at different rates, indicating that irregular particles can result in non-uniform surface charge distribution during powder handling processes. The non-uniform surface charge distribution is also observed for particles of arbitrary shapes as discussed in Chapter 6. Ireland (2012) observed that, when elliptic particles with different roundness ratio, i.e. the short axis radius divided by the long axis radius, impacted on a tilted surface, various contact modes (bouncing, sliding, and rotating) occurred. When the particles were bouncing or sliding on the surface, only the contact region of the particle surface became charged. While a particle rotated, the particle surface became charged more uniformly. Thus particle

shape can lead to various contact modes and dynamic behaviour of particles and subsequently influence the charge distribution and accumulation (Appendix B). The non-uniform surface charge distribution can alter the electrostatic interactions between particles, which may lead to segregation of particles as discussed above and demonstrated in Figure 7.1. In addition, it was found that a smaller fill ratio of particles in a rotating drum can lead to faster charge accumulation process (Chapter 6), indicating that the operating conditions for powder handling processes can also influence the charging process.

The DEM-CFD method can be used to link the particle properties to the dynamics of the particle system during powder handling processes. In this study, the contact electrification model and the electrostatic interaction model utilize the properties of individual particle to describe the charge transfer process and the interparticle interactions. By implementing these models into DEM, the dynamics of the particle system can be analyzed numerically based on the particle properties and the powder handling conditions. Therefore, the DEM-CFD method can perform an analysis from single particles to the particle system.

CHAPTER 8 CONCLUSIONS AND FUTURE WORK

8.1. Introduction

In this chapter, the achievements of the current study are summarised and discussed. Accordingly, some necessary future works are also considered.

8.2. Conclusions

In this study, to explore the influence of contact electrification and electrostatic interactions in particle systems, an in-house DEM-CFD code is adapted and developed in four strands:

(1) A condenser model is implemented to analyze the contact electrification of particles;

(2) The Coulomb force model is incorporated to determine the electrostatic interactions between particles;

(3) A hybrid particle-cell (HPC) algorithm is developed to compare with the conventional direct truncation (DT) method to effectively model the long-range nature of the electrostatic interactions;

(4) Symmetric and sphere-tree multi-sphere methods is also incorporated to investigate the effects of particle shape on contact electrification.

The advanced DEM-CFD is then used to explore electrostatic phenomena and dynamic behaviours of particles in various powder handling processes, including: 1) contact electrification of spherical particles during fluidization; 2) deposition of mono-charged and bi-charged particles; 3) contact electrification and electrostatic interactions of spherical particles

during fluidization; 4) contact electrification of elongated particles in a vibrating container; and 5) contact electrification of particles with arbitrary shape in a rotating drum.

For charge transfer process, successive contact electrification between an insulating spherical particle and a metal substrate is analyzed with the condenser model. It is found that, for each contact, the transferred charge is a function of the maximum contact area, the charge of the particle and the contact potential difference between materials. During successive contacts, the charge accumulates on the particle exponentially and eventually reaches an equilibrium value. For particles with different sizes, the equilibrium surface charge density is identical but the equilibrium charge-to-mass ratio is inversely proportional to the particle size.

In addition, the charge accumulation and distribution of particles due to contact electrification during fluidization is investigated. During fluidization, the particle charge evolves from the region near the walls to the centre of the fluidized bed. The charge of the fluidized bed accumulates exponentially during fluidization and eventually reaches an equilibrium value. In addition, a higher gas velocity leads to a faster accumulating process in which a larger charging coefficient is obtained.

For the deposition of the mono-charged and bi-charged particles, it is shown that, for mono-charged particles, dispersed granular beds are observed because of the repulsive forces between particles. The particle concentration decreases from the bottom to the top of the granular bed. The granular temperature of the granular bed increases at the initial stage to a maximum value and then decreases until the granular bed becomes stable. In addition, the deposition of mono-charged particles is simulated with the HPC and DT algorithm. It is found

that the height of the granular bed, the radial distribution function and the granular temperature simulated by the DT method vary with the cut-off distances while those obtained with the HPC method are insensitive to the cut-off distance. For bi-charged particles, agglomeration occurs during deposition. The deposition process can be divided into three stages: particle clustering; agglomerate breakage and granular bed repacking. Agglomerates of crystalline structures are also formed during the deposition. Due to the formation of agglomerates, the air sensitivity of the granular system is decreased. Therefore, the difference between deposition rates in a vacuum and in air for particles with higher charge is smaller than that for particles with lower charge.

The combined effects of contact electrification and electrostatic interactions on fluidization were also investigated. Particles with different work functions are used and charged positively and negatively during fluidsation. Particles of opposite charges form agglomerates, which can hinder the fluidization process. Charged granular beds with low gas velocities cannot be fluidized, because of the formation of agglomerates. High gas velocities can break up the agglomerates and drag particles in the fluidized bed, which leads to a faster charge accumulation and a sparse charge distribution in the fluidized bed.

For contact electrification of elongated particles in a vibrating container, the elongated particle is approximated using a row of primary spheres and the contact electrification during the container vibration is modelled with the condenser model. Particles are classified into 5 groups using a shape factor, δ, which is defined as the radius difference between the distal and central spheres divided by the average radius. It is found that the charging behaviour depends on the particle shape. In terms of charge distribution, the net charge is higher on the larger

primary sphere of each group. Although the surface charge density is always higher on the distal primary sphere, the surface charge difference between the distal primary sphere and the central sphere increases as the shape factor increases at the early stage of the vibration. The surface charge density eventually becomes essentially identical between distal and central spheres except the particles of δ = 0.65. The central sphere of these particles cannot achieve an equilibrium surface charge density due to the lack of contacts, which leads to a large surface charge difference between the distal sphere and the central sphere even at the end of the vibration. With respect to the charge accumulation process, the surface charge density on particles with different shape factors accumulates exponentially during vibration and eventually achieves an equilibrium value. The particles of δ = -0.65 and -0.22 have larger charging rate coefficients due to the smaller surface charge density difference between primary spheres, while the groups of δ = 0.0 and 0.22 have smaller charging rate coefficients. In addition, the group of δ = 0.65 has a relatively larger charging rate coefficient because of the lack of charge on the central primary sphere.

For contact electrification of particles with arbitrary shapes in a rotating drum, the particle shape is approximated using overlapped primary spheres based on the sphere-tree multi-sphere method and the contact electrification during drum rotation is modelled with the condenser model. The Sauter mean diameter (D_{32}) and sphericity are used to represent the particle shape. Contact electrification in a rotating drum is modelled. As the drum rotates, the particle charge evolves from the region near the drum surface to the top layer of the inclined surface of the granular bed. Eventually, the surface charge density of the particles achieves an equilibrium state, which shows an exponential trend. However, it is observed that a smaller

Sauter mean diameter leads to a faster charge accumulation due to a smaller fill ratio and a better mixing process.

8.3. Future work

DEM-CFD is a robust method to analyze the influence of contact electrification and electrostatic interactions on powder handling processes. Nevertheless, further development and investigation are still required especially for the numerical models, numerical analysis and experiment validation.

The further analysis of contact electrification and the electrostatic interaction can be combined with the multi-sphere method. Development should consider:

(1) the influence of the image effect and external electric field (space charge) on contact electrification between particles and within the particle system;

(2) the non-uniform charge distribution on a particle represented using multi-sphere method and its influence on contact electrification and electrostatic interactions;

(3) the charge relaxation and dissipation on particles during powder handling processes.

(4) detailed studies of the accuracy of the multi-sphere method for contact electrification and electrostatic interactions, such as a comparison between the spherical particle model and multi-sphere model; the influence of the number of primary spheres for the same particle shape, etc.

Due to the complexity and diversity, it is difficult to generalize the electrostatic phenomena in powder handling processes. Therefore, detailed research on electrostatic phenomena

combined with contact electrification and electrostatic interaction in various powder handling processes should be focused on in the further study. Numerical analysis of electrostatic phenomena during powder handling processes can be further expanded into many aspects, such as:

(1) the effects of particle size and shape on contact electrification and electrostatic interactions;

(2) parametric studies on contact electrification and electrostatic interaction in specific powder handling processes, such as, die filling, blending, pneumatic conveying, etc.

DEM-CFD simulations with long-range interaction forces are computer-intensive. The long-range interactions like electrostatics can further compromise the computational efficiency (Chapter 4). In this study, to simulate the fluidization of 2500 charged particles for a physical time of 2 s, it requied 1-2 weeks of computational time. Clearly, the DEM-CFD method for contact electrification and electrostatic interactions is very time-consuming especially for larger systems. Parallel computing methods are rapidly developing and have been applied to solve problems with large systems. Therefore, it is necessary to develop and implement a robust parallel DEM-CFD program to ensure that the numerical analysis is comparable to the experimental scale or even the industrial scale.

The simulation results in this study have shown some close agreements with experimental observations. However, quantitative validations of DEM-CFD analysis should also be considered in future work. The contact electrification and electrostatic interaction models are based on each pair of particles, for which the corresponding experiments should be established. Some experimental have been recently advanced, such as particle image

velocimetry (PIV) and positron emission particle tracking (PEPT), that will assist the analysis of dynamics of the particle system. These methods are capable of providing detailed information on the dynamics of particles, which can be used to validate and compare with the corresponding numerical simulations.

APPENDIX A HPC AND DT METHODS FOR BI-CHARGED PARTICLES

To further compare the dynamics of bi-charged particles using DT and HPC methods, the deposition of bi-charged particles are modelled by the DT and HPC methods with the same setup in Section 4.3.

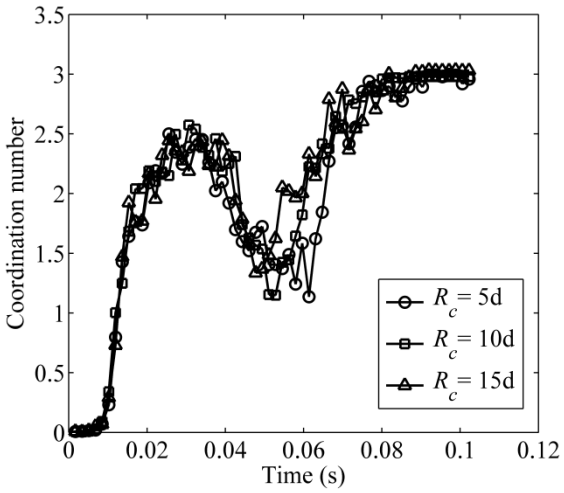

Figure A.1 The evolution of coordination number (ξ = 42.0, in air, with image force) by DT method with different cut-off distances.

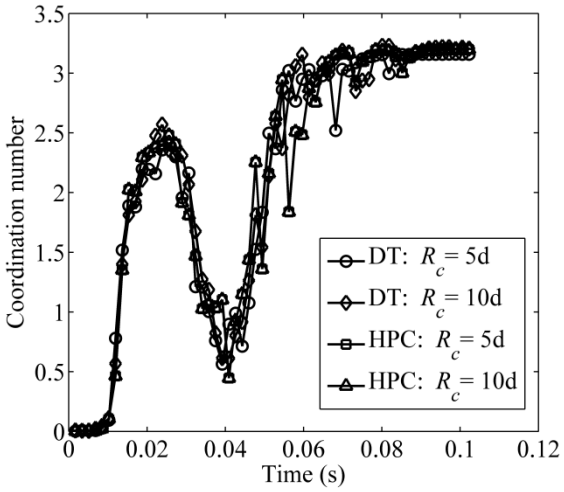

Figure A.2 The evolution of coordination number (ξ = 42.0, in a vacuum, without image force) by DT and HPC methods with different cut-off distances.

Figure A.1 shows the evolution of coordination number for particles (ξ = 42.0, in a vacuum, without image force) modelled by the DT method with different cut-off distances. It can be seen that all cases with different cut-off distances present similar results as discussed in Chapter 4, indicating that the evolution of coordination number for bi-charged particles is not sensitive to the cut-off distance of DT method. Similarly, Figure A.2 gives the evolution of coordination number (ξ = 42.0, in a vacuum, without image force) modelled by DT and HPC methods with different cut-off distances. The results are also similar and insensitive to the DT and HPC methods.

Bi-charged particles form agglomerates with crystalline structures (Figure 4.25). The agglomerates are showing Coulombic order (e.g., (+)(-)(+)(-)) (McCarty *et al.*, 2007a). Generally, each charged particle is surrounded by oppositely charged particles. Therefore, the electrostatic interaction of the charged underlying particle is screened and even reduced to nearly zero beyond a certain screening distance. This phenomenon, i.e. the electrostatic interaction shows short-range nature, is usually referred to as electrostatic screening effects (Kalsin *et al.*, 2006; Grzybowski *et al.*, 2009; Orlik *et al.*, 2009). Due to this short-range nature, the dynamics of bi-charged particles in this study can be modelled by DT method (with relatively larger cut-off distance than the screening distance) without showing significant sensitivity to the cut-off distances. However, how to the determine the screening effects (distance) and the relationship between the screening effects and the structure of the agglomerate still need further research (Kalsin *et al.*, 2006).

APPENDIX B CHARGE ACCUMULATION OF MULTI-SPHERES WITH SAME EQUIVALENT SPHERICAL DIAMETER

In this appendix, the charge accumulation of various irregular particles with the same equivalent (volume) spherical diameter is investigated. The shapes of the particles are modelled using sphere-tree multi-sphere method (Chapter 6) as listed in Table 6.4. The equivalent (volume) spherical diameter (ESD), D_v, is defined as the diameter of the sphere with the equivalent volume of the irregular particle. All particles (Figure 6.22) are of the same ESD. The geometrical properties of particles are listed in Table B.1. The model setup of the charge accumulations in a rotating drum is the same as in Section 6.3 (Figure 6.20).

Table B.1 Geometrical properties of various particles

ID	Particle	D_v (m)	V_p (m^3)	A_p (m^2)	D_{32} (m)	D_{max} (m)	Fill ratio
I	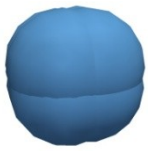	3.27×10^{-4}	1.84×10^{-11}	3.41×10^{-7}	3.16×10^{-4}	3.48×10^{-4}	0.156
II	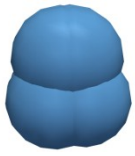	3.27×10^{-4}	1.84×10^{-11}	3.50×10^{-7}	3.15×10^{-4}	3.67×10^{-4}	0,156
III	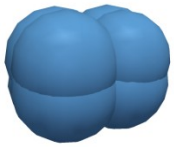	3.27×10^{-4}	1.84×10^{-11}	3.63×10^{-7}	3.03×10^{-4}	4.00×10^{-4}	0.156
IV	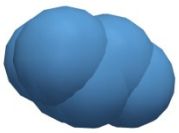	3.27×10^{-4}	1.84×10^{-11}	3.68×10^{-7}	2.99×10^{-4}	4.40×10^{-4}	0.156

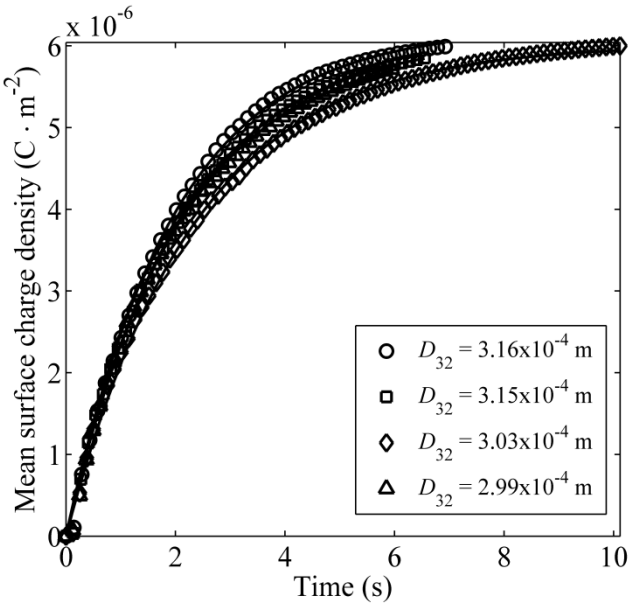

Figure B.1 The evolution of mean surface charge density of various particles with the same ESD.

Table B.2 The charging coefficients of various particles with the same ESD.

ID	D_{32} (m)	k_c
I	3.16×10^{-4}	0.50
II	3.15×10^{-4}	0.48
III	3.03×10^{-4}	0.43
IV	2.99×10^{-4}	0.49

Figure B.1 shows the mean surface charge density of various particles with the same ESD. The solid line is the fitting line of Eq. (6.16). The mean surface charge density of various particles increases exponentially to the same equilibrium. Generally, for particles with the same ESD, the surface charge density of particles with a larger D_{32} (D_{32} = 3.16×10^{-4} m) increase faster than that with a smaller D_{32} (D_{32} = 3.03×10^{-4} m), indicating that a larger D32 can lead to a faster charge accumulation. However, it is also found that the surface charge density of particles with D_{32} = 2.99×10^{-4} m increases faster than that with D_{32} = 3.03×10^{-4} m.

In addition, the differences between the charging coefficients of various particles with the same ESD (Table B.1) are relatively small, compared with those of various particles with the same maximum diameter (Table 6.5).

The effect of D_{32} for various particles with the same ESD on the charging process is different from the effect of D_{32} for various particles with the same maximum diameter. In Section 6.3, a smaller D_{32} leads to a smaller particle volume and a smaller fill ratio. Due to the smaller fill ratio, particles with a smaller D_{32} can mix more effectively in the rotating drum and get charged more rapidly. In this section, the fill ratios in the rotating drum for various particles are identical. Therefore, the differences between the charging coefficients of various particles with the same ESD (Table B.1) are relatively small. In addition, a larger D_{32} lead to a larger sphericity. Particles with larger sphericity may tend to rotate and roll in the rotating drum more easily, which can result in a faster charging process. However, how the shape of the particle can alter the mode of contact (sliding, bouncing and rotating) (Ireland, 2010) and the relevant charging process need to be further determined.

APPENDIX C AN EXAMPLE OF INPUT FILE

The DEM-CFD program needs to read the model setup from the input file in order to perform the simulation. The model setup includes the calculation domain, properties of particles and physical walls, control parameters for the simulation (e.g. time step and number of cycles) and other relevant parameters for plotting and outputting information. An example of input files for contact electrification and electrostatic interactions in fluidization is listed below.

C.1. Deposition of particles in a column

```
*Set up the calculation domain
start 0.011 0.041 0.0005 1804 5000 15 log
Deposition

* 2-D simulation
2-D
*specify particle properties
*Diameter
dia 0.0001  1

*Elastic modulus
ymd 8.7e9 1
ymd 8.7e9 2
ymd 210e9 3

*Poisson ratio
prat 0.30 1
prat 0.30 2
prat 0.30 3
```

```
*Density
dens 1.5e3 1
dens 1.5e3 2
dens 7.8e3 3

*Friction P-P and P-W
fric 0.30 1
fric 0.30 2
fric 0.30 3
fric 0.30 4
fric 0.30 5
fric 0.30 6

*Large yield strength limit to ensure elastic deformation
yie 1.9306e30 1
yie 1.9306e30 2
yie 1.9306e30 3
yie 1.9306e30 6

*P-P & P-w damping
damp 0.05 0.5 1 0 1
damp 0.10 0.5 1 0 0

*Gravitational acceleration
grav 0.0 -9.81  0.0

*Physical walls for column
dwall  fp(0.0005 0.0005 0.00025  0.0055 0.0005 0.00025) vel(0.0 0.0 0.0) mat(3)
dwall  fp(0.0005 0.0005 0.00025  0.0005 0.0405 0.00025) vel(0.0 0.0 0.0) mat(3)
dwall  fp(0.0055 0.0005 0.00025  0.0055 0.0405 0.00025) vel(0.0 0.0 0.0) mat(3)
```

```
*specify "agglomerate" region for generating particles

agglom cub 1  0.0005 0.0055 0.0005 0.04 0.0 0.0005

*Randomly generate particles

rgenerate  1250 1 1 1
rgenerate  1250 1 2 1

*Reduce time step by the fraction
frac 0.3

*Plot setting
anim on 50000
layers 20
plot wal fvel ball

*output setting
vtp ball fcel wall
cyc 50000
vtp ball fcel
cyc 50000
vtp ball fcel
cyc 50000
vtp ball fcel
cyc 50000
vtp ball fcel
cyc 50000
vtp ball fcel
cyc 50000
vtp ball fcel
cyc 50000
vtp ball fcel
cyc 50000
```

```
vtp ball fcel
cyc 50000
vtp ball fcel
cyc 50000
vtp ball fcel
cyc 50000
vtp ball fcel
*Save restart file
save 001sav

……

*Stop the simulation
stop
```

C.2. Fluidization

```
*restart from the deposition for fluidization
res 005sav
Fluidization

*Introduce the gas
gas

*Switch on the electrostatic interaction (flag)
electrostatics 6

*Switch on the contact electrification (flag)
chd 3

*Assign work function potentials to materials
```

```
wkf 5.9 1
wkf 4.1 2
wkf 3.5 3

*Assign initial charge to materials
charge 0.0e-13 0.0e-13 5.0 1
charge 0.0e-13 0.0e-13 5.0 2
charge 0.0e-13 0.0e-13 5.0 3


*Plot setting
anim on 50000
plot wal ball fvel

*Output setting
vtp bal fcel wal
cyc 500000
vtp ball fcel
cyc 500000
vtp ball fcel
cyc 500000
vtp ball fcel
cyc 500000
vtp ball fcel
cyc 500000
vtp ball fcel
cyc 500000
vtp ball fcel
cyc 500000
vtp ball fcel
cyc 500000
vtp ball fcel
cyc 500000
vtp ball fcel
```

cyc 500000
vtp ball fcel
cyc 500000
vtp ball fcel
save 001flu

……

*Stop simulation
Stop

C.3. CFD setup

Hydrodynamics model	PGF
X fluid cells in bed	10
Y fluid cells in bed	1
Z fluid cells in bed	80
Bed x-origin, xb0	0.0005
Bed y-origin, yb0	0.0000
Bed z-origin, zb0	0.0005
Bed x-dimension, xbed (m)	0.0050
Bed y-dimension, ybed (m)	0.0005
Bed z-dimension, zbed (m)	0.0405
Maximum Newton method iterates, itm_new	1000
Maximum ICG Method Iterates,itm_icg	1000
Relative error Newton iterates, eps_new	1.0e-6
Relative error ICG iterates, eps_icg	1.0e-12
Left boundary cell-flag, hxl	3
Right boundary cell-flag, hxh	3
Back boundary cell-flag, hyl	3

Front boundary cell-flag, hyh	3
Bottom boundary cell-flag, hzl	4
Top boundary cell-flag, hzh	6
Fluid temperature, TK (K)	293.0
Fluid shear viscosity, Mhu_gas (kg/ms)	1.8e-5
Fluid bulk viscosity, Labda_gas (kg/ms)	0.0
Average gas molar mass, M_gas (kg/mol)	2.88e-2
Initial x-fluid velocity (m/s)	0.0
Initial y-fluid velocity (m/s)	0.0
Initial z-fluid velocity (m/s)	0.0
Initial fluid pressure (pa)	101325.0
Left boundary fluid velocity (m/s)	0.0
Right boundary fluid velocity (m/s)	0.0
Back boundary fluid velocity (m/s)	0.0
Front boundary fluid velocity (m/s)	0.0
Bottom boundary fluid velocity (m/s)	0.100
Top boundary fluid velocity (m/s)	0.0
Left boundary fluid pressure (Pa)	101325.0
Right boundary fluid pressure (m/s)	101325.0
Back boundary fluid pressure (m/s)	101325.0
Front boundary fluid pressure (m/s)	101325.0
Bottom boundary fluid pressure (m/s)	101325.0
Top boundary fluid pressure (m/s)	101325.0
Number of obstacles, nobs	0

APPENDIX D SELECTIONS OF DEVELOPED CODES

The contact electrification and electrostatic interaction models are implemented into the DEM-CFD code (Kafui et al., 2002). For contact electrification, the charge transfer is considered when the particles are separated after contact, which is implemented in the Subroutine *hford*. For electrostatic interactions, the direct truncation and hybrid particle-cell methods are implemented into the Subroutine *cycle* to determine the forces in each step. The developed codes for contact electrification and electrostatic interactions are listed in this appendeix.

D.1. Codes for contact electrification

Subroutine hford

```
! contact force calculation
…….

! for cotact charging, find the maximum contact radius

      if(chdflag)then
            c(33)=max(c(33),c(17))
      endif

……

! if contact is about to be deleted (seperation) , transfer the charge and then
!reset the maximum contact radius c(33)
```

```
        if(chdflag)then
                if(c(33)>0.0)then
                        sss=pi*c(33)*c(33)
                        kq0a=260.0e-9/(4*8.854e-12*pi*ra*ra)

! linear superposition is assumed, potentials on particles are calculated separately

                        qqq1=wkf(itpm1)+kq0a*b1(37)
                        if(wflag)then           ! if particle – wall contact
                                if(chd_nu==1.or.chd_nu==3)then
                                        qqq2=wkf(itpm2)
                                else
                                        goto 500
                                endif
                        else                    ! if particle – particle contact
                                if(chd_nu==2.or.chd_nu==3)then
                                       kq0b=260-9/(4*8.854e-12*pi*rb*rb)
                                        qqq2=wkf(itpm2)+kq0b*b2(37)
                                else
                                        goto 500
                                endif
                        endif
! calculate the transferred charge and distribute the charge to particles; wall is ignored.
                        qqq0=kq1*sss*(qqq1-qqq2)
                        b1(37)=b1(37)-qqq0
                        if(.not.wflag) b2(37)=b2(37)+qqq0
                        !write(10030,'(3e15.6)') ntot*tdel,b1(37), c(33)
                endif
        500     c(33)=-1.0e-30
 endif
```

D.2. Codes for electrostatic interactions

```
Subroutine cylcle
! main loop to update particle & wall information
…….
! map particles into cells (boxesv)
                    if (elecflag) then
                        if(e_nu>=4)then
                            boxesv(1:max_boxes)%np=0
                            boxesv(1:max_boxes)%nw=0
                            boxesv(1:max_boxes)%charge=0
                            boxmin(1:3)=nx(1:3)
                            boxmax(1:3)=1
                            nxy=nx(1)*nx(2)
                            do i=1, nball
                                pp=(i-1)*nvarb+1
                                nbx=int((a(pp)+a(pp+3))/del(1))+1
                                if(nbx<boxmin(1))boxmin(1)=nbx
                                if(nbx>boxmax(1))boxmax(1)=nbx
                                nby=int((a(pp+1)+a(pp+4))/del(2))+1
                                if(nby<boxmin(2))boxmin(2)=nby
                                if(nby>boxmax(2))boxmax(2)=nby
                                nbz=int((a(pp+2)+a(pp+5))/del(3))+1
                                if(nbz<boxmin(3))boxmin(3)=nbz
                                if(nbz>boxmax(3))boxmax(3)=nbz
                                nbxyz=nbx+nx(1)*(nby-1)+nxy*(nbz-1)
                                boxesv(nbxyz)%np=boxesv(nbxyz)%np+1
                                boxesv(nbxyz)%part(boxesv(nbxyz)%np)=pp
                                boxesv(nbxyz)%charge =
boxesv(nbxyz)%charge + a(pp + 36)
                                !write(lunw,*)nbxyz
```

```
                                        enddo
                                        do i=1,nball
                                                call sselec(i)
                                        enddo

                                else
! deprecated due to wrong truncation method;
                                        do i=1,nball
                                                call elecforce(i)
                                        enddo
                                endif

……

end subroutine cycle

subroutine sselec(i)
        use grcom
        use fxconst
        use ioproc
        implicit none
        integer, intent (in) :: i
        integer:: iab,iab1,iab2,ibb
        real :: r_cut,xcall(3),l(3),ll,llen,ef(3),eff
        integer::ii,jj,kk,iii,jjj,nw
        integer::nbmin(3),nbmax(3),nxy,nbxyz
        real :: x0,y0,z0,a0,b0,c0,d0,wx,wy,wz,dd,ddd,tt,ei

        iab=(i-1)*nvarb+1
        if(cutr>0.0) r_cut=cutr*rmax
        nxy=nx(1)*nx(2)
        !write(lunw,*)iab,nx
```

```
        do ii = 1, 3
                iab1 = iab + ii - 1
                iab2 = iab + ii + 2
                xcall (ii) = a (iab1) + a (iab2)
        enddo

        do ii=1,3
                nbmin(ii)=int((xcall(ii)-r_cut)/del(ii))+1
                if(nbmin(ii)<1) nbmin(ii)=1
                nbmax(ii)=int((xcall(ii)+r_cut)/del(ii))+1
                if(nbmax(ii)>nx(ii)) nbmax(ii)=nx(ii)
        enddo
        !write(lunw,*)(nbmin(ii),ii=1,3)
        !write(lunw,*)(nbmax(jj),jj=1,3)

!!! p - p calculation
        do kk=nbmin(3),nbmax(3)
                do jj=nbmin(2),nbmax(2)
                        do ii=nbmin(1),nbmax(1)
                                nbxyz=ii+nx(1)*(jj-1)+nxy*(kk-1)
                                !write(lunw,*)nbxyz
                                if(boxesv(nbxyz)%np>0)then
                                        do iii=1,boxesv(nbxyz)%np
                                                ibb=boxesv(nbxyz)%part(iii)
                                                ll=0.0
                                                if(ibb==iab) cycle
                                                do jjj=1,3
                                                        l(jjj)=xcall(jjj)-a(ibb+jjj-1)-a(ibb+jjj+2)
                                                        ll=ll+l(jjj)**2
                                                enddo
                                                !write(lunw,*)ll
                                                if(e_nu==4)then  ! DT method
```

```
                                        if(ll>(r_cut**2.0)) cycle
                                    endif
                                    llen=sqrt(ll)
                                    eff=es*a(iab+36)*a(ibb+36)/ll
                                    !write(lunw,*)eff
! p-p force in each direction
                                    do jjj=1,3
                                    a(iab+17+jjj)=a(iab+17+jjj)+eff*l(jjj)/llen
                                    enddo
                                enddo
                            endif
                        enddo
                    enddo
                enddo

                !!! p - m calculation, HPC method
                if(e_nu==5)then
                    if(nbmin(3)>boxmin(3))then
                        !call mpforce(1,nx(1),1,nx(2),1,nbmin(3)-1,nxy,iab,xcall)
                        call
mpforce(boxmin(1),boxmax(1),boxmin(2),boxmax(2),boxmin(3),nbmin(3)-1,nxy,iab,xcall)
                    endif
                    if(nbmax(3)<boxmax(3))then
                        !call mpforce(1,nx(1),1,nx(2),nbmax(3)+1,nx(3),nxy,iab,xcall)
                        call
mpforce(boxmin(1),boxmax(1),boxmin(2),boxmax(2),nbmax(3)+1,boxmax(3),nxy,iab,xcall)
                    endif
                    if(nbmin(2)>boxmin(2))then
                        !call mpforce(1,nx(1),1,nbmin(2)-1,nbmin(3),nbmax(3),nxy,iab,xcall)
                        call mpforce(boxmin(1),boxmax(1),boxmin(2),nbmin(2)-
1,nbmin(3),nbmax(3),nxy,iab,xcall)
                    endif
```

```
                if(nbmax(2)<boxmax(2))then
                        !call
mpforce(1,nx(1),nbmax(2)+1,nx(2),nbmin(3),nbmax(3),nxy,iab,xcall)
                        call
mpforce(boxmin(1),boxmax(1),nbmax(2)+1,boxmax(2),nbmin(3),nbmax(3),nxy,iab,xcall)
                endif
                if(nbmin(1)>boxmin(1))then
                        !call mpforce(1,nbmin(1)-
1,nbmin(2),nbmax(2),nbmin(3),nbmax(3),nxy,iab,xcall)
                        call mpforce(boxmin(1),nbmin(1)-
1,nbmin(2),nbmax(2),nbmin(3),nbmax(3),nxy,iab,xcall)
                endif
                if(nbmax(1)<boxmax(1))then
                        !call
mpforce(nbmax(1)+1,nx(1),nbmin(2),nbmax(2),nbmin(3),nbmax(3),nxy,iab,xcall)
                        call
mpforce(nbmax(1)+1,boxmax(1),nbmin(2),nbmax(2),nbmin(3),nbmax(3),nxy,iab,xcall)
                endif
        endif

! image force calculation

        if(e_nu==6)then
                do ii=1,nwall
                        nw=m2+(ii-1)*nvarw
                        d0=a(nw)
                        a0=a(nw+1)
                        b0=a(nw+2)
                        c0=a(nw+3)
                        x0=a(iab)+a(iab+3)
                        y0=a(iab+1)+a(iab+4)
                        z0=a(iab+2)+a(iab+5)
```

```
!plane:ax+by+cz=d  point:(x0,y0,z0) perpendicular foot:w(x,y,z),parameter: tt
!so: w=(x0+a*tt,y0+b*tt,z0+c*tt)
!introduce w with parameter tt into plane,
!then tt = (d-(a*x0+b*y0+c*z0))/(a**2+b**2+c**2)
                        tt=(d0-(a0*x0+b0*y0+c0*z0))/(a0**2+b0**2+c0**2)
                        wx=x0+a0*tt
                        wy=y0+b0*tt
                        wz=z0+c0*tt
                        if(wx>=(a(nw+25)-1.0e-6).and.wx<=(a(nw+26)+1.0e-
6).and.wy>=(a(nw+27)-1.0e-6).and.&
                                &wy<=(a(nw+28)+1.0e-6).and.wz>=(a(nw+29)-1.0e-
6).and.wz<=(a(nw+30)+1.0e-6))then
                                dd=(2.0*(x0-wx))**2+(2.0*(y0-wy))**2+(2.0*(z0-wz))**2
                                if(dd>r_cut**2.0)cycle
                                ddd=sqrt(dd)
                                ei=es*a(iab+36)*a(iab+36)/dd
                                !ei=e*charge(itypmiab)*charge(itypmiab)/dd
                                a(iab+18)=a(iab+18)+ei*(2*(wx-x0)/ddd)
                                a(iab+19)=a(iab+19)+ei*(2*(wy-y0)/ddd)
                                a(iab+20)=a(iab+20)+ei*(2*(wz-z0)/ddd)
                        endif
                !       eix=eix+ei*(2*(wx-x0)/ddd)
                !       eiy=eiy+ei*(2*(wy-y0)/ddd)
                !       eiz=eiz+ei*(2*(wz-z0)/ddd)

                enddo
        endif
end subroutine sselec


subroutine mpforce(nbxmin,nbxmax,nbymin,nbymax,nbzmin,nbzmax,nxy,iab,xcall)
! particle – cell force calculation
```

```
        use grcom
        use fxconst
        use ioproc
        implicit none
        integer, intent (in) :: nbxmin,nbxmax,nbymin,nbymax,nbzmin,nbzmax,nxy,iab
        real, intent(in) :: xcall(3)
        real :: l(3),ll,eff,llen
        integer:: ii,jj,kk,iii,jjj,nbxyz

        do kk=nbzmin,nbzmax
                do jj=nbymin,nbymax
                        do ii=nbxmin,nbxmax
                                nbxyz=ii+nx(1)*(jj-1)+nxy*(kk-1)
                                if(boxesv(nbxyz)%np>0)then
                                        ll=0.0
                                        do jjj=1,3
                                                l(jjj)=xcall(jjj)-boxesv(nbxyz)%pos(jjj)
                                                ll=ll+l(jjj)**2
                                        enddo
                                        llen=sqrt(ll)
                                        eff=es*a(iab+36)*boxesv(nbxyz)%charge/ll
                                        do jjj=1,3
                                                a(iab+17+jjj)=a(iab+17+jjj)+eff*l(jjj)/llen
                                        enddo
                                endif
                        enddo
                enddo
        enddo

end subroutine mpforce
```

REFERENCES

Adachi, M., Okuyamaand, K. and Kousaka, Y. (1985) Electrostatic dispersion of aerosol carrying unipolar charge particles. **Journal of Chemical Engineering of Japan**, 18 (6): 502–509.

An, X., Yang, R., Dong, K., *et al.* (2005) Micromechanical simulation and analysis of one-dimensional vibratory sphere packing. **Physical Review Letters**, 95 (20): 205502.

Anderson, T.B. and Jackson, R.O.Y. (1967) A fluid mechanical description of fluidized beds. equations of motion. **Industrial and Engineering Chemistry Fundamentals**, 6 (4): 527–539.

Armour-Chélu, D.I. and Woodhead, S.R. (2002) Comparison of the electric charging properties of particulate materials in gas – solids flows in pipelines. **Journal of Electrostatics**, 56: 87–101.

Arridge, R.G.C. (1967) The static electrification of nylon 66. **British Journal of Applied Physics**, 18: 1311–1316.

Bailey, A.G. (1984) Electrostatic phenomena during powder handling. **Powder Technology**, 37: 71–85.

Beleca, R., Abbod, M., Balachandran, W., *et al.* (2010) Investigation of electrostatic properties of pharmaceutical powders using phase doppler anemometry. **IEEE Transactions on Industry Applications**, 46: 1181–1187.

Bi, H.T. (2005) Electrostatic phenomena in gas-solids fluidized beds. **China Particuology**, 3 (6): 395–399.

Bichoutskaia, E., Boatwright, A.L., Khachatourian, A., *et al.* (2010) Electrostatic analysis of the interactions between charged particles of dielectric materials. **The Journal of Chemical Physics**, 133 (2): 024105.

Bierwisch, C., Kraft, T., Riedel, H., *et al.* (2009) Die filling optimization using three-dimensional discrete element modeling. **Powder Technology**, 196 (2): 169–179.

Bradshaw, G. and O'Sullivan, C. (2004) Adaptive medial-axis approximation for sphere-tree construction. **ACM Transactions on Graphics**, 23 (1): 1–26.

Brattain, W.H. and Bardeen, J. (1953) Surface properties of germanium. **Bell System Technical Journal**, 32: 1–41.

Cappella, B. and Dietler, G. (1999) Force-distance curves by atomic force microscopy. **Surface Science Reports**, 34 (1-3): 1–104.

Castle, G.S.P. and Schein, L.B. (1995) General model of sphere sphere insulator contact electrification. **Journal of Electrostatics**, 36 (2): 165–173.

Chaudhuri, B., Muzzio, F.J. and Tomassone, M.S. (2006) Modeling of heat transfer in granular flow in rotating vessels. **Chemical Engineering Science**, 61 (19): 6348–6360.

Chen, A.H., Bi, H.T. and Grace, J.R. (2007) Charge distribution around a rising bubble in a two-dimensional fluidized bed by signal reconstruction. **Powder Technology**, 177 (3): 113–124.

Chen, A.H., Bi, H.T. and Grace, J.R. (2003) Measurement of particle charge-to-mass ratios in a gas-solids fluidized bed by a collision probe. **Powder Technology**, 135-136: 181–191.

Chung, Y.C. and Ooi, J.Y. (2007) Influence of discrete element model parameters on bulk behavior of a granular solid under confined compression. **Particulate Science and Technology**, 26 (1): 83–96.

Cleary, P.W. (2001) Recent advances in dem modelling of tumbling mills. **Minerals Engineering**, 14 (10): 1295–1319.

Cleary, P.W. and Sawley, M.L. (2002) DEM modelling of industrial granular flows: 3d case studies and the effect of particle shape on hopper discharge. **Applied Mathematical Modelling**, 26 (2): 89–111.

Cleary, P.W., Sinnott, M. and Morrison, R. (2006) Prediction of slurry transport in sag mills using SPH fluid flow in a dynamic DEM based porous media. **Minerals Engineering**, 19 (15): 1517–1527.

Coube, O., Cocks, A.C.F. and Wu, C.Y. (2005) Experimental and numerical study of die filling, powder transfer and die compaction. **POWDER METALLURGY**, 48 (1): 68–76.

Cross, J.A. (1987) **Electrostatics: Principles, Problems and Applications**. Bristol: Adam Hilger.

Cundall, P.A. (1988) Formulation of a three-dimensional distinct element model--part i. a scheme to detect and represent contacts in a system composed of many polyhedral blocks. **International Journal of Rock Mechanics and Mining Sciences & Geomechanics Abstracts**, 25 (3): 107–116.

Cundall, P.A. and Strack, O.D.L. (1979) A discrete numerical model for granular assemblies. **Géotechnique**, 29 (1): 47–65.

Davies, D.K. (1969) Charge generation on dielectric surfaces. **Journal of Physics D: Applied Physics**, 2: 1533–1537.

Dawson, J.M. (1983) Particle simulation of plasmas. **Reviews of Modern Physics**, 55 (2): 403–447.

Derjaguin, B. V, Muller, V.M. and Toporov, Y.P. (1975) Effect of contact deformations on the adhesion of particles. **Journal of Colloid and Interface Science**, 53 (2): 314–326.

Diaz, A., Fenzel-Alexander, D., Miller, D.C., *et al.* (1990) Ionomers as charge additives. **Journal of Polymer Science Part C: Polymer Letters**, 28 (3): 75–80.

Diaz, A.F. (1998) Contact electrification of materials: the chemistry of ions on polymer surfaces. **Journal of Adhesion**, 67: 111–122.

Diaz, A.F. and Guay, J. (1993) Contact charging of organic materials: ion vs. electron transfer. **IBM Journal of Research and Development**, 37 (2): 249–260.

Duff, N. and Lacks, D.J. (2008) Particle dynamics simulations of triboelectric charging in granular insulator systems. **Journal of Electrostatics**, 66 (1-2): 51–57.

Eilbeck, J., Rowley, G., Carter, P.A., *et al.* (2000) Effect of contamination of pharmaceutical equipment on powder triboelectrification. **International Journal of Pharmaceutics**, 195 (1-2): 7–11.

Elajnaf, A., Carter, P. and Rowley, G. (2006) Electrostatic characterisation of inhaled powders: effect of contact surface and relative humidity. **European Journal of Pharmaceutical Sciences**, 29 (5): 375–384.

Engers, D.A., Fricke, M.N., Newman, A.W., *et al.* (2007) Triboelectric charging and dielectric properties of pharmaceutically relevant mixtures. **Journal of Electrostatics**, 65 (9): 571–581.

Engers, D.A., Fricke, M.N., Storey, R.P., *et al.* (2006) Triboelectrification of pharmaceutically relevant powders during low-shear tumble blending. **Journal of Electrostatics**, 64 (12): 826–835.

Esselink, K. (1995) A comparison of algorithms for long-range interactions. **Computer Physics Communications**, 87 (3): 375–395.

Favier, J.F., Abbaspour-Fard, M.H., Kremmer, M., *et al.* (1999) Shape representation of axisymmetrical, non-spherical particles in discrete element simulation using multi-element model particles. **Engineering Computations**, 16 (4): 467–480.

Felice, R. Di (1994) The voidage function for fluid-particle interaction systems. **International Journal of Multiphase Flow**, 20 (1): 153–159.

Feng, J.Q. and Hays, D.A. (2003) Relative importance of electrostatic forces on powder particles. **Powder Technology**, 135-136: 65–75.

Feng, Y.T., Han, K. and Owen, D.R.J. (2007) Coupled lattice boltzmann method and discrete element modelling of particle transport in turbulent fluid flows: computational issues. **International Journal for Numerical Methods in Engineering**, 72 (9): 1111–1134.

Gady, B., Schleef, D., Reifenberger, R., *et al.* (1996) Identification of electrostatic and van der waals interaction forces between a micrometer-size sphere and a flat substrate. **Physical Review B**, 53 (12): 8065–8070.

Goldhirsch, I. (2008) Introduction to granular temperature. **Powder Technology**, 182 (2): 130–136.

Greason, W.D. (2000) Investigation of a test methodology for triboelectrification. **Journal of Electrostatics**, 49: 245–256.

Grzybowski, B.A., Winkleman, A., Wiles, J.A., *et al.* (2003) Electrostatic self-assembly of macroscopic crystals using contact electrification. **Nature Materials**, 2 (4): 241–245.

Guardiola, J., Rojo, V. and Ramos, G. (1996) Influence of particle size, fluidization velocity and relative humidity on fluidized bed electrostatics. **Journal of Electrostatics**, 37 (1-2): 1–20.

Gui, N., Fan, J.R. and Luo, K. (2008) DEM–LES study of 3-D bubbling fluidized bed with immersed tubes. **Chemical Engineering Science**, 63 (14): 3654–3663.

Guo, Y., Kafui, K.D., Wu, C.Y., *et al.* (2009) A coupled DEM/CFD analysis of the effect of air on powder flow during die filling. **AICHE Journal**, 55 (1): 49–62.

Guo, Y., Wu, C. and Thornton, C. (2013) Modeling gas-particle two-phase flows with complex and moving boundaries using DEM-CFD with an immersed boundary method. **AICHE Journal**, 59 (4): 1075–1087.

Guo, Y., Wu, C.Y., Kafui, K.D., *et al.* (2010) Numerical analysis of density-induced segregation during die filling. **Powder Technology**, 197 (1-2): 111–119.

Guo, Y., Wu, C.-Y., Kafui, K.D., *et al.* (2011) 3d DEM/CFD analysis of size-induced segregation during die filling. **Powder Technology**, 206 (1-2, SI): 177–188.

Harper, W.R. (1967) **Contact and frictional electrification**. London: Oxford University Press.

Harper, W.R. (1951) Interpretation of experiments on frictional electrification. **Nature**, 167 (4245): 400–401.

Hassani, M. a., Zarghami, R., Norouzi, H.R., *et al.* (2013) Numerical investigation of effect of electrostatic forces on the hydrodynamics of gas–solid fluidized beds. **Powder Technology**, 246: 16–25.

Hersh, S.P. and Montgomery, D.J. (1955) Static electrification of filaments: experimental techniques and results. **Textile Research Journal**, 25 (4): 279–295.

Hockney, R.W. and Eastwood, J.W. (1988) **Computer simulation using particles**. Bristol and New York: Adam Hilger.

Hoffmann, R. (2006) DEM simulations of toner particles with an O (N log N) hierarchical tree code algorithm. **Granular Matter**, 8 (3-4): 151–157.

Hogue, C. (1998) Shape representation and contact detection for discrete element simulations of arbitrary geometries. **Engineering Computations**, 15 (2-3): 374–390.

Hogue, M.D., Buhler, C.R., Calle, C.I., *et al.* (2004) Insulator-insulator contact charging and its relationship to atmospheric pressure. **Journal of Electrostatics**, 61 (3-4): 259–268.

Hogue, M.D., Calle, C.I., Weitzman, P.S., *et al.* (2008) Calculating the trajectories of triboelectrically charged particles using discrete element modeling (dem). **Journal of Electrostatics**, 66 (1-2): 32–38.

Höhner, D., Wirtz, S., Kruggel-Emden, H., *et al.* (2011) Comparison of the multi-sphere and polyhedral approach to simulate non-spherical particles within the discrete element method: influence on temporal force evolution for multiple contacts. **Powder Technology**, 208 (3): 643–656.

Hoomans, B.P.B., Kuipers, J. a. M., Briels, W.J., *et al.* (1996) Discrete particle simulation of bubble and slug formation in a two-dimensional gas-fluidised bed: a hard-sphere approach. **Chemical Engineering Science**, 51 (1): 99–118.

Hu, G., Hu, Z., Jian, B., *et al.* (2011) On the determination of the damping coefficient of non-linear spring-dashpot system to model Hertz contact for simulation by discrete element method. **Journal of Computers**, 6 (5): 984–988.

Ireland, P.M. (2012) Dynamic particle-surface tribocharging: the role of shape and contact mode. **Journal of Electrostatics**, 70 (6): 524–531.

Ireland, P.M. (2008) The role of changing contact in sliding triboelectrification. **Journal of Physics D: Applied Physics**, 41 (2): 025305.

Ireland, P.M. (2010a) Triboelectrification of particulate flows on surfaces: part I -- experiments. **Powder Technology**, 198 (2): 189–198.

Ireland, P.M. (2010b) Triboelectrification of particulate flows on surfaces: part II -- mechanisms and models. **Powder Technology**, 198 (2): 199–210.

Ji, S.Y. and Shen, H.H. (2009) Two-dimensional simulation of the angle of repose for a particle system with electrostatic charge under lunar and earth gravity. **Journal of Aerospace Engineering**, 22 (1): 10–14.

Johnson, K.L. (1985) **Contact mechanics**. Cambridge: Cambridge University Press.

Johnson, K.L., Kendall, K. and Roberts, A.D. (1971) Surface energy and the contact of elastic solids. **Proceedings of the Royal Society of London. Series A, Mathematical and Physical Sciences**, 324 (1558): 301–313.

Kafui, K.D., Thornton, C. and Adams, M.J. (2002) Discrete particle-continuum fluid modelling of gas-solid fluidised beds. **Chemical Engineering Science**, 57 (13): 2395–2410.

Karner, S. and Urbanetz, N.A. (2011) The impact of electrostatic charge in pharmaceutical powders with specific focus on inhalation-powders. **Journal of Aerosol Science**, 42 (6): 428–445.

Ketterhagen, W.R., am Ende, M.T. and Hancock, B.C. (2009) Process modeling in the pharmaceutical industry using the discrete element method. **Journal of Pharmaceutical Sciences**, 98 (2): 442–470.

Ketterhagen, W.R., Curtis, J.S., Wassgren, C.R., *et al.* (2007) Granular segregation in discharging cylindrical hoppers: a discrete element and experimental study. **Chemical Engineering Science**, 62 (22): 6423–6439.

Kittaka, S. (1959) The generation of static charge on high polymer. **Journal of The Physical Society of Japan**, 14 (4): 532–538.

Kodam, M., Bharadwaj, R., Curtis, J., *et al.* (2009) Force model considerations for glued-sphere discrete element method simulations. **Chemical Engineering Science**, 64 (15): 3466–3475.

Kolikov, K., Ivanov, D., Krastev, G., *et al.* (2012) Electrostatic interaction between two conducting spheres. **Journal of Electrostatics**, 70 (1): 91–96.

Kong, C.M. and Lannutti, J.J. (2000) Localized densification during the compaction of alumina granules: the stage I – II transition. **Journal of the American Ceramic Society**, 83 (4): 685–690.

Kornfeld, M.I. (1976) Frictional electrification. **Journal of Physics D: Applied Physics**, 9 (8): 1183–1192.

Kremmer, M. and Favier, J.F. (2001) A method for representing boundaries in discrete element modelling—part II kinematics. **International Journal for Numerical Methods in Engineering**, 51 (12): 1423–1436.

Kuang, S.B., Chu, K.W., Yu, A.B., *et al.* (2008) Computational investigation of horizontal slug flow in pneumatic conveying. **Industrial & Engineering Chemistry Research**, 47 (2): 470–480.

Kuo, H.P., Knight, P.C., Parker, D.J., *et al.* (2002) The influence of DEM simulation parameters on the particle behaviour in a v-mixer. **Chemical Engineering Science**, 573621–3638.

Kwok, P.C.L. and Chan, H.K. (2008) Effect of relative humidity on the electrostatic charge properties of dry powder inhaler aerosols. **Pharmaceutical Research**, 25 (2): 277–288.

Lachiver, E.D., Abatzoglou, N., Cartilier, L., *et al.* (2006) Insights into the role of electrostatic forces on the behavior of dry pharmaceutical particulate systems. **Pharmaceutical Research**, 23 (5): 997–1007.

Lacks, D.J. and Mohan Sankaran, R. (2011) Contact electrification of insulating materials. **Journal of Physics D: Applied Physics**, 44 (45): 453001.

LaMarche, K.R., Liu, X., Shah, S.K., *et al.* (2009) Electrostatic charging during the flow of grains from a cylinder. **Powder Technology**, 195 (2): 158–165.

LaMarche, K.R., Muzzio, F.J., Shinbrot, T., *et al.* (2010) Granular flow and dielectrophoresis: the effect of electrostatic forces on adhesion and flow of dielectric granular materials. **Powder Technology**, 199 (2): 180–188.

Langston, P.A., Tüzün, U. and Heyes, D.. (1994) Continuous potential discrete particle simulations of stress and velocity-fields in hoppers—transition from fluid to granular flow. **Chemical Engineering Science**, 491259–1275.

Langston, P.A., Tüzün, U. and Heyes, D.M. (1995) Discrete element simulation of granular flow in 2D and 3D hoppers—dependence of discharge rate and wall stress on particle interactions. **Chemical Engineering Science**, 50967–987.

Latham, J.-P. and Munjiza, a (2004) The modelling of particle systems with real shapes. **Philosophical Transactions. Series A, Mathematical, Physical, and Engineering Sciences**, 362 (1822): 1953–1972.

Li, J. and Kuipers, J. a. M. (2007) Effect of competition between particle–particle and gas–particle interactions on flow patterns in dense gas-fluidized beds. **Chemical Engineering Science**, 62 (13): 3429–3442.

Li, J. and Kuipers, J. a. M. (2002) Effect of pressure on gas–solid flow behavior in dense gas-fluidized beds: a discrete particle simulation study. **Powder Technology**, 127 (2): 173–184.

Li, L. and Ma, W. (2011) Experimental study on the effective particle diameter of a packed bed with non-spherical particles. **Transport in Porous Media**, 89 (1): 35–48.

Li, L., Thornton, C. and Wu, C. (2000) Impact behaviour of elastoplastic spheres with a rigid wall. **Proceedings of the Institution of Mechanical Engineers, Part C: Journal of Mechanical Engineering Science**, 214 (8): 1107–1114.

Li, Y., Zhang, J. and Fan, L. (1999) Numerical simulation of gas-liquid-solid fluidization systems using a combined CFD-VOF-DPM method: bubble wake behavior. **Chemical Engineering Science**, 54 (21): 5101–5107.

Liao, C.-C., Hsiau, S.-S. and Huang, T.-Y. (2011) The effect of vibrating conditions on the electrostatic charge in a vertical vibrating granular bed. **Powder Technology**, 208 (1): 1–6.

Lim, E.W.C., Zhang, Y. and Wang, C.H. (2006) Effects of an electrostatic field in pneumatic conveying of granular materials through inclined and vertical pipes. **Chemical Engineering Science**, 61 (24): 7889–7908.

Lim, W.L. and McDowell, G.R. (2007) The importance of coordination number in using agglomerates to simulate crushable particles in the discrete element method. **Geotechnique**, 57 (8): 701–705.

Lin, X. and Ng, T.-T. (1997) A three-dimensional discrete element model using arrays of ellipsoids. **Géotechnique**, 47 (2): 319 –329.

Liu, G., Marshall, J.S., Li, S.Q., *et al.* (2010) Discrete-element method for particle capture by a body in an electrostatic field. **International Journal for Numerical Methods in Engineering**, 84 (13): 1589–1612.

Liu, L., Seyam, A.M. and Oxenham, W. (2013) Frictional electrification on polymeric flat surfaces. **Journal of Engineered Fibers and Fabrics**, 8 (1): 126–136.

Liu, L.F., Zhang, Z.P. and Yu, A.B. (1999) Dynamic simulation of the centripetal packing of mono-sized spheres. **Physica A: Statistical and Theoretical Physics**, 268 (3-4): 433–453.

Loeb, L.B. (1945) The basic mechanisms of static electrification. **Science**, 102 (2658): 573–576.

Lowell, J. (1975) Contact electrification of metals. **Journal of Physics D: Applied Physics**, 853–63.

Lowell, J. and Roseinnes, A.C. (1980) Contact electrification. **Advances in Physics**, 29 (6): 947–1023.

Lu, L.-S. and Hsiau, S.-S. (2005) Mixing in vibrated granular beds with the effect of electrostatic force. **Powder Technology**, 160 (3): 170–179.

Luding, S. (1997) Stress distribution in static two dimensional granular model media in the absence of friction. **Physical Review E**, 554720–4729.

Luty, B.A. and VanGunsteren, W.F. (1996) Calculating electrostatic interactions using the particle-particle particle-mesh method with nonperiodic long-range interactions. **Journal of Physical Chemistry**, 100 (7): 2581–2587.

Martin, C.L., Bouvard, D. and Delette, G. (2006) Discrete element simulations of the compaction of aggregated ceramic powders. **Journal of the American Ceramic Society**, 89 (11): 3379–3387.

Masuda, H. (2009) Dry dispersion of fine particles in gaseous phase. **Advanced Powder Technology**, 20 (2): 113–122.

Masuda, H. and Iinoya, K. (1978) Electrification of particles by impact on inclined metal plates. **AICHE JOURNAL**, 24 (6): 950–956.

Masuda, H., Komatsu, T. and Iinoya, K. (1976) The static electrification of particles in gas-solids pipe flow. **AICHE Journal**, 22 (3): 558–564.

Masui, N. and Murata, Y. (1983) Electrification of polymer particles by impact on a metal plate. **Japanese Journal of Applied Physics Part 1-Regular Papers Short Notes & Review Papers**, 22 (6): 1057–1062.

Matsusaka, S., Ghadiri, M. and Masuda, H. (2000) Electrification of an elastic sphere by repeated impacts on a metal plate. **Journal of Physics D: Applied Physics**, 33 (18): 2311–2319.

Matsusaka, S., Maruyama, H., Matsuyama, T., *et al.* (2010) Triboelectric charging of powders: a review. **Chemical Engineering Science**, 65 (22): 5781–5807.

Matsuyama, T., Ogu, M., Yamamoto, H., *et al.* (2003) Impact charging experiments with single particles of hundred micrometre size. **Powder Technology**, (135-136): 14–22.

Matsuyama, T. and Yamamoto, H. (1995a) Characterizing the electrostatic charging of polymer particles by impact charging experiments. **Advanced Powder Technology**, 6 (3): 211–220.

Matsuyama, T. and Yamamoto, H. (1997) Charge-relaxation process dominates contact charging of a particle in atmospheric condition .2. the general model. **Journal of Physics D-Applied Physics**, 30 (15): 2170–2175.

Matsuyama, T. and Yamamoto, H. (1995b) Electrification of single polymer particles by successive impacts with metal targets. **Industry Applications, IEEE Transactions On**, 31 (6): 1441–1445.

Matsuyama, T. and Yamamoto, H. (2006) Impact charging of particulate materials. **Chemical Engineering Science**, 61 (7): 2230–2238.

Mazumder, M.K., Wankum, D.L., Sims, R.A., *et al.* (1997) Influence of powder properties on the performance of electrostatic coating process. **Journal of Electrostatics**, 40&41369–374.

McCarty, L.S. and Whitesides, G.M. (2008) Electrostatic charging due to separation of ions at interfaces: contact electrification of ionic electrets. **Angewandte Chemie International Edition**, 47 (12): 2188–2207.

McCarty, L.S., Winkleman, A. and Whitesides, G.M. (2007a) Electrostatic self-assembly of polystyrene microspheres by using chemically directed contact electrification. **Angewandte Chemie International Edition**, 46 (1-2): 206–209.

McCarty, L.S., Winkleman, A. and Whitesides, G.M. (2007b) Ionic electrets: electrostatic charging of surfaces by transferring mobile ions upon contact. **Journal of the American Chemical Society**, 129 (13): 4075–4088.

Medley, J.A. (1953) Frictional electrification of polar polymers. **Nature**, 171 (4363): 1077.

Melitz, W., Shen, J., Kummel, A.C., *et al.* (2011) Kelvin probe force microscopy and its application. **Surface Science Reports**, 66 (1): 1–27.

Mindlin, R.D. (1949) Compliance of elastic bodies in contact. **Journal of Applied Mechanics-Transactions of The ASME**, 16259–268.

Mindlin, R.D. and Deresiewicz, H. (1953) Elastic spheres in contact under varying oblique forces. **Journal of Applied Mechanics-Transactions of The ASME**, 20 (3): 327–344.

Mirtich, B. (1996) Fast and accurate computation of polyhedral mass properties. **Journal of Graphics Tools**, 1 (2): 31–50.

Mohammad, D.R.A., Khan, N.U. and Ramamurti, V. (1995) On the role of rayleigh damping. **Journalof Sound and Vibration**, 185 (2): 207–218.

Moore, A.D. (1973) **Eletrostatics and its applications**. London: John Wiley & Sons, Inc.

Moreno-Atanasio, R., Antony, S.J. and Williams, R.A. (2009) Influence of interparticle interactions on the kinetics of self-assembly and mechanical strength of nanoparticulate aggregates. **Particuology**, 7 (2): 106–113.

Morrison, R.D. and Cleary, P.W. (2004) Using DEM to model ore breakage within a pilot scale sag mill. **Minerals Engineering**, 17 (11-12): 1117–1124.

Moyle, B.D. and Hughes, J.F. (1985) Powder coating - corona versus tribo charging. **Journal of Electrostatics**, 16 (2-3): 277–286.

Müller, C.R., Holland, D.J., Sederman, A.J., *et al.* (2008) Granular temperature: comparison of magnetic resonance measurements with discrete element model simulations. **Powder Technology**, 184 (2): 241–253.

Munjiza, A. and Latham, J.P. (2004) Comparison of experimental and FEM/DEM results for gravitational deposition of identical cubes. **Engineering Computations**, 21249–264.

Nakajima, Y. and Sato, T. (1999) Calculation of electrostatic force between two charged dielectric spheres by the re-expansion method. **Journal of Electrostatics**, 45 (3): 213–226.

Nifuku, M. and Katoh, H. (2003) A study on the static electrification of powders during pneumatic transportation and the ignition of dust cloud. **Powder Technology**, 135-136234–242.

Nwose, E.N., Pei, C. and Wu, C.-Y. (2011) Modelling die filling with charged particles using dem/cfd. **Particuology**,

Parisi, D.R., Masson, S. and Martinez, J. (2004) Partitioned distinct element method simulation of granular flow within industrial silos. **Journal of Engineering Mechanics**, 130 (7): 771–779.

Pei, C., England, D., Byard, S., *et al.* (2012) A discrete element model for contact electrification. In: C.-Y. Wu & W Ge (eds.). **Particulate Materials: Synthesis, Characterisation, Processing and Modelling**. The Royal Society of Chemistry. pp. 233–239.

Pei, C., Wu, C.-Y., Adams, M., *et al.* (2013a) A DEM model for contact electrification of irregular shaped particles. **AIP Conference Proceedings**, 1542 (1): 101–104.

Pei, C., Wu, C.-Y., Byard, S., *et al.* (2010) Numerical analysis of electrostatic effects during powder deposition using DEM/CFD. **Journal of Pharmacy and Pharmacology**, 62 (10, SI): 1454–1455.

Pei, C., Wu, C.-Y., England, D., *et al.* (2013b) Numerical analysis of contact electrification using DEM–CFD. **Powder Technology**, DOI: 10.1016/j.powtec.2013.04.014

Potapov, A. V, Hunt, M.L. and Campbell, C.S. (2001) Liquid–solid flows using smoothed particle hydrodynamics and the discrete element method. **Powder Technology**, 116 (2-3): 204–213.

Potapov, A. V. and Campbell, C.S. (1996) Computer simulation of hopper flow. **Physics of Fluids**, 8 (11): 2884.

Pu, Y., Mazumder, M. and Cooney, C. (2009) Effects of electrostatic charging on pharmaceutical powder blending homogeneity. **Journal of Pharmaceutical Sciences**, 98 (7): 2412–2421.

Rajamani, R.K., Mishra, B.K., Venugopal, R., *et al.* (2000) Discrete element analysis of tumbling mills. **Powder Technology**, 109 (1-3): 105–112.

Ren, J., Lu, S., Shen, J., *et al.* (2001) Electrostatic dispersion of fine particles in the air. **Powder Technology**, 120 (3): 187–193.

Di Renzo, A. and Di Maio, F.P. (2004) Comparison of contact-force models for the simulation of collisions in dem-based granular flow codes. **Chemical Engineering Science**, 59 (3): 525–541.

Richardson, D.C., Walsh, K.J., Murdoch, N., *et al.* (2011) Numerical simulations of granular dynamics: i. hard-sphere discrete element method and tests. **Icarus**, 212 (1): 427–437.

Rokkam, R.G., Sowinski, a., Fox, R.O., *et al.* (2013) Computational and experimental study of electrostatics in gas–solid polymerization fluidized beds. **Chemical Engineering Science**, 92146–156.

Rowley, G. (2001) Quantifying electrostatic interactions in pharmaceutical solid systems. **International Journal of Pharmaceutics**, 227 (1-2): 47–55.

Saeki, M. (2006) Vibratory separation of plastic mixtures using triboelectric charging. **Particulate Science and Technology**, 24 (2): 153–164.

Saleh, K., Traore Ndama, A. and Guigon, P. (2011) Relevant parameters involved in tribocharging of powders during dilute phase pneumatic transport. **Chemical Engineering Research and Design**, 89 (12): 2582–2597.

Schein, L.B. and LaHa, M. (1991) Electrostatic charging of two insulating powders. **Journal of Applied Physics**, 69 (10): 6817–6826.

Schein, L.B., LaHa, M. and Novotny, D. (1992) Theory of insulator charging. **Physics Letters A**, 167 (1): 79–83.

Seville, J.P.K., Tüzün, U. and Clift, R. (1997) **Processing of particulate solids**. London: Blackie Academic & Professional.

Sharmene Ali, F., Adnan Ali, M., Ayesha Ali, R., *et al.* (1998) Minority charge separation in falling particles with bipolar charge. **Journal of Electrostatics**, 45 (2): 139–155.

Shimada, J., Kaneko, H. and Takada, T. (1993) Efficient calculations of coulombic interactions in biomolecular simulations with periodic boundary-conditions. **Journal of Computational Chemistry**, 14 (7): 867–878.

Shinohara, K., Oida, M. and Golman, B. (2000) Effect of particle shape on angle of internal friction by triaxial compression test. **Powder Technology**, 107131–136.

Shirakawa, Y., Ii, N., Yoshida, M., *et al.* (2010) Quantum chemical calculation of electron transfer at metal/polymer interfaces. **Advanced Powder Technology**, 21 (4, SI): 500–505.

Sowinski, A., Miller, L. and Mehrani, P. (2010) Investigation of electrostatic charge distribution in gas–solid fluidized beds. **Chemical Engineering Science**, 65 (9): 2771–2781.

Sowinski, A., Salama, F. and Mehrani, P. (2009) New technique for electrostatic charge measurement in gas–solid fluidized beds. **Journal of Electrostatics**, 67 (4): 568–573.

Stewart, R.L., Bridgwater, J., Zhou, Y.C., *et al.* (2001) Simulated and measured ow of granules in a bladed mixer — a detailed comparison. **Chemical Engineering Science**, 565457–5471.

Šupuk, E., Hassanpour, A., Ahmadian, H., *et al.* (2011) Tribo-electrification and associated segregation of pharmaceutical bulk powders. **KONA Powder and Particle Journal**, 29 (29): 208–223.

Šupuk, E., Zarrebini, A., Reddy, J.P., *et al.* (2012) Tribo-electrification of active pharmaceutical ingredients and excipients. **Powder Technology**, 217427–434.

Tanoue, K.-I., Yamaguchi, M. and Masuda, H. (1999) Electrostatic control of particle deposition. **Advanced Powder Technology**, 10 (2): 119–132.

Telko, M.J., Kujanpää, J. and Hickey, A.J. (2007) Investigation of triboelectric charging in dry powder inhalers using electrical low pressure impactor (ELPI^{TM}). **International Journal of Pharmaceutics**, 336 (2): 352–360.

Thomas, A., Saleh, K., Guigon, P., *et al.* (2009) Characterisation of electrostatic properties of powder coatings in relation with their industrial application. **Powder Technology**, 190 (1-2): 230–235.

Thornton, C. (1997) Coefficient of restitution for collinear collisions of elastic-perfectly plastic spheres. **Journal of Applied Mechanics**, 64 (2): 383–386.

Thornton, C. (1991) Interparticle sliding in the presence of adhesion. **Journal of Physics D: Applied Physics**, 24: 1942–1946.

Thornton, C., Ciomocos, M.. and Adams, M.. (2004) Numerical simulations of diametrical compression tests on agglomerates. **Powder Technology**, 140 (3): 258–267.

Thornton, C. and Ning, Z. (1998) A theoretical model for the stick/bounce behaviour of adhesive, elastic-plastic spheres. **Powder Technology**, 99 (2): 154–162.

Thornton, C. and Yin, K.K. (1991) Impact of elastic spheres with and without adhesion. **Powder Technology**, 65 (1-3): 153–166.

Tsuji, T., Yabumoto, K. and Tanaka, T. (2008) Spontaneous structures in three-dimensional bubbling gas-fluidized bed by parallel DEM-CFD coupling simulation. **Powder Technology**, 184 (2): 132–140.

Tsuji, Y., Kawaguchi, T. and Tanaka, T. (1993) Discrete particle simulation of 2-dimensional fluidized-bed. **Powder Technology**, 77 (1): 79–87.

Vu-Quoc, L., Lesburg, L. and Zhang, X. (2004) An accurate tangential force-displacement model for granular-flow simulations: contacting spheres with plastic deformation, force-driven formulation. **Journal of Computational Physics**, 196 (1): 298–326.

Vu-Quoc, L. and Zhang, X. (1999) An accurate and efficient tangential force-displacement model for elastic frictional contact in particle-flow simulations. **Mechanics of Materials**, 31 : 235–269.

Wadell, H. (1935) Volume, shape and roundness of quartz particles. **The Journal of Geology**, 43: 250–280.

Walton, O.R. (1993) Numerical simulation of inclined chute flows of monodisperse inelastic, frictional spheres. **Mechanics of Materials**, 16: 239–247.

Walton, O.R. and Braun, R.L. (1986) Viscosity, granular-temperature, and stress calculations for shearing assemblies of inelastic, frictional disks. **Journal of Rheology**, 30 (5): 949–980.

Wang, R., Zhou, K., Snyder, J., *et al.* (2006) Variational sphere set approximation for solid objects. **The Visual Computer**, 22 (9-11): 612–621.

Watanabe, H., Ghadiri, M., Matsuyama, T., *et al.* (2007) Triboelectrification of pharmaceutical powders by particle impact. **International Journal of Pharmaceutics**, 334 (1-2): 149–155.

Watano, S., Saito, S. and Suzuki, T. (2003) Numerical simulation of electrostatic charge in powder pneumatic conveying process. **Powder Technology**, 135: 112–117.

Wen, C.Y. and Yu, Y.H. (1966) A generalized method for predicting the minimum fluidization velocity. **AIChE Journal**, 12 (610–612): .

Wu, C.Y. (2008) DEM simulations of die filling during pharmaceutical tabletting. **Particuology**, 6 (6): 412–418.

Wu, C.Y. and Cocks, A.C.F. (2006) Numerical and experimental investigations of the flow of powder into a confined space. **Mechanics of Materials**, 38 (4): 304–324.

Wu, C.Y., Cocks, A.C.F. and Gillia, O.T. (2003) Die filling and powder transfer. **International Journal of Powder Metallurgy**, 39 (4): 51–64.

Wu, S.C., Wasan, D.T. and Nikolov, A.D. (2005) Structural transitions in two-dimensional hard-sphere systems. **Physical Review E**, 71 (0561125Part 2): .

Wu, S.C., Wasan, D.T. and Nikolov, A.D. (2008) Two-dimensional self-assembly of similarly charged granular particles. **Industrial & Engineering Chemistry Research**, 47 (15): 5005–5015.

Xiang, J. and McGlinchey, D. (2004) Numerical simulation of particle motion in dense phase pneumatic conveying. **Granular Matter**, 6 (2-3): 167–172.

Xiong, Y., Zhang, M. and Yuan, Z. (2005) Three-dimensional numerical simulation method for gas–solid injector. **Powder Technology**, 160 (3): 180–189.

Xu, B.H., Yu, a. B., Chew, S.J., *et al.* (2000) Numerical simulation of the gas–solid flow in a bed with lateral gas blasting. **Powder Technology**, 109 (1-3): 13–26.

Xu, B.H. and Yu, A.B. (1997) Numerical simulation of the gas-solid flow in a fluidized bed by combining discrete particle method with computational fluid dynamics. **Chemical Engineering Science**, 52 (16): 2785–2809.

Ye, Q., Steigleder, T., Scheibe, A., *et al.* (2002) Numerical simulation of the electrostatic powder coating process with a corona spray gun. **Journal of Electrostatics**, 54 (2): 189–205.

Yoshida, M., Shimosaka, A., Shirakawa, Y., *et al.* (2003) Estimation of electrostatic charge distribution of flowing toner particles in contact with metals. **Powder Technology**, 13523–34.

Yu, S., Guo, Y. and Wu, C.-Y. (2009) DEM/CFD modelling of the deposition of dilute granular systems in a vertical container. **Chinese Science Bulletin**, 54 (23): 4318–4326.

Zhang, Z.P., Liu, L.F, Yuan, Y.D., *et al.* (2001) A simulation study of the effects of dynamic variables on the packing of spheres. **Powder Technology**, 116 (1): 23–32.

Zhao, H., Castle, G.S.P. and Inculet, I.I. (2002) The measurement of bipolar charge in polydisperse powders using a vertical array of faraday pail sensors. **Journal of Electrostatics**, 55 (3-4): 261–278.

Zhou, Y.C., Xu, B.H., Zou, R.P., *et al.* (2003) Stress distribution in a sandpile formed on a deflected base. **Advanced Powder Technology**, 14 (4): 401–410.

Zhu, H.P., Zhou, Z.Y., Yang, R.Y., *et al.* (2008a) Discrete particle simulation of particulate systems: a review of major applications and findings. **Chemical Engineering Science**, 63 (23): 5728–5770.

Zhu, H.P., Zhou, Z.Y., Yang, R.Y., *et al.* (2007a) Discrete particle simulation of particulate systems: theoretical developments. **Chemical Engineering Science**, 62 (13): 3378–3396.

Zhu, K., Ng, W.K., Shen, S., *et al.* (2008b) Design of a device for simultaneous particle size and electrostatic charge measurement of inhalation drugs. **Pharmaceutical Research**, 25 (11): 2488–2496.

Zhu, K., Tan, R.B.H., Chen, F., *et al.* (2007b) Influence of particle wall adhesion on particle electrification in mixers. **International Journal of Pharmaceutics**, 328 (1): 22–34.